Molecular assemblies and their electric properties

Carlotti, Marco

Molecular Assemblies and Their Electric Properties

Marco Carlotti

Molecular Assemblies and Their Electric Properties

Marco Carlotti
University of Groningen, Netherlands

ISBN: 978-94-034-1543-7 (printed)
978-94-034-1542-0 (electronic)

This project was carried out in the research group Chemistry of Molecular Materials and Devices which is part of Stratingh Institute for Chemistry and Zernike Institute for Advanced Materials, University of Groningen, The Netherlands.
This work was funded by European Research Council, ERC Starting Grant 335473 (MOLECSYNCON).

Printed by: Ridderprint BV, Ridderkerk, The Netherlands
Cover Picture by Marco Carlotti

An electronic version of this dissertation is available at

http://www.rug.nl/research/portal.

university of groningen / faculty of science and engineering

rijksuniversiteit
groningen

Molecular Assemblies and their Electric Properties

Proefschrift

ter verkrijging van de graad van doctor aan de
Rijksuniversiteit Groningen
op gezag van de
rector magnificus prof. dr. E. Sterken
en volgens besluit van het College voor Promoties.

De openbare verdediging zal plaatsvinden op

vrijdag 17 mei 2019 om 16.15 uur

door

Marco Carlotti

geboren op 28 september 1989
te Pontedera, Italië

Promotores

Prof. dr. R.C. Chiechi

Prof. dr. J.C. Hummelen

Beoordelingscommissie

Prof. dr. C.A. Nijhuis

Prof. dr. L.J.A. Koster

Prof. dr. S.S. Faraji

CONTENTS

1

INTRODUCTION

Molecules are small. Very small.
And because of that, they can do funny things.[1]

It is simple to notice the incommensurable differences in chemical and physical properties of molecules compared to the collection of atoms they are made from, but, it is also remarkable to appreciate the differences that arise when the same atoms have different connections. This is obvious to the chemist, who plays around these differences to prepare and characterize new compounds, but it can also become apparent to everyone who is asked to smell few drops of exanoic acid (also known as capronic acid for the pungent odour) and its structural isomer ethyl butanoate (that smells like pineapple).

The pattern of atoms in space defines the properties of an isolated molecule — such as the dipole moment, the energy and geometry of its orbitals, or the reactivity — but also dictate the interactions that molecules can have with each other, thus affecting the macro-properties of a material. It is their small size of that allows for little changes in the structure to result in incredibly different properties: the addition of one oxygen atom to the liquid, apolar, symmetric benzene can make the solid, polar, IR (more) active phenol, while if we added the same oxygen atom to a polymer with a molecular weight of several kDa the overall effect on the material properties would be insignificant; the same can be

said even for highly-specialized molecules like proteins, as they can often perform the same tasks despite a mutation in their sequence.[2]

A thorough understanding of the interactions that play a role at the molecular level allows for careful engineering of nano-structured environments capable of showing properties that go beyond those of their respective bulk. In this sense, nanotechnology is a very broad and diverse field in which the properties of spacial arrangement of atoms in space (as in molecules and specific nanostructures) are designed and harvested to create functional materials whose characteristics are direct product of the quantum-mechanical nature of their constituents: atoms, molecules, molecular assemblies, and materials that are 'nano' in at least one of their dimension, are all able show behaviors that arise from their intrinsically small size and that cannot find analogues in a classic approach.

Chemists cover a primary role in this field. Not only they are able to synthesize new molecules and characterize them, but — more importantly — they also carry the knowledge to modify these molecules so that they can show specific properties and functions.

This thesis is about small changes in small molecules and how they affect macro and measurable properties, such as the flow of electric current between two electrodes.

1.1. A LITTLE HISTORY

When reading any piece of work about molecular electronics — from journal articles to books — one is very likely to find in the introduction a definition that describes it as the field of science that aims to the understanding of charge transport through molecules and how to use those principles to make electronic components in which the active element is one molecule thick.

Besides the fundamental interest in knowing how charges move at the nanometer scale, the motivations that drive such area are mainly two: one is that molecule are inherently small, thus offering a privileged starting point for a bottom-up miniaturization of electronics; the other has to do with the fact that, thanks to their size, their quanto-mechanic nature differs from the classical description of bulk materials and can result

in exotic behaviors which do not have a straightforward parallel in silicon technology.

Surprisingly enough, these are not different from the reasons that laid the basis for the field of molecular electronics more than 60 years ago: in the opening speech of a jointed conference between the American Air Research and Development Command and the National Security Industrial Association in 1958, Colonel C.H. Lewis, finding himself unhappy with the slow pace at which progress was made in the scaling down of transistors, proposed that molecules should be used as a starting point for electronics, since they are not only small but also "their inherent molecular structure will exhibit certain electronics properties phenomena" which can enable us to "tailor materials with predetermined characteristics".[3] The conference title was 'Molecular Electronics', in line with the 'Molecular Engineering' approach captained by von Hippel few years before.[4]

Nowadays, with 10 nm-transistors commercially available and the state-of-the-art research working on 5 nm-nodes, the technology for the production of silicon-based electronics is reaching the molecular dimensions, thus making the 'size' argument in favour of molecular electronics a weak one. On the other hand, the quantum nature of molecules unarguably allows for interesting functions: this was already recognized, in 1974, by Aviram and Ratner that proposed a single molecule that could act as a diode when placed between two electrodes.[5] The issue molecular electronics was — and still largely is — the experimental challenge of finding ways to contact molecules and harness these functions to translate them to actual devices.

Despite the fact that tunnelling junctions comprising organic molecules were characterized as early as in 1971,[6] the lack of wide-spread experimental methodologies and technological limitations for the measurement and the characterization of molecular junctions restrained the expansion of the field. The inventions of atomic force and scan tunnelling microscopy techniques from IBM in Zurich during the 80s injected new interest in the field, providing new experimental platforms to contact molecules and resolve materials with atomistc detail.[7] The application of these techniques to measure molecular conductance, pioneered by research groups like that of James Tour,[8] stimulated the interest of chemists, physicists, and theoretical groups, which resulted in the boom in publications concerning molecular electronics in the early 2000s (Figure 1.1).

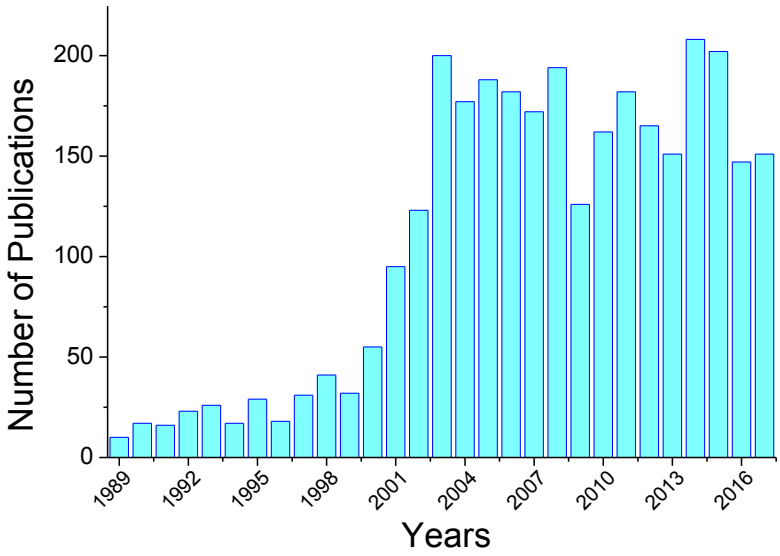

Figure 1.1 Number of publications and conference abstracts containing 'Molecular Electronics' in the title, abstract, or main text per year from 1989.

As experimental data started flowing in, stimulating the research in developing the theory behind charge transport in molecular junctions, new inputs and ideas came from theoretical groups that were craving for validation and the need for new experimental platforms.[9]

The developing of large-area techniques, able to contact areas covering billions of molecules, and their systematic study, allowed better focus on the engineering challenges and the practical problems that characterize the production of devices that we can integrate with our current electronics.[10, 11] Thanks to this approach, the first electronic component based on molecular junctions, invented by McCreary and collaborators, was commercialized for use in audio modulation.[12] Companies like Philipps and IBM also showed interest in the potential application in large-area molecular junctions, developing innovative ideas to fabricate devices faster and with increased yield.[13, 14]

Today it is of immense importance for molecular electronics to understand the physics and the role played by all the diverse interaction in large-area molecular junctions so to be able to translate the full potential of the quantum nature offered by the small molecules to actual devices.

1.2. DESCRIBING THE TRANSPORT

A 'molecular junction' identifies a system made of a molecule (or a molecular monolayer) and two electrodes with which the former can interact, thus forming a sort of bridge-connection. The separation between the electrodes is defined by the molecular length, which is usually about few nanometers: at this scale, the charge transport happens mainly through tunnelling, a quantum phenomenon that describe the probability of a particle with a certain energy to traverse a classically insurmontable barrier. This assumption is particularly valid as most of the organic molecules are characterized by a wide band gap (*i.e.*, they are insulators or large-band semiconductors) and do not have a continuous distribution of energy levels as required for band conduction. Indeed, coherent off-resonant tunnelling is the most common charge transport mechanism observed in such platforms. Increasing the molecular length (over about 10 nm) or using compounds characterized by frontier orbitals close in energy to the Fermi energy of the electrode can make other types of transport more favourable such as resonant tunnelling or thermally-activated hopping.[10, 15] The characteristics of off-resonant tunnelling transport were outlined by Simmons in 1963 to describe electrons flowing through a thin insulating layer placed between two electrodes.[16] An approximation of such model was found to work well for molecular junctions, in particular in relating the observed current density (J) to the molecular length (d) as described in Equation 1.1

$$J = J_0 e^{-\beta d} \tag{1.1}$$

where J_0 is the pre-exponential factor (also referred to as 'injection current') and β is the tunnelling decay coefficient. β determines how J changes with d and it is related to the details of the energy levels inside the tunnelling barrier. β is extremely sensitive to the nature of the molecule in the junctions (*e.g.*, conjugated, saturated, aromatic, etc.) and it became an extremely useful tool to compare different experimental platforms as, while J_0 might change, β usually does not. This was of paramount importance in defying that the molecules indeed dominate the tunnelling transport and do not just function as dull spacers between the electrodes (*e.g.*, the current scales with the molecular length and not with the effective separation of the electrodes).[17]

While Simmons' approximation offers a useful tool to analyze and compare experimental results, it does not give much information about the quantum mechanisms and atomistic details that control the transport of charge through a molecule. Theoretical model often make use of a formalism developed by Landauer in 1957.[18] In this case, the conductance of a molecular junction, $\mathscr{G}$, can be considered to originate from the contribution of the transmission probabilities calculated for an electron tunnelling from one electrode to another through every current-carrying eigenmode of the system Hamiltonian as depicted in Equation 1.2

$$\mathscr{G} = \frac{2e^2}{h} \sum_{n=1}^{N} T_n \tag{1.2}$$

where T_n represent the individual transmission of the eigenmodes; e and h are the electron charge and Plank's constant respectively. Solving this equation provides the relation between transmission probability and energy of the particle. However, such calculations are extremely complex in the case of a molecule and no analytical solution can be obtained.

For this reason other approaches were introduced, the most successful of which is the use of non-equilibrium Green's function formalism.[19] In the latter, molecules and electrodes are treated separately and the transmission probability spectra of a lead-molecule-lead system can by calculated by Equation 4.1

$$T(E) = Tr[\Gamma_L \mathbf{G} \Gamma_R \mathbf{G}^T] \tag{1.3}$$

where $\mathbf{G}$ is the nonequilibrium Green's function matrix and $\Gamma_{L/R}$ is the broadening function matrix for the respective electrode. A qualitative discussion about the molecule transport properties can be limited to a simple approximation of the Green's function at the Fermi energy of the system (assuming weak coupling between the molecules and the electrodes) shown in Equation 4.2.[20]

$$\mathbf{G}(E_F) \approx \mathbf{G}^{(0)}(E_F) = [(E_F + i\eta)\mathbf{I} - \mathbf{H}]^{-1} \tag{1.4}$$

where $\mathbf{I}$ is the unit matrix, $\mathbf{H}$ is the Hamiltonian matrix and η is a infinitesimal positive number. In this sense $\mathbf{G}$ (and thus $T(E)$) is related to the molecular Hamiltonian. By

operating on **H** it is possible to obtain information on the transport that is a direct consequence of the identity of the molecule in the junction. This is particularly useful as it allows the use of established methodologies to compute **H** and to use it in transport calculations: thus, the language and concepts of molecular electronic structures and orbital theories can be used to describe charge transport in molecular tunnelling junctions, and even allow for more intuitive descriptions of transport phenomena.[21]

1.3. MAKING OF A MOLECULAR JUNCTION

It is relatively easy to imagine a molecular junction as a molecule sandwiched between two electrodes, but the development of experimental platforms to reliably characterize such systems was an endeavour that characterized the whole existence of molecular electronics. We can use different methodologies that define the different experimental approaches to the field. In broad general terms, we can divide these platforms in two: those that make use of *top-down* techniques, where molecules go to fill pre-made gaps obtained from larger structures, and those that follow a *bottom-up* approach, in which the molecules define the smallest dimension and the starting point for the assembly of the junction. The former is mostly used in single-molecule junctions, while the latter is practical in the case of molecular assemblies.

1.3.1. SINGLE-MOLECULE JUNCTIONS

Molecular junctions comprising single-molecules attract interest because they are easy to calculate and model *in silico*. Thus, they can be easily backed by solid theoretical structures and used to separate different molecular contribution in the charge transport. However, the highly dynamic nature of molecules makes these systems impractical for the application in actual electronic components, and thus single molecule junctions are better described as spectroscopic techniques rather than device-like platforms.[22]

The best established experimental methods revolves around the concept of 'break junction', a platform in which two electrodes, separated by a controlled nanometer-sized gap, are formed from a single wire. Such system can be achievend using mechanical stress (*e.g.*, in mechanically controlled break junctions, MCBJ),[23] electric migra-

tion (*e.g.*, in electromigration junctions),[24] or with an STM tip by pressing it in contact with the metal substrate and slowly withdrawing (STM-BJ).[25] Other approaches have been proposed but are not widely used.[26] One can observe the formation of the break junction by monitoring the current flowing to the wire: as the section shrinks, the value of the current gets lower, until only one atom remains bridging the gap and the current value reaches the quantum conductance (*i.e.*, the conductance of one atom of gold, $G_0 = 2e^2/h$, 7.74×10^{-5} S); finally the wire breaks, the two electrodes are formed, and the current flows between them through tunnelling. If a molecule happens to end up in the gap, then the transport characteristics of the junctions change and the effect of the molecule can be recorded.

One of the main concerns with this kind of measurement has to do with the uncertainty with which the molecules bind to the electrodes and the geometry they assume. On the atomic scale, the electrodes used in break-junctions are not well defined and the molecules can bind in different sites and with different geometries:[27] these differences affect the transport properties and cannot be externally controlled. Additionally, the measurement of single-molecules are inherently affected by a low signal-to-noise ratio since the latter scales with the degrees of freedom of the system as $1/\sqrt{n}$ (where n is the number of atoms in the molecule). Large data sets and rigorous statistical analysis are required to extrapolate meaningful data from these experiments and make valid comparisons.

1.3.2. LARGE-AREA MOLECULAR JUNCTIONS

Compared to the cases just presented, large-area molecular junctions, in which the electrodes are separated by a large number of molecules, do not suffer of the same intrinsic variability and thus are more relevant toward device application.[11] Still, these systems are incredibly complex to model and calculate, which makes in many occasions the connections between molecular properties and electric behavior of the junctions not straightforward: phenomena arising from peculiar interactions with the electrodes,[28] geometrical factors,[29] and collective effects arising from the close packing of the molecules,[30] can add factors that can significantly contribute to the transport besides the

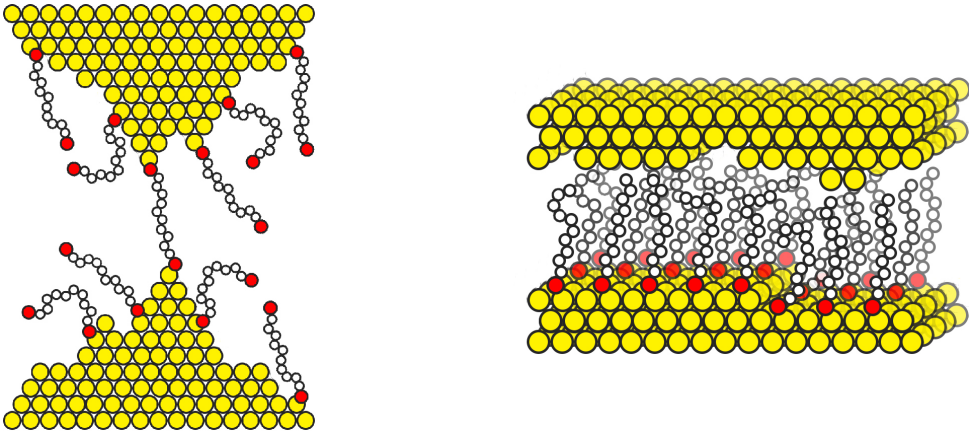

Figure 1.2 Cartoon representation of single-molecule junction (left) and large-area junction (right).

molecular contribution. These types of molecular junctions are usually formed in a bottom-up fashion staring from a monolayer grown on one electrode and applying a second one to contact the molecules across their whole length. The first measurement of tunnelling junctions across organic molecules (in 1971) was performed in large area junctions comprising Langmuir-Blodgett films of fatty acid salts and a mercury top electrode.[6] With few notable exceptions,[10, 31] nowadays large-area molecular junctions commonly make use of self-assembled monolayers (SAMs). These are one-molecule-thick, two-dimensional, supramolecular assemblies that forms spontaneously on a metal surface when put in contact with a molecule bearing a group that is capable of binding to the electrode (*e.g.*, sulfides, fullerenes, and acetylides can bind to gold, the most used metal for these applications). They are well-ordered, robust, they spans the entire metal surface, and they are formed in a thermodynamic regime: thanks to these characteristics, their properties are well defined, reproducible, and well-characterizable using many techniques, thus offering a privileged platform for their use in molecular electronics.

Compared to the idealized concept of a SAM, real ones are not defect free: defects on the surface (*i.e.*, cracks, grain boundaries, high roughness, step edges), impurities in the materials used, and the presence of dust particles, can introduce defects in the SAM that may drastically and anisotropically influence its properties. The use of ultra-smooth metal surfaces, such as those obtained by template-stripping from a silicon[111]

substrate[32] or depositing gold on flat mica (as well as the use of pure compounds when preparing the SAM and working in clean conditions) can significantly improve the quality of the monolayers for their use in molecular electronics.[33] Notably, there are copious amounts of studies, spanning several techniques, showing that we can reliably obtain coherent results from SAM-based junctions that are inherently connected to the molecular properties. It is also worth mentioning that, unlike the single-molecule junctions discussed previously, one can characterize SAMs by independent techniques which help to understand the nature of the system and interpret the data they generate once incorporated inside junctions.[34, 35]

To prepare a molecular junction comprising a SAM it is necessary to place an electrode on the top part of the monolayer. Many experimental methodologies have been proposed to do so, using different approaches and materials. Mercury drops, common electrode material in electrochemistry, were used often as top electrodes to contact a SAM (or to make mercury-SAM-SAM-mercury junctions in solution).[36] Nowadays it is very rare to find studies that make use of such material as it is potentially harmful to the operator, the junctions formed are very large and prone to the effect of defects, and extra-care and precautions need to be taken in order to prevent mercury to form amalgams with the bottom electrode. The deposition of a metal top electrode is an appealing way to prepare junctions with precise control over the dimensions. Unfortunately, in most of the deposition conditions, evaporated atoms have enough energy to penetrate and damage the SAM.[37] Specific groups at the top-interface can prevent this from happening[38] but such solution severely limits the number of compounds that can be used.

Akkerman *et al.* showed that metal evaporation could be avoided and a layer of conductive polymer, such as PEDOT:PSS, could be used instead.[39] Their devices showed promising results, but encountered problems with the series resistance offered by the polymeric layer, which is too high to reliably measure junctions comprising molecules with a small decay coefficient (β). Lörtsher *et al.* at IBM in Zurich, proposed an innovative way to protect the SAM during evaporation by firstly depositing a layer of metal nanoparticles that act both as contact and as protection from hot atoms that forms dur-

ing the subsequent evaporation step.[14]

These last two methods are perfect examples to show how devices comprising SAM-based large-area molecular junctions can be realized on a wafer-scale using existing technology, and made ready for the implementation with our technological platforms. It is worth mentioning that the preparation is laborious and requires multiple steps, thus making these platform non-ideal for the fast screening of multiple compounds.

1.3.3. EUTECTIC GALLIUM-INDIUM ALLOY AS TOP ELECTRODE

The use of the alloy of Gallium and Indium at its eutectic composition (EGaIn, 75% In and 25% Ga by weight, m.p.= 15.5 °C) as material for top electrode was proposed by Chiechi *et al.* in 2008.[40] As in the case of mercury discussed earlier, EGaIn is a liquid at room temperature and can be used to form soft and conformal contacts with the SAM without damaging it. Anyway, compared to the former, EGaIn shows several advantages. Firstly, it shows non-Newtonian properties that allow the formation of very small and sharp tips (with a diameter of about 20 µm, Figure 1.3). This is possible thanks to a thin layer of passivating Ga_2O_3 (about 0.7 nm thick) that forms when EGaIn is exposed to the oxygen in the atmosphere. The ability to contact smaller areas for the junctions, reduces the chance of probing defects, thus resulting in more reliable data and in an increase in the yield of working junctions.[33]

Secondly, it is commercially available, non-toxic, it does not form amalgams when in contact with other metals, and it can be easily applied and manipulated using a syringe, making it easy to work with, even for inexperienced users. On top of that, the use of EGaIn to measure the electrical properties of a SAM does not require any special apparatus — contrary to the case for the single-molecule junctions described earlier — and it can be done using readily available materials such as a syringe, a multimeter, and a camera to measure the size of the junctions. All these characteristics translate to the main advantage of the use of EGaIn as top electrode: high throughput. The ability of collecting large data sets in a small amount of time allows a precise and reliable characterization of junctions comprising large sets of different molecules by ruling out the junction-to-junction variation in the contact: the EGaIn methodology is thus a useful resource for

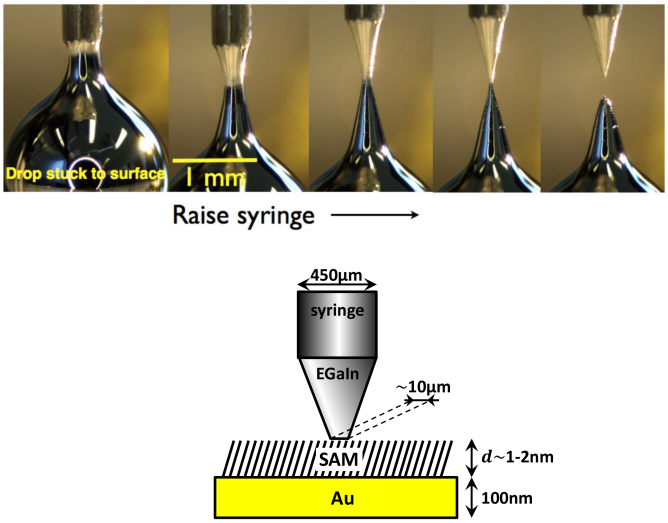

Figure 1.3 Formation of an EGaIn tip to be used as top electrode (top). Cartoon representation of an EGaIn junction (bottom).

the physical organic chemist, who makes use of large series of molecules to investigate the separate variables that influence charge transport in molecular junctions.

A similar technique, also capable of high throughput, concern the use of AFM equipped with conductive probes (CP-AFM): as in the case of EGaIn, a conductive AFM tip can be gently brought in contact with the SAM to measure the tunnelling current; as the measurement does not require any special treatment of the sample, large data sets can be rapidly collected. The metal-SAM-AFM junctions obtained this way (comprising between 80-100 molecules) are smaller than those obtained in other large area techniques, and thus CP-AFM is often referred to as a 'few-molecule' platform.[41] The drawback of this methodology is that the measured current suffer of tip-to-tip variability as well as being dependent on the force that is used to bring in contact the tip and the SAM. These observations limit the usefulness of comparing of CP-AFM data sets acquired in different periods and/or conditions. Despite the presence of the oxide layer and the not-well defined interface between EGaIn and the SAM, which have been source of critics toward the use of this technique, EGaIn junctions were proven to be extremely sensitive to characterize molecular phenomena in SAMs such as the 'odd-even effect', quantum

interference, electrode work-function shifts, and currently detain the record for the best performing molecular rectifier.

1.4. THESIS OUTLINE

This thesis will mainly focus on the study of large-area tunnelling junctions comprising SAMs of π-conjugated molecules obtained using an EGaIn top electrode.

In **Chapter 2** we describe the development of a new methodology for the reliable characterization of the electronic properties of the tunnelling junctions comprising fully conjugated oligo(phenylene-ethynylenes) molecular wires (OPEs). SAMs of such compounds are usually too fragile and prone to oxidation to be accurately measured in EGaIn tunnelling junctions. Here we show how this difficulty can be overcome by carefully controlling the atmosphere where the measurements are carried: the use of an oxygen concentration between 1 and 3% and a relative humidity below 15% was demonstrated to be optimal for the characterization of the molecular junctions. We ascribe this result to the different rehology of the EGaIn tip under these new conditions.

In **Chapter 3** we investigate the effect on the charge transport characteristics of molecular dipoles and the degree of interaction with the electrode. In particular we study SAMs of fluorinated OPEs characterized by identical molecular formula but different dipoles moments obtained by changing the substitution pattern; we control the degree of interaction with the electrode by comparing the latter compounds with their analogues bearing an extra methylene unit between the metal and the conjugated part. We also investigate the effect of other polar groups (pyridino, methoxy, sulfide) with particular attention to their influence at the SAM-EGaIn interface. We find that, in the case of OPEs, the presence of polar groups at the interfaces and the degree of interaction with the electrode affects the electric characteristics of the junctions more than the internal dipoles do.

In **Chapter 4** we explore the effects on tunnelling transport of through-space conjugation. In particular we characterize the electrical properties of molecules in which pi-conjugated fragments are arranged face-on or edge-on and hold in close proximity by

short σ-spacers). These two conformations are predicted to lead to destructive quantum interference. We find that the observation of these effects requires trapping molecules in a non-equilibrium conformation, which we accomplish using SAMs. In contrast, interference effects are not present in simulations on the equilibrium, gas-phase conformation.

In **Chapter 5** we examine the connection between destructive quantum interference and cross-conjugation in tunnelling junctions. In particular we investigate a series of molecular wires characterized by an identical cross-conjugated anthraquinoid skeleton but bearing different substituents that affect the energies and localization of their frontier orbitals and that can tune the quantum interference effects. We compare experimental results across three different experimental platforms, including both single-molecule and large-area junctions, and combine them with theoretical models in order to separate the intrinsic properties of the molecules from other platform-specific effects.

In **Chapter 6** we discuss the peculiar case of a redox-active molecular wire introduced in Chapter 5. In particular we show that SAMs of the latter undergo a partial charge transfer with the underlying metal which change the bond topology of the core: this result in a variation of the conductance without changing the connectivity of the tunnelling length. We then exploit this phenomena to realize two-terminal, non-volatile memory proto-devices that are based on the on-off switching of destructive quantum interference.

BIBLIOGRAPHY

[1] Feynman, R. P. *Egineering adn Science* **1960**, 22 – 36.

[2] Shakhnovich, E.; Gutin, A. *Journal of Theoretical Biology* **1991**, *149*, 537–546.

[3] Choi, H.; Mody, C. C. M. **2009**, *39*, 11–50.

[4] von Hippel, A. **1956**, *123*, 315–317.

[5] Aviram, A.; Ratner, M. A. *Chem. Phys. Lett.* **1974**, *29*, 277–283.

[6] Mann, B.; Kuhn, H. *Journal of Applied Physics* **1971**, *42*, 4398–4405.

[7] Ratner, M. *Nature Nanotechnology* **2013**, *8*, 378–.

[8] Blum, A. S.; Kushmerick, J. G.; Long, D. P.; Patterson, C. H.; Yang, J. C.; Henderson, J. C.; Yao, Y.; Tour, J. M.; Shashidhar, R.; Ratna, B. R. *Nat. Mater.* **2005**, *4*, 167–.

[9] Metzger, R. M. *Chem. Rev.* **2003**, *103*, 3803–3834.

[10] Lacroix, J. C. *Current Opinion in Electrochemistry* **2018**, *7*, 153–160.

[11] Vilan, A.; Aswal, D.; Cahen, D. *Chem. Rev.* **2017**, *117*, 4248–4286.

[12] Bergren, A. J.; Zeer-Wanklyn, L.; Semple, M.; Pekas, N.; Szeto, B.; McCreery, R. L. *J. Phys.: Condens. Matter* **2016**, *28*, 094011–.

[13] Valkenier, H.; Huisman, E. H.; van Hal, P. A.; de Leeuw, D. M.; Chiechi, R. C.; Hummelen, J. C. *J. Am. Chem. Soc.* **2011**, *133*, 4930–4939.

[14] Puebla-Hellmann, G.; Venkatesan, K.; Mayor, M.; Lörtscher, E. *Nature* **2018**, *559*, 232–235.

[15] Nijhuis, C. A.; Reus, W. F.; Whitesides, G. M. *J. Am. Chem. Soc.* **2010**, *132*, 18386–18401.

[16] Simmons, J. G. *J. Appl. Phys.* **1963**, *34*, 1793–1803.

[17] Simeone, F. C.; Yoon, H. J.; Thuo, M. M.; Barber, J. R.; Smith, B.; Whitesides, G. M. *J. Am. Chem. Soc.* **2013**, *135*, 18131–18144.

[18] Landauer, R. *IBM Journal of Research and Development* **July 1957**, *1*, 223–231.

[19] Williams, A. R.; Feibelman, P. J.; Lang, N. D. *Phys. Rev. B* **1982**, *26*, 5433–5444.

[20] Tsuji, Y.; Hoffmann, R.; Movassagh, R.; Datta, S. *J. Chem. Phys.* **2014**, *141*, 224311–.

[21] Valkenier, H.; Guedon, C. M.; Markussen, T.; Thygesen, K. S.; van der Molen, S. J.; Hummelen, J. C. *Phys. Chem. Chem. Phys.* **2014**, *16*, 653–662.

[22] Metzger, R. M. *Chem. Rev.* **2015**, *115*, 5056–5115.

[23] Xiang, D.; Jeong, H.; Lee, T.; Mayer, D. *Adv. Mater.* **2013**, *25*, 4845–4867.

[24] Taychatanapat, T.; Bolotin, K. I.; Kuemmeth, F.; Ralph, D. C. *Nano Lett.* **2007**, *7*, 652–656.

[25] Zhou, X.-S.; Liang, J.-H.; Chen, Z.-B.; Mao, B.-W. *Electrochemistry Communications* **2011**, *13*, 407–410.

[26] Tsutsui, M.; Taniguchi, M. Single Molecule Electronics and Devices. 2012.

[27] Yoshida, K.; Pobelov, I. V.; Manrique, D. Z.; Pope, T.; Mészáros, G.; Gulcur, M.; Bryce, M. R.; Lambert, C. J.; Wandlowski, T. *Scientific Reports* **2015**, *5*, 9002–.

[28] Lambert, C. J. *Chem. Soc. Rev.* **2015**, *44*, 875–888.

[29] Carlotti, M.; Kovalchuk, A.; Wächter, T.; Qiu, X.; Zharnikov, M.; Chiechi, R. C. *Nat. Commun.* **2016**, *7*, 13904.

[30] Kovalchuk, A.; Egger, D. A.; Abu-Husein, T.; Zojer, E.; Terfort, A.; Chiechi, R. C. *RSC Adv.* **2016**, *6*, 69479–69483.

[31] Seo, S.; Min, M.; Lee, S. M.; Lee, H. *Nat. Commun.* **2013**, *4*, 1920–.

[32] Weiss, E. A.; Kaufman, G. K.; Kriebel, J. K.; Li, Z.; Schalek, R.; Whitesides, G. M. *Langmuir* **2007**, *23*, 9686–9694.

[33] Jiang, L.; Sangeeth, C. S. S.; Wan, A.; Vilan, A.; Nijhuis, C. A. *J. Phys. Chem. C* **2015**, *119*, 960–969.

[34] Sangeeth, C. S. S.; Wan, A.; Nijhuis, C. A. *J. Am. Chem. Soc.* **2014**, *136*, 11134–11144.

[35] Carlotti, M.; Soni, S.; Kumar, S.; Ai, Y.; Sauter, E.; Zharnikov, M.; Chiechi, R. C. *Angew. Chem.* **2019**, *130*, 15907–15911.

[36] Rampi, M. A.; Whitesides, G. M. *Chemical Physics* **2002**, *281*, 373–391.

[37] Fisher, G. L.; Walker, A. V.; Hooper, A. E.; Tighe, T. B.; Bahnck, K. B.; Skriba, H. T.; Reinard, M. D.; Haynie, B. C.; Opila, R. L.; Winograd, N.; Allara, D. L. *J. Am. Chem. Soc.* **2002**, *124*, 5528–5541.

[38] de Boer, B.; Frank, M. M.; Chabal, Y. J.; Jiang, W.; Garfunkel, E.; Bao, Z. *Langmuir* **2004**, *20*, 1539–1542.

[39] Akkerman, H. B.; Blom, P. W. M.; de Leeuw, D. M.; de Boer, B. *Nature* **2006**, *441*, 69.

[40] Chiechi, R. C.; Weiss, E. A.; Dickey, M. D.; Whitesides, G. M. *Angew. Chem., Int. Ed.* **2008**, *120*, 148–150.

[41] Xie, Z.; Bâldea, I.; Demissie, A. T.; Smith, C. E.; Wu, Y.; Haugstad, G.; Frisbie, C. D. *J. Am. Chem. Soc.* **2017**, *139*, 5696–5699.

2

PRONOUNCED ENVIRONMENTAL EFFECTS IN EGAIN TUNNELING JUNCTIONS COMPRISING SELF-ASSEMBLED MONOLAYERS

The majority of studies involving large-area tunneling junctions using eutectic Ga-In (EGaIn) as a top contact have focused on saturated molecules in which the frontier orbitals are either highly localized or energetically inaccessible. We show that self-assembled monolayers of wire-like oligo(phenylene-ethynylenes), which are fully conjugated, only exhibit length-dependent tunneling behavior in a low-O_2 environment. We attribute this unexpected behavior to the sensitivity of injection current on environment.

I would like to thank M. Degen and Dr. Y. Zhang for the help provided in collecting the data.

2.1. INTRODUCTION

Since the dawn of molecular electronics, a wide variety experimental platforms was provided to investigate the role of molecule in tunnelling junctions.[1–3] Much attention has been directed toward techniques involving single- or few-molecule junctions such as mechanically controlled and STM break junctions (MCBJ, STM-BJ) or conductive probe AFM (CP-AFM) respectively,[1] because results are relatively straightforward to model *in silico*;[2, 4, 5] yet, these experimental platforms are often hard to operate and do not readily translate to devices, which carry the practical constraints of needing to be integrated into a circuit and be reliable and reproducible.[6] Large-area junctions such as those comprising EGaIn, on the other hand, better resemble the possible architecture of an actual molecular electronic device.[1, 7] Usually they make use of SAMs on metal electrodes as the active element and the template to define the uni-molecular thickness of the junction in a bottom-up fashion.[8] Moreover, the use of SAMs can induce new properties of the tunneling systems which are not present when one or few molecules alone are investigated.[9]

Studies concerning large area junctions typically make use of saturated thiols on coinage metals.[7, 10, 11] These SAMs are, in most cases, straight-forward to prepare/acquire, extensively characterized and their transport characteristics are well-established; for these reasons they are often used as test beds.[3, 7, 12–17] Yet, save *ad hoc* functionalization is involved, they only act as a dull barrier: the frontier orbitals are far from the Fermi level of the electrodes and do not strongly participate in the charge transport across the junction. On the other hand, conjugated molecules, with more accessible frontier orbitals and the possibility to interact with the electrode on the electronic level, have shown properties such a negative differential resistance,[18–23] conductance switching,[24–26] memory effects (see Chapter 6),[21] quantum interference (see Chapters 4 and 5),[27, 28] and the ability to modify the Fermi energy and the electrostatics of the electrodes.[9, 29, 30] Polyphenylenes, OPEs and similar conjugated structures have long been proposed as active elements in molecular electronics.[3, 5, 20, 22, 31–35] In particular, OPEs can be easily functionalized without distorting the conjugated backbone,[31, 36–39] yet they are rarely investigated in large-area junctions.[10] This scarcity of ex-

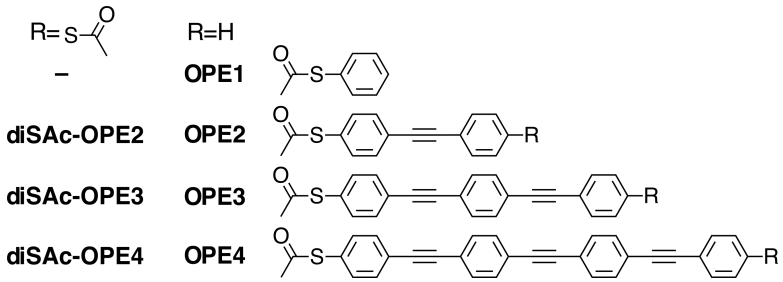

Figure 2.1 The OPE compounds used to prepare self-assembled monolayers.

perimental data may be due to difficulties in growing densely-packed SAMs from rigid molecules with an extended π-system[11, 28] or their sensitivity to oxidation; that is, saturated molecules are simply easier to handle.

In an effort to facilitate working with sensitive π-conjugated molecules, we built an EGaIn measurement setup inside a large flowbox capable of maintaining a low-O_2 environment such that the Ga_2O_3 can form, but that sensitive compounds and SAMs can still be handled without appreciable oxidation. Surprisingly, we found a large influence of the environmental conditions on the electrical properties of junctions comprising SAMs of OPEs, in stark contrast to SAMs of alkanethiolates, which showed only a systematic shift in injection current.

2.2. ENVIRONMENTAL EFFECTS ON SAMS OF OPES

We first investigated the OPEs shown in Fig.2.1 under ambient conditions on template-stripped Au (Au^{TS}).[40] The resulting data were characterized by unusually large dispersion, low current values and low yield of working junctions, rendering them uninterpretable (Fig. 2.2A). We then grew SAMs from the same compounds inside the flowbox from toluene solutions using 1,8-diazabicyclo[5.4.0]undec-7-ene (DBU) as an *in situ* deprotecting agent (see Experimental) and measured them without any exposure to ambient conditions. These results are shown in Fig. 2.2B; in an atmosphere of N_2 maintained at 1 % to 3 % O_2 and < 15 % relative humidity (RH), the yields of working junctions increased dramatically, the current-densities increased by approximately two orders of magnitude and a clear length-dependence emerged.

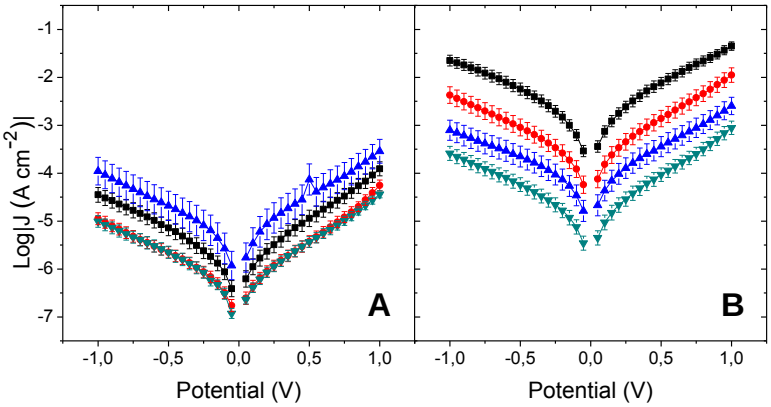

Figure 2.2 Plot of $Log|J|$ vs. V vs. V for EGaIn/Ga_2O_3//OPE/Au^{TS} junctions: **OPE1** (black), **OPE2** (red), **OPE3** (blue), and **OPE4** (dark cyan). **A**: Data collected in ambient conditions. **B**: Data collected in a flowbox environment of N_2, 1-3 % O_2 and RH <15 %. Error bars are per-junction confidence intervals calculated using $\alpha = 0.95$.

Table 2.1 Summary of electrical data on SAMs of OPEs.

	Compound			
Measurement	**OPE1**	**OPE2**	**OPE3**	**OPE4**
Log $\|J\|$@−0.5 V (flowbox) [Acm^{-2}]	−2.25	−3.04	−3.65	−4.24
Log $\|J\|$@−0.5 V (ambient) [Acm^{-2}]	−5.14	−5.65	−4.68	−5.65
Yield of working junctions (flowbox) [%]	92	90	93	97
Yield of working junctions (ambient) [%]	75	74	67	84

Figure 2.3 shows a comparison of the histograms of Log $|J|$ at−0.5 V from SAMs prepared inside the flowbox and measured in the same controlled environment and under ambient conditions. Ambient data are characterized by broader histograms and by a systematically lower current. Although the peaks of the histograms shift somewhat, they do not follow an obvious trend. Flowbox data, however, yield narrow histograms with well-defined peaks that follow a clear trend in molecular length. Additionally, the yield of the non-shorting junctions increased from ~75 % in ambient to >90 % in the flowbox. These data are summarized in Table 3.2.

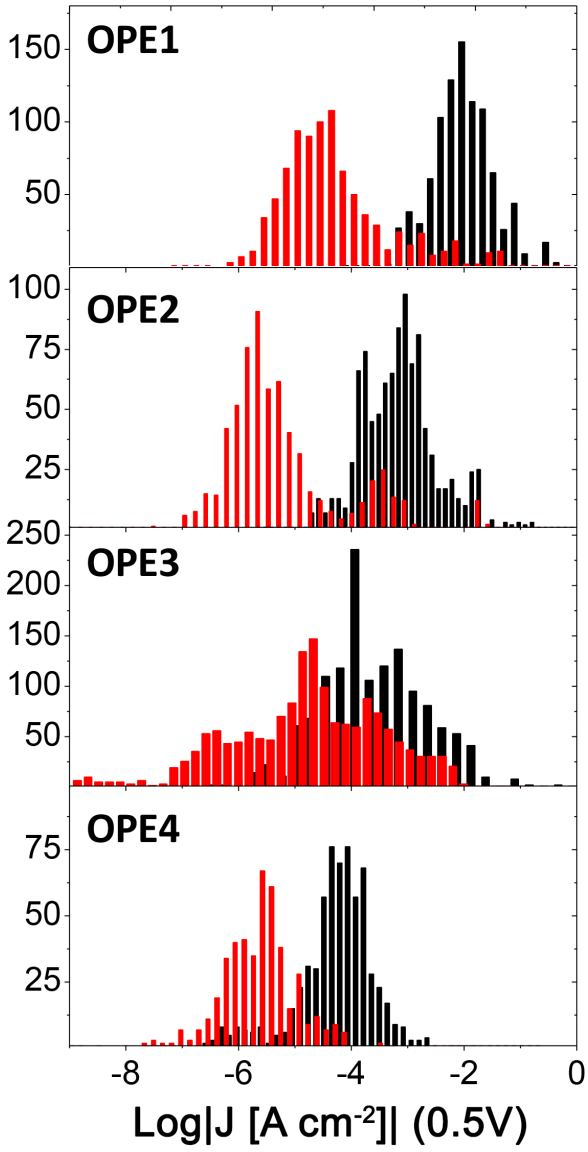

Figure 2.3 Histograms of all J/V data for **OPE1**, **OPE2**, **OPE3** and **OPE4** in ambient (red) and in the flowbox environment (black) at −0.5 V. Y-axes are counts. The histograms in ambient are broad and the peak values show no obvious trend, while the histograms in the flowbox are sharp and the peaks follow a clear trend with molecular length.

For a more quantitative description of the electrical properties and to facilitate comparisons with studies of OPEs in other platforms, we analyzed the data using a simplified version of Simmons' equation[41] (Eq. 2.1)

$$J = J_0 e^{-\beta d} \tag{2.1}$$

where J_0 represent the injection current, β is the tunnelling decay factor, and d is the molecular length. From the flowbox data we calculated a value of $\beta = 0.23(1)\,\text{Å}^{-1}$ at 0.5 V using the theoretical end-to-end distances of the minimized geometries (Table 2.3). This value is in agreement with theoretical predictions[5] and those reported by Lu *et al.*[42] and Kaliginedi *et al.*[32] using MCBJ and Liu *et al.*[43] using CP-AFM (Table 2.2). The same analysis was not possible with ambient data.

Table 2.2 A comparison of values of β for OPEs determined by different methods.

Ref.	Technique	Atmosphere	β [Å^{-1}]
5	Theoretical	-	0.25
44	Theoretical	-	0.19
43	CP-AFM	Ambient	0.20 ± 0.07
42	MCBJ	Ambient	0.202 ± 0.002
32	MCBJ	Inert	0.34 ± 0.01
45	STM[a]	Inert	0.32 ± 0.1
45	STM[b]	Inert	0.05 ± 0.01
This work	EGaIn	N_2 + 1-3 % O_2 RH <15 %	0.23 ± 0.01

[a]Thiol linkers [a]Carbodithioate linkers

In addition to reporting a value of β, Lu *et al.* observed a change in the transport mechanism on going from **OPE1** to **OPE4** for Au/SAM/Au junctions comprising a series of bis-amino-terminated OPEs using STM-BJ and CP-AFM (though in the latter case the transition was not well pronounced). A similar transition in EGaIn junctions was reported more recently by Sangeeth *et al.*[46] for a series of oligo(phenylene imine) wires; in particular, they reported a transition from tunneling to hopping for junctions comprising molecules with a molecular backbone longer than 25 Å to 30 Å. In both cases, a hop-

Table 2.3 Comparison of molecular S-S distances in gas-phase minimized geometries and thickness of the SAM obtained by ellipsometry.

	Theoretical length (Å)	Ellispometric thickness (Å)
OPE1	5.6	11.4
OPE2	12.1	23.7
OPE3	18.7	25.1
OPE4	25.2	26.4
OPE2-diSAc	12.9	13.6
OPE3-diSAc	19.3	15.0
OPE4-diSAc	25.9	17.1

ping mechanism was distinguished via variable temperature conductance data; hopping is a thermally activated process that follows the Arrhenius reltionship, while tunneling does not depend on temperature.[47] To test for this transition in Au/SAM//EGaIn junctions we performed variable temperature studies on SAMs prepared in the flowbox and measured in microfluidic EGaIn junctions under an inert atmosphere. (Low-temperature measurements are incompatible with O_2 and H_2O vapor.) Figure 2.4 and 2.5 show no dependence of conductance on temperature from which we conclude that there is no thermally activated process and, therefore, no tunneling to hopping transition.

2.3. EFFECT OF THE ENVIRONMENT ON THE EGAIN-SAM INTERFACE

The presence of some O_2 is necessary to form the self-limiting Ga_2O_3 skin responsible for the non-Newtonian behavior of EGaIn that permits it to retain sharp tips instead of relaxing to a Gaussian geometry.[48] Figure 2.6 shows tips formed in ambient and in the flowbox; 1 % to 3 % O_2 is sufficient to form tips in a reproducible fashion and collect reproducible data. While atomistic detail of the surface of EGaIn/Ga_2O_3 is currently experimentally inaccessible, the tips formed in the flowbox differ qualitatively from those

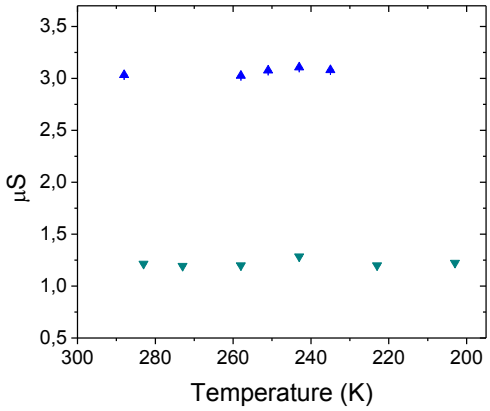

Figure 2.4 Arrhenius plots of low-bias conductance vs. temperature for junctions comprising **OPE3** (blue up-triangles) and **OPE4** (cyan down-triangles). The invariance with temperature is characteristic of tunneling transport and indicates a lack of thermally activated processes. The low bias conductance is reported as the slope of the J-V traces in the 0.1V/-0.1V window. Data are shown down to the temperatures at which the majority of the junctions failed.

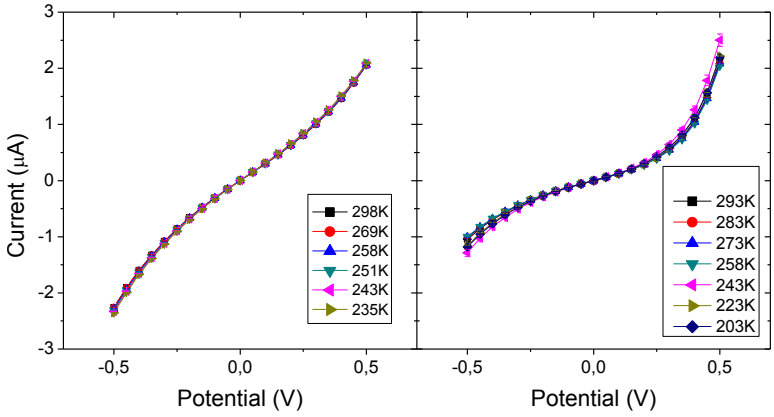

Figure 2.5 Variable temperature I-V plots for **OPE3** (left) and **OPE4** (right) at different temperature. Error bars are confidence intervals calculated with $\alpha = 0.05$.

formed in ambient. In particular, in the low-O_2, low-RH flowbox environment, EGaIn does not appear to wet the metal of the syringe needle, leading to the formation of a long column of liquid metal before the hourglass shape between the needle and the surface ruptures to form the tips used for measurements. The tips formed inside the flowbox also appear sharper and smoother and the surface shows less buckling compared to tips

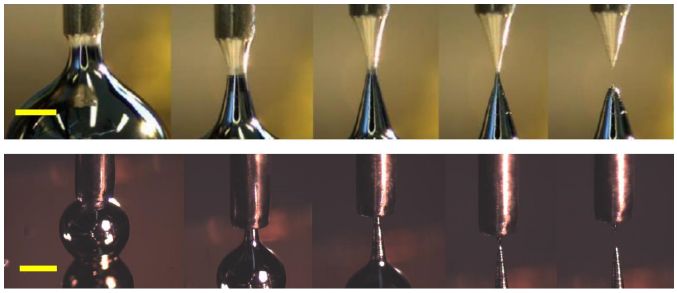

Figure 2.6 Formation of tips of EGaIn in ambient conditions (top) and in a flowbox kept at 2.5 % O_2, RH < 15 % (bottom). The yellow scale bar is 500 μm. Although the process of necking into an hourglass shape and severing into sharp tips is the same in both cases, in the flowbox EGaIn does not wet the metallic syringe needle.

formed in ambient. The apparent sharpness does not necessarily affect the the apex of the tip, which is typically on the order of 20 µm in diameter. These are qualitative observations based on optical micrographs, however, we speculate that they could be due to a systematic difference in the wetting and/or mechanical properties of the Ga_2O_3 skin due to the different conditions under which they form. There is both a significantly reduced amount of O_2 and lower RH and either or both could influence the kinetics and/or thermodynamics of the formation of Ga_2O_3 and/or its chemical composition, crystal structure, surface states, electronic properties, thickness, etc.; it is a complex system and further study will be required to elucidate the exact mechanism. Irrespective of these microscopic details, there are clear qualitative differences in the tips of EGaIn and clear quantitative differences in the J/V characteristics of tunneling junctions comprising OPEs.

To confirm that the dramatic environmental effects seen with OPEs are not generalizable, we measured Ag^{TS}/SAM//EGaIn junctions comprising alkanethiolates in ambient and in the flowbox environment. We chose these SAMs and Ag^{TS} substrates because they been studied extensively in EGaIn junctions and are widely considered to be a benchmark in molecular electronics.[3, 12, 14–17] The resulting data summarized in Table 2.4, revealing a systematic shift to lower values of Log $|J|$ and higher yields of working junctions in the flowbox compared to ambient. There are two important findings; i) a clear trend in Log $|J|$ with molecular length is present in both sets of data and ii) Log $|J|$ shifts

Table 2.4 Summary of electrical data on SAMs of alkanethiolates.

	$CH_3(CH_2)_nSH$			
Measurement	$n=9$	$n=11$	$n=13$	$n=15$
Log $\|J\|$@ +0.5 V flowbox [Acm^{-2}]	−3.48	−4.10	−4.81	−5.95
Log $\|J\|$@ +0.5 V ambient [Acm^{-2}]	−1.52	−2.44	−3.31	−4.82
Yield of working junctions flowbox [%]	70	75	79	90
Yield of working junctions ambient [%]	60	50	93	74

in the opposite direction compared to the SAMs of OPEs.

Using eq. 2.1, we calculated values of β for the series of alkanethiols; $\beta = 0.79 \pm 0.02$ and 0.71 ± 0.05 $Å^{-1}$ in ambient and flowbox conditions, respectively, in perfect agreement with literature values (acquired under ambient conditions).[15, 49] These data are plotted in Fig. 2.8; there is a negligible change to the distance-dependence, strongly suggesting that the transport mechanism is insensitive to environmental conditions for alkanethiols.[4]. There is, however, a difference in the values of J_0, which appears to be larger for the measurements performed in ambient conditions (*i.e.*, the contact resistance increases in the flowbox.) Simeone *et al.* reported a value of Log $|J_0[Acm^{-2}]| = 3.6 \pm 0.3$ @0.5 V for Ag^{TS}/SAM//EGaIn junctions in ambient conditions.[15] We found Log $|J_0[Acm^{-2}]| = 2.9 \pm 0.1$ in ambient and Log $|J_0[Acm^{-2}]| = 0.5 \pm 0.3$ in the flowbox. That the injection current, J_0, is three orders of magnitude lower in the flowbox, yet the decay constant, β is unaffected suggests that the environmental effects on SAMs of alkanethiolates are confined to an interface. And since the Ag^{TS}/SAM and Au^{TS}/SAM interfaces do not change between ambient and flowbox conditions, it is reasonable to assume that the effects of a low-O_2, low-RH are confined to the SAM//EGaIn interface and that the effects of the different environments are affecting the formation/properties of the Ga_2O_3 layer.

To investigate this hypotesis even further, we measured the properties of **OPE3** SAMs first in the flowbox, then after moving the samples to ambient, and then again in the flowbox (the details of this experiment are better described in the Experimantal Section). The histograms of J in the different conditions are presented in Figure 2.7. As we already

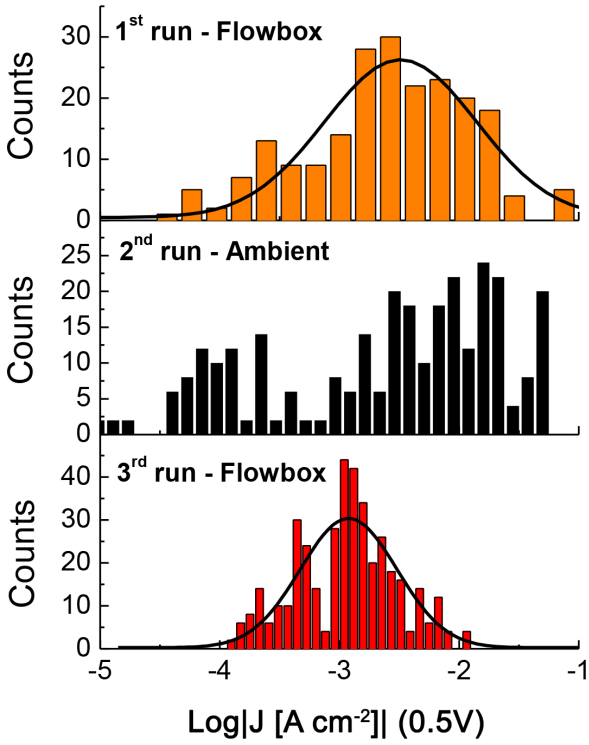

Figure 2.7 Histograms for Log $|J|$ at −0.5 V for Au^{TS}/**OPE3**//Ga_2O_3/EGaIn junctions measured: in the flowbox, first run (top); and then in ambient, second run (middle); and finally again in the flowbox, third run (bottom). The solid black lines are Gaussian fits for the measurements, which were only possible for data acquired in the flowbox.

discussed for Fig. 2.3, the data measured inside the flowbox present a much narrower distribution and higher yield of working junctions: surprisingly this is true for the data acquired both before and after exposure to ambient, thus indicating that the peculiar environmental conditions in the flowbox play the major role in the detection of J in the case of OPEs. Contrarily to what stated for the alkanethiols, the effect, however, does not reduce to an increase in contact resistance in a low-N_2, low-RH atmosphere because SAMs of OPEs can only be measured in the flowbox, where the values of J increase compared to ambient, *lowering* the contact resistance.

An alternative hypothesis is simply that the differences in the geometry of the tips introduce a systematic under-estimation of the areas of the junctions in the flowbox

(and/or an over-estimation in ambient), but the differences in the magnitude in J would require a systematic error in the measured diameters of a factor of 5-15 between the flowbox and ambient conditions. (The diameter of the junctions we form is about 20-25 μm, with an error lower than 10%.) Although we cannot rule out a microscopic difference in the surface of the EGaIn tip causing affecting a change in effective contact area, we can exclude the possibility that such error is systematic. We performed conductivity measurements using the EGaIn tips formed identically to those used to measure SAMs on an n-doped Si wafer bearing a native oxide (cleaned with O_2 plasma) and exfoliated highly oriented pyrolytic graphite (HOPG). In ambient conditions, the conductivity (at -0.5 V) was a factor of 2 and 6 times higher than in the flowbox for Si and HOPG respectively. The differences in J for SAMs of alkenthiolates are on the order of 100 and, therefore, experimental error in determining the effective contact-area is not responsible for the difference in J_0. This latter is specific to SAMs of alkanethiolates and do not reduce to a difference in the geometry/topology of the tip. This hypothesis is also unable to explain the inability to resolve a length-dependence from OPEs or the commensurate broadening of the histograms in ambient conditions.

One of the principal advantages of using thiols and coinage metals in molecular electronics is that Au is essentially inert and the Au-S bond is sufficiently strong to compete with advantageous adsorbates, however, the details of the surface chemistry of the Ga_2O_3 layer remain a mystery. Barber *et al.* studied the influence of the environment on the transport properties of saturated SAMs in Ag/SAM//EGaIn junctions and found no effect provided sufficient O_2 was present to form the Ga_2O_3 layer.[17] Their methodology differed somewhat from ours: the tips used to form the junctions were prepared in air or pure O_2 before being transferred in different environments, while we prepared the SAMs, formed the tips and performed the measurements in either ambient or in the flowbox. Thus, our observation that there is a negligible effect on β for SAMs of alkanethiolates is consistent as well as our observation that SAMs of OPEs are affected dramatically and that J_0 is affected for SAMs of alkanethiolates.

To explore the hypothesis that the environmental effects can be ascribed to the SAM//EGaIn interface, we measured SAMs formed from symmetric dithioacetate (diSAc) deriv-

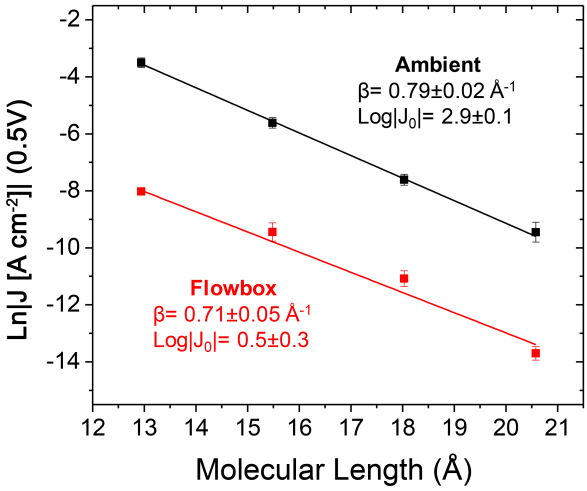

Figure 2.8 Plots of Ln J(+0.5V) vs. molecular length in Å for Ag^{TS}/SAM//EGaIn junctions comprising $CH_3(CH_2)_9SH$, $CH_3(CH_2)_{11}SH$, $CH_3(CH_2)_{13}SH$, and $CH_3(CH_2)_{15}SH$. The data collected in the flowbox environment (N_2 atmosphere with 1-3 % O_2, RH <15 %) are reported in red, while those obtained in ambient conditions are in black. Error bars are per-junction confidence intervals calculated using $\alpha = 0.95$. The straight lines are linear fits of the data.

atives of **OPE2**, **OPE3** and **OPE4** (denoted **diSAc-OPE2**, **diSAc-OPE3** and **diSAc-OPE4**, respectively) in Au^{TS}/SAM//EGaIn junctions in ambient condition and in the flowbox. (**diSAc-OPE1** does not form densely-packed, upright SAMs.) Figure 2.9 clearly shows that the same environmental effect is present for this series; a trend in J molecular length is evident only when the molecules are measured in the controlled atmosphere of the flowbox, but it collapses when the same experiments are performed in ambient. The *in situ* deprotection procedure results in predominantly free thiol (SH) groups at the SAM//EGaIn interface, with some residual thioacetate ($SC(O)CH_3$) groups.[11] Thus, the interaction is chemically very different than for the OPE series, which presents a bare phenyl group. Thiols, by comparison, have a higher surface free energy (lower contact angle with water) and can be considered more strongly interacting by virtue of the lone pairs of the sulfur atoms present at the SAM// EGaIn interface for the diSAc-OPE series. Yet the data acquired from SAMs of diSAc-OPEs and OPEs in ambient conditions are virtually indistinguishable.

The values of Log $|J|$ acquired in the flowbox show clear length-dependence and are

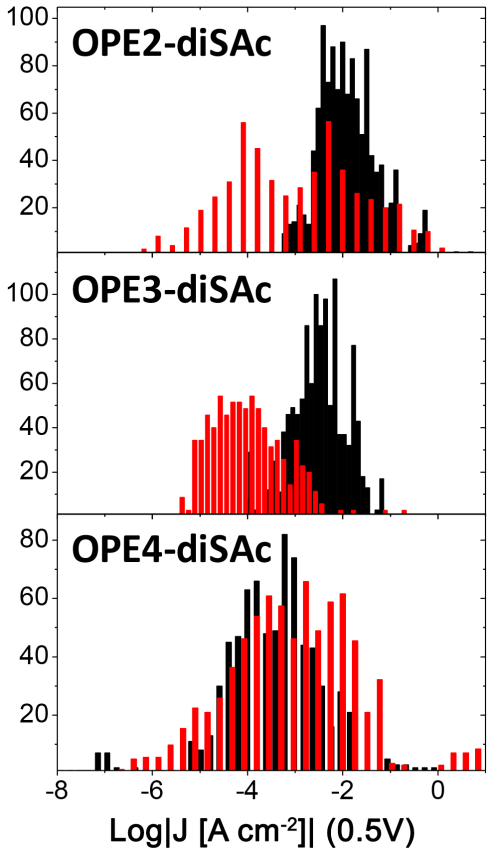

Figure 2.9 Histograms of all J/V data for **diSAc-OPE2** (top), **diSAc-OPE3** (middle), and **diSAc-OPE4** (bottom) in ambient (red) and in the flowbox environment (black; N_2 atmosphere with 1-3 % O_2, RH < 15 %) at −0.5 V. Y-axis are counts. The data acquired in air and characterized by broad distributions with no obvious trend while the data acquired in the flowbox are distributed more narrowly and the peak values follow a clear trend with molecular length.

systematically higher for the diSAc-OPE series as compared to the (mono-diSAc) OPE analogues, meaning that there is a higher injection current (and lower contact resistance) when a thiol is present at the SAM//EGaIn interface; Log $|J_0[\mathrm{Acm}^{-2}]| = -1.6 \pm 0.1$ and Log $|J_0[\mathrm{Acm}^{-2}]| = -0.3 \pm 0.3$ for the mono-SAc and diSAc OPEs, respectively. Using eq. 2.1 we found $\beta = 0.23 \pm 0.01$ Å^{-1} and $\beta = 0.23 \pm 0.05$ Å^{-1} for the OPE and diSAc-OPE series respectively (Fig. 2.10.) Thus, modifying the SAM//EGaIn interface chemically and measuring SAMs of OPEs in the flowbox affects the J/V data analogously to chan-

ging the environment for SAMs of alkanthiols without altering the SAM//EGaIn interface chemically. This observation further supports the hypothesis that the Ga_2O_3 layer present at the surface of EGaIn is affected by the environment.

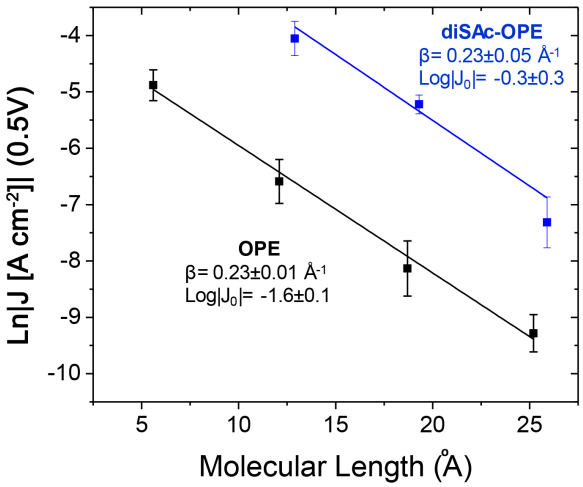

Figure 2.10 Plots of Ln J (0.5 V) vs. molecular length in Å for Au^{TS}/SAM//EGaIn junctions formed from mono- (black) and di- (red) thioacetate derivatives of OPEs of varying length in the flowbox environment (structures are shown in Fig. 2.1.) Error bars are per-junction confidence intervals calculated using $\alpha = 0.95$. The straight lines are linear fits of the data.

In the absence of the ability to acquire experimental data on the atomistic details of the oxide layer, we can estimate the influence of the low-O_2 atmosphere by considering the thermodynamics and kinetics. The change in the free-energy of formation of Ga_2O_3 is negligible; $\Delta_r G$ goes from $-998\,\mathrm{kJ\,mol^{-1}}$ under ambient conditions to roughly -981 at 1 % O_2.[50] And the frequency of collisions between O_2 molecules and the surface of EGaIn at 1 % O_2 is on the order of $10^{15}\,\mathrm{s^{-1}}$, excluding O_2 as a rate-limiting step in the formation of the oxide (assuming a conical tip with diameter of 0.5 mm, a height of 1 mm and perfect gas behavior of O_2). Moreover, the non-Newtonian properties of EGaIn are retained in the flowbox with oxygen levels as low as 300 ppm, although under such conditions the reproducible formation of tips becomes prohibitively difficult. Doudrick *et al.* reported that in the case of Galistan (a Ga/In/Sn ternary liquid alloy) a partial-pressure of O_2 of 0.03 mPa is sufficient for the oxide to form.[51] Thus, we are con-

fident that the thickness of the surface of EGaIn/Ga_2O_3 is unaffected by the reduction of the partial pressure of O_2. It is also unlikely that the effect originates entirely from RH, as it varies seasonally and geographically and EGaIn junctions have been studied year-round and on at least three continents.[8, 17] It is possible that surfaces of EGaIn/Ga_2O_3 formed in a controlled atmosphere may have a different contact resistance because they are free of contaminants and dopants from the ambient environment,[52] however, that explanation is inconsistent with experiments that find SAM/EGaIn interfaces formed in ambient conditions comparable to SAM//Au[53] and molecule/Au[54] interfaces. Given that the the environmental effects are localized to the SAM//EGaIn interface and that they cannot be ascribed to a thinner or chemically different Ga_2O_3 layer altering the coupling and/or contact resistance and that the differences in injection currents cannot be explained by experimental error in the determination of the area of the junction, we conclude that the effects can be ascribed to a difference in wetting. The qualitative differences in the tips shown in Fig. 2.6 suggest very different wetting behavior of EGaIn in different environments. (The wetting behavior of the SAMs, estimated qualitatevly with the contact angle of glicerine in the flowbox and in ambient, does not seem to change.) This difference could lead to differences in the mechanical stresses at the SAM/EGaIn interface arising from adhesive forces; a 'gentler' contact may be necessary to measure fragile SAMs of OPEs. Likewise, such a contact could explain the increase in the yields of working junctions and increased injection currents of SAMs of alkanethiolates. Moreover, increasing the surface free-energy of SAMs of OPEs by introducing thiol groups mimics the behavior of measuring SAMs of alkanethiols in ambient conditions, which is consistent with the hypothesis that injection currents scale with wetting and that tips of EGaIn formed in ambient conditions wet SAMs better than those prepared in the flowbox.

2.4. CONCLUSIONS

The environment under which SAMs and junctions of large-area Au^{TS}/SAM//Ga_2O_3/EGaIn junctions comprising SAMs of mono- and di-thiol OPEs and Ag^{TS}/SAM//Ga_2O_3/GaIn junctions comprising SAMs of alkanethiolates are formed has a pronounced, system-

atic affect on tunneling charge-transport. The resistance of SAMs of OPEs decreases in low-O_2, low-humidity environments, while the resistance of SAMs of alkanethiolates increases. The quantifiable effect is the injection current of the latter; SAMs of mono- and di-thiol OPEs do not produce meaningful trends under ambient conditions. By comparing SAMs of OPEs that present either a bare phenyl group (Ph) or a thiophenol group (Ph-SH) to the EGaIn interface and SAMs of alkanethiolates under ambient conditions and a controlled atmosphere of N_2 with 1 % to 3 % O_2 and RH <15 % we unambiguously ascribe the effects to the nature of the SAM/Ga_2O_3; injection currents (J_0), but not decay constants (β) are influenced by the environment under which measurements are performed and by the chemistry of the interface. Variable temperature measurements establish the mechanism of transport through OPEs—which can only be measured at low-O_2 and low-RH—as tunneling.

This work identifies the wetting properties of the SAM//Ga_2O_3/EGaIn interface as a critical component that can become limiting the case for π-conjugated molecules with small values of β (relative to n-alkanes). This observation may also explain the statistical variance of injection currents of SAMs of alkanethiolates measured with EGaIn. The ability to adjust the injection current sufficiently to measure conjugated molecules underscores the universality of EGaIn as a top-contact for the formation of large-area tunneling junctions and enables future studies on more exotic molecular systems.

2.5. EXPERIMENTAL SECTION

FLOWBOX

The flowbox was realized using a Terra Universal stainless steel glove box Series 400 SS (60"x33"x37") equipped with a Dual Purge flow regulator (Terra Universal) connected to the house nitrogen. To keep the levels of O_2 and RH under established limits (3 % and 15 % respectively) the flow regulator was connected to a NitroWatch^{TM} RH controller equipped with a Humex Sensor (Terra Universal) and to an oxygen analyzer (Illinois Instruments Mod. 810.) The nitrogen flow was kept at approximately 0.25 l min^{-1} when the box was not used (to preserve the atmosphere inside) and was increased to 2.4 l min^{-1} during the measurements and the handling of chemicals and substrates. The entire EGaIn measurement setup was housed inside the flowbox.

MATERIALS

Compounds benzenethiol (**OPE1**), 1-decanethiol (**C10SH**), 1-dodecanethiol (**C12SH**), 1-tetradecanethiol (**C14SH**), 1-hexadecanethiol (**C16SH**) were obtained from Sigma-Aldrich and purified by coloumn cromatography (silica, hexane) with the excaption of **OPE1** which was used as received. The synthesis of **OPE2**, **OPE3**, **diSAc-OPE2**, **diSAc-OPE3**, and **diSAc-OPE4** is described elsewhere.[32] All compounds were stored in nitrogen-flushed vials and in the dark. Their structures were verified by acquiring ^{1}H-NMR and IR spectra immediately prior to use and comparing to the spectra acquired immediately after purification. **OPE4** was prepared starting from 1-ethynyl-4-((4-(phenylethynyl) phenyl)ethynyl)benzene as described in the Synthesis Section.

SAM FORMATION AND CHARACTERIZATION

SAMs of the OPE series compounds were formed by incubating the thioacetate precursors with 1x1 cm template-stripped Au surfaces (100 nm-thick) overnight in 3 mL of 50 μM solution of the respective compound in freshly distilled toluene followed by addition of 0.05 mL of 17 mM diazabicycloundec-7-ene (DBU) solution in toluene 1h prior the measurement. The substrates were then rinsed with ethanol and let to dry for 15 minutes. This procedure was used for both mono- and di-SAc terminated OPEs and performed in the flowbox controlled environment. In case of di-SAc derivatives, prolonged contact with the deprotecting agent, increased the risk of multi-layers formation. SAMs of alkanethiols on Ag^{TS} (200 nm-thick, 1x1 cm surface) were growth from 3 mM solutions of the respective alkanethiol in degassed EtOH overnight, they were then

rinsed and dried as previously described. The thicknesses of the OPE SAMs were measured by ellispometry. These measurements were acquired on fresh samples in air on a V-Vase Rotating Analyzer equipped with a HS-190 monochromator ellipsometer and calculated via a two-layer model consisting of a bottom Au layer, for which optical constants were calculated from freshly prepared template stripped Au surfaces, and a Cauchy layer with a chosen value of n= 1.5 an k= 0 at all wavelengths (A=1.5, B=C=0).[11]. The obtained values are reported in Table 2.3 together with theoretical lengths obtained from the minimized geometry of the molecules (as S-terminal CH distance). These latter have been used in the calculation of the β-values.[55]

EGaIn J-V MEASUREMENT

EGaIn measurements were carried on two identical setups, one positioned on a laboratory bench (ambient conditions) and one positioned in the flowbox described above. The details of the EGaIn setup are described elsewhere.[28] For each compound 3-4 substrates were prepared and at least 15 Au^{TS}/SAM//Ga_2O_3/EGaIn junctions per sample were measured (10scans from 0 V → 1 V → −1 V → 0 V, steps of 0.05 V) for a total of at least 450 traces per SAM for the OPE series and at least 100 for the alkanethiols. A new EGaIn tip was prepared every 5-8 junctions and flattened by gently pushing it on a Si wafer few times according to the procedure reported by Simeone *et. al.*[15]. In Table 3.2 are reported the number of traces collected for the different compounds and the yield of working junctions obtained by the number of junctions that did not fail during the bias scanning or when initially tested with a potential of 0.5 V divided by the total number of junctions formed. The number of working junctions can be obtained dividing by 10 the number of traces. The data were acquired as described and then parsed in a "hands-off" manner using Scientific Python to produce histograms of J for each value of V and the associated Gaussian fits (using a least-squares fitting routine). The confidence intervals for $\mu_{\log J}$ (Gaussian mean) depicted as error bars in the J/V plots were calculated using $\alpha = 0.95$ from $\sigma_{\log J}$ (standard deviation) taken from Gaussian fits and a number of degree of freedom equal to the number of junctions −1.

To investigate the reasons behind the differences in conductivity of Au^{TS}/SAM//Ga_2O_3/EGaIn junctions upon environment, SAMs of **OPE3** were prepared and and initially measured inside the flowbox (20 junctions, 1^{st} run); then the same sample was transferred outside and measured with the EGaIn setup in the open environment (20 junctions, 2^{nd} run); finally it was transferred back in the flowbox where it was measured again (20 junctions, 3^{rd} run). This experiment was repeated two times and the data merged together. In Figure 2.7 are reported the current density histograms with Gaussian fits. The yield of working junctions was 91%, 73% and 91% for the 1^{st} run (flowbox),

Table 2.5

	Flowbox		Ambient	
	n. of traces	Yield (%)	n. of traces	Yield (%)
OPE1	650	92	450	75
OPE2	480	90	450	74
OPE3	650	93	510	67
OPE4	640	97	450	84
OPE2-diSAc	600	88	560	32
OPE3-diSAc	600	92	490	60
OPE4-diSAc	450	88	570	40
C10SH	270	70	120	60
C12SH	270	75	390	50
C14SH	190	79	140	93
C16SH	100	90	170	74

2^{nd} run (ambient), and the 3^{rd} run (flowbox) respectively. It is worth mentioning that the two EGaIn setup are completely identical and give identical results when placed in the same environment.

SYNTHESIS OF **OPE4**

OPE4 was prepared according to the scheme in Fig. 2.11. 1-ethynyl-4-((4-(phenylethynyl)phenyl)-ethynyl)benzene (**1**) was synthesized elsewhere.[32] Pipsyl chloride (95%), *N*,*N*-dimethylacetamide (99.8%), acetyl chloride (99%) and dichlorodimethylsilane (≥ 98.5%) were purchased from Sigma-Aldrich and used as received. $Pd(PPh_3)_3$ and CuI were purchased from ACROS Organics and stored under nitrogen in the dark at 4 °C. NEt_3 was distilled over CaH prior use. Tetrohydrofuran (THF) was obtained dry from a solvent purification system present in the lab. The rest of the solvents were used as received. ^{1}H-NMR and ^{13}C-NMR spectra were recorded on a Varian AMX400 (400 MHz) and a Varian VXR-400 (400 MHz) at room temperature. All the spectra were referenced to the solvent line of $CDCl_3$ relative to tetramethylsilane (H, 7.26 ppm; C, 77.0 ppm). FT-IR spectra were recorded on a Nicolet Nexus spectrometer using the SMART iTR for ATR measurement (diamond).

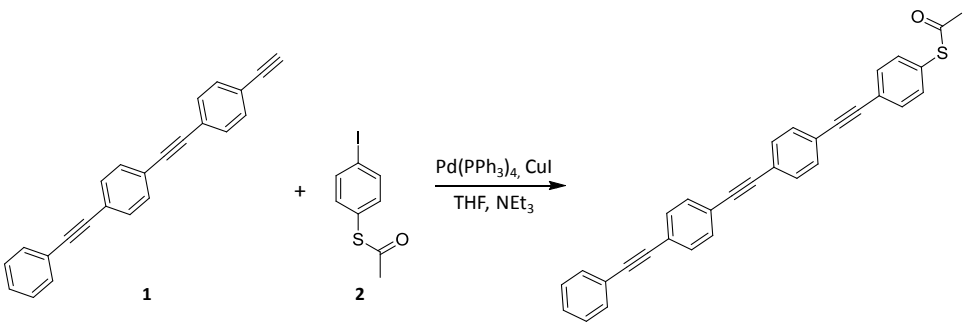

Figure 2.11 Reaction scheme for **OPE4** synthesis.

(4-iodophenyl)ethanethioate, 2

The procedure for the synthesis of this compound was taken from the literature.[56] In a flask under inert atmosphere (N_2), 3.073 g of pipsyl chloride (10.2 mmol) and 2.8 mL of *N,N*-dimethylacetamide (2.63 g, 30,2 mmol) were dissolved in 80 mL of degassed 1,2-dichloroethane. In a different flask under inert atmosphere (N_2), 2.36 g of Zn (36.3 mmol) and 4.3 mL of Cl_2SiMe_2 (4.58 g, 53.3 mmol) were stirred in 80 mL of degassed 1,2-dichloroethane at 60 °C for 30 minutes, then the first solution was added. The reaction mixture was heated to 75 °C and left for 2 h. Absence of pipsyl chloride was checked via TLC (Rf ~ 0.4 in hexane). The solution was then cooled to 45 °C and 0.94 mL of acetyl chloride (1.038 g, 13.2 mmol) were added. The reactor was left at 50 °C for 30 minutes. The reaction mixture was filtered still hot and the filtrate poured in 300 mL of water. The aqueous phase was extracted with dichloromethane (3x150 mL). The organic solvent was evaporated *in vacuo* and the product purified by sublimation (70 °C, $5 \cdot 10^{-4}$ mbar) to obtain 2.420 g of white crystals (83% yield). ^{1}H-NMR (400 MHz, $CDCl_3$) δ 7.74(m, 2H), 7.13(m, 2H), 2.42(s, 3H). IR (ATR, cm^{-1}): 1691, 1464, 1381, 1353, 1119, 1087, 1004.

S-(4-((4-((4-(phenylethynyl)phenyl)ethynyl)phenyl)ethynyl)phenyl) ethanethioate, OPE4

In a dry flask under nitrogen atmosphere 26.1 mg of **1** (86 μmol), 26.6 mg of **2** (96 μmol), 3.0 mg of $Pd(PPh_3)_4$ (2.6 μmol), and 1.4 mg of CuI (7.3 μmol) were dissolved in 3.5 mL of dry THF and 35 μL of NEt_3. The system was heated to 50 °C for 1 hour and then slowly allowed to room temperature over 16 hours. The reaction mixture was poured in 200 mL of water which was carefully acidified with few drops of HCl 6 M until slight acidity was reached. The water phase was extracted with DCM (3x30 mL), the organic phase was dried over Na_2SO_4, and the solvent removed under

vacuum. The product was preabsorbed on silica and purified by column chromatography (SiO_2, hexane:DCM 1:1) and recrystallized from chloroform. 17 mg of product as yellow powder were collected (35% yield). ^{1}H-NMR (400 MHz, $CDCl_3$) δ 7.55 (m, 4H), 7.52 (s, 8H), 7.38 (m, 5H), 2.44 (s, 3H).

VARIABLE TEMPERATURE *J-V* MEASUREMENTS

Using a mask and metal deposition we prepared arrays of 3 Au electrodes (300 μm wide, 1.5 cm long, and 100 nm thick; larger round pads at the end of the electrode were used to easily contact the lines) on Si/SiO_2 wafers. The arrays were then transfer on glass slides (1.5x2x0.2 cm) using template stripping techniques. Since the optical adhesive (OA, Norland, No. 61) adheres strongly to Si/SiO_2 and prevents the lift off of the electrodes, we functionalized the wafer with 1H,1H,2H,2H-perfluorooctyltrichlorosilane by gas phase deposition of the FOTS for 1.5 hours.

SAMs of **OPE3** and **OPE4** were grown in the flowbox controlled environment (1-3% oxygen, humidity <10%) by immersion of the electrodes in 10 mL of a 50 μM solution of the desired OPE compound in distilled toluene overnight, followed by addition of 0.1 mL of a 17 mM DBU solution in distilled toluene 1 hour before the measurement. The samples were then rinsed with EtOH and let dry for 10 minutes. PDMS channels (15 μm and 30 μm wide, 50 μm deep, 1 cm long) were obtained by polymerizing the PDMS over a master that was prepared using standard photolitography techniques. The channels were oxidized in oxygen plasma (500 mbar, 300 s) and moved in the flowbox where they were placed over the samples (perpendicular to the electrodes) and carefully filled with EGaIn apllying one drop of alloy on one inlet and reduced pressure on the other.

The samples were placed in a cryogenic chamber filled with nitrogen. We biased the EGaIn top-electrode and grounded the Au bottom-electrode, and acquired J at different potentials to obtain J(V) curves. We performed scans in the +0.5 V/-0.5 V range (5 scans per junction from 0 V$\rightarrow$ 0.5 V $\rightarrow$ $-$0.5 V $\rightarrow$ 0 V, steps of 0.05 V) initially at room temperature and then slowly stepwise lowering the temperature with liquid nitrogen to 188 K for **OPE3** and 153 K for **OPE4** (these temperatures were dictated by short circuits). The results proposed in Figure 2.5 and Figure 2.4 are averages of 2 samples (6 junctions) per compound. As it possible to observe, J only varies slightly with the temperature as it is expected for tunneling junctions (Fig. 2.5).

BIBLIOGRAPHY

[1] Wang, G.; Kim, T.-W.; Lee, T. *J. Mater. Chem.* **2011**, *21*, 18117–18136.

[2] Leary, E.; La Rosa, A.; Gonzalez, M. T.; Rubio-Bollinger, G.; Agrait, N.; Martin, N. *Chem. Soc. Rev.* **2015**, *44*, 920–942.

[3] Metzger, R. M. *Chem. Rev.* **2015**, *115*, 5056–5115.

[4] Khoo, K. H.; Chen, Y.; Li, S.; Quek, S. Y. *Phys. Chem. Chem. Phys.* **2015**, *17*, 77–96.

[5] Nishizawa, S.; Hasegawa, J.-y.; Matsuda, K. *J. Phys. Chem. C* **2013**, *117*, 26280–26286.

[6] Bergren, A. J.; Zeer-Wanklyn, L.; Semple, M.; Pekas, N.; Szeto, B.; McCreery, R. L. *J. Phys.: Cond. Matt. Phys.* **2016**, *28*, 094011.

[7] Akkerman, H. B.; Blom, P. W. M.; de Leeuw, D. M.; de Boer, B. *Nature* **2006**, *441*, 69–72.

[8] Zhang, Y.; Zhao, Z.; Fracasso, D.; Chiechi, R. C. *Isr. J. Chem.* **2014**, *54*, 513–533.

[9] Kovalchuk, A.; Abu-Husein, T.; Fracasso, D.; Egger, D. A.; Zojer, E.; Zharnikov, M.; Terfort, A.; Chiechi, R. C. *Chem. Sci.* **2016**, *7*, 781–787.

[10] Kronemeijer, A. J.; Huisman, E. H.; Akkerman, H. B.; Goossens, A. M.; Katsouras, I.; van Hal, P. A.; Geuns, T. C. T.; van der Molen, S. J.; Blom, P. W. M.; de Leeuw, D. M. *Appl. Phys. Lett.* **2010**, *97*, 173302.

[11] Valkenier, H.; Huisman, E. H.; van Hal, P. A.; de Leeuw, D. M.; Chiechi, R. C.; Hummelen, J. C. *J. Am. Chem. Soc.* **2011**, *133*, 4930–4939.

[12] Yoon, H. J.; Bowers, C. M.; Baghbanzadeh, M.; Whitesides, G. M. *J. Am. Chem. Soc.* **2014**, *136*, 16–19.

[13] Bowers, C. M.; Liao, K.-C.; Zaba, T.; Rappoport, D.; Baghbanzadeh, M.; Breiten, B.; Krzykawska, A.; Cyganik, P.; Whitesides, G. M. *ACS Nano* **2015**, *9*, 1471–1477.

[14] Jiang, L.; Sangeeth, C. S. S.; Wan, A.; Vilan, A.; Nijhuis, C. A. *J. Phys. Chem. C* **2015**, *119*, 960–969.

[15] Simeone, F. C.; Yoon, H. J.; Thuo, M. M.; Barber, J. R.; Smith, B.; Whitesides, G. M. *J. Am. Chem. Soc.* **2013**, *135*, 18131–18144.

[16] Engelkes, V. B.; Beebe, J. M.; Frisbie, C. D. *J. Am. Chem. Soc.* **2004**, *126*, 14287–14296.

[17] Barber, J. R.; Yoon, H. J.; Bowers, C. M.; Thuo, M. M.; Breiten, B.; Gooding, D. M.; Whitesides, G. M. *Chem. Mater.* **2014**, *26*, 3938–3947.

[18] Perrin, M. L.; Frisenda, R.; Koole, M.; Seldenthuis, J. S.; Celis, G. A.; Valkenier, H.; Hummelen, J. C.; Renaud, N.; Grozema, F. C.; Thijssen, J. M.; Dulić, D.; van der ZantHerre S. J., *Nat. Nanotechnol.* **2014**, *9*, 830–834.

[19] Kim, S.-U.; Shin, H.-K.; Kwon, Y.-S. *Colloids Surf. A* **2005**, *257–258*, 211–214.

[20] Fan, F.-R. F.; Yao, Y.; Cai, L.; Cheng, L.; Tour, J. M.; Bard, A. J. *J. Am. Chem. Soc.* **2004**, *126*, 4035–4042.

[21] Tour, J. M.; Rawlett, A. M.; Kozaki, M.; Yao, Y.; Jagessar, R. C.; Dirk, S. M.; Price, D. W.; Reed, M. A.; Zhou, C.-W.; Chen, J.; Wang, W.; Campbell, I. *Chem. Eur. J.* **2001**, *7*, 5118–5134.

[22] Fan, F.-R. F.; Yang, J.; Cai, L.; Price, D. W.; Dirk, S. M.; Kosynkin, D. V.; Yao, Y.; Rawlett, A. M.; Tour, J. M.; Bard, A. J. *J. Am. Chem. Soc.* **2002**, *124*, 5550–5560.

[23] Chen, J.; Reed, M. A.; Rawlett, A. M.; Tour, J. M. *Science* **1999**, *286*, 1550–1552.

[24] Lewis, P. A.; Inman, C. E.; Yao, Y.; Tour, J. M.; Hutchison, J. E.; Weiss, P. S. *J. Am. Chem. Soc.* **2004**, *126*, 12214–12215.

[25] Stapleton, J. J.; Harder, P.; Daniel, T. A.; Reinard, M. D.; Yao, Y.; Price, D. W.; Tour, J. M.; Allara, D. L. *Langmuir* **2003**, *19*, 8245–8255.

[26] Donhauser, Z. J.; Mantooth, B. A.; Kelly, K. F.; Bumm, L. A.; Monnell, J. D.; Stapleton, J. J.; Price, D. W.; Rawlett, A. M.; Allara, D. L.; Tour, J. M.; Weiss, P. S. *Science* **2001**, *292*, 2303–2307.

[27] Guedon, C. M.; Valkenier, H.; Markussen, T.; Thygesen, K. S.; Hummelen, J. C.; van der Molen, S. J. *Nat. Nanotechnol.* **2012**, *7*, 305–309.

[28] Fracasso, D.; Valkenier, H.; Hummelen, J. C.; Solomon, G. C.; Chiechi, R. *J. Am. Chem. Soc.* **2011**, *133*, 9556–9563.

[29] Obersteiner, V.; Egger, D. A.; Heimel, G.; Zojer, E. *J. Phys. Chem. C* **2014**, *118*, 22395–22401.

[30] Obersteiner, V.; Egger, D. A.; Zojer, E. *J. Phys. Chem. C* **2015**, *119*, 21198–21208.

[31] Wei, Z. et al. *Adv. Funct. Mater.* **2015**, *25*, 1700–1708.

[32] Kaliginedi, V.; Moreno-García, P.; Valkenier, H.; Hong, W.; García-Suárez, V. M.; Buiter, P.; Otten, J. L. H.; Hummelen, J. C.; Lambert, C. J.; Wandlowski, T. *J. Am. Chem. Soc.* **2012**, *134*, 5262–5275.

[33] Luo, L.; Choi, S. H.; Frisbie, C. D. *Chem. Mater.* **2011**, *23*, 631–645.

[34] Tour, J. M. *Acc. Chem. Res.* **2000**, *33*, 791–804.

[35] Venkataraman, L.; Klare, J. E.; Nuckolls, C.; Hybertsen, M. S.; Steigerwald, M. L. *Nature* **2006**, *442*, 904–907.

[36] Maya, F.; Flatt, A. K.; Stewart, M. P.; Shen, D. E.; Tour, J. M. *Chem. Mater.* **2004**, *16*, 2987–2997.

[37] Klare, J. E.; Tulevski, G. S.; Sugo, K.; de Picciotto, A.; White, K. A.; Nuckolls, C. *J. Am. Chem. Soc.* **2003**, *125*, 6030–6031.

[38] Bunz, U. H. F. *Chem. Rev.* **2000**, *100*, 1605–1644.

[39] Tour, J. M.; Jones, L.; Pearson, D. L.; Lamba, J. J. S.; Burgin, T. P.; Whitesides, G. M.; Allara, D. L.; Parikh, A. N.; Atre, S. *J. Am. Chem. Soc.* **1995**, *117*, 9529–9534.

[40] Weiss, E. A.; Kaufman, G. K.; Kriebel, J. K.; Li, Z.; Schalek, R.; Whitesides, G. M. *Langmuir* **2007**, *23*, 9686–9694.

[41] Simmons, J. G. *Appl. Phys. Let.* **1963**, *34*, 1793–1803.

[42] Lu, Q.; Liu, K.; Zhang, H.; Du, Z.; Wang, X.; Wang, F. *ACS Nano* **2009**, *3*, 3861–3868.

[43] Liu, K.; Li, G.; Wang, X.; Wang, F. *J. Phys. Chem. C* **2008**, *112*, 4342–4349.

[44] Liu, H.; Wang, N.; Zhao, J.; Guo, Y.; Yin, X.; Boey, F. Y. C.; Zhang, H. *ChemPhysChem* **2008**, *9*, 1416–1424.

[45] Xing, Y.; Park, T.-H.; Venkatramani, R.; Keinan, S.; Beratan, D. N.; Therien, M. J.; Borguet, E. *J. Am. Chem. Soc.* **2010**, *132*, 7946–7956.

[46] Sangeeth, C. S. S.; Demissie, A. T.; Yuan, L.; Wang, T.; Frisbie, C. D.; Nijhuis, C. A. *J. Am. Chem. Soc.* **2016**, –.

[47] Wang, W.; Lee, T.; Reed, M. *Phys. Rev. B* **2003**, *68*, 035416.

[48] Dickey, M. D.; Chiechi, R. C.; Larsen, R. J.; Weiss, E. A.; Weitz, D. A.; Whitesides, G. M. *Adv. Func. Mater.* **2008**, *18*, 1097–1104.

[49] Weiss, E. A.; Chiechi, R. C.; Kaufman, G. K.; Kriebel, J. K.; Li, Z.; Duati, M.; Rampi, M. A.; Whitesides, G. M. *J. Am. Chem. Soc.* **2007**, *129*, 4336–4349.

[50] Haynes, W. M., Ed. *CRC Handbook of Chemistry and Physics, 97th Edition*; CRC Press, 2016.

[51] Doudrick, K.; Liu, S.; Mutunga, E. M.; Klein, K. L.; Damle, V.; Varanasi, K. K.; Rykaczewski, K. *Langmuir* **2014**, *30*, 6867–6877.

[52] Kong, G. D.; Kim, M.; Yoon, H. J. *J. Electrochem. Soc.* **2015**, *162*, H703–H712.

[53] Ocampo, O. E. C.; Gordiichuk, P.; Catarci, S.; Gautier, D. A.; Herrmann, A.; Chiechi, R. C. *J. Am. Chem. Soc.* **2015**, *137*, 8419–8427.

[54] Garrigues, A. R.; Yuan, L.; Wang, L.; Mucciolo, E. R.; Thompon, D.; del Barco, E.; Nijhuis, C. A. *Sci. Rep.* **2016**, *6*, 26517.

[55] Salomon, A.; Cahen, D.; Lindsay, S.; Tomfohr, J.; Engelkes, V.; Frisbie, C. *Adv. Mater.* **2003**, *15*, 1881–1890.

[56] Gryko, D. T.; Clausen, C.; Roth, K. M.; Dontha, N.; Bocian, D. F.; Kuhr, W. G.; Lindsey, J. S. *The Journal of Organic Chemistry* **2000**, *65*, 7345–7355.

3

CHARGE TRANSPORT AND MOLECULAR DIPOLES IN CONJUGATED MOLECULAR WIRES

Collective effects arising from dipoles alignment in SAM-based large-area EGaIn molecular junctions can drastically affect the charge transport characteristics. In this Chapter we discuss the design, the synthesis, and the electric characterization of SAMs of oligo(henylene-ethynylene) wires in which we systematically vary i) the direction and module of the dipole along the molecular axis, ii) the packing angle in the monolayer, iii) the degree of coupling with the bottom electrode, and iv) the interaction between different polar groups and EGaIn.

I would like to thank Dr. A. Kovalchuck and A. Ozcelik for the help in the synthesis of the compounds, X. Qiu for performing AFM measurements on the SAMs, and S. Soni for the help with the computational part.

3.1. INTRODUCTION

If we could divide the research in Molecular Electronics into two large groups, those would include the research done on single molecules and that involving large-area molecular junctions. While the former are easily to calculate and model *in silico*, they do not posses the characteristics to be integrated into electronic components. The latter, on the other hand, are more relevant toward device fabrication despite being inherently more complicated to compute: this is because large-area molecular junctions usually make use of self-assebled monolayers (SAMs) whose properties closely depends on their dynamic nature and interactions, thus making them too computationally demanding.[1–3] Compared to single molecules, collective effects in SAMs that arise from the packing of the molecules in the monolayer can dominate the charge transport: when dipoles are packed close together they can give rise to strong electric fields that can affect the work function (ψ) of the electrode or the level alignment in the junction.[2–4] While these phenomena have being studied in theory and their related effects measured in SAMs using different techniques,[3, 4] it is not clear how and to which extent, the these collective properties affect the charge transport properties in a large-area molecular junction. For what concerns EGaIn-based junctions, the Whiteside's group showed in a series of papers concerning SAMs of saturated compounds, that changing the anchoring group (*i.e.*, , the bottom interfacial dipole), inserting dipoles with different orientation in the middle of the junction, or placing different end-groups at the SAM//EGaIn interface, did not affect significantly the charge transport properties.[5–8] According to them, only the fluorination of the molecule at the SAM/EGaIn interface was reported to lower the injection current (J_0) without altering the transport mechanism, as a result of lower wetting of the EGaIn electrode (which translate to a smaller contact area).[9] Yet, a recent study from Bruce *et al.* on similar fluorinated mercaptoalkanes showed no straightforward effect.[10] Kong *et al.* also reported a reduction in J_0 when halogens are present at the SAM/EGaIn interface but could not separate the effect of different atoms.[11] In yet another study, Wang *et al.* found the resistance of halogen-terminated SAMs to decrease linearly with the polarizability of the halogen.[12] According to most of these studies, only molecules characterized by molecular states accessible to the electrodes in the bias

window will affect the electrical properties of the junctions.[8, 13, 14]

It is worth mentioning that all these studies analyzed the electrical properties of the junctions only in terms of J_0 and the tunnelling decay coefficient (β) described by the Simmons model, summarized in Equation 3.1:[15]

$$J = J_0 e^{-\beta d} \tag{3.1}$$

In doing so, they did not consider other features of the J/V line shape that can respond to dipole-induced collective effects such as the transition voltage (V_t) or rectification. For example, Fracasso *et al.* observed that on going from a byphenyl- to *p*-phenylpyridine-terminated SAM (with the nitrogen at the SAM/EGaIn interface) affected both the magnitude of the current and the value of V_t, which responded to the measured shift in work function of the metal substrate when the SAM is present.[16] Similarly, Kovalchuck *et al.* reported how embedding a dipole in a polyphenylene-like wire bearing a pyrimidine ring can affect both V_t and the direction of the J/V asymmetry upon reorientation.[17, 18]

In this study we synthesized a series of compounds based on the **OPE3** structure bearing strong dipoles parallel to the long molecular axis and we measured their charge transport properties in large area Au^{TS}/SAM//EGaIn tunnelling junctions (where '/' and '//' denotes covalent and van der Waals interactions respectively).

OPEs are considered very versatile molecules in Molecular Electronics because of their conjugated backbone that can be easily functionalized without distorting the flatness of the molecule too much. Compared to saturated molecules of similar dimensions, their HOMO-LUMO gap is much smaller and the frontier orbitals can participate in the transport and show a greater response to dipoles-induced eletctric fields. We made use of a physical-organic approach to investigate and isolate the different effects that dipoles originating from different functionalities can have on tunnelling junction.

We synthesized **OPE** structures that placed the 1,3-difluoro functionality in different positions of the molecular structure, effectively tuning the module and the direction of the dipole along the molecular length while keeping the molecular formula unchanged (**OPEF**, Figure 3.1 top).

By adding a CH_2 unit between the conjugated wire and the anchoring sulfur group

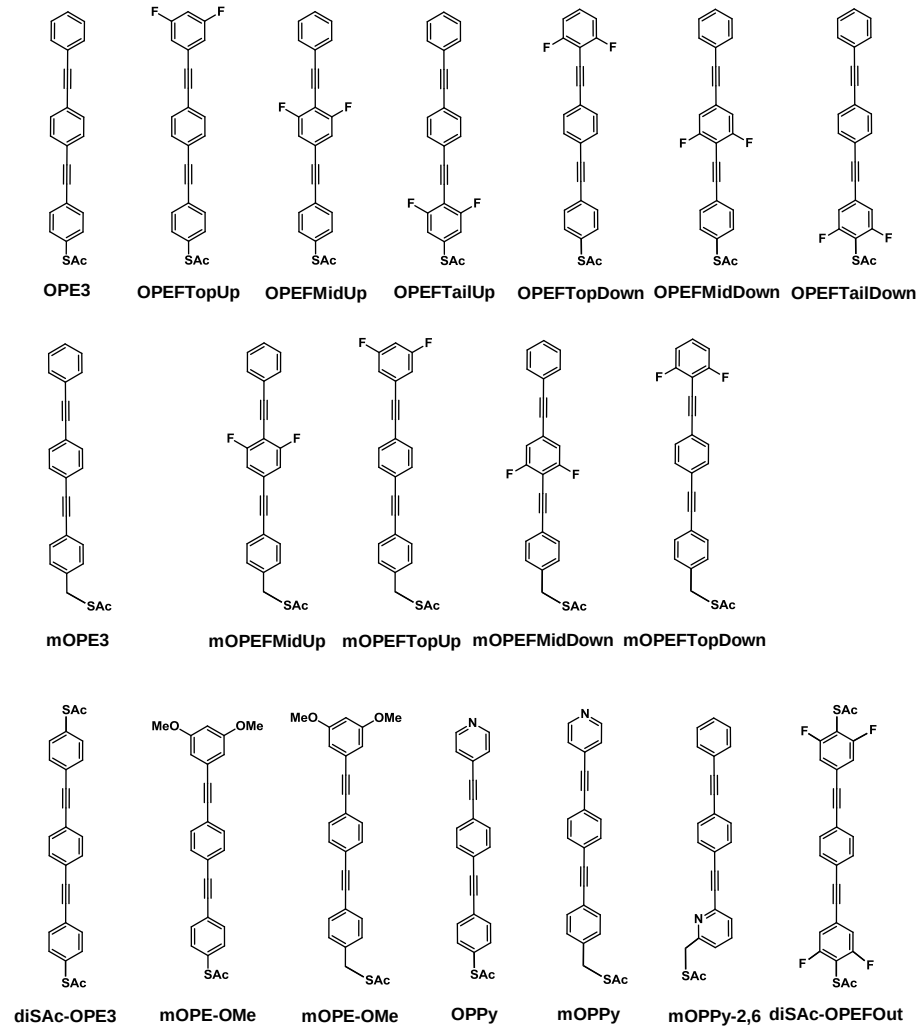

Figure 3.1 The OPE-related compounds investigated: **OPEF** series (Top), **mOPEF** sries (middle), F-free wires (bottom).

(**mOPEF**, Figure 3.1 middle), we could probe the effect of other variables such as the angle between the dipole and the metal surface and the extent of the coupling with the bottom electrode.

We finally studied the effect of dipoles of different nature at the interface between the SAM and the EGaIn electrode making use of different terminations (Figure 3.1 bottom) — namely thioacetate (**diSAc-**), pyridine (**OPPy)**, and methoxy groups (**OPE-OMe**).

3.2. DESIGN AND SYNTHESIS

In the **OPEF** series depicted in the top of Figure 3.1, we were able to change drastically the dipole moment of the molecules without altering the chemical formula or the HOMO-LUMO levels. These effects are summarized in Table 3.1. The HOMO and the LUMO energies lie within -5.8 ± 0.1 eV and -2.1 ± 0.1 eV respectively across the whole series. Compared to the unsubstituted **OPE3**, addition of the fluorines lowers the energy of both the frontier orbitals by about 0.2 eV. The effect of fluorine atoms on the dipole of an aromatic compound can be complex due to the nature of halogens on aromatic rings being both electron-withdrawing by induction and electron-donating by resonance. The order of magnitude for the dipoles pointing toward the sulfur follows the order **OPEFTailDown** > **OPEFMidDown** > **OPEFTailUp**, while for the dipoles pointing toward the other direction is **OPEFTopUp** > **OPEFTopDown** > **OPEFMidUp**. The strongest dipole was found for **OPEFTailDown** showing how the two local dipoles generated by the C-S and the two C-F bonds can add constructively, while being the furthest from the molecular center. A similar argument can be made to explain why the dipole of **OPEFMidDown** is larger than that of **OPEFTailUp** despite the fluorine of the latter having the F atoms further away from the molecular center. The possibility of drawing resonance structures for **OPEFMidDown** where the fluorines can π donate to the bottom ring could also explain the difference in dipoles between the latter and **OPEFTailUp**.

The dipoles predicted for the other half of the series are pointing away from the sulfur and have, by comparison, a lower magnitude. Trivial explanation for this is the opposite orientation (with respect to the center of the molecule) of the local dipoles created by the fluorines and the sulfur. **OPEFTopUp** is characterized by the strongest dipole moment

Table 3.1 Summary of HOMO-LUMO levels and dipole moments calculated by DFT for the series presented in Figure 3.1.

	HOMO (eV)	LUMO (eV)	Band gap (eV)	Dipole (D)
OPE3	-5.59	-1.93	3.66	-1.32
OPEFTopUp	-5.82	-2.12	3.70	3.04
OPEFTopDown	-5.70	-2.12	3.58	1.73
OPEFMidUp	-5.85	-2.25	3.60	1.59
OPEFMidDown	-5.80	-2.25	3.55	-2.70
OPEFTailUp	-5.77	-2.11	3.66	-1.09
OPEFTailDown	-5.86	-2.21	3.65	-3.65
mOPE3	-5.69	-1.95	3.74	-1.68
mOPEFTopUp	-5.97	-2.27	3.70	4.13
mOPEFTopDown	-5.83	-2.14	3.69	1.71
mOPEFMidUp	-5.96	-2.27	3.69	2.67
mOPEFMidDown	-5.96	-2.27	3.69	-2.28
diSAc-OPE3	-5.53	-1.95	3.58	0
OPPy	-5.81	-2.25	3.56	3.65
mOPPy	-5.94	-2.22	3.72	4.99
mOPPy-2,6	-5.84	-2.08	3.76	-1.58
OPE-OMe	-5.53	-1.84	3.69	4.22
mOPE-OMe	-5.63	-1.87	3.76	3.54
diSAc-OPEFOut	-5.97	-2.27	3.70	0

thanks to the C-F bonds pointing the furthest away from the molecular center and the fact that it can only inductively attract charge density to the top ring. Unlike the bottom half, now the compound with the fluorinated outer ring (**OPEFTopDown**) shows a larger dipole than the one with the fluorinated middle ring (**OPEFMidUp**).

We prepared the **OPEF** compounds starting from the appropriate fluorinated rings and expanding the wire by means of Sonogashira couplings as depicted in Figures 3.3-3.4. We introduced the tail containing the sulfur to bind to the metal substrates last using S-(4-iodophenyl)ethanethioate, as the thioacetate group gave generally lower yields when involved in Sonogashira couplings.

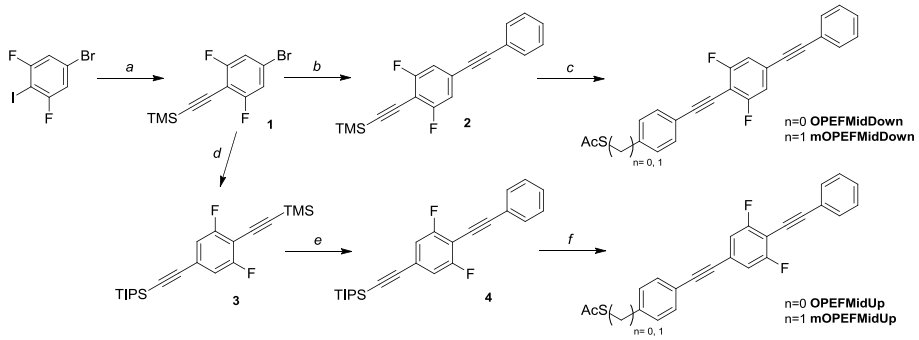

Figure 3.2 Reaction scheme for the synthesis of **OPEFMidUp**, **OPEFMidDown**, **mOPEFMidUp**, and **mOPEFMidDown**. *a*: TMS-acetylene, $Pd(PPh_3)_4$, CuI, NEt_3, THF; *b*: i) phenylacetylene, $Pd(PPh_3)_4$, CuI, NEt_3, THF; ii) K_2CO_3, EtOH; *c*: **IPhSAc** (n=0)/**IBzSAc** (n=1), $Pd(PPh_3)_4$, CuI, NEt_3, THF; *d*: TIPS-acetylene, $Pd(PPh_3)_4$, CuI, NEt_3, THF; *e*: i) K_2CO_3, MeOH; ii) iodobenzene, $Pd(PPh_3)_4$, CuI, NEt_3, THF (**4.1**); *f*: i) TBAF, THF/H_2O; ii) **IPhSAc** (n=0)/**IBzSAc** (n=1), $Pd(PPh_3)_4$, CuI, NEt_3, THF.

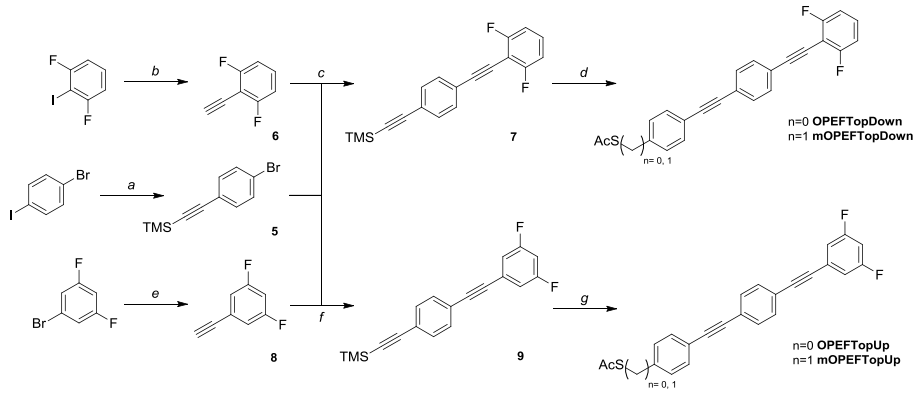

Figure 3.3 Reaction scheme for the synthesis of **OPEFTopUp**, **OPEFTopDown**, **mOPEFTopUp**, and **mOPEFTopDown**. *a*: TMS-acetylene, $Pd(PPh_3)_4$, CuI, NEt_3, THF; *b*: i) TMS-acetylene, $Pd(PPh_3)_4$, CuI, NEt_3, THF; ii) K_2CO_3, MeOH; *c*: **5**, $Pd(PPh_3)_4$, CuI, NEt_3, THF; *d*: i) TBAF, THF (**7.1**); ii) **IPhSAc** (n=0)/**IBzSAc** (n=1), $Pd(PPh_3)_4$, CuI, NEt_3, THF; **e**: i) TMS-acetylene, $Pd(PPh_3)_4$, CuI, NEt_3, THF; ii) K_2CO_3, EtOH; *f*: **5**, $Pd(PPh_3)_4$, CuI, NEt_3, THF; *g*: i) TBAF, THF (**9.1**); ii) **IPhSAc** (n=0)/**IBzSAc** (n=1), $Pd(PPh_3)_4$, CuI, NEt_3, THF.

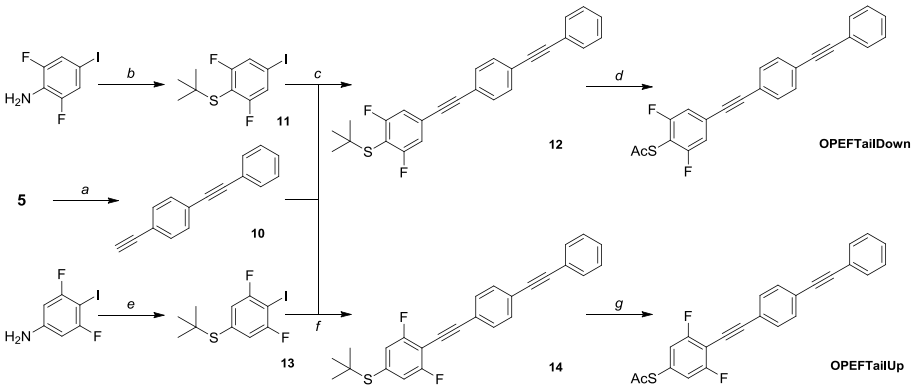

Figure 3.4 Reaction scheme for the synthesis of **OPEFTailUp** and **OPEFTailDown**. *a*: i) phenylacetylene, $Pd(PPh_3)_4$, CuI, NEt_3, THF; ii) K_2CO_3, MeOH; *b*: tBuSStBu,tBu(ONO); *c*: **10**, $Pd(PPh_3)_4$, CuI, NEt_3, THF; *d*: $TiCl_4$, AcCl, DCM; *e*: tBuSStBu,tBu(ONO); *f*: **10**, $Pd(PPh_3)_4$, CuI, NEt_3, THF; *g*: $TiCl_4$, AcCl, DCM.

If instead of the latter, S-(4-iodobenzyl)ethanethioate is used, the wires will have an extra $-CH_2-$ between the conjugated part and the S-metal bond in the SAM (Figures 3.3 and 3.2).

This change significantly affects the packing and the nature of the molecules in the SAM: i) compared to the **OPE** series, the tilt angle of the conjugated part in SAMs of **mOPE** molecules is closer to the surface normal,[19] which means that, inside the junction, the perpendicular component of the molecular dipole is larger; ii) the benzylic $-CH_2-$ also lowers the coupling between the molecules and the substrate by effectively separating the positions of the orbitals from the metal surface.[20, 21]; iii) the presence of a $-CH_2-$ instead of the S also affect slightly the electronic characteristics of the compounds, lowering the HOMO and the LUMO of about 0.2 eV. According to our calculations, **mOPEFTopDown** shows the lowest lying HOMO in the **mOPEF** series as it also does for the corresponding **OPEF** (Table 3.1). The reason for this difference is unclear.

Next to the fluorinated **OPEs**, we also wanted to explore the different effects that dipoles generated by other electron-withdrawing functionalities would have on the electrical characteristics of a tunnelling junction. Control experiments as these are important since in tunnelling junctions molecular properties arising from the unique nature of the atoms involved can dominate the effect of trends predicted by simple geomet-

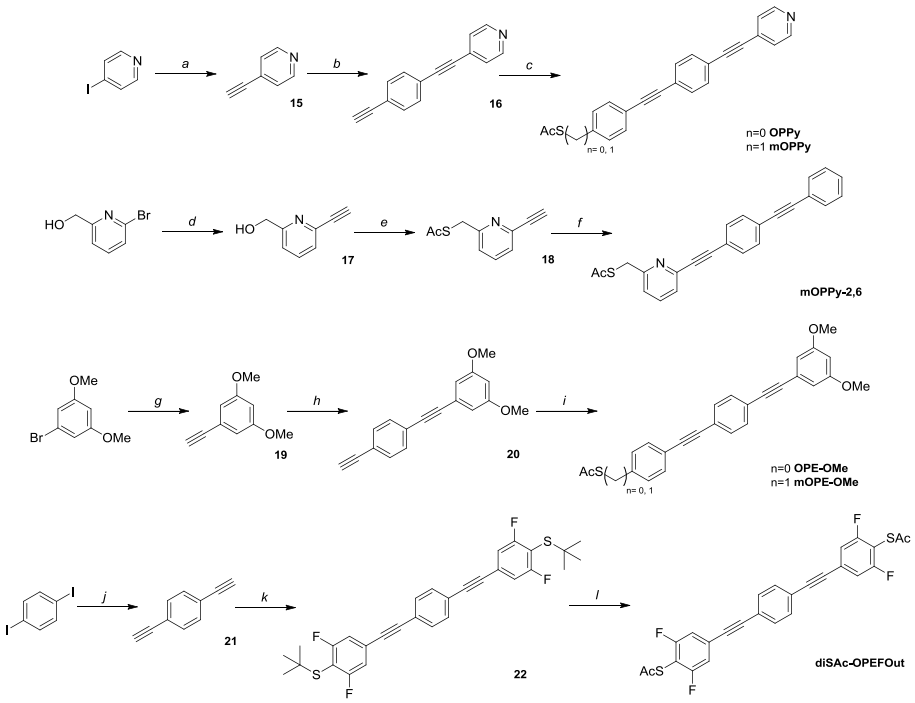

Figure 3.5 Reaction scheme for the synthesis of **OPPy, mOPPy, mOPPy-2,6**, **OPE-OMe**, **mOPE-OMe**, and **diSAc-OPEFOut**. *a*: i) TMS-acetylene, $Pd(PPh_3)_4$, CuI, NEt_3, THF; ii) TBAF, H_2O, THF; *b*: i) **5**, $Pd(PPh_3)_4$, CuI, NEt_3, THF; ii) TBAF, H_2O, THF; *c*: **IPhSAc** (n=0)/**IBzSAc** (n=1), $Pd(PPh_3)_4$, CuI, NEt_3, THF; *d*: i) TMS-acetylene, $Pd(PPh_3)_4$, CuI, NEt_3, THF; ii) TBAF, H_2O, THF; *e*: i) NEt_3, $MeSO_2Cl$, DCM; ii) KSac, DMF; *f*: 1-bromo-4-(phenylethynyl)benzene, $Pd(PPh_3)_4$, CuI, NEt_3, THF; *g*: i) TMS-acetylene, $Pd(PPh_3)_4$, CuI, NEt_3; ii) TBAF, H_2O, THF; *h*: i) **TIPS-5**, $Pd(PPh_3)_4$, CuI, NEt_3; ii) TBAF, H_2O, THF; *i*: **IPhSAc** (n=0)/**IBzSAc** (n=1), $Pd(PPh_3)_4$, CuI, NEt_3, THF.

rical or energetic considerations. We will explore this more in depth in Chapter 6 but the same themes were also highlighted in a recent work by Bruce *et al.*.[10] We therefore prepared the **OPPy** and **OPE-OMe** wires containing a pyridine ring and methoxy groups at the SAM/EGaIn interface. The wires were prepared starting from 4-iodopyridine and 1-bromo-3,5-dimethoxybenzene through a series of Sonogashira couplings similar to approach used for the **OPEFTop** compounds. Figure 3.5 summarizes these procedures.

While these different end-groups also generate a strong dipole of a magnitude comparable to that of (**m**)**OPEFTopUp**, the chemical interactions they can make are remarkably different. The SAMs of **OPPy**-wires, for instance, show on the surface nitrogen

atoms that are basic and have coordinating character that can influence the interaction with the EGaIn electrode. We decided to include **mOPPy-2,6** to study how moving the nitrogen from the top to the bottom of the wire (thus changing the dipole direction and removing the coordinating ability) affect the tunnelling process.

The synthesis for this wire was done following a similar approach to that of **OPEFTail** compounds (Figure 3.5). The different substitution pattern in the bottom ring (in the *meta* position instead of the *para*), which makes the comparison less robust, is due to the impossibility of synthesizing the *para* derivative.

Compared to all the compounds discussed so far, **OPE-OMe** and **mOPE-OMe** are characterized by the largest dipoles. Contrary to the example of pyridine-containing wires, they present methyl groups to the surface of the SAM, creating an environment that should be more similar to that of saturated molecules while still retaining the same molecular length and the conjugation as the other compounds in this study.

Finally, we decided to synthesize **diSAc-OPEFOut** to combine the effect of substitution patterns that were able to affect the transport characteristics (see later sections) and investigate whether they would be additive or one one dominate over the other.

3.3. ELECTRICAL CHARACTERIZATION OF THE SAMS

3.3.1. OPEF SERIES

The electric properties of SAMs of the compounds proposed in Figure 3.1 were investigated in large area Au^{TS}/SAM//Ga_2O_3/EGaIn junctions (where Au^{TS} represent template stripped gold surface;[22]). The measurements were performed in the low-oxygen, low-humidity setup introduced in Chapter 2 using a similar methodology. The J/V data obtained for the **OPEF** series are presented in Figure 3.6a.

We found no apparent correlation between the molecular dipoles and the J/V curves across the whole series: most of the SAMs gave statistically indistinguishable results for both magnitude and line shape. The only exceptions where found to be **OPEFTailUp** and **OPEFTailDown** which gave the largest and lowest current density in the series respectively, showing that only the fluorination of the rings close to the Au electrode seems to

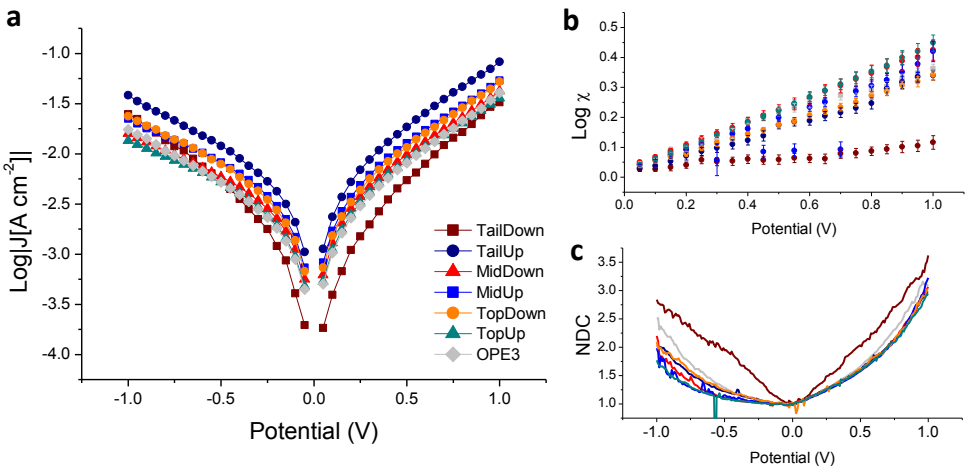

Figure 3.6 a: Plot of $Log|J|$ vs. V for Au^{TS}/SAM//Ga_2O_3/EGaIn junctions comprising the compounds of the **OPEF** series (see legend). We removed the error bars for clarity. b: Plot of $Log\chi$ vs. V for the same junctions. Error bars represent confidence intervals with $\alpha = 0.05$. c: NDC plot for the same junctions.

affect the transport.

In order to obtain more information about the line shape, we also calculated the asymmetry of the J/V lines ($\chi = J(V_+)/J(V_-)$) and the Normalized Differential Conductance (NDC, $dJ/dV \cdot V/I$) for all the different SAMs. These results are shown in Figure 3.6b and c.

The study of the asymmetry of the the J/V plots, χ, can give information about the energy levels alignment in the junction and the mechanism of transport.[13, 16, 23, 24] Large-area EGaIn molecular junctions usually give rise to a small asymmetry, which was traditionally ascribed to the different electrodes/contacts involved.[17] Recent studies also pointed to the fact that the Stark effect could play a role in this phenomenon.[24] Usually the degree of asymmetry is similar for molecule of similar nature measured in identical conditions: we showed this effect already, for both conjugated **OPEs** and saturated molecules, in Chapter 2.

In the case of the **OPEF** series we observed no difference between the fluorinated compounds and **OPE3**: the majority of the compounds produced a Log-linear relation between χ and V, reaching a maximum of about 0.3 – 0.4 at 1 V. Again, **OPEFTailDown** behaved differently, giving more symmetrical J/V curves, with $Log\chi < 0.1$ across the en-

tire bias window. The reason for this behavior is unknown, but evidences suggest that the presence of the fluorine atoms close to the metal surface and pointing toward it strongly affects the interaction between the molecule and the electrode.

We can observe the unique transport properties of junctions comprising **OPEFTail Down** also in the NDC plot (Figure 3.6). These plots can be used to extract information about the transport between the electrodes: off-resonant tunnelling should describe a bowl-shaped curve with a minimum of 1 at 0 V, while deviation from this mechanism can affect the line shape.[25, 26] (As example, see Chapter **5** for a discussion of the effect of cross conjugation on NDC.) Indeed, a NDC plot resembling a bowl is found for all the compounds in the series except **OPEFTailDown**, for which the NDC is narrower and more linear. This finding points to the fact the the tunnelling mechanism for the latter, in addition to the considerations mentioned above, could be different and we must proceed carefully when trying to rationalize the whole series as one.

Another feature of the NDC plot is that we can use them to estimate the value of V_t. This parameter was introduced to get information about the tunnelling barrier and was used to estimate the energies of the levels inside the junction.[27–30] Usually it is calculated as the minimum in Fowler-Nordheim plot ($J(1/V^2)$), but this analysis can be misleading when V_t falls outside or very close to the extremes of the experimental bias window as it is the case for most of the compounds analyzed in this Chapter. The use of NDC plots can help in these cases as, in these latter, V_t appears as the V value at which NDC equals 2, but can also be extracted by mathematical means from any point in the measured bias.[25] From Figure 3.6c we can observe how, for every compound of the **OPEF** series, the values of V_t- are expected to fall around or below -1 V, a smaller value compared to **OPE3**. The relations between V_t and the frontier orbitals were already highlighted in previous studies, while others also discussed the effect on the former of molecular dipole and the shift in the work function of the electrode (ϕ).[17] Yet, in the present case no correlation between dipole moments, ϕ, and V_t was found (Figure 3.7).

High-order and dipole alignment are often credited to explain the effect of dipoles on the electrical characteristic of a large-area junction:[18, 31] the missing connection in the present case can indicate that the SAMs are either too disordered (or tilted) to provide

a sufficient cooperative interaction between the dipoles. This behavior could be an expression of the nature of fluorinated molecules for which intermolecular interactions based on dispersion forces tend to be weaker: as a result, fluorinated hydrocarbons tend to have lower boiling and melting points than their un-fluorinated analogues; which, in SAMs, could translate to a lower degree of order, meaning that the chemical nature of the molecules more than to their electrical characteristics that we can compute for single-molecules in gas phase can dominate the transport. In other words, collective effects become measurable only when high degree of cooperative interaction are found in the SAM.[32]

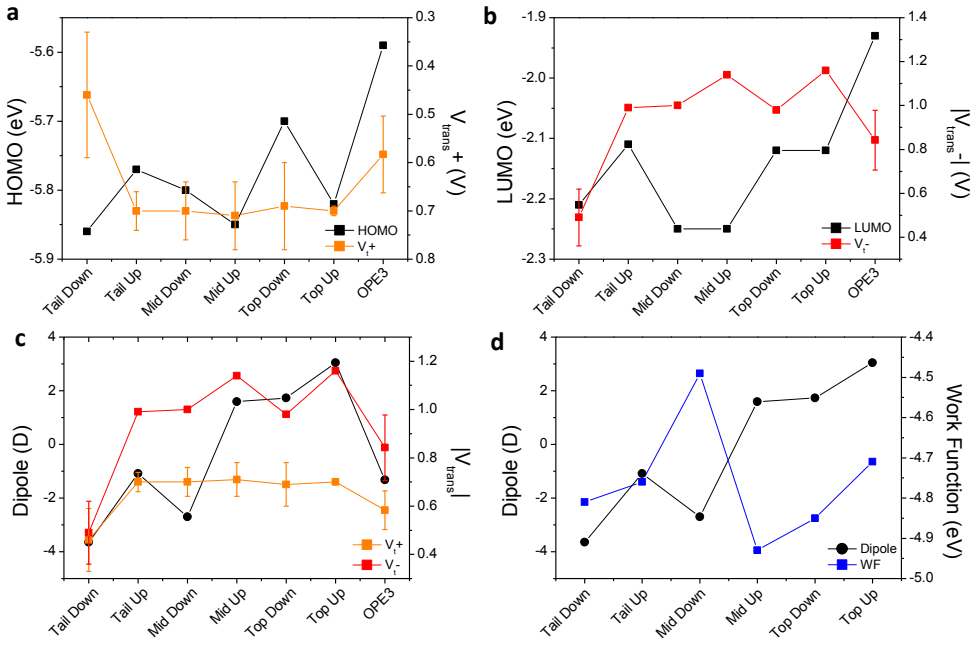

Figure 3.7 Double-y plots to emphasize the correlations between HOMO and V_t+ (a), LUMO and V_t-(b), dipole and V_t(c), and dipole and ϕ (d) for the different compounds in the **OPEF** series.

An extra-factor that we should consider when discussing V_t is the non-intuitive effects that highly electronegative elements can have on the distribution of charge and the delocalization of MO when the molecule is placed in an electric field:[18] in this sense, a trend between V_t and idealized properties such as the DFT energy of the orbitals of an isolated molecule might be too simplistic to describe a detailed picture. Further analysis

is needed to try to separate the different contributions that can affect the final measurement.

To summarize, in the case of the **OPEF** series, we found no strong correlation between the magnitude and direction of the dipoles and the J/V characteristics (or ϕ). This is in sharp contrast with what was found in other studies for other conjugated molecules.[16, 17] It is worth mentioning that, compared to these latter studies which comprised compounds bearing at least one methylene unit between the electrode and the conjugated part, our molecules are fully conjugated to the electrode, allowing a higher degree of pinning and mixing of states. **OPEFTailDown** behaved differently from all the other compounds in the series, but it is not clear whether we can ascribe these differences to the molecular dipoles and collective effects present in the SAM.

3.3.2. mOPEF SERIES

In order to increase the dipole alignment and the order in the SAM, we studied the electrical properties of junctions comprising a subset of **OPEF** structural analogues bearing an extra methylene between the sulfur and the conjugated part. This apparently small change has the effect of increasing the order of the SAM and diminishing the coupling between the conjugated part and the electrode.[19–21] The addition of the $-CH_2-$ unit to **OPE3** to make **mOPE3** did not influence the magnitude of J much as we can see in figure 3.8a. Yet, we can observe an effect on the asymmetry of the J/V curve: while we found a maximum of $Log\chi$ of 0.34 for **OPE3** (as we discussed for the **OPEF** series), **mOPE3** only went as high as 0.16 at 1 V (Figure 3.8b). This decrease had been reported to be related to a smaller degree of interaction between the molecule and the bottom electrode.[33]

In addition to the aforementioned, when compared to **OPE3**, **mOPE3** had a similar V_t- ($-0.84(14)$ and -0.92 V respectively) but a higher V_t+ (0.58(8) and 0.8(1) V respectively) which is likely due to the fact that these two molecules have similar LUMO and that the HOMO of **mOPE3** is lower in energy (by 0.1 eV).

The **mOPEF** series showed some interesting features when compared to its non-fluorinated analogues. As we can see in Figure 3.9a, where the J/V curves of the former

are plot together with those of their non-methylated analogues, the magnitude of J is smaller.

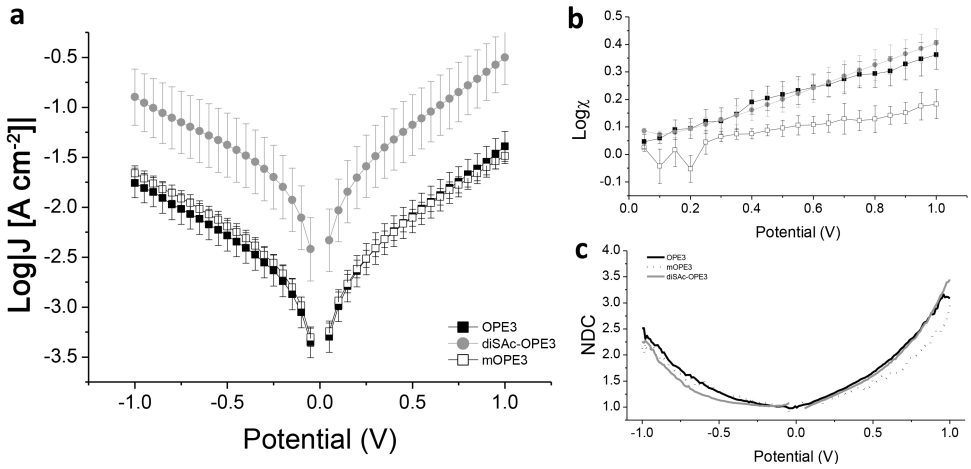

Figure 3.8 a: Plot of $Log|J|$ vs. V for Au^{TS}/SAM//Ga_2O_3/EGaIn junctions comprising non-fluorinated **OPE3**, **mOPE3**, and **diSAc-OPE3**. b: Plot of $Log\chi$ vs. V for the same junctions. Error bars represent confidence intervals with $\alpha = 0.05$. c: NDC plot for the same junctions.

Among the **mOPEF** compounds we are able to identify two groups of molecules: the molecules characterized by the fluorine atoms on the middle ring gave a somewhat lower J compared to those where the latter were found on the top ring. This fact hints to the important role that dipoles can have when placed at the EGaIn/SAM interface,[16] as we briefly mentioned in the previous Chapter. These observations will be discussed in more detail in the following section.

In Figure 3.9b and c we present the $Log\chi$ and NDC plots for junctions of the **mOPEF** series respectively. Similar to the non-fluorinated case, the maximum $Log\chi$ values (at 1 V), ranging between 0.2 and 0.3, are somewhat smaller than those of the non-methylated series (yet, larger than that of **mOPE3**). The NDC plots of junctions comprising these compounds are all bowl-shaped, indicating that the transport mechanism is similar across the series. While we can clearly observe the different behavior of **mOPEFMidDown**, the only one in the series with the dipole pointing toward the electrode, we have no clear evidence to ascribe this behavior to the effect of the dipoles nor the HOMO-LUMO. In particular, V_t- for **mOPEFMidDown** was measured to be $-0.80(13)$ V, which is smaller

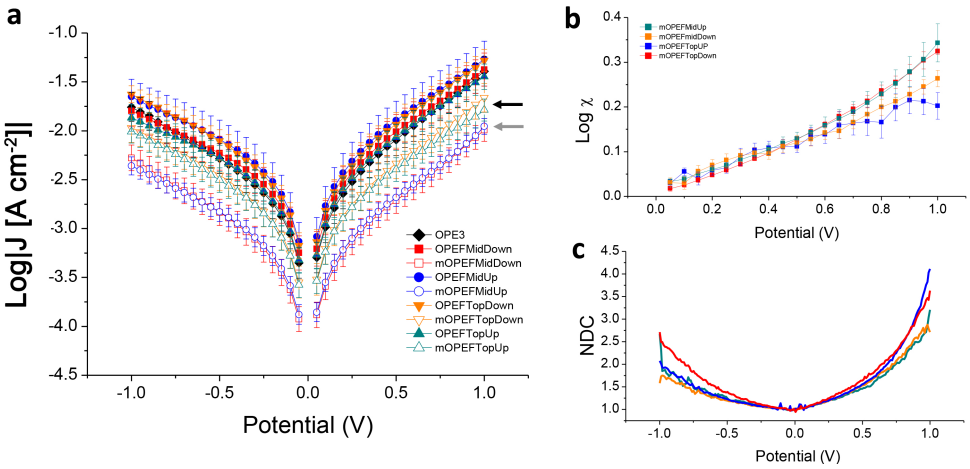

Figure 3.9 a: Plot of $Log|J|$ vs. V for Au^{TS}/SAM//Ga_2O_3/EGaIn junctions comprising **OPEF** and **mOPEF** (see legend). The black and gray arrows highlight the lots for fluorinated compounds substituted in the top and the middle ring respectively. b: Plot of $Log\chi$ vs. V for junctions comprising **mOPEF** compounds (see legend). Error bars represent confidence intervals with $\alpha = 0.05$. c: NDC plot for the same junctions.

in absolute value than that of **mOPE3** (estimated to be −0.92 V): from orbital considerations, the latter should show a smaller V_t- out of the higher lying LUMO with respect to the fluorinated analogue; while Kovalchuck *et al.* reported the opposite shift in V_t for a compound characterized by the same dipole direction of **mOPEFMidDown** as a result of the dipole-induced shift of the ϕ.[17] Yet, it is worth mentioning that the electronic characteristics of **mOPEFTopDown** are notably different from all the other fluorinated compounds in the **mOPEF** series.

Contrary to what we reported for the **OPEF** series, in the case of the methylene-bearing compounds the alignment of the dipoles seems to affect ϕ (Figure 3.10d). As mentioned earlier, this effect could be a consequence of the lower tilt angle of the **mOPE** compounds that allows better alignment of the molecules and a larger dipole component on the surface normal. Surprisingly enough, we found that ϕ varies with the local orientation of the dipoles rather than the molecular ones: ϕ shifts to higher values (compared to the **mOPE3**) in the case of the fluorine atoms pointing toward the electrode and to lower values for the fluorine atoms pointing the other direction.

Unfortunately we were not able to resolve this differences in the tunnelling junctions

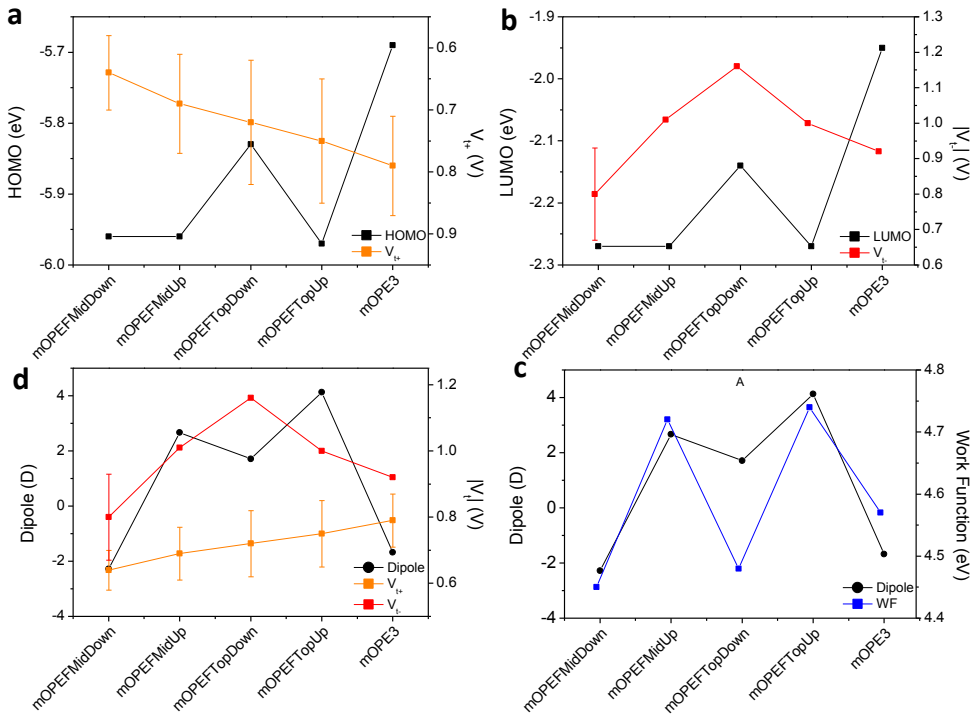

Figure 3.10 Double-y plots to emphasize the correlations between HOMO and V_t+ (a), LUMO and V_t-(b), dipole and V_t(c), and dipole and ϕ (d) for the different compounds in the **mOPEF** series.

experimentally, as we could find no clear trend around V_t. The question around the latter observable is complicated, as the way the $\Delta\phi$ should shift the values of V_t in the **OPEF** molecules in general is the opposite of what we would observe from the considerations arising around E_f-HOMO and E_f-LUMO for the same molecules.

These observations point to the fact that, in the case of the **mOPEF** series, the interaction with the electrodes dominates the transport and hides most of the possible feature that would arise from other molecular considerations. Compared to the previous series (without added methylene), we observed a smaller magnitude of J and we were able to find a relation between the direction of the internal dipoles and $\Delta\phi$. On top of that, the compounds characterized by a local dipole at the SAM/EGaIn interface showed different conductances. We will investigate the effect of dipoles at this interface in the next section.

3.3.3. THE EFFECT OF POLAR GROUPS AT THE SAM/EGAIN INTERFACE

In Chapter 2 we already discussed how junctions comprising SAMs of **diSAc-OPEs** were characterized by a larger J_0 compared to their mono-SAc analogues. We ascribed this difference to the more polar surface offered by the **diSAc**-SAMs, which increase the wettability of the monolayer as a result of a more favourable interaction with the EGaIn electrode.[34, 35] EGaIn behaves as a non-Newtonian fluid thanks to a sub-nm layer of Ga_2O_3 that forms at the interface between the metal and the environment.[36] The interaction between the SAM and the gallium oxide layer is traditionally assumed to be dominated by Van der Waals forces and therefore is — in principle — subject to the influence of stronger interactions, like dipole-dipole and dipole-induced dipole. Terminal groups with the ability of efficiently coordinating Ga(III) (or be coordinated by the oxide/hydroxide ion) should also affect the characteristic of a junction. To test this hypothesis we decided to synthesize and measure **OPE3** analogues bearing different dipoles on the top ring (Figure 3.1): next to **OPEFTopUp** and **OPEFTopDown** we already introduced, that offer local dipoles pointing upward and downward respectively at the interface, and **diSAc-OPE3** from Chapter 2, we prepared **OPE-OMe** and **OPPy** which are both characterized by strong dipoles but different coordinating properties (*i.e.*, the methyl groups in the **OPE-OMe** SAMs are pointing upwards toward the surface and thus do not show appreciable coordinating abilities). Since our synthetic approach easily allowed it, we prepared the methylene-SAc analogues of the previous compounds (**mOPE-OMe** and **mOPPy)** as well.

The data for **diSAc-OPE3** are reproduced in Figure 3.8 together with those for **OPE3** and **mOPE3**: it is evident how the former resulted in an increase in J of about one order of magnitude across the entire bias window. On the other hand other transport characteristics are not affected by the change at the interface: the asymmetry of the curve is indistinguishable from that of **OPE3** (Figure 3.8b), NDC plots are both bowl-shaped (Figure 3.8c), and the V_t values are comparable to that of **OPE3** (0.62(4) and −0.89(9) V for **diSAc-OPE3**; 0.58(8) and −0.84(14) V for **OPE3**) as one would expect from the fact that HOMO and LUMO for these two molecules are similar. These considerations indicate that the transport mechanism and the coupling to the bottom electrode are comparable

and the more polar surface only affects the magnitude of the current (*i.e.*, it increase the injection current, J_0). The most viable hypothesis is that, in the case of **diSAc-**molecules, the favourable interactions with the EGaIn electrode (*i.e.*, the higher surface free energy compared to **OPE3**) increase the number or molecules contacted and thus the effective area of the junction rather than the conductance of the single molecules.[35]

The interface chemistry for SAMs of the **OPE-OMe** compounds is strikingly different from that of the case just discussed: the methyl groups of the methoxy units are pushed outwards toward the interface as a result of steric constraints, thus showing to the EGaIn electrode an environment that more closely resembles that of saturated molecules. This can lower the overall transport by adding a portion of molecule characterized by a higher β value and affecting the interaction between SAM and EGaIn.[37] (Addition of an extra carbon at the top interface, where Van der Waals interactions dominate, can affect the transport more that the addiction of the carbon at the bottom interface, as larger spacers are needed between the binding group and the conjugated part to effectively decouple it from the elctrode.[26]) As we can see in Figure 3.11a, we indeed found J for these systems to be smaller than that for **OPE3**, while the other transport characteristics (as described by $Log\chi$ and NDC, Figure 3.11c and e) are similar to the unsubstituted wires despite the significant difference in molecular dipoles (Table 3.1). As observed previously for **diSAc-OPE3**, the nature of the interfaces dominates J_0 for these compounds as well.

We further investigated the role of dipoles at the interface by characterizing molecular junctions comprising SAMs of structural analogues of **OPE3**, but bearing a pyridine ring at the SAM-EGaIn interface, **OPPy** and **mOPPy.** As in the case of **diSAc-OPE3**, these compounds display a highly polar group to the EGaIn interface that can also act as a ligand for the Ga(III) in the oxide skin. The coordinating power of pyridine toward Ga(III) is higher than that of an alkylsulfide: in Hard and Soft Acids and Bases formalism, RS^- is considered soft and pyridine intermediate, while Ga(III) is hard; on top of that, pyridine is a neutral ligand, which could only be able to coordinate vacant sites in the gallium oxide structure.

The $J-V$ curves obtained for pyridine-containing SAMs are notably different from those of the other compounds presented in this study (Figure 3.13a): while the values

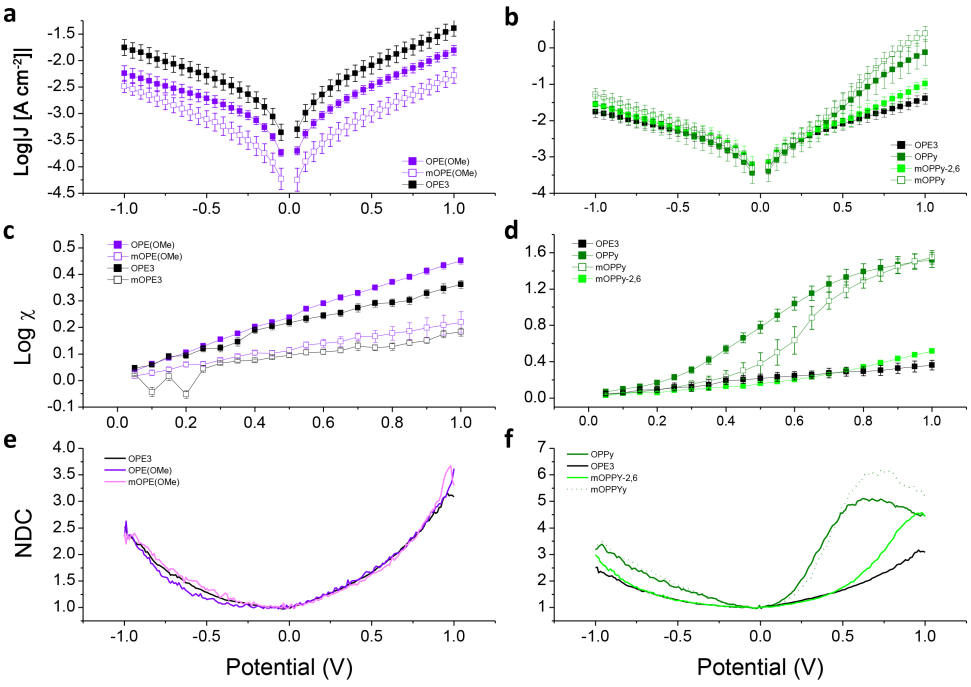

Figure 3.11 a, b: plots of $Log|J|$ vs. V for Au^{TS}/SAM//Ga_2O_3/EGaIn junctions comprising **OPE-OMe** and **OPPy**(see legends). c, d: plot of $Log\chi$ vs. V for junctions comprising the same compounds. e, f: NDC plot for junctions comprising the same compounds. Error bars in a, b, c, and d represent confidence intervals with $\alpha = 0.05$.

of J at negative bias are similar to those of **OPE3**, both **OPPy** and **mOPPy** show current densities that are 1.5 order of magnitude higher at positive bias (Figure 3.11b and d). In the present case, $Log\chi$ does not scale linearly with bias but shows an almost sigmoidal trend, with a onset around 0.2 V and 0.4 V for **OPPy** and **mOPPy** respectively. The peculiar behavior of these systems is also highlighted in the NDC plots (Figure 3.11f), which are characterized by a shoulder at positive bias with a maximum around 0.55 V. To collect evidence that these observations are related to SAM-EGaIn interface and not to the nitrogen-containing nature of these molecules, we also measured in similar conditions SAMs of **mOPPy-2,6**, a compound in which the nitrogen is located close to the gold electrode, on the opposite side of the molecule: in this case, we found charge transport properties similar to those of **OPE3** (Figure 3.11b, d, and f) despite a slightly more

pronounced asymmetry.

The unusual behavior of **OPPy** and **mOPPy** could be a result the peculiar interaction between the SAM and the EGaIn electrode. A 'shoulder' feature in NDC plot can be ascribed to the presence of accessible states in the junction that are approached by the electrode under a certain bias.[25, 26] One can expect the pyridine moiety to act as a neutral ligand that can coordinate Ga(III) centers in the oxide skin in close contact with the SAM: being neutral, it cannot displace the oxide anions in solid Ga_2O_3, rather it fills vacancies in the surface. These sites will be further stabilized by the new interaction thus generating new states that can have an energy accessible in the explored bias window. When the newly-formed states are not taking part in the transport (*i.e.*, at negative bias) then the electric characteristics are close to that of **OPE3** as a result of the similar surface energy. A similar mechanism is precluded to the sulfides (which are charged) and to non-coordinating groups. This hypothesis implies that the peculiar $J-V$ line-shape of Au/(**m**)**OPPy**//EGaIn junctions is unique this system and by changing the top electrode the asymmetry will disappear. To test this, we measured **OPPy** in Au/SAM//Au^{AFM} junctions (where Au^{AFM} denotes a Au-coated conductive probe AFM tip): the results are presented in Figure 3.12, showing a clear absence of pronounced asymmetry.

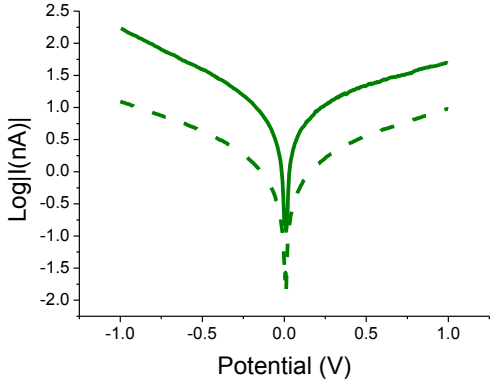

Figure 3.12 Electrical characterization of Au^{TS}/SAM//Au^{AFM} tunneling junctions comprising **OPPy** (solid line) and **mOPPy** (dashed line). Error bars are omitted for clarity.

Finally, to highlight the role of the interfacial dipoles in determining the charge transport characteristics of molecular junctions comprising **OPEs**, in Figure 3.13a we sum-

marize the different $J-V$ curves reported for the different compounds presented in this section: when comparing these results, it is obvious how the nature of the dipole (rather than its absolute magnitude) can affect the charge transport. To stress this point further, we measured the electric properties of a SAM of a compound bearing two thioacetate and four fluorine atoms pointing outwards, **diSAc-OPEFOut**: this molecule has no net dipole, a lower HOMO and LUMO compared to the bi-fluorinated compunds, and its SAMs are characterized by bottom interface similar to that of **OPEFTailDown** and a top one similar to **diSAc-OPE3**. As we can observe in Figure 3.13b and c, the electric characteristics of junctions comprising the latter compound are not different from that of **diSAc-OPE3** (with the exception of a smaller V_t- and a larger V_t+), without the peculiar transport features that we reported for **OPEFTailDown**

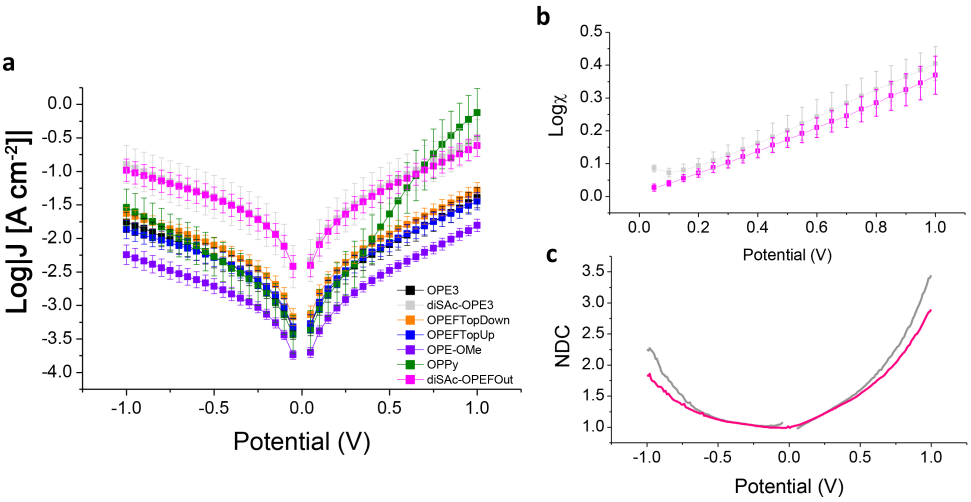

Figure 3.13 a: plots of $Log|J|$ vs. V for Au^{TS}/SAM//Ga_2O_3/EGaIn junctions comprising the investigated compounds characterized by a dipole at the SAM/EGaIn interface (see legend) and **OPE3** (black). b: plot of $Log\chi$ vs. V for junctions comprising **diSAc-OPE3** and **diSAc-OPEFOut**. c: NDC plot for the latter junctions. Error bars represent confidence intervals with $\alpha = 0.05$.

3.4. CONCLUSIONS

In this Chapter we investigated the charge transport properties of Au^{TS}/SAM//EGaIn molecular junctions comprising SAMs of conjugated molecules characterized by a strong

dipole moment. In particular we wanted to study how the current density and other characteristics of the $J-V$ curves (*e.g.*, V_t and NDC plots) would change upon changing the strength and direction of the dipole, the angle of the dipoles with respect with the surface normal, the degree of interaction with the bottom electrode, and the nature of the dipole at the interface with the EGaIn electrode.

We started the discussion with a series of **OPE3** analogues bearing two fluorine atoms in the 1 and 3 positions on the different phenyl rings of the molecule and with different orientations. In most cases, the direction and the magnitude of the dipole did not significantly affect the transport characteristics: this could be a consequence of the worse packing of fluorinated molecules compared to non-fluorinated analogues or of the large tilt angle that characterize **OPE** molecules in the SAM, both of which could hinder the effective alignment of the dipoles on the surface. This is suggested by the lack of correlation between the dipoles and the work function of the SAMs; further characterization of the SAMs is necessary to elucidate its nature. Only the compound in which the fluorine atoms were found close to the metal surface show different transport properties: a more symmetrical $J-V$ curve compared to the other compounds suggest a weaker coupling with the bottom electrode, but without a strong model to explain this phenomenon, one cannot draw any conclusion on the mechanism.

By adding a methylene unit between the conjugated part and the binding thioacetate group, it is possible to limit the molecular inclination and weak the coupling between the conjugated part of the molecule and the electrode. Indeed, in this molecular series, we observed more symmetrical $J-V$ curves, hinting to the weaker coupling with the gold. We also found a correlation between J and the distance between the dipole and the SAM-EGaIn interface and a variation of ϕ matching the direction of the dipole similar to what observed by Kovalchuk *et al.*:[17] this suggest that, compared to the previous series, the added methylene unit can highlight the role of collective effects that are ineffective if the dipole alignment is not ideal. Contrary to the presented study, where bipyridyl oligo-phenylenes were investigated, we found no relation between ψ and V_t or other observables. The relations between dipoles, collective effects, and transport properties in tunnelling junctions are not always clear, and some findings might be system specific

rather than general design rules for molecular electronics:

We finally investigated the effect of different polar groups (–S, –OMe, phenyl, difluorophenyl, pyridyl) at the SAM/EGaIn interface and found that the nature of the group rather than the strength of the dipole has a drastic effect on J: the current density increases on going from methyl-, to (difluoro-)phenyl-, to sulfide- terminated SAMs. Also in this case as the previous, the addition of a methylene unit reduced the asymmetry of the curve, thus suggesting that the effect on J has to do with the injection current at the SAM-EGaIn interface rather than the transport characteristics. This observation is important as it proves that one can modulate the magnitude of the current without altering the transport mechanism: in the next chapters, we will make use of this finding to measure and reliably characterize systems that show intrinsic low conductances. In the case of junctions comprising pyridyl-terminated SAMs, we observed an asymmetry in the $J-V$ curves of about two orders of magnitude at 1 V: we ascribed this difference to a peculiar interaction between the terminal pyridyl ring and the gallium centers in the oxide layer which result in the creation of new states in the junction, accessible in the bias window. While we have only limited evidence to support this claim, we encourage further study of the phenomenon.

3.5. EXPERIMENTAL SECTION

MATERIALS AND METHODS

All reagents were purchased from Sigma-Aldrich, Acros, or TCI Europe and used as received unless otheriwse stated. Triethylamine and $CHCl_3$ were distilled over CaH and P_2O_5 respectively, and used within 10 days. Acetonitrile, toluene, dichloromethane (DCM), and tetrahydrofuran (THF), dimethylformamide (DMF) were obtained anhydrous from a house system. For non-anhydrous reactions, THF was stirred for 1 hour with basic alumina to remove BHT. NMR spectra were recorded on a Varian AMX400 (400MHz) and referenced to the solvent peak ($CDCl_3$: H, 7.26 ppm; C, 77 ppm) relative to tetramethylsilane. We introduced **OPE3** and **diSAc-OPE3** in chapter 2. We described the preparation of S-(4-iodophenyl)ethanethioate (**IPhSAc** in Chapter 2. The synthesis of **OPE3** is described somehwere else.[38] Template stripped metal substrates were prepared by depositing a 100 nm-thick layer of Au on a Si wafer. 1x1x0.3 cm glass slides were glued to the deposited metal using an UV-curable optical adhesive (Norland series 60). The samples were cleaved from the wafer with the help of a razor and immediately used. SAMs of the compounds in this Chapter were prepared in dry toluene solutions by *in situ* deprotection using DBU according to the procedure already reported in Chapter 2.

EGAIN J-V MEASUREMENT AND DATA PROCESS

The details of the EGaIn setup are described elsewhere.[34] For each compound 3-4 substrates were prepared and at least 12 Au^{TS}/SAM//Ga_2O_3/EGaIn junctions per sample were measured (5scans from $0\,V \rightarrow 1\,V \rightarrow -1\,V \rightarrow 0\,V$, steps of 0.05 V) for a total of at least 180 traces per SAM. A new EGaIn tip was prepared every 6 junctions and flattened by gently pushing it on a Si wafer few times according to the procedure reported by Simeone *et. al.*[35]. In Table 3.2 are reported the number of traces collected for the different compounds and the yield of working junctions obtained by the number of junctions that did not fail during the bias scanning or when initially tested with a potential of 0.5 V divided by the total number of junctions formed. The number of working junctions can be obtained dividing by 10 the number of traces. The data were acquired as described and then parsed in a "hands-off" manner using Scientific Python to produce histograms of J for each value of V and the associated Gaussian fits (using a least-squares fitting routine). The data for **OPE3** and **diSAc-OPE3** were already presented in Chapter 2 and their values adjusted for the new series resistance of the setup.

Table 3.2 Number of working junctions and total yield for the compounds mentioned in this chapter.

	n. of junctions	Yield (%)
mOPE3	29	52
OPEFTailDown	36	90
OPEFTailUp	46	92
OPEFMidDown	48	89
OPEFMidUp	48	83
OPEFTopDown	48	73
OPEFTopUp	44	96
mOPEFMidDown	56	65
mOPEFMidUp	29	69
mOPEFTopDown	36	72
mOPEFTopUp	31	31
OPE-OMe	29	83
mOPE-OMe	41	96
OPPy	35	88
mOPPy	36	88
mOPPy-2,6	35	92
diSAc-OPEFOut	36	82

ELECTRICAL CHARACTERIZATION OF SMALL AREA CP-AFM JUNCTIONS

CP-AFM $I-V$ measurements were performed on a Bruker AFM Multimode MMAFM-2 equipped with a PeakForce TUNA Application Module (Bruker). The SAMs were contacted with a Au-coated silicon nitride tip with a nominal radius of 130 nm (NPG-10, Bruker; tip A, resonant frequency = 65 kHz, spring constant = 0.35 N/m; tip B, resonant frequency = 23 kHz, spring constant = 0.12 N/m; tip C, resonant frequency = 56 kHz, spring constant 0.24 N/m; tip D, resonant frequency = 18 kHz, spring constant 0.06 N/m; tip A was chosen in this work) in TUNA mode. The AFM tip was grounded and all samples were prepared on Au^{TS} and biased from -1.5 V to +1.5 V and from +1.5 V to -1.5 V or from -1.0 V to +1.0 V to record the I-V curves: a max of 10 trace/retrace cycles per junction were captured and each trace contains 512 data points. The top electrode was removed from SAMs and reapplied between junctions.

DFT CALCULATIONS

As a final support for the validity of our experimental observations and their interpretation, we also performed quantum-mechanical calculations using the Density Functional Theory (DFT) software packages. We performed the calculations using the GAUSSIAN 09 software packages[39].

We drew all the molecules in the gaussview program and optimized them with terminal thiol groups using the $B3LYP/G$ method incorporating the $6-31+g(d,p)$ basis sets in the gaussian package. The optimized gas-phase geometry was then directly used to compute the single-point gas-phase energies in GAUSSIAN 09 employing the $B3LYP/G$ method with the double-zeta quality $LANL2DZ$ basis sets. We used these calculations to extract the energy values of the frontier π-levels, *i.e.*, the HOMO and LUMO, and also the dipole moment values (total and the x, y and z components), which are tabulated in Table 3.1.

SYNTHESIS

S-(4-((2,6-difluoro-4-(phenylethynyl)phenyl)ethynyl)phenyl) ethanethioate, 1

In an oven dry flask under N_2, 2 g of 5-bromo-1,3-difluoro-2-iodobenzene (6.3 mmol) were dissolved in 25 mL of THF and the solution degassed with N_2 for 30 min. 0.9 mL of (trimethylsilyl)acetylene (0.62 g, 6.3 mmol), 146 mg of $Pd(PPh_3)_4$ (0.13 mmol), 40 mg of CuI (0.19 mmol), and 5 mL of NEt_3. The solution was left under stirring over 48 hours at ambient temperature. The solvent was removed under vacuum and the product purified via column chromatography (hexane) to yield a colorless oil (1.56 g, 86% yield). ^{1}H NMR ($CDCl_3$, 400MHz): 7.06-7.00 (m, 2H), 0.25 (s, 9H).

2-ethynyl-1,3-difluoro-5-(phenylethynyl)benzene, 2

In an oven dry flask under N_2, 600 mg of **1** (2.1 mmol) were dissolved in 25 mL of THF and the solution degassed with N_2 for 30 min. 240 mg of phenylacetylene (2.3 mmol), 49 mg of $Pd(PPh_3)_4$ (0.04 mmol), 12 mg of CuI (0.06 mmol), and 2 mL of NEt_3. The solution was heated to 80 °C and left under stirring overnight. The solvent was removed under vacuum and the TMS-protecred compound purified via column chromatography (hexane, $R_f = 0.5$) to obtain a colorless oil (1.56 g, 86% yield). The oil was dissolved in degassed EtOH and 0.4 g of K_2CO_3 (2.7 mmol) were added. the reaction was left overnight. 1 M HCl was added until a precipitate formed. The mixture was extracted with DCM and the organic phase dried over Na_2SO_4. The solvent was removed under vacuum to yield a pale yellow oil which crystallized upon standing (290 mg, 79% yield over 2 steps). ^{1}H NMR ($CDCl_3$, 400MHz): 7.53 (dd, $J = 6.6, 2.9$ Hz, 2H), 7.40 – 7.35 (m, 3H), 7.10 – 7.04 (m, 2H), 3.58 (s, 1H).

S-(4-((2,6-difluoro-4-(phenylethynyl)phenyl)ethynyl)phenyl) ethanethioate, OPEFMidDown

In an oven dry flask under N_2, 290 mg of **2** (1.21 mmol) and 370 mg of **IPhSAc** (1.33 mmol) were dissolved in 25 mL of THF and the solution degassed with N_2 for 30 min. 28 mg of $Pd(PPh_3)_4$ (0.02 mmol), 7 mg of CuI (0.04 mmol), and 1 mL of NEt_3. The solution was heated to 80 °C and left under stirring overnight. The solvent was removed under vacuum and the residue preadsorbed on silica. The compound was purified via column chromatography (hexane/ethyl acetate 9:1, R_f = 0.5) followed by recrystallization from hexane. The product was obtained as a pale yellow solid (186 mg, 40% yield). ^{1}H NMR ($CDCl_3$, 400MHz): 7.61 (d, J = 8.3Hz, 2H), 7.53 (dd,J = 6.5,3.1Hz, 2H), 7.42 (d, J = 8.2Hz, 2H), 7.40-7.35 (m, 3H), 7.07-7.13 (m, 2H), 2.44 (s, 3H). ^{13}C NMR ($CDCl_3$, 101 MHz): 195.78, 165.13 (dd, J = 254.1, 6.5 Hz), 136.86, 134.97, 134.44, 131.78, 131.15, 127.83 (d, J = 11.9 Hz), 126.20, 124.77, 117.25 – 116.82 (m), 102.34, 95.91, 89.79, 80.46, 32.96. ^{19}F NMR ($CDCl_3$, 376 MHz): 107.49 (d, J = 7.5 Hz).

S-4-((2,6-difluoro-4-(phenylethynyl)phenyl)ethynyl)benzyl ethanethioate, mOPEFMidDown

In an oven dry flask under N_2, 170 mg of **2** (0.71 mmol) and 230 mg of **IBzSAc** (0.78 mmol) were dissolved in 25 mL of THF and the solution degassed with N_2 for 30 min. 16 mg of $Pd(PPh_3)_4$ (0.01 mmol), 4 mg of CuI (0.02 mmol), and 0.5 mL of NEt_3. The solution was heated to 80 °C and left under stirring overnight. The solvent wa sremoved under vacuum and the residue preadsorbed on silica. The compound was purified via column chromatography (hexane/ethyl acetate 10:1, R_f = 0.4) followed by recrystallization from hexane. The product was obtained as a pale yellow solid (148 mg, 52% yield). ^{1}H NMR ($CDCl_3$, 400MHz): 7.55 – 7.51 (m, 2H), 7.41 (d, J = 8.4 Hz, 2H), 7.35 - 7.39 (m, 3H), 7.16 (d, J = 8.3 Hz, 2H), 7.06 - 7.12 (m, 2H), 4.05 (s, 2H), 2.35 (s, 3H). ^{19}F NMR ($CDCl_3$, 376 MHz): 107.73 (d, J = 7.2 Hz).

((2,6-difluoro-4-((triisopropylsilyl)ethynyl)phenyl)ethynyl)trimethylsilane, 3

In an oven dry flask under N_2, 902 mg of **1** (3.11 mmol), 1.6 mL of (triisopropylsylil)acetylene (1.3 g, 7.16 mmol), 180 mg of $Pd(PPh_3)_4$ (0.16 mmol), 59 mg of CuI (0.31 mmol), and 15 mL of NEt_3 were dissolved in 40 mL of THF. The solution was heated to 30 °C and left under stirring overnight. The solution was then extracted with NH_4Cl aq. sat. and the organic phase dried over Na_2SO_4. The product was purified via column chromatography (hexane, R_f = 0.9) to obtain a colorless oil

(878 mg, 73% yield). ^{1}H NMR ($CDCl_3$, 400MHz): 7.03 – 6.93 (m, 2H), 1.13 (s, 20H), 1.17 – 1.05 (m, 8H), 0.29 (s, 9H).

((3,5-difluoro-4-(phenylethynyl)phenyl)ethynyl)triisopropylsilane, 4

In a flask, 878 mg of **3** (2.43 mmol), were dissolved in 125 mL of degassed MeOH and 672 mg of K_2CO_3 (4.86 mmol) were added. The reaction was left overnight and 1 M HCl was added until a precipitate formed. The mixture was extracted with $CHCl_3$ and the organic phase dried over Na_2SO_4. The solvent was removed under vacuum to yield a pale yellow oil 652 mg). In an oven dry flask under N_2, 490 mg of the latter oil (1.54 mmol), 0.35 mL of iodobenzene (638 mg, 3.13 mmol), 116 mg of $Pd(PPh_3)_4$ (0.10 mmol), 36 mg of CuI (0.19 mmol), and 5 mL of NEt_3 were dissolved in 50 mL of THF. The solution was left at 40 °C for 2 days. The solution was then extracted with NH_4Cl aq. sat. and the organic phase dried over Na_2SO_4. The solvent was removed and the product was purified by filtration over a short silica plug (hexane) to obtain an opalescent colorless oil (510 mg, 58% yield over 2 steps). ^{1}H NMR ($CDCl_3$, 400MHz): 7.60 (dd, J = 6.7, 3.0 Hz, 2H), 7.43 – 7.32 (m, 3H), 7.05 (d, J = 7.1 Hz, 2H), 1.15 (d, J = 2.8 Hz, 21H). ^{13}C NMR ($CDCl_3$, 101 MHz): 165.04 (dd, J = 253.6, 6.5 Hz), 134.47, 131.71, 131.04, 127.42 (t, J = 11.6 Hz), 125.06, 117.79 – 117.04 (m), 107.04, 105.70 (t, J = 19.9 Hz), 103.26, 98.16, 78.77, 21.26, 13.90. ^{19}F NMR ($CDCl_3$, 376 MHz): -107.91.

5-ethynyl-1,3-difluoro-2-(phenylethynyl)benzene, 4.1

In a flask, 510 mg of **4** (1.29 mmol) were dissolved in 150 mL of degassed THF and the solution put in an ice bath. 2.58 mL of a 1 M tetrabutylammonium fluoride solution in THF containign 5% vv. H_2O (2.58 mmol) were added dropwise and the reaction allowed to rt overnight. The solutes were preadsorbed on silica and the product purified by filtration over a short silica plug (hexane) to obtain white needle crystals (274 mg, 89% yield). ^{1}H NMR ($CDCl_3$, 400MHz): 7.60 (dd, J = 6.6, 2.9 Hz, 2H), 7.38 (dd, J = 5.3, 1.9 Hz, 3H), 7.06 (d, J = 7.0 Hz, 2H), 3.25 (s, 1H). ^{13}C NMR ($CDCl_3$, 101 MHz): 165.04 (dd, J = 253.8, 6.4 Hz), 134.51, 131.82, 131.07, 126.04 (t, J = 11.7 Hz), 118.23 – 117.06 (m), 106.38 (t, J = 19.9 Hz), 103.54 (t, J = 3.3 Hz), 83.90 (t, J = 3.8 Hz), 83.47, 78.52, 20.81, 16.09. ^{19}F NMR ($CDCl_3$, 376 MHz): -107.29 (d, 6.5 Hz).

S-(4-((3,5-difluoro-4-(phenylethynyl)phenyl)ethynyl)phenyl) ethanethioate, OPEFMidUp

In an oven dry seleable Schlenk under N_2, 133 mg of **4.1** (0.56 mmol), 228 mg of **IPhSAc** (0.82 mmol), 32 mg of $Pd(PPh_3)_4$ (0.03 mmol), 10 mg of CuI (0.06 mmol), and 1 mL of NEt_3 were dissolved in 15 mL of THF. The solution was heated to 55 °C and left under stirring overnight. The solvent

was removed under vacuum and the residue preadsorbed on silica. The compound was purified via column chromatography (hexane/ethyl acetate 9:1, R_f = 0.4) followed by recrystallization from hexane. The product was obtained as a off-white solid (97 mg, 55% yield). ^{1}H NMR ($CDCl_3$, 400MHz): 7.59 (dd, J = 6.7, 3.0 Hz, 2H), 7.55 (d, J = 8.2 Hz, 2H), 7.42 (d, J = 8.1 Hz, 2H), 7.38 (dd, J = 5.3, 1.7 Hz, 3H), 7.10 (d, J = 7.1 Hz, 2H), 2.45 (s, 3H). ^{19}F NMR ($CDCl_3$, 376 MHz): -107.52 (d, J = 7.1 Hz).

S-4-((3,5-difluoro-4-(phenylethynyl)phenyl)ethynyl)benzyl ethanethioate, mOPEFMidUp

In an oven dry seleable Schlenk under N_2, 250 mg of **4.1** (1.05 mmol), 368 mg of **IBzSAc** (1.26 mmol), 60 mg of $Pd(PPh_3)_4$ (0.05 mmol), 20 mg of CuI (0.11 mmol), and 1 mL of NEt_3 were dissolved in 15 mL of THF. The solution was heated to 40 °C and left under stirring overnight. The reaction was filtered, the solvent was removed under vacuum, and the residue preadsorbed on silica. The compound was purified via column chromatography (hexane/ethyl acetate 9:1) followed by recrystallization from hexane. The product was obtained as a off-white solid (177 mg, 42% yield). ^{1}H NMR ($CDCl_3$, 400MHz): 7.53 (dd, *J* = 5.9, 2.2 Hz, 2H), 7.51 (d, *J* = 8.1 Hz, 2H), 7.40 – 7.35 (m, 3H), 7.29 (d, *J* = 8.2 Hz, 2H), 7.12 – 7.06 (m, 2H), 4.13 (s, 2H), 2.36 (s, 3H). ^{13}C NMR ($CDCl_3$, 101 MHz): 197.43, 166.36 (d, J = 6.7 Hz), 163.84 (d, J = 6.7 Hz), 141.60, 134.65, 134.48, 131.73, 131.65, 131.06, 127.29 (t, J = 11.8 Hz), 125.05, 123.75, 117.73 – 116.39 (m), 105.52 (t, J = 19.9 Hz), 103.32, 95.39, 90.10, 78.83, 35.89, 32.97. ^{19}F NMR ($CDCl_3$, 376 MHz): -107.73 (d, J = 7.1 Hz).

((4-bromophenyl)ethynyl)trimethylsilane, 5, and 1,4-bis((trimethylsilyl)ethynyl)benzene, TMS-21

In a oven dry flask, 5 g of 4-bromo-iodobenzene (17.7 mmol), 32 mL of (trimethylsilyl)acetylene (22.4 g, 19.5 mmol), 150 mg of $Pd(PPh_3)_4$ (0.13 mmol), 50 mg of CuI (0.26 mmol), and 10 mL of NEt_3 were dissolved in 30 mL of THF. The reaction was left at rt over the weekend. It was then filtered in stirring hexane and water and 6 M HCl was added until net acidity. The organic phase was washed with water, dried over Na_2SO_4, and the solvent removed under vacuum. The residue was purified via column chromatography (hexane) to obtain pure **5** (2.61 g, 58% yield) and **TMS-21** (284 mg, 6% yield) as white solids. **5**: ^{1}H NMR ($CDCl_3$, 400MHz): 7.47 – 7.37 (m, 2H), 7.38 – 7.27 (m, 2H), 0.24 (s, 9H). ^{13}C NMR ($CDCl_3$, 101 MHz): 133.35, 131.44, 122.71, 122.07, 103.83, 95.56, -0.14. **TMS-21**: ^{1}H NMR ($CDCl_3$, 400MHz): 7.39 (s, 4H), 0.24 (s, 18H).

2-ethynyl-1,3-difluorobenzene, 6

In an oven dry seleable Schlenk under N_2, 2 g of 2,6-difluoro-iodobenzene (8.33 mmol), 1.73 mL of (trimethylsilyl)acetylene (1.21 g, 12.5 mmol), 150 mg of $Pd(PPh_3)_4$ (0.13 mmol), 50 mg of CuI (0.26 mmol), and 10 mL of NEt_3 were dissolved in 10 mL of THF. The reaction was left at 60 °C overnight. It was then filtered in stirring hexane and water and 6 M HCl was added until net acidity. The organic phase was washed with water, dried over Na_2SO_4, and the solvent removed under vacuum. The residue was purified by filtration over a short silica plug (hexane) to obtain the TMS-protected **6** as an opalescent oil (1.50 g, 86% yield). 1.1 g of the latter (5.26 mmol), were dissolved in 70 mL of degassed MeOH and 1.09 g of K_2CO_3 (7.89 mmol) were added. The reaction was left overnight and in a stirring mixture of DCM and water. The organic phase was washed with water, dried over Na_2SO_4, and the solvent removed under vacuum to yield a colourless volatile liquid (650 mg, 77% yield over 2 steps). ^{1}H NMR ($CDCl_3$, 400MHz): 7.37 – 7.21 (m, 1H), 6.98 – 6.85 (m, 2H), 3.51 (s, 1H). ^{19}F NMR ($CDCl_3$, 376 MHz): -107.65 (d, 6.7 Hz).

((4-((2,6-difluorophenyl)ethynyl)phenyl)ethynyl)trimethylsilane, 7

In an oven dry seleable Schlenk under N_2, 650 mg of **6** (4.71 mmol), 954 mg of **5** (3.77 mmol), 210 mg of $Pd(PPh_3)_4$ (0.18 mmol), 70 mg of CuI (0.37 mmol), and 10 mL of NEt_3 were dissolved in 5 mL of THF. The reaction was left at 60 °C over the weekend. The solvent was removed under vacuum and the residue dissolved in hexane and filtered. The product was purified via column chromatography (hexane/ethyl acetate 10:1) to obtain a pale green oil (640 mg, 56% yield). ^{1}H NMR ($CDCl_3$, 400MHz): 7.53 – 7.49 (m, 2H), 7.48 – 7.44 (m, 2H), 7.34 – 7.18 (m, 1H), 7.02 – 6.86 (m, 2H), 0.26 (s, 9H). ^{19}F NMR ($CDCl_3$, 376 MHz): -107.33 (t, J = 6.5 Hz).

2-((4-ethynylphenyl)ethynyl)-1,3-difluorobenzene, 7.1

In a flask, 640 mg of **7** (2.1 mmol) were dissolved in 100 mL of degassed THF and the solution put in an ice bath. 2.3 mL of a 1 M tetrabutylammonium fluoride solution in THF (2.3 mmol) and 0.1 mL of H_2O were added dropwise and the reaction allowed to rt overnight. The solutes were preadsorbed on silica and the product purified by filtration over a short silica plug (hexane) to a white needle solid (500 mg, 99% yield). ^{1}H NMR ($CDCl_3$, 400MHz): 7.66 – 7.43 (m, 5H), 7.00 – 6.81 (m, 2H), 3.19 (s, 1H). ^{19}F NMR ($CDCl_3$, 376 MHz): -107.27 (d, 6.5 Hz).

S-(4-((4-((2,6-difluorophenyl)ethynyl)phenyl)ethynyl)phenyl) ethanethioate, OPEFTopDown

In an oven dry seleable Schlenk under N_2, 270 mg of **7.1** (1.1 mmol), 347 mg of **IPhSAc** (1.2 mmol), 60 mg of $Pd(PPh_3)_4$ (0.05 mmol), 20 mg of CuI (0.11 mmol), and 1 mL of NEt_3 were dissolved in

15 mL of THF. The solution was heated to 60 °C and left under stirring overnight. The reaction was filtered, the solvent was removed under vacuum, and the residue preadsorbed on silica. The compound was purified via column chromatography (hexane/ethyl acetate 3:1, R_f = 0.6) followed by recrystallization from DCM/hexane. The product was obtained as a off-white solid (202 mg, 52% yield). ^{1}H NMR ($CDCl_3$, 400MHz): 7.60 – 7.49 (m, 6H), 7.43 – 7.39 (m, 3H), 6.95 (dd, J = 8.4, 7.0 Hz, 2H), 2.44 (s, 3H). ^{13}C NMR ($CDCl_3$, 101 MHz): 196.00 , 165.59 (dd, J = 254.1, 5.4 Hz), 136.87, 135.07, 134.83, 134.37, 134.26, 134.02, 133.50, 132.53 (t, J = 10.1 Hz), 131.02, 126.84, 126.05, 125.26, 114.73 – 112.83 (m), 93.36, 93.26, 32.94. ^{19}F NMR ($CDCl_3$, 376 MHz): -107.31 (d, J = 6.6 Hz).

S-4-((4-((2,6-difluorophenyl)ethynyl)phenyl)ethynyl)benzyl ethanethioate, mOPEFTopDown

In an oven dry seleable Schlenk under N_2, 230 mg of **7.1** (1 mmol), 310 mg of **IBzSAc** (1.1 mmol), 60 mg of $Pd(PPh_3)_4$ (0.05 mmol), 20 mg of CuI (0.11 mmol), and 1 mL of NEt_3 were dissolved in 15 mL of THF. The solution was heated to 60 °C and left under stirring overnight. The reaction was filtered, the solvent was removed under vacuum, and the residue preadsorbed on silica. The compound was purified via column chromatography (hexane/ethyl acetate 4:1, R_f = 0.5) followed by recrystallization from DCM/hexane. The product was obtained as a off-white solid (93 mg, 23% yield). ^{1}H NMR ($CDCl_3$, 400MHz): 7.60 – 7.49 (m, 6H), 7.43 – 7.39 (m, 3H), 6.95 (dd, J = 8.4, 7.0 Hz, 2H), 2.44 (s, 3H). ^{13}C NMR ($CDCl_3$, 101 MHz): 197.57, 165.58 (dd, J = 254.0, 5.3 Hz), 140.90, 134.52, 134.36, 134.19, 132.53 (t, J = 10.0 Hz), 131.57, 126.39, 124.95, 124.56, 114.21 – 113.48 (m), 101.41, 93.93, 91.93, 80.67, 35.92, 33.00. ^{13}C NMR ($CDCl_3$, 101 MHz): 197.52, 165.58 (dd, J = 253.9, 5.3 Hz), 140.88, 134.51, 134.34, 134.17, 132.49 (t, J = 10.0 Hz), 131.55, 126.40, 124.96, 124.56, 114.25 – 113.09 (m), 101.40, 93.91, 91.91, 80.63, 35.92, 32.98. ^{19}F NMR ($CDCl_3$, 376 MHz): -107.28 (d, J = 6.6 Hz).

5-ethynyl-1,3-difluorobenzene, 8

In an oven dry flask under N_2, 5 g of 1-bromo-3,5-difluoro-benzene (26 mmol) were dissolved in 25 mL of THF and the solution degassed with N_2 for 30 min. 4.15 mL of (trimethylsilyl)acetylene (2.94 g, 29 mmol), 300 mg of $Pd(PPh_3)_4$ (0.26 mmol), 100 mg of CuI (0.53 mmol), and 10 mL of NEt_3 were were added and the reaction was left at 80 °C overnight. The solvent was removed under vacuum and the TMS-protecred compound purified via column chromatography (hexane, R_f = 0.7) to obtain a colorless oil (5.4 g, 99% yield). 1.2 g of the latter (5.76 mmol), were dissolved in degassed EtOH and 1.2 g of K_2CO_3 (8.64 mmol) were added. 1 M HCl was added until a precipitate formed. The mixture was extracted with DCM and the organic phase dried over Na_2SO_4. The solvent was

removed under vacuum to yield a white solid (648 mg, 82% yield over 2 steps) ^{1}H NMR ($CDCl_3$, 400MHz): 7.03 – 6.97 (m, 2H), 6.82 (tt, J = 8.9, 2.2 Hz, 1H), 3.14 (s, 1H).

((4-((3,5-difluorophenyl)ethynyl)phenyl)ethynyl)trimethylsilane, 9

In an oven dry flask under N_2, 600 mg of **8** (4.34 mmol) and 1.32 g of **5** (38.5 mmol) were dissolved in 25 mL of THF and the solution degassed with N_2 for 30 min. 100 mg of $Pd(PPh_3)_4$ (0.09 mmol), 25 mg of CuI (0.13 mmol), and 5 mL of NEt_3 were added and the reaction was left at 80 °C overnight. The solvent was removed under vacuum and compound purified via column chromatography (hexane) to obtain a pale yellow oil which solidified upon standing (1.02 g, 76% yield). ^{1}H NMR ($CDCl_3$, 400MHz): 7.46 (s, 4H), 7.07 – 7.00 (m, 2H), 6.81 (tt, J = 9.0, 2.3 Hz, 1H), 0.26 (s, 9H).

1-((4-ethynylphenyl)ethynyl)-3,5-difluorobenzene, 9.1

In a flask, 509 mg of **9** (1.64 mmol) were dissolved in 100 mL of degassed THF. 4.1 mL of a 1 M tetrabutylammonium fluoride solution in THF (4.1 mmol) were added dropwise and the reaction left overnight. H_2O and Et_2O were added to the solution and the organic phase washed with H_2O and brine. The product purified by column chromatography (hexane) to obtain a white solid (297 mg, 76% yield). ^{1}H NMR ($CDCl_3$, 400MHz): 7.48 (s, 4H), 7.07 – 7.00 (m, 2H), 6.82 (tt, J = 8.9, 2.3 Hz, 1H), 3.19 (s, 1H).

S-(4-((4-((3,5-difluorophenyl)ethynyl)phenyl)ethynyl)phenyl) ethanethioate, OPEFTopUp

In an oven dry flask under N_2, 88 mg of **9.1** (0.37 mmol) and 114 mg of **IPhSAc** (0.41 mmol) were dissolved in 25 mL of THF and the solution degassed with N_2 for 30 min. 8.6 mg of $Pd(PPh_3)_4$ (7.4 µmol), 2.1 mg of CuI (11.1 µmol), and 0.1 mL of NEt_3 were added and the reaction was left at 80 °C overnight. The solvent was removed under vacuum and compound purified via column chromatography (hexane/$CHCl_3$ 1:1, R_f = 0.7) followed by recrystallization from hexane to obtain a off-white solid (80 mg, 56% yield). ^{1}H NMR ($CDCl_3$, 400MHz): 7.56 (d, J = 8.3 Hz, 2H), 7.52 (s, 4H), 7.41 (d, J = 8.3 Hz, 2H), 7.08 – 7.01 (m, 2H), 6.82 (tt, J = 8.9, 2.3 Hz, 1H), 2.44 (s, 3H).

S-(4-((4-((3,5-difluorophenyl)ethynyl)phenyl)ethynyl)benzyl) ethanethioate, mOPEFTopUp

In an oven dry flask under N_2, 300 mg of **9.1** (1.26 mmol) and 400 g of **IBzSAc** (1.4 mmol) were dissolved in 25 mL of THF and the solution degassed with N_2 for 30 min. 29 mg of $Pd(PPh_3)_4$ (0.03 mmol), 7 mg of CuI (0.04 µmol), and 0.5 mL of NEt_3 were added and the reaction was left at

80 °C overnight. The precipitate was filtered off and the the residue preadsorbed on silica. The compound was purified via column chromatography (hexane/ethyl acetate 10:1, R_f = 0.6) followed by recrystallization from hexane to obtain a off-white solid (201 mg, 40% yield). ^{1}H NMR ($CDCl_3$, 400MHz): 7.50 (s, 4H), 7.46 (d, J = 8.2 Hz, 2H), 7.28 (d, J = 8.2 Hz, 2H), 7.08 – 7.01 (m, 2H), 6.81 (tt, J = 8.8, 2.3 Hz, 1H), 4.12 (s, 2H), 2.36 (s, 3H).

1-ethynyl-4-(phenylethynyl)benzene, 10

In an oven dry seleable Schlenk under N_2, 980 mg of **5** (3.87 mmol), 0.65 mL of phenylacetylene (0.65 g, 6.37 mmol), 150 mg of $Pd(PPh_3)_4$ (0.96 mmol), 50 mg of CuI (0.26 mmol), and 5 mL of NEt_3 were dissolved in 15 mL of THF. The reaction was left at 50 °C overnight. The reaction was filtered in a stirring mixture of hexane and water. 50 mL of HCl 1 M were added. The organic phase was washed with water until neutrality and dried over Na_2SO_4. The TMS-protected compound was purified via column chromatography (hexane/ethyl acetate 40:1) to obtain flaky white crystals (725 mg, 68% yield). These latter were dissolved in 125 mL of MeOH and 570 mg of K_2CO_3 (4.2 mmol) were added and the solution left overnight under stirring. The content of the flask was then poured in a stirring mixture of water and DCM. 50 mL of 6 M HCl were added and the organic phase extracted with water. It was then dried over Na_2SO_4 and the solid preadsorbed on silica. The desired compound was purified via column chromatography (hexane) to obtained a white solid (407 mg, 52% yield over 2 steps). ^{1}H NMR ($CDCl_3$, 400MHz): 7.57 – 7.53 (m, 2H), 7.49 (s, 4H), 7.37 (dd, J = 5.0, 1.8 Hz, 3H), 3.19 (s, 1H). ^{13}C NMR ($CDCl_3$, 101 MHz): 132.07, 131.64, 131.47, 128.54, 128.40, 123.78, 122.94, 121.87, 91.40, 88.85, 83.30, 78.92.

***tert*-butyl(2,6-difluoro-4-iodophenyl)sulfane, 11**

In a rotavapor flask, 495 mg of 2,6-difluori4-iodio-aniline (1.94 mmol) were dissolved in 8 mL of degassed di-*tert*-butyl-disulfide and the solution placed in a bath a 65 °C. After reaching the desired temperature, 0.36 mL of *tert*-butyl-nitrite 0.31 g, 3 mmol) were added dropwise. As soon as gas evolution stopped, the excess the flask was placed at the rotary evaporator to remove the volatile compounds and finally the di-*tert*-butyl-disulfide was removed under vacuum distillation (1 mtorr, 33 °C). The dark residue was preadsorbed on silica and purified via column chromatography (hexane, R_f = 0.6) to obtain the desired product as a colorless oil (250 mg, 39% yield). ^{1}H NMR ($CDCl_3$, 400MHz): 7.36 – 7.31 (m, 2H), 1.30 (s, 9H). ^{13}C NMR ($CDCl_3$, 101 MHz): 166.81 (dd, J = 252.7, 4.3 Hz), 124.01 (dd, J = 28.9, 2.6 Hz), 112.33 (t, J = 23.2 Hz), 96.46 (t, J = 10.6 Hz), 51.60, 33.64. ^{19}F NMR ($CDCl_3$, 376 MHz): -100.55 (d, J = 5.6 Hz).

***tert*-butyl(2,6-difluoro-4-((4-(phenylethynyl)phenyl)ethynyl)phenyl)sulfane, 12**

In an oven dry seleable Schlenk under N_2, 250 mg of **11** (0.76 mmol), 100 mg of **10** (0.49 mmol), 36 mg of $Pd(PPh_3)_4$ (0.03 mmol), 13 mg of CuI (0.07 mmol), and 5 mL of NEt_3 were dissolved in 10 mL of THF. The reaction was left at 60 °C overnight. The reaction was filtered in a stirring mixture of hexane and water. HCl 1 M was added slowly until acidity was reached. The organic phase was washed with water until neutrality and dried over Na_2SO_4. The final compound was purified via filtration over a short plug of silica using hexane/ethyl acetate 50:1 to obtain a white solid (116 mg, 38% yield). ^{1}H NMR ($CDCl_3$, 400MHz): 7.54 (t, J = 3.7 Hz, 2H), 7.52 (d, J = 3.0 Hz, 4H), 7.39 – 7.30 (m, 3H), 7.16 – 7.09 (m, 2H), 1.35 (s, 9H). ^{13}C NMR ($CDCl_3$, 101 MHz): 132.07, 131.64, 131.47, 128.54, 128.40, 123.78, 122.94, 121.87, 91.40, 88.85, 83.30, 78.92. ^{19}F NMR ($CDCl_3$, 376 MHz): -101.67 (d, J = 6.3 Hz).

S-(2,6-difluoro-4-((4-(phenylethynyl)phenyl)ethynyl)phenyl) ethanethioate, OPEFTailDown

In an oven dry flask under N_2, 116 mg of **12** (0.29 mmol) and 4.1 mL of acetylchloride (4.53 g, 58 mmol) were dissolved in 25 mL of DCM. 0.03 mL of $TiCl_4$ were added. After 1 hour the content of the flask was poured in a stirring mixture of DCM and water and the Na_2CO_3 aq. sat. was added slowly until neutrality. The organic phase was then extracted with water, dried over Na_2SO_4, and preabsorbed on silica. The final compound was purified via column chromatography (hexane/ethyl acetate 100:1 increasing to 40:1) and recrystallized from DCM/hexane to obtain an off-white solid (55 mg, 49% yield). ^{1}H NMR ($CDCl_3$, 400MHz): 7.57 – 7.47 (m, 6H), 7.38 - 7.35 (m, 3H), 7.20 – 7.10 (m, 2H), 2.49 (s, 3H). ^{13}C NMR ($CDCl_3$, 101 MHz): 192.49, 164.80 (dd, J = 251.1, 5.6 Hz), 134.40, 134.30, 134.27, 131.24, 131.05, 126.80, 125.51, 124.35, 117.68 – 117.21 (m), 95.33, 94.45, 91.49, 91.09, 32.67. ^{19}F NMR ($CDCl_3$, 376 MHz): -104.10 (d, J = 7.1 Hz).

***tert*-butyl(3,5-difluoro-4-iodophenyl)sulfane, 13** In a vacuum flask, 501 mg of 3,5-difluori4-iodio-aniline (1.96 mmol) were dissolved in 7 mL of degassed di-*tert*-butyl-disulfide and the solution placed in a bath a 65 °C. After reaching the desired temperature, 0.36 mL of *tert*-butyl-nitrite 0.31 g, 3 mmol) were added dropwise. As soon as gas evolution stopped, the excess the flask was placed at the rotary evaporator to remove the volatile compounds and finally the di-*tert*-butyl-disulfide was removed under vacuum distillation (1 mtorr, 33 °C). The dark residue was preadsorbed on silica and purified via column chromatography (hexane, $R_f = 0.8$) to obtain the desired

product as an orange oil (203 mg, 32% yield). ^{1}H NMR ($CDCl_3$, 400MHz): 7.08 – 7.00 (m, 2H), 1.31 (s, 9H). ^{19}F NMR ($CDCl_3$, 376 MHz): -92.57 (d, J = 6.0 Hz).

***tert*-butyl(3,5-difluoro-4-((4-(phenylethynyl)phenyl)ethynyl)phenyl)sulfane, 14**

In an oven dry seleable Schlenk under N_2, 200 mg of **13** (0.61 mmol), 100 mg of **10** (0.49 mmol), 28 mg of $Pd(PPh_3)_4$ (0.02 mmol), 10 mg of CuI (0.05 mmol), and 5 mL of NEt_3 were dissolved in 10 mL of THF. The reaction was left at 60 °C overnight. The reaction was filtered in a stirring mixture of hexane and water. HCl 1 M was added slowly until acidity was reached. The organic phase was washed with water until neutrality, dried over Na_2SO_4 and preadsorbed on silica. The final compound was purified via column chromatography (hexane/ethyl acetate 100:1) to obtain a white solid (104 mg, 53% yield). ^{1}H NMR ($CDCl_3$, 400MHz): 7.60 – 7.48 (m, 6H), 7.36 (dd, J = 5.1, 1.9 Hz, 3H), 7.17 – 7.06 (m, 2H), 1.34 (s, 9H). ^{19}F NMR ($CDCl_3$, 376 MHz): -107.85 (d, J = 7.1 Hz)

S-(2,6-difluoro-4-((4-(phenylethynyl)phenyl)ethynyl)phenyl) ethanethioate, OPEFTailUp

In an oven dry flask under N_2, 100 mg of **12** (0.25 mmol) and 3.5 mL of acetylchloride (3.86 g, 50 mmol) were dissolved in 25 mL of DCM. 0.03 mL of $TiCl_4$ were added. After 1 hour the content of the flask was poured in a stirring mixture of DCM and water and the Na_2CO_3 aq. sat. was added slowly until neutrality. The organic phase was then extracted with water, dried over Na_2SO_4, and preabsorbed on silica. The final compound was purified via column chromatography (hexane/ethyl acetate 5:1, R_f = 0.6) and recrystallized from DCM/hexane to obtain an off-white solid (25 mg, 26% yield). ^{1}H NMR ($CDCl_3$, 400MHz): 7.62 – 7.47 (m, 6H), 7.41 – 7.31 (m, 3H), 7.11 – 6.99 (m, 2H), 2.45 (s, 3H). ^{19}F NMR ($CDCl_3$, 376 MHz): -104.10 (d, J = 7.1 Hz).

S-4-((4-(phenylethynyl)phenyl)ethynyl)benzyl ethanethioate, mOPE3

In an oven dry flask under N_2, 100 mg of **10** (0.49 mmol) and 158 mg of **IBzSAc** (0.54 mmol) were dissolved in 15 mL of NEt_3 and the solution degassed with N_2 for 30 min. 15 mg of $Pd(PPh_3)_4$ (0.01 mmol) and 3 mg of CuI (0.02 mmol) were added and the reaction was left at 80 °C overnight. The precipitate was filtered off and the the residue preadsorbed on silica and the solvent removed under vacuum. The compound was purified via column chromatography (hexane/$CHCl_3$ 1:1, R_f = 0.7) followed by recrystallization from hexane to obtain a off-white solid (50 mg, 30% yield). ^{1}H NMR ($CDCl_3$, 400MHz): 7.55 – 7.51 (m, 2H), 7.50 (s, 4H), 7.46 (d, J = 8.1 Hz, 2H), 7.35 (dd, J = 5.1, 2.0 Hz, 3H), 7.29 (s, 2H), 4.12 (s, 2H), 2.36 (s, 3H).

4-ethynylpyridine, 15

In an oven dry seleable Schlenk under N_2, 2 g of 4-iodo-pyridine (9.8 mmol), 2 mL of (trimethylsilyl)acetylene (1.42 g, 15 mmol), 150 mg of $Pd(PPh_3)_4$ (0.13 mmol), 50 mg of CuI (0.26 mmol) were dissolved in 10 mL of NEt_3. The reaction was left at 60 °C over the weekend. The solvent was removed under vacuum and the residue extracted with hot hexane. The TMS-protected compound was purified by filtration over a short plug of silica using hexane/ethyl acetate 5:1 and obtained as a brown oil (1.42 g, 83% yield). The latter was dissolved in 70 mL of THF and the solution placed in an ice bath. 9.6 mL of a tetrabutylammonium fluoride solution 1 M in THF (9.6 mM) and 0.48 mL of H_2O were added dropwise and the bath removed. After 25 minutes, the solution was dried with Na_2SO_4 and the product preadsorbed on silica. The final compound was purified via filtration over a short plug of silica using hexane/ethyl acetate 3:1 to obtain white flaky crystals (440 mg, 35% yield over 2 steps) which were immediately used in the next step. ^{1}H NMR ($CDCl_3$, 400MHz): 8.60 – 8.53 (m, 2H), 7.36 – 7.28 (m, 2H), 3.28 (s, 1H).

4-((4-ethynylphenyl)ethynyl)pyridine, 16

In an oven dry seleable Schlenk under N_2, 1 g of 5 (4.1 mmol), 420 mg of **15** (4.1 mmol), 150 mg of $Pd(PPh_3)_4$ (0.13 mmol), 50 mg of CuI (0.26 mmol), and 4.5 mL of NEt_3 were dissolved in 10 mL of THF. The reaction was left at 60 °C overnight. The solvent was removed under vacuum and the residue extracted with hot hexane. The TMS-protected compound was purified via column chromatography (hexane/ethyl acetate 3:1) and obtained as yellow crystals (473 mg, 42% yield). These latter were dissolved in 40 mL of THF and the solution placed in an ice bath. 1.8 mL of a tetrabutylammonium fluoride solution 1 M in THF (1.8 mM) and 0.09 mL of H_2O were added dropwise and the bath removed. After 25 minutes, the solution was dried with Na_2SO_4 and the product preadsorbed on silica. The final compound was purified via filtration over a short plug of silica using hexane/ethyl acetate 2:1 to obtain a white solid (231 mg, 30% yield over 2 steps) which was immediately used in the next step. ^{1}H NMR ($CDCl_3$, 400MHz): 8.63 (s, 2H), 7.50 (s, 4H), 7.42 - 7.41 (m, 2H), 3.21 (s, 1H).

S-(4-((4-(pyridin-4-ylethynyl)phenyl)ethynyl)phenyl) ethanethioate, OPPy

In an oven dry seleable Schlenk under N_2, 190 mg of 16 (0.93 mmol), 286 mg of **IPhSAc** (1.03 mmol), 54 mg of $Pd(PPh_3)_4$ (0.04 mmol), 24 mg of CuI (0.13 mmol), and 1 mL of NEt_3 were dissolved in 10 mL of THF. The reaction was left at 60 °C overnight. The solvent was removed under vacuum and the residue preadsorbed on silica. The product was purified via column chromatograpy (hex-

ane/ethyl acetate 1:1) and recrystallized from hexane to obtain a off-white solid (102 mg, 31% yield). ^{1}H NMR ($CDCl_3$, 400MHz): 8.62 (d, J = 5.5 Hz, 2H), 7.56 (d, J = 8.2 Hz, 2H), 7.54 (s, 4H), 7.43 – 7.33 (m, 4H), 2.44 (s, 3H). ^{13}C NMR ($CDCl_3$, 101 MHz): 195.96, 152.47, 136.89, 134.83, 134.48, 134.36, 133.85, 131.14, 128.16, 126.72, 126.44, 124.72, 96.16, 93.64, 93.07, 91.09, 32.95.

S-4-((4-(pyridin-4-ylethynyl)phenyl)ethynyl)benzyl ethanethioate, mOPPy

In an oven dry seleable Schlenk under N_2, 97 mg of 16 (0.27 mmol), 87 mg of **IBzSAc** (0.30 mmol), 30 mg of $Pd(PPh_3)_4$ (0.03 mmol), 10 mg of CuI (0.05 mmol), and 0.3 mL of NEt_3 were dissolved in 10 mL of THF. The reaction was left at 50 °C overnight. The solvent was removed under vacuum and the residue preadsorbed on silica. The product was purified via column chromatograpy (hexane/ethyl acetate 3:2) and recrystallized from hexane to obtain a off-white solid (81 mg, 81% yield). ^{1}H NMR ($CDCl_3$, 400MHz): 8.65 (s, br, 2H), 7.52 (s, 4H), 7.49 – 7.44 (m, 2H), 7.40 (s, br, 2H), 7.28 (d, J = 8.1 Hz, 2H), 4.11 (s, 2H), 2.35 (s, 3H). 197.51, 141.00, 134.51, 134.44, 134.27, 131.57, 126.77, 124.45, 124.44, 96.17, 94.18, 91.73, 91.01, 35.90, 32.98.

(6-ethynylpyridin-2-yl)methanol, 17

In an oven dry flask equipped with a condenser under N_2, 1.22 g of (6-bromopyridin-2-yl)methanol (6.38 mmol), 1.6 mL of (trimethylsilyl)acetylene (1.15 g, 11.5 mmol), 50 mg of CuI (0.26 mmol), 150 mg of $Pd(PPh_3)_4$ (0.13 mmol), and 7.1 mL of NEt_3 were dissolved in 30 mL of THF. The reaction was kept at reflux overnight. The solvents were removed under vacuum and the TMS-protected compound purified via filtration though a short plug of silica using hexane/ethylacetate 1:1 to obtain a brown oil (1.12 g, 89% yield). 935 mg of the latter (4.55 mmol) were dissolved in 40 mL of THF and the solution placed in an ice bath. 9.1 mL of a tetrabutylammonium fluoride solution 1 M in THF (9.1 mM) were added dropwise and the bath removed. After 20 hours, water was added to the solution which was then extracted with ethylacetate. The organic phase was washed with brine and dried over Na_2SO_4. The final compound was purified via column chromatography (hexane/ethyl acetate 1:1) to obtain a pale yellow solid (542 mg, 90% yield). ^{1}H NMR ($CDCl_3$, 400MHz): 7.66 (t, J = 7.8 Hz, 1H), 7.39 (d, J = 7.6 Hz, 1H), 7.28 (d, J = 7.7 Hz, 1H), 4.75 (s, 2H), 3.28 (s, br, 1H), 3.17 (s, 1H).

S-((6-ethynylpyridin-2-yl)methyl) ethanethioate, 18

In a oven dry flask under N_2, 300 mg of **17** (2.26 mmol) and 0.5 mL of NEt_3 (343 mg, 3.4 mmol) were dissolved in 22 mL of DCM and the solution cooled in an ice bath. 0.21 mL of methanesulfonyl chloride (311 mg, 2.71 mmol) were added dropwise and the reaction left overnight. The solvent

was removed under vacuum, the flask rapidly put under N_2, and the residue dissolved in 6 mL of dry DMF. The reaction was placed in an ice bath and 395 mg of potassium thioacetate (3.46 mmol) added in portions over 1 hour. The bath was thgen removed and the reaction kept under stirring for 20 hours. Water was then added to the flask and the solution extracted with DCM. The organic phase was washed with water, LiCl aq. sat., and it was dried over Na_2SO_4. The product was purified via column chromatography (hexane/ethyl acetate 3:1) to obtain a dark yellow oil (344 mg, 80% yield). ^{1}H NMR ($CDCl_3$, 400MHz): 7.60 (t, J = 7.8 Hz, 1H), 7.35 (d, J = 7.7 Hz, 1H), 7.34 (d, J = 7.6 Hz, 1H), 4.24 (s, 2H), 3.15 (s, 1H), 2.35 (s, 3H).

S-((6-((4-(phenylethynyl)phenyl)ethynyl)pyridin-2-yl)methyl) ethanethioate, mOPPy-2,6

In an oven dry flask equipped with a condenser under N_2, 200 mg of 1-bromo-4-(phenylethynyl)-benzene (0.78 mmol), 179 mg of **18** (0.93 mmol), 45 mg of $Pd(PPh_3)_4$ (0.04 mmol), 15 mg of CuI (0.08 mmol), and 1 mL of NEt_3 were dissolved in 5 mL of THF. The reaction was kept at reflux for 2 days. The final compound was purified via column chromatography (hexane/ethyl acetate 6:1) and recrystallized from hexane to obtain a pale yellow solid (4.1 mg, 2% yield). ^{1}H NMR ($CDCl_3$, 400MHz): 7.64 (t, J = 7.8 Hz, 1H), 7.58 (d, J = 8.3 Hz, 2H), 7.55 – 7.50 (m, 4H), 7.42 (d, J = 7.7 Hz, 1H), 7.38 – 7.33 (m, 4H), 4.28 (s, 2H), 2.37 (s, 3H).

1-ethynyl-3,5-dimethoxybenzene, 19

In an oven dry seleable Schlenk under N_2, 5 g of 1-bromo-3,5-dimethoxybenzene (23 mmol), 4.88 mL of (trimethylsilyl)acetylene (3.39 g, 35 mmol), 1.33 g of $Pd(PPh_3)_4$ (1.15 mmol), 307 mg of CuI (1.61 mmol) were dissolved in 50 mL of NEt_3. The reaction was left at 75 °C overnight. The reaction mixture was poured in a stirring mixture of water and DCM and the water phase acidified by adding slowly 70 mL of HCl 6 M. The TMS-protected product was purified by filtration over two short silica plugs using DCM and hexane as eluents for the first and the latter respectively and was recovered and a pale yellow solid (1.92 g, 37% yield). 0.5 g of the latter (2.13 mmol) were dissolved in 10 mL of THF and the solution placed in an ice bath. 3.2 mL of a tetrabutylammonium fluoride solution 1 M in THF (3.2 mmol) and 0.15 mL of H_2O were added dropwise and the reaction allowed to rt overnight. The final compound was purified via filtration over a short plug of silica using DCM to obtain an off-white solid (301 mg, 32% yield over 2 steps). ^{1}H NMR ($CDCl_3$, 400MHz): 6.58 (t, J = 2.4, 2H), 6.40 (t, J = 2.3 Hz, 1H), 3.70 (s, 6H), 3.03 (s, 1H).

((4-bromophenyl)ethynyl)triisopropylsilane, TIPS-5

In a oven dry flask, 10 g of 4-bromo-iodobenzene (35 mmol), 8.6 mL of (triisopropylsilyl)acetylene (6.99 g, 38.5 mmol), 150 mg of $Pd(PPh_3)_4$ (0.13 mmol), 50 mg of CuI (0.26 mmol), and 10 mL of NEt_3 were dissolved in 15 mL of THF. The reaction was left at 30 °C over the weekend. The solvent was removed and the product purified via column chromatography (hexane) to obtain a colourless oil (9.26 g, 81% yield). ^{1}H NMR ($CDCl_3$, 400MHz): 7.43 (d, J = 8.7 Hz, 2H), 7.33 (d, J = 8.7 Hz, 2H), 1.12 (s, 21H).

1-((4-ethynylphenyl)ethynyl)-3,5-dimethoxybenzene, 20

In an oven dry seleable Schlenk under N_2, 550 mg of 19 (3.39 mmol), 1.35 g of **TIPS-5** (4.01 mmol), 198 mg of $Pd(PPh_3)_4$ (0.17 mmol), 65 mg of CuI (0.34 mmol) were dissolved in 15 mL of NEt_3. The reaction was left at 80 °C overnight. The solvent was removed under vacuum and the residue preadsorbed on silica. The latter was washed with hexane and the TIPS-protected compound collected using chloroform as a white solid (701 mg, 49% yield). 650 mg of these latter 1.64 mmol were dissolved in THF and the solution placed in an ice bath. 3.3 mL of a tetrabutylammonium fluoride solution 1 M in THF (3.3 mmol) were added dropwise and rea left overnight. water and Et_2O were added to the mixture and the organich phase washed with water and dried over Na_2SO_4. The product was purified via column chromatography (hexane) to yield a white solid (615 mg, 48% yield over 2 steps). ^{1}H NMR ($CDCl_3$, 400MHz): 7.47 (s, 4H), 6.68 (d, J = 2.3 Hz, 2H), 6.47 (t, J = 2.3 Hz, 1H), 3.81 (s, 6H), 3.17 (s, 1H).

S-(4-((4-((3,5-dimethoxyphenyl)ethynyl)phenyl)ethynyl)phenyl) ethanethioate, OPE-OMe

In a dry flask equipped with a condenser, 470 mg of **20** (1.8 mmol), 560 mg **IPhSAc** (2 mmol), 42 mg of $Pd(PPh_3)_4$ (0.04 mmol), 10 mg of CuI (0.5 mmol), and 1 mL of NEt_3 were dissolved in 25 mL of THF. The reaction was kept at 80 °C for 2 days. The solvent was removed under vacuum and the product purified via column chromatography (hexane/ethyl acetate 4:1, R_f = 0.4) followed by recrystallization from hexane to yield 460 mg of an off-white solid (62 % yield). ^{1}H-NMR ($CDCl_3$, 400MHz) 7.55 (d, J = 8.3 Hz, 2H), 7.51 (s, 4H), 7.40 (d, J = 8.2 Hz, 2H), 6.69 (d, J = 2.3 Hz, 2H), 6.48 (t, J = 2.3 Hz, 1H), 3.81 (s, 6H), 2.44 (s, 3H). ^{13}C NMR ($CDCl_3$, 101 MHz): 196.02, 163.22, 136.87, 134.81, 134.25, 130.95, 126.91, 126.89, 125.89, 125.43, 112.03, 104.71, 94.05, 93.36, 93.13, 91.23, 58.10, 32.94.

S-4-((4-((3,5-dimethoxyphenyl)ethynyl)phenyl)ethynyl)benzyl ethanethioat, mOPE-OMe

In a dry flask equipped with a condenser, 470 mg of **20** (1.8 mmol), 584 mg **IBzSAc** (2 mmol), 42 mg of $Pd(PPh_3)_4$ (0.04 mmol), 10 mg of CuI (0.5 mmol), and 1 mL of NEt_3 were dissolved in 25 mL of THF. The reaction was kept at 80 °C for 2 days. The solvent was removed under vacuum and the product purified via column chromatography (hexane/ethyl acetate 4:1, R_f = 0.4) followed by recrystallization from hexane to yield 436 mg of an off-white solid (57 % yield). ^{1}H-NMR ($CDCl_3$, 400MHz) 7.55 (d, J = 8.3 Hz, 2H), 7.51 (s, 4H), 7.40 (d, J = 8.2 Hz, 2H), 6.69 (d, J = 2.3 Hz, 2H), 6.48 (t, J = 2.3 Hz, 1H), 3.81 (s, 6H), 2.44 (s, 3H). ^{13}C NMR ($CDCl_3$, 101 MHz): 197.52, 163.21, 140.81, 134.48, 134.21, 134.16, 131.54, 126.93, 125.77, 125.58, 124.63, 112.02, 104.68, 93.89, 93.64, 91.98, 91.29, 58.10, 35.92, 32.98.

1,4-diethynylbenzene, 21

1.91 g of **TMS-21** (7.06 mmol) and 1.50 g ofK_2CO_3 (10.6 mmol) were dissolved in 20 mL of MeOH and 5 mL of EtOH. After 2 hours of vigorous stirring, the solution was diluted using 50 mL of water and extracted with Et_2O. The organic phase was washed with brine and dried over $MgSO_4$. The solvent was removed in vacuum to obtain **21** as a brownish soldi sufficiently pure for further elaborations. ^{1}H-NMR ($CDCl_3$, 400MHz) 7,44 (s, 4H), 3.17 (s, 2H).

1,4-bis((4-(tert-butylthio)-3,5-difluorophenyl)ethynyl)benzene, 22

In an oven dry seleable Schlenk under N_2, 102 mg of 11 (0.31 mmol), 20 g of **21** (0.16 mmol), 30 mg of $Pd(PPh_3)_4$ (0.03 mmol), 10 mg of CuI (0.05 mmol) were dissolved in 6 mL of THF and 2 mL of NEt_3. The reaction was left at 60 °C overnight. The solvent was removed under vacuum and the residue preadsorbed on silica. The product was purified via column chromatography (hexane:ethylacetate 5:1) to yield a white solid (35 mg, 67% yield). ^{1}H-NMR ($CDCl_3$, 400MHz) 7.53 (s, 2H), 7.13 (d, J = 6.2 Hz, 2H), 1.34 (s, 9H) .^{19}F NMR ($CDCl_3$, 376 MHz): -102.52 (d, J= 6.2 Hz).

S,S'-((1,4-phenylenebis(ethyne-2,1-diyl))bis(2,6-difluoro-4,1-phenylene)) diethanethioate, diSAc-OPEFOut

In an oven dry flask under N_2, 133 mg of **22** (0.25 mmol) and 3.6 mL of acetylchloride (3.96 g, 50 mmol) were dissolved in 25 mL of DCM. 0.06 mL of $TiCl_4$ (0.09 g, 0.51 mmol) were added. After 1 hour the content of the flask was poured in a stirring mixture of DCM and water and the Na_2CO_3 aq. sat. was added slowly until neutrality. The organic phase was then extracted with water, dried over Na_2SO_4, and preabsorbed on silica. The final compound was purified via column chromatography (hexane/ethyl acetate 5:1, R_f = 0.6) and recrystallized from DCM/hexane to obtain an

off-white solid (21 mg, 17% yield). ^{1}H-NMR ($CDCl_3$, 400MHz) 7.53 (s, 4H), 7.16 (d, J = 7.0 Hz, 4H), 2.49 (s, 6H). ^{13}C NMR ($CDCl_3$, 101 MHz): 192.43, 164.81 (dd, J = 251.1, 5.8 Hz), 134.51, 129.94 (t, J = 10.1 Hz), 125.40, 117.51 (dd, J = 26.1, 2.7 Hz), 94.97, 91.58, 32.68. ^{19}F NMR ($CDCl_3$, 376 MHz): -103.97 (d, J = 7.1 Hz).

3

BIBLIOGRAPHY

[1] Heimel, G.; Rissner, F.; Zojer, E. *Adv. Mater.* **2010**, *22*, 2494–2513.

[2] Kretz, B.; Egger, D. A.; Zojer, E. *Advanced Science* **2015**, *2*, 1400016–.

[3] Cabarcos, O. M.; Schuster, S.; Hehn, I.; Zhang, P. P.; Maitani, M. M.; Sullivan, N.; Giguère, J.-B.; Morin, J.-F.; Weiss, P. S.; Zojer, E.; Zharnikov, M.; Allara, D. L. *The Journal of Physical Chemistry C* **2017**, *121*, 15815–15830.

[4] Alloway, D. M.; Hofmann, M.; Smith, D. L.; Gruhn, N. E.; Graham, A. L.; Colorado, R.; Wysocki, V. H.; Lee, T. R.; Lee, P. A.; Armstrong, N. R. *J. Phys. Chem. B* **2003**, *107*, 11690–11699.

[5] Bowers, C. M.; Liao, K.-C.; Zaba, T.; Rappoport, D.; Baghbanzadeh, M.; Breiten, B.; Krzykawska, A.; Cyganik, P.; Whitesides, G. M. *ACS Nano* **2015**, *9*, 1471–1477.

[6] Yoon, H. J.; Shapiro, N. D.; Park, K. M.; Thuo, M. M.; Soh, S.; Whitesides, G. M. *Angew. Chem. Int. Ed.* **2012**, *51*, 4658–4661.

[7] Yoon, H. J.; Bowers, C. M.; Baghbanzadeh, M.; Whitesides, G. M. *J. Am. Chem. Soc.* **2014**, *136*, 16–19.

[8] Baghbanzadeh, M.; Pieters, P. F.; Yuan, L.; Collison, D.; Whitesides, G. M. *ACS Nano* **2018**, –.

[9] Liao, K.-C.; Bowers, C. M.; Yoon, H. J.; Whitesides, G. M. *J. Am. Chem. Soc.* **2015**, *137*, 3852–3858.

[10] Bruce, R. C.; You, L.; Förster, A.; Pookpanratana, S.; Pomerenk, O.; Lee, H. J.; Marquez, M. D.; Ghanbaripour, R.; Zenasni, O.; Lee, T. R.; Hacker, C. A. *J. Phys. Chem. C* **2018**, *122*, 4881–4890.

[11] Kong, G. D.; Kim, M.; Jang, H.-J.; Liao, K.-C.; Yoon, H. J. *Phys. Chem. Chem. Phys.* **2015**, *17*, 13804–13807.

[12] Wang, D.; Fracasso, D.; Nurbawono, A.; Annadata, H. V.; Sangeeth, C. S. S.; Yuan, L.; Nijhuis, C. A. *Adv. Mater.* **2015**, *27*, 6689–6695.

[13] Nijhuis, C. A.; Reus, W. F.; Whitesides, G. M. *J. Am. Chem. Soc.* **2010**, *132*, 18386–18401.

[14] Kong, G. D.; Kim, M.; Cho, S. J.; Yoon, H. J. *Angew. Chem. Int. Ed.* **2016**, *55*, 10307–10311.

[15] Simmons, J. G. *Journal of Applied Physics* **1963**, *34*, 1793–1803.

[16] Fracasso, D.; Muglali, M. I.; Rohwerder, M.; Terfort, A.; Chiechi, R. C. *J. Phys. Chem. C* **2013**, *117*, 11367–11376.

[17] Kovalchuk, A.; Abu-Husein, T.; Fracasso, D.; Egger, D. A.; Zojer, E.; Zharnikov, M.; Terfort, A.; Chiechi, R. C. *Chem. Sci.* **2016**, *7*, 781–787.

[18] Kovalchuk, A.; Egger, D. A.; Abu-Husein, T.; Zojer, E.; Terfort, A.; Chiechi, R. C. *RSC Adv.* **2016**, *6*, 69479–69483.

[19] Love, J. C.; Estroff, L. a.; Kriebel, J. K.; Nuzzo, R. G.; Whitesides, G. M. *Chem. Rev.* **2005**, *105*, 1103–1170.

[20] Yuan, L.; Nerngchamnong, N.; Cao, L.; Hamoudi, H.; del Barco, E.; Roemer, M.; Sriramula, R. K.; Thompson, D.; Nijhuis, C. A. *Nature Communications* **2015**, *6*, 6324–.

[21] Neaton, J. B.; Hybertsen, M. S.; Louie, S. G. *Phys. Rev. Lett.* **2006**, *97*, 216405–.

[22] Weiss, E. A.; Kaufman, G. K.; Kriebel, J. K.; Li, Z.; Schalek, R.; Whitesides, G. M. *Langmuir* **2007**, *23*, 9686–9694.

[23] Yoon, H. J.; Liao, K.-C.; Lockett, M. R.; Kwok, S. W.; Baghbanzadeh, M.; Whitesides, G. M. *J. Am. Chem. Soc.* **2014**, *136*, 17155–17162.

[24] Ai, Y.; Kovalchuk, A.; Qiu, X.; Zhang, Y.; Kumar, S.; Wang, X.; Kühnel, M.; Nørgaard, K.; Chiechi, R. C. *Nano Lett.* **2018**, –.

[25] Vilan, A. *Phys. Chem. Chem. Phys.* **2017**, *19*, 27166–27172.

[26] Zhang, Y.; Soni, S.; Krijger, T. L.; Gordiichuk, P.; Qiu, X.; Ye, G.; Jonkman, H. T.; Herrmann, A.; Zojer, K.; Zojer, E.; Chiechi, R. C. *J. Am. Chem. Soc.* **2018**, *140*, 15048–15055.

[27] Beebe, J. M.; Kim, B.; Frisbie, C. D.; Kushmerick, J. G. *ACS Nano* **2008**, *2*, 827–832.

[28] Lefèvre, X.; Moggia, F.; Segut, O.; Lin, Y.-P.; Ksari, Y.; Delafosse, G.; Smaali, K.; Guérin, D.; Derycke, V.; Vuillaume, D.; Lenfant, S.; Patrone, L.; Jousselme, B. *J. Phys. Chem. C* **2015**, *119*, 5703–5713.

[29] Huisman, E. H.; Guédon, C. M.; van Wees, B. J.; van der Molen, S. J. *Nano Lett.* **2009**, *9*, 3909–3913.

[30] Guo, S.; Hihath, J.; Díez-Pérez, I.; Tao, N. *J. Am. Chem. Soc.* **2011**, *133*, 19189–19197.

[31] Abu-Husein, T.; Schuster, S.; Egger, D. A.; Kind, M.; Santowski, T.; Wiesner, A.; Chiechi, R. C.; Zojer, E.; Terfort, A.; Zharnikov, M. *Adv. Funct. Mater.* **2015**, *25*, 3943–3957.

[32] Dubi, Y. *J. Phys. Chem. C* **2014**, *118*, 21119–21127.

[33] Batra, A.; Meisner, J. S.; Darancet, P.; Chen, Q.; Steigerwald, M. L.; Nuckolls, C.; Venkataraman, L. *Faraday Discuss.* **2014**, *174*, 79–89.

[34] Carlotti, M.; Degen, M.; Zhang, Y.; Chiechi, R. C. *J. Phys. Chem. C* **2016**, *120*, 20437–20445.

[35] Simeone, F. C.; Yoon, H. J.; Thuo, M. M.; Barber, J. R.; Smith, B.; Whitesides, G. M. *J. Am. Chem. Soc.* **2013**, *135*, 18131–18144.

[36] Chiechi, R.; Weiss, E.; Dickey, M.; Whitesides, G. *Angew. Chem., Int. Ed.* **2008**, *47*, 142–144.

[37] Liao, K.-C.; Hsu, L.-Y.; Bowers, C. M.; Rabitz, H.; Whitesides, G. M. *J. Am. Chem. Soc.* **2015**, *137*, 5948–5954.

[38] Kaliginedi, V.; Moreno-García, P.; Valkenier, H.; Hong, W.; García-Suárez, V. M.; Buiter, P.; Otten, J. L. H.; Hummelen, J. C.; Lambert, C. J.; Wandlowski, T. *J. Am. Chem. Soc.* **2012**, *134*, 5262–5275.

[39] Frisch, M. J. et al. Gaussian09 Revision E.01. 2009; Gaussian Inc. Wallingford CT 2009.

4

CONFORMATION-DRIVEN QUANTUM INTERFERENCE EFFECTS MEDIATED BY THROUGH-SPACE CONJUGATION

We show an experimental evidence of conformation-driven interference effects by examining through-space conjugation in which pi-conjugated fragments are arranged face-on or edge-on in sufficiently close proximity to interact through-space. Observing these effects in the latter requires trapping molecules in a non-equilibrium conformation, which we accomplish using self-assembled monolayers to construct bottom-up, large-area tunneling junctions. In contrast, interference effects are completely absent in zero-bias simulations on the equilibrium, gas-phase conformation.

I would like to thank Prof. E. Otten for the help provided in the collection of the crystal structures. and prof. R.C. Chiechi for the help in the computational part.

4.1. INTRODUCTION

A central challenge in molecular electronics is uncertainty in the conformation and binding geometry of a molecule between two electrodes. Small differences exert large effects on tunneling charge-transport,[1] yet it is this sensitivity that drives scientific interest because functionality arises from precise control over conformation and geometry.[2–4] Nature accomplishes this level of control through self-assembly, in which molecular systems can be arranged precisely enough to support long-range electron transfer over several microns.[5] In self-assembled monolayers (SAMs), molecules are fixed in a specific conformation and binding geometry, arranging themselves in ordered, two-dimensional crystal-like domains. Tunneling junctions comprising SAMs, therefore, fix molecules in a specific conformation and binding geometry that defines the smallest dimension of the junction, through which charges tunnel; they are a form of bottom-up nanotechnology.[6, 7] The effects of conformational confinement on molecular charge-transport are particularly interesting in the case of π-conjugated molecules because conductivity (hopping) and transmission (tunneling) are strongly related to the extent of electronic delocalization. Quantum interference (QI) effects[8] arising from cross-conjugation in such conjugated molecules have been demonstrated experimentally[9, 10], but they have also been predicted for π systems that are close enough in space to interact.[11] Unlike for conjugation patterns, which are an intrinsic property, this type of QI is extremely sensitive to conformation; the two π systems must be precisely aligned to form a through-space conjugation interaction.

Single-molecule conductance techniques are not well suited for observing effects that require precise control over conformation because they apply force to molecules and the geometry of the junction differs with each observation.[12, 13] And although SAMs are crystalline and can be highly ordered over small areas, defects and grain boundaries can influence the current-density versus voltage (J/V) properties in large-area (μm^2) measurements.[14] In addition to these experimental challenges, distinguishing between destructive QI and differences in conductance arising from conjugation length require fortuitous level-alignment in the assembled junction.[15] Through-space QI is potentially useful beyond validating theoretical predictions as it could couple small struc-

tural or conformational changes (*e.g.*, from external mechanical forces) into exponential changes in conductance. It is also synthetically advantageous because cross-conjugation tends to involve heteroatoms, which can introduce unexpected and complex electrostatic effects.[16]

In this chapter, I describe through-space destructive QI effects in tunneling charge-transport through SAMss comprising molecules in which the central aromatic rings are spatially separated by saturated methylene bridges. These effects are consistently present in simulated transmission spectra derived from the X-ray crystal structures of the compounds used to form the SAMs, but not in minimzed, gas-phase geometries. We resolved these effects experimentally by conducting-probe atomic force microscopy (CP-AFM) and in large-area junctions using eutectic Ga-In (EGaIn) as a top-contact.[17] These results prove that the J/V characteristics are not the result of defects and demonstrate both that a single conformation resembling that of the bulk crystal dominates transport in a SAM, mitigating the problem of uncertainty in the geometry of tunneling junction, and that symmetric Au contacts can be used to model electronic effects qualitatively in large-area junctions with EGaIn top-contacts.

4.2. CONFORMATION WITHIN THE SAM

We investigated tunneling transport in in Au^{TS}/SAM//EGaIn and Au^{mica}/SAM//Au^{AFM} junctions (where '/' and '//' denote covalent and van der Waals contacts, respectively, Au^{TS} is template-stripped Au, Au^{mica} is Au-on-mica and Au^{AFM} is a Au-coated AFM tip) comprising molecular systems characterized by two phenyl rings in either a vertical, face-on (*pseudo-p*-bis((4-(acetylthio)phenyl) ethynyl)-*p*-[2,2]cyclophane, **PCP**) or edge-on (2,6-bis(((4-acetylthio)phenyl)ethynyl)-9,10-dihydroantracene, **AH**) arrangement and that are held in close proximity with saturated ethylene bridges. In both cases the precise alignment of the π systems is controlled by packing in the SAM on the Au substrates. We measured 1,4-bis(((4-acetylthio)phenyl)ethynyl)benzene (**OPE**) and 2,6-bis(((4-acetylthio)phenyl)ethynyl)antracene (**AC**)[18] to compare molecules with the same end-to-end lengths as **PCP** and **AH**, but that are conjugated through-bond; the structures and tunneling pathways are shown in Figure 4.1.

Edge-on transport is difficult to address experimentally because at room temperature **AH** is in rapid equilibrium between bent and planar conformers in solution and in the gas phase, preferring the bent conformation by 3.5 kcal mol^{-1} (see Table 4.5 in the Experimental Section) in a single-molecule junction.[10] In the crystalline state, however, **AH** adopts a planar conformation to minimize the free volume. To establish experimentally the precise spacial arrangements of the phenyl rings comprising the through-space elements, we obtained the X-ray crystal structures of **AH** and **PCP**, which we denote as **AH-crystal** and **PCP**-crystal. These structures and data are shown in Figure 4.2 and 4.3, and Table 5.8.

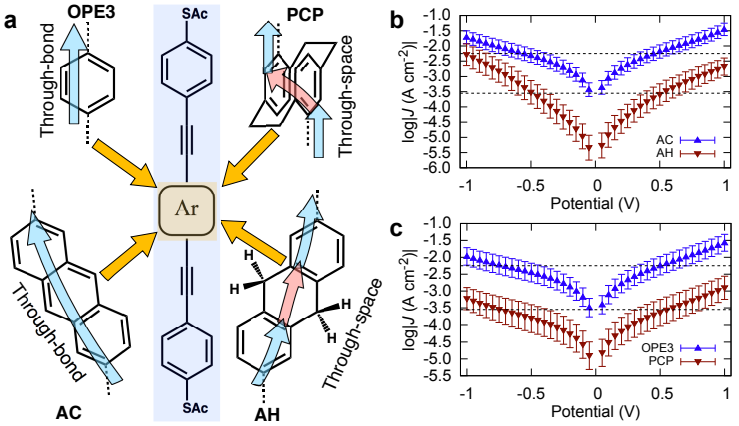

Figure 4.1 Molecular conformation effects on charge transport in tunneling junctions. a; The structures of the compounds from which SAMs were grown on Au^{TS}. The blue arrows show through-bond pathways and the red arrows through-space pathways. b; Current-density versus voltage plots of Au^{TS}/SAM//EGaIn junctions of **AH** (red triangles) and **AC** (blue triangles) and c; **PCP** (red triangles) and **OPE** (blue triangles). The dashed lines are to guide the eyes. Each data point is the peak of a Gaussian fit of log-normal plots of $|J|$ for that voltage. Error bars are confidence intervals. Tunneling junctions were formed by contacting grounded Au^{TS}/SAM substrates with sharp tips of EGaIn and applying a potential.

We determined the tunneling transport properties by comparing the magnitude of $\log|J|$ in Au^{TS}/SAM//EGaIn junctions comprising SAMs of **OPE**, **PCP**, **AH**, and **AC**, which we grew from symmetric bis-thioacetates via *in situ* deprotection as described already in Chapter 2. We characterized the SAMs by ellipsometry, high-resolution X-ray photoelectron spectroscopy (HRXPS) and near-edge X-ray absorption fine structure (NEXAFS)

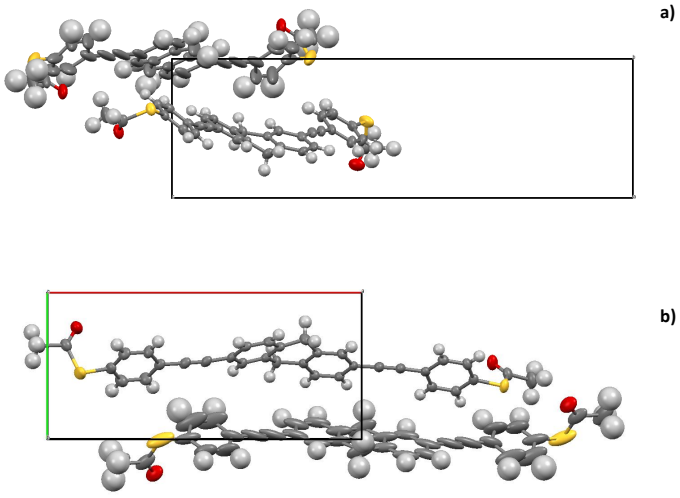

Figure 4.2 Crystal structure for AH. a) View along **a**-axis; b) view along **c**-axis. Color code: C, grey; H, white; S, yellow; O, red.

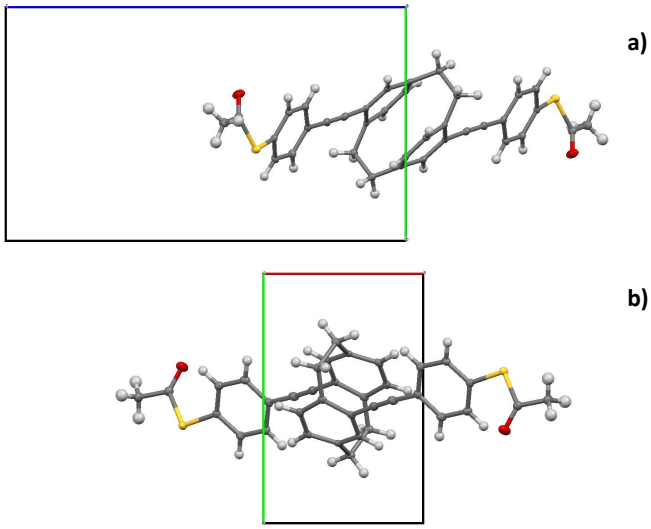

Figure 4.3 Crystal structure for PCP. a) View along **a**-axis; b) view along **c**-axis. Color code: C, grey; H, white; S, yellow; O, red.

Table 4.1 Summary of SAMs characterization and Au^{TS}/SAM//EGaIn junctions properties.

Compound	**AH**	**AC**	**PCP**	**OPE**	**SC18**
XPS Thickness (Å)	23.9 (19.0[a])	16.2 (25.1[a])	15.8	13.7 (17.5[b])	20.9
Ellipsometric Thickness[c] (Å)	25.4 ± 0.5	17.0 ± 0.5	14.6 ± 0.4	14.3 ± 0.6 (20.6[b])	20.2 ± 0.5
Density (10^{14} molecules/cm^2)	4.7	4.6	3.9	3.5	4.6
$\log\lvert J\rvert$@0.5 V (Acm^{-2})	-3.37 ± 0.84	-2.18 ± 0.44	-3.63 ± 0.80	-2.27 ± 0.30	-4.96 ± 0.87
Yield of working junctions (%)	96	98	94	92	79
Number of working junctions	55	56	75	60	28
Number of traces	550	560	750	600	280

[a] From Ref. 9.

[b] From Ref. 19.

[c] Using n= 1.5.

spectroscopy. These data are summarized in Table 4.1 along with literature and benchmark values for SAMs of $CH_3(CH_2)_{17}S$ (**SC18**) for comparison. The spectra are shown in the Method Section Figures 6.18 and 6.19. The principal difference appears to be the tilt angles, which are slightly higher for Au^{TS} than Au^{mica}, thus the SAMs are slightly thinner (except for **AH**), but still quite dense (on the order of 10^{14} molecules/cm^2). The S 2p X-ray photoelectron spectra of the SAMs exhibited characteristic signals of thiolate and unbound SH/SAc groups, with much higher intensity of the latter signals, because of the differences in the attenuation.[20] These spectra suggest that the molecules are indeed assembled upright in the SAMs, with one of the terminal sulfur atoms bound to the substrate and another one exposed to the SAM-ambient interface, where it can be contacted by EGaIn or Au^{AFM}. Upright molecular orientation is also apparent from the NEXAFS spectra, which exhibited quite small but distinct linear dichroism corresponding to an average molecular tilt angle of approximately 40°. In addition, the spectra exhibited the characteristic absorption resonances of OPE-like compounds (Supplementary Note 1), establishing the identity of the **AC**, **AH**, **OPE**, and **PCP** films. Significantly, there were no traces of contamination, demonstrating the high purity of the prepared monolayers. Measuring well characterized, high-quality SAMs is paramount as, unlike top-down, single molecule techniques (break junctions, etc.) or few molecules techniques (conducting probe AFM, etc.), EGaIn is a bottom-up, large-area technique[7] and is therefore

sensitive to the detailed structure of the SAM as it defines the physical shape of the junction and the EGaIn//SAM interface.[21–23]

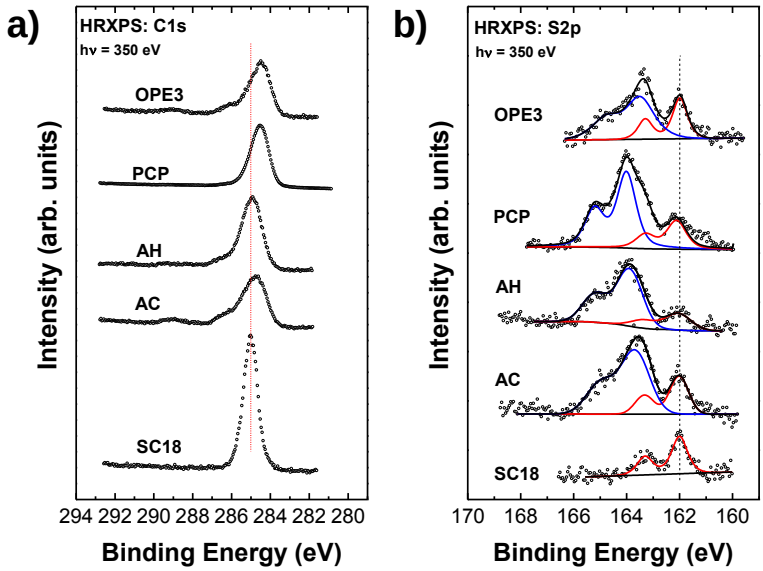

Figure 4.4 C 1s (a) and S 2p (b) HRXP spectra of the SAMs studied as well as reference SC18 monolayer. The spectra were acquired at a PE of 350 eV. The peaks in the S 2p spectra are decomposed into individual doublets associated with the thiolate headgroup at the Au/SAM interface and a -SAc group at the SAM/ambient interface (see text for details).

4.3. CHARGE TRANSPORT CHARACTERISTICS

In through-space conjugation two π systems are held close enough in space to interact without the aid of an underlying σ framework. Electronic overlap and, therefore, tunneling charge-transport is extraordinarily sensitive to the conformation imposed by the junction geometry because there is no rigid framework to keep π systems aligned and their relative displacement is subject to interactions with neighboring molecules. This sensitivity is why through-space QI effects are difficult to resolve experimentally; *e.g.*, destructive QI is predicted in stacked benzene rings, but only through specific pathways and precise arrangements of the two rings.[11] Previous break-junction measurements on *p*-2,2-cyclophane moieties (which are similar to **PCP**) probed tunneling charge trans-

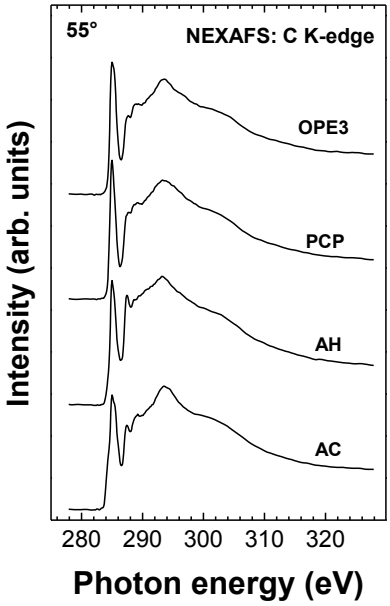

Figure 4.5 C K-edge NEXAFS spectra of the SAM studied. The spectra were measured at an X-ray incidence angle of 55° and are exclusively representative of the electronic structure of the monolayers.[24] The spectra exhibit the characteristic shape and the characteristic absorption resonances of the OPE compounds,[25] above all the slightly asymmetric, joint p* resonance at approximately 285.0 eV. No traces of contamination, above all a very pronounced resonance of carboxyl (most frequent contamination) at 288.8 eV,[26] are observed, revealing a purity of the monolayers.

port perpendicular to the plane of the phenyl rings (*i.e.*, down the stack).[27] And the conductance of **AH** was *higher* than **AC** in break-junctions, where the former exhibited a decrease in conductance with increasing electrode separation.[10] No QI was predicted or observed in either of these studies. (An electron tunneling through space, the red arrows in Fig. 4.1 A, is not itself a predictor of QI or of different magnitudes of tunneling transport compared to their through-bond analogs.)

Figures 4.1 B and C show the J/V curves for **AC**, **AH**, **OPE**, and **PCP**. The SAMs on Au^{TS} are robust enough to scan to ±1V, revealing the onset of asymmetric conductivity ($\log|J|@1\,V \neq \log|J|@-1\,V$) in **AH**, possibly because the two halves of **AH** approach resonance independently of each other due to the disparate contacts.[28] Data from Au^{mica}/SAM/Au^{AFM} junctions acquired using CP-AFM show the same trends in conduct-

ance, although we could not resolve the low-bias regions of **PCP** or **AH** (Figure 4.6). Nonetheless, these data confirm that the trend is not due to defects in the SAM (the contact area of CP-AFM is on the order of 80-100 molecules) or the influence of the Ga_2O_3 layer on the EGaIn electrode. Both the Au^{mica}/SAM/Au^{AFM} and Au^{TS}/SAM/EGaIn junctions of **OPE** and **AC** exhibit larger magnitudes of J by about a factor of 100 than **PCP** and **AH**, respectively (which may be a sign that destructive QI is dominant in the latter two SAMs).

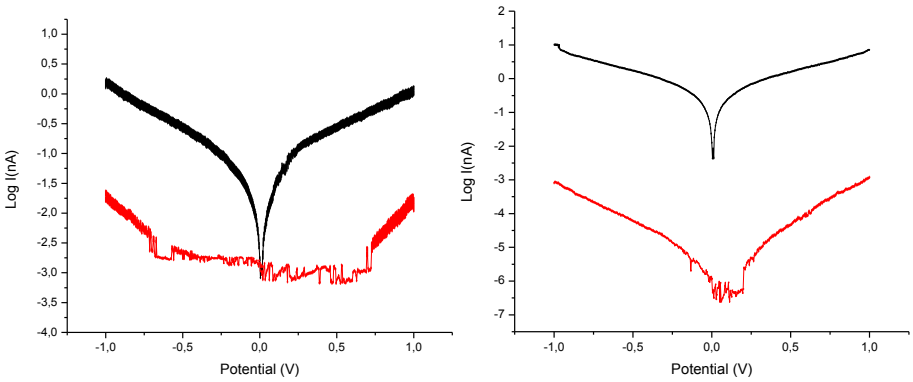

Figure 4.6 Semilog plot of $|I|$ vs. V for CP-AFM junctions comprising: left, **AC** (black) and **AH** (red);right, **OPE** (black) and **PCP** (red). The error bars are calculated using α= 0.95 and n= 40.

Unambiguously ascribing transport data to destructive QI effects is difficult because the observable is smaller magnitudes of $\log|J|$, which is sensitive to myriad of factors.[29] Thus, we applied various tests for QI, which is predicted for **PCP** and **AH**, but not **OPE** or **AC**, in agreement with the J/V data in Fig 4.1. One simple approach is to analyze the Green's function associated with the systems.

The transmission probability spectra of a lead-molecule-lead system as a funtion of the electron energy ($T(E)$) depends on the non-equlibrium Green's matrix (**G**) as defined by Eq. 4.1

$$T(E) = Tr[\Gamma_L \mathbf{G} \Gamma_R \mathbf{G}^T] \tag{4.1}$$

where $\Gamma_{L/R}$ are the broadening function matrix for the respective elctrodes.[30] Tsuji et al. showed that a qualitative discussion about the molecule transport properties can

be limited to a simple approximation of the Green's function at the Fermi energy of the system (assuming weak coupling between the molecules and the electrodes) shown in Eq. 4.2.[15]

$$\mathbf{G}(E_F) \approx \mathbf{G}^{(0)}(E_F) = [(E_F + i\eta)\mathbf{I} - \mathbf{H}]^{-1} \tag{4.2}$$

where **I** is the unit matrix, **H** is the Hückel Hamiltonian matrix and η is a infinitesimal positive number. Assuming that E_F doesn't correspond to any eigen-energies of **H** and referring it to 0 ($E_F = 0$), the so-called 0^{th}-order Green's function matrix is obtained, with its elements given by Eq. 4.3.

$$G(r,s) \approx [-\mathbf{H}^{-1}]_{r,s} \tag{4.3}$$

By "contacting" the molecule in the positions noted by r and s along the molecule's conjugation path, information about the molecular transport can be obtained from $G(r,s)$. In particular a 0-element in the latter represents a channel in which the transport is not permitted by quantum interference, while a non-0 equals to an open channel. As suggested in Eq. 4.1, the transport properties depend as well on the broadening function matrices, which describe the interaction between the molecule and the electrodes: for reasons of simplicity, in our Green's function analysis we considered that the matrices $\Gamma_{L/R}$ have only one non-zero element each and therefore the transmission probability will be proportional to the $G(r,s)$ matrix elements.[15] We therefore calculated $G(r,s)$ for the cores of **OPE, AC**, **PCP** and **AH** as described by 4.3. To keep our analysis as simple as possible, we constructed the **H** matrix using the energy units of the resonance integral which describes the interaction between two adjacent π orbitals, in this case all the near-neighbor interactions carry the value 1, near-neighbor through-space interactions 0.1, while all the others can be set to 0. This approach ignores features like different bond distances and neighbors interactions, which, anyway, do not change the output of a qualitative approach. We decide to treat trough-space conjugated π-systems as if the sp^2 carbons belonging to the separated π-systems were interacting as adjacent entities but with a lower overlap resonance integral due to the longer spacial separation (0.1 instead of 1). For **PCP**, the carbons in the stacked phenyl rings were assumed to interact

trough-space with their eclipsed neighbor on the other ring. In the case of **AH,** we assumed no contribution from the sp^3 carbons in the anthracene positions 9 and 10, and a trough-space interaction between the closer rings across the gap. We show the resulted analyses in Figure 4.7 where white elements in the matrices indicates QI suppressed transport. It is clear how for equivalent injection sites, both **AH** and **PCP** have a different behavior than their linearly conjugated parents. It is worth mentioning that, in the case of **AH,** if a role of the saturated carbons in the transport is considered (for example as a consequence of hyperconjugation), then the interference is expected to vanish and its matrix to resemble that of **AC**.

Another test for QI, is to consider the sign of the product of the coefficients of the frontier orbitals on the termini of a molecule (*i.e.*, , wehere we consider the leads to be attached): if they are the same, destructive QI is predicted between those orbitals.[8] This test is shown in Fig. 4.8 for **AH** and **AH-crystal**. Compared to the previous method, where the molecules where considered as 2D-mathematical representations, now the geometry and the symmetry of the molecule can affect the distribution of the orbitals. Interestingly, the change in the signs of the orbital coefficients between **AH** and **AH-crystal** is accompanied by an increase in distance between the phenyl rings of 0.06 Å, at which point the two halves (separated by the CH_2 bridges) become almost coplanar, aligning the two phenyl π-systems and allowing for better electronic overlap. In this conformation the two phenyl rings are connected by through-space conjugation and this form of through-space conjugation apparently induces QI analogously to the face-on arrangement in **PCP**. QI has not previously been predicted for **AH** because only the gas-phase minimized structure has been considered. Destructive QI may be "switched on" in **AH** by small changes in conformation that tend to planarize the core.

4.4. DISCUSSION

For further insight into the predicted transport properties, we simulated transmission spectra for isolated molecules of **AC**, **AH**, **OPE**, and **PCP** bound to Au electrodes. To isolate relative effects of molecular structure, we performed density function theory (DFT) calculations with 12-atom Au(111) clusters bound to the terminal sulfurs at hexagonal

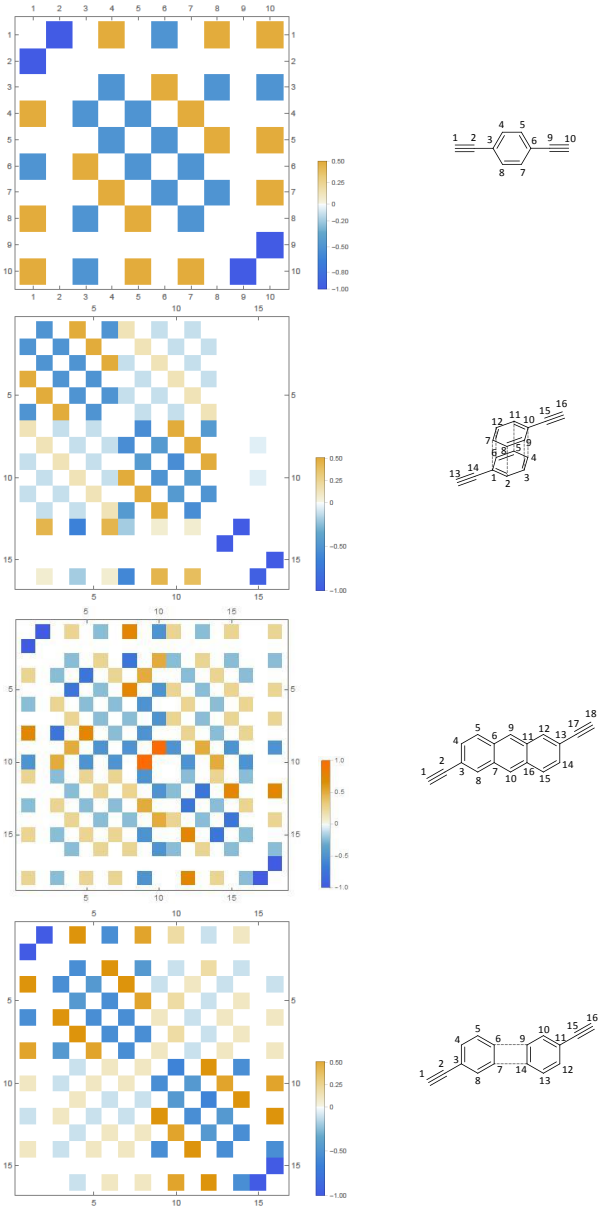

Figure 4.7 Colored representation of the $G(s,r)$ matrix for **OPE, PCP**, **AC**, and **AH.** White positions represent zero-elements ascribable to quantum interference in the path trough the atoms labeled r and s. Dashed lines depict through-space interaction (see main text). Numbering of the molecule is presented on the right side of the figure.

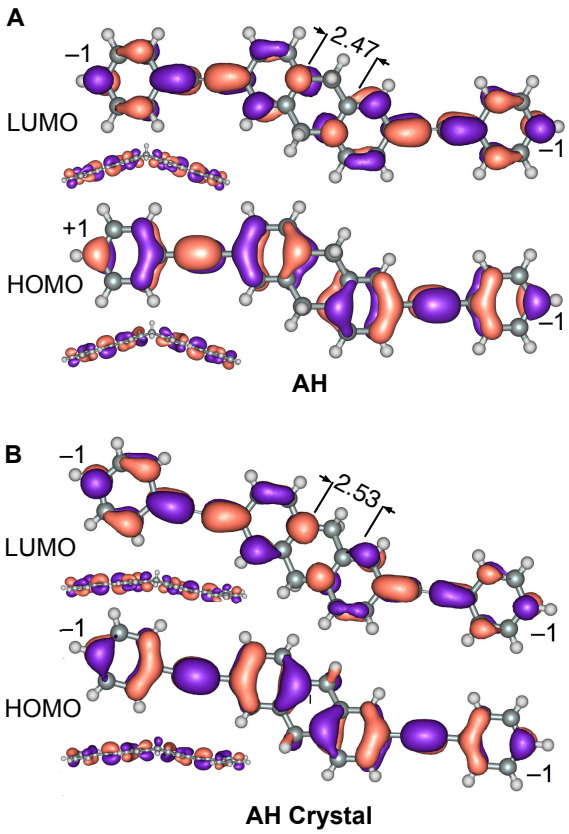

Figure 4.8 Impact of molecular geometry on molecular orbitals.The HOMO and LUMO of **AH** (A) and **AH-crystal** (B) with through-space distances indicated in Å. The signs of the orbital coefficients at the terminal sites are shown at these sites.

close-pack hollow sites. These calculations are not models of Au^{TS}/SAM//EGaIn or Au^{mica}/SAM/Au^{AFM} junctions, rather they are computational experiments on idealized systems to isolate the effects of electronic structure and conformation on zero-bias transmission by using single molecules bound to small clusters of Au. There are numerous collective effects in SAMs that can affect the electrostatics and level-alignment that cannot be captured by single-molecule calculations.[31–34] Without detailed knowledge of the packing of the molecules in the SAM and atomistic detail of the Ga_2O_3 electrode and SAM//Ga_2O_3EGaIn interface, none of which are available, it is impossible to construct an accurate model capable of predicting these effects. The principal limitations of us-

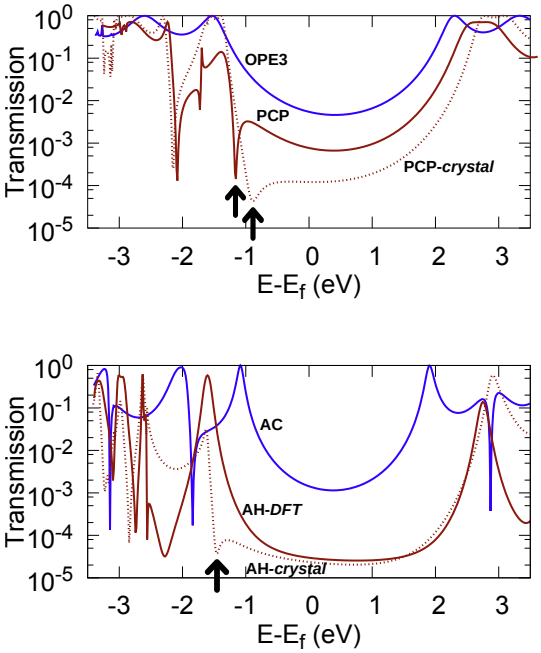

Figure 4.9 Charge transmission probability plots. Transmission plots comparing, top: **PCP** (red), **OPE** (blue) and **PCP**-crystal (dashed red) and bottom: **AH** (red), **AC** (blue), and **AH-crystal**. The 'crystal' suffix denotes X-ray crystal structures; the others are gas-phase minimized structures. The energy of the Fermi level E_f was computed by adding V_{trans} to the highest-occupied π state. Destructive quantum interference features are marked with thick black arrows.

ing a model Au/molecule/Au junction is that we cannot reliably estimate the Fermi level E_f and the relative level-alignments will not reflect any collective effects such as broadening or electrostatic shifts[35] (*e.g.*, the 0.4 eV to 0.5 eV shift induced by S-Au bonds in SAMs.[36]) However, we can still compare (similar) molecular structures and draw meaningful (qualitative) conclusions in combination with experimental data from Au^{TS}//SAM//EGaIn junctions.[9] We estimated E_f by adding the calculated highest-occupied π state (HOPS) to the experimentally-derived transition voltages[35, 37] V_{trans} for each Au^{TS}/SAM//EGaIn junction (Table4.3 in Experimental Section) to establish the relative level-alignment between related structures (*i.e.*, **OPE** and **PCP**; **AH** and **AC**.)

The top plot of Figure 4.9 shows the resulting transmission spectra from DFT calcu-

lations for **OPE** and **PCP** Au/molecule/Au junctions. The U-shape centered at approximately 0.5 eV is indicative of transmission probabilities in the frontier orbital gap of the molecule. The lower overall transmission of **PCP** and **PCP**-crystal is the result of the the break in conjugation at the cyclophane ring, *i.e.*, there is no formal resonance structure connecting the two halves of the molecule. The plots for **PCP** and **PCP**-crystal also exhibit sharp dips around −1 eV, which is a sign of QI; at this energy the frontier orbitals interfere destructively and a node appears in the wave function, suppressing transmission sharply. The most pronounced differences between **PCP** and **PCP**-crystal are that the transmission is higher everywhere for the former and the energy and magnitude of the dip ascribed to QI shifts by approximately 0.5 eV (*i.e.*, the positions and lengths of the solid red arrows in Fig. 4.9 A differ.) This observation highlights the utility and limitations of using zero-bias, single-molecule junctions as models for Au^{TS}/SAM//EGaIn junctions; both the overall conductance (the integrated transmission near E_f) and the position of the QI feature are sensitive to minor conformation changes. Figure 4.10 compares some of these differences, which are a small as 0.05 Å in the cyclophane core. The net effect is that the x-axes in Fig. 4.9 as well as the relative position of the dip in transmission will be shifted in the actual junctions.

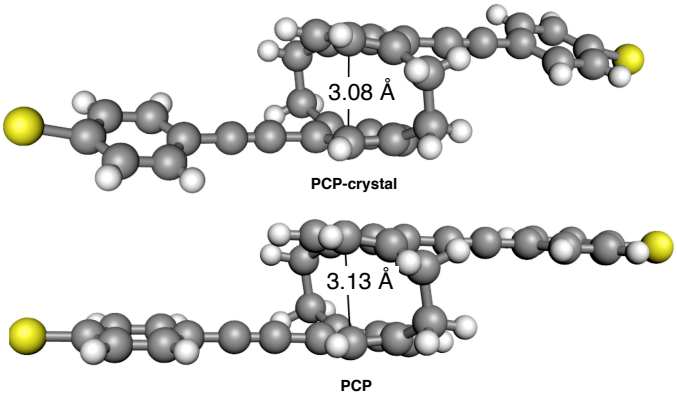

Figure 4.10 Ball-and-stick models of **PCP** and **PCP**-crystal showing slight difference in through-space distances and the more pronounced differences in the phenylacetylene groups.

The bottom plot of Figure 4.9 shows the transmission spectra of **AC** and **AH** Au/molecule/Au junctions. Analogously to **OPE**, **AC** shows a U-shaped curve centered at approximately

0.5 eV; unlike **OPE** and **PCP**, however, the positive resonances (not QI) near the frontier orbitals for **AC** are closer to 0 eV than they are for **AH** because there is a more pronounced change in the frontier orbital gap between linear and through-space conjugation in the edge-on case (**AH**) than the face-on case (**PCP**.) It is tempting to ascribe this difference between the investigated systems to the lower conductivity of **AH** compared to **AC**—one is conjugated and one is not—whereas cyclophanes exhibit similar properties to phenyl rings (for example, functional groups direct identical pseudo *para*/*meta* substitution.) Figures 4.1 B and C, however, show that SAMs of **PCP** are experimentally much less conductive than SAMs of **OPE** across the entire bias window, while **AH** approaches the conductivity of **AC**, nearly crossing at −1 V. This behavior is consistent with hypothesis that the conductance of **AH** in the low-bias regime is dominated by a sharp, destructive QI feature and that, as the bias is increased, transmission increases rapidly; *i.e.*, the dip in the dashed line (**AH-crystal**) in Figure 4.9 B is shifted close to E_f in actual Au^{TS}/SAM//EGaIn junctions. The solid line in Figure 4.9 B is the minimized, gas-phase conformation of **AH**; unlike the case of **PCP** and **PCP**-crystal, the interference feature present for **AH-crystal** vanishes entirely with **AH**. We ascribe this difference to the changes in the frontier orbitals shown in Fig. 4.8 when **AH** adopts a planar conformation in the solid-state. This comparison does not imply that **AH-crystal** reflects the exact conformation of **AH** in a SAM; however, if **AH** adopts a planar conformation in a bulk crystal, it is very likely that it does so when confined to a two-dimensional molecular film on a solid substrate.

The extreme sensitivity of through-space QI effects on molecular conformation demonstrated by the DFT calculations presents a significant experimental challenge that has confounded past efforts to characterize the effects of through-space conjugation on tunneling charge-transport. Wire-like *p*-2,2-cyclophane moieties similar to **PCP** probed by crossed-wires, scanning tunneling microscopy (STM) and CP-AFM in mixed monolayers and sparse SAMs—*i.e.*, not in dense SAMs like those formed from **PCP**—exhibited only slightly suppressed conductance.[38, 39] And attempts to compare edge-on through-space and through-bond conduction pathways (analogous to **AH**) were similarly frustrating; although through-space interactions were found in the crystal structure, there

was no correlation with conductance measurements in break-junctions.[40] The inconsistency of these observations may be a reflection of the sensitivity of through-space effects to conformation (or simply better experimental techniques). These results underscore the importance of considering the different geometries molecules adopt in solid, gas or dissolved phases and in single-molecule junctions and the challenges of growing densely-packed SAMs from π-conjugated molecules.

We are confident in ascribing the low conductivity of SAMs of **PCP** to QI because it has been predicted for face-on through-space transport,[11] however, the most robust experimental proof of destructive QI is the appearance of negative curvature in conductance heatmap plots of differential conductance $\log|\frac{dJ}{dV}|$ versus V.[41] This curvature only appears if the energy of the interference in the assembled junction is close enough to E_f that the feature lies almost entirely within the bias window.[15] The dip in transmission for **PCP** and **AH-crystal** in Fig. 4.9 is far from E_f, but (as described above) these calculations do not reflect the actual level-alignment in the Au^{TS}/SAM//EGaIn junctions. Differential conductance heatmaps of **OPE**, **AC**, **PCP**, and **AH** are shown in Fig. 4.11.

These plots are constructed from histograms of $\log|\frac{dJ}{dV}|$ obtained from numerical derivatives of individual J/V plots. (One advantage of EGaIn measurements is that J/V curves do not require smoothing; these are 'raw' derivatives.) The plots of **OPE**, **AC** and **PCP** are all U-shaped and slightly asymmetric, reflecting non-resonant tunneling with somewhat asymmetric coupling. This observation is consistent with recent work comparing Au/molecule/Au and Ag^{TS}/SAM//EGaIn junctions.[42] The magnitudes of **PCP** and **AH** are also lower than **OPE** and **AC**, however, the **AH** curve is sharp with obvious negative curvature. This difference is direct, experimental evidence of a destructive QI feature very close to E_f, supporting the hypothesis that **AH** in a SAM adopts a planar conformation closer to that of **AH-crystal** than to (the minimized, gas-phase conformation of) **AH** (Fig. 4.8). No direct evidence was obtained in the case of **PCP** on our experimental platform, yet this compound was successfully used in the preparation of SAM-based QI-mediated vertical molecular tunneling transistors which rely on the QI properties of the cyclophane core.

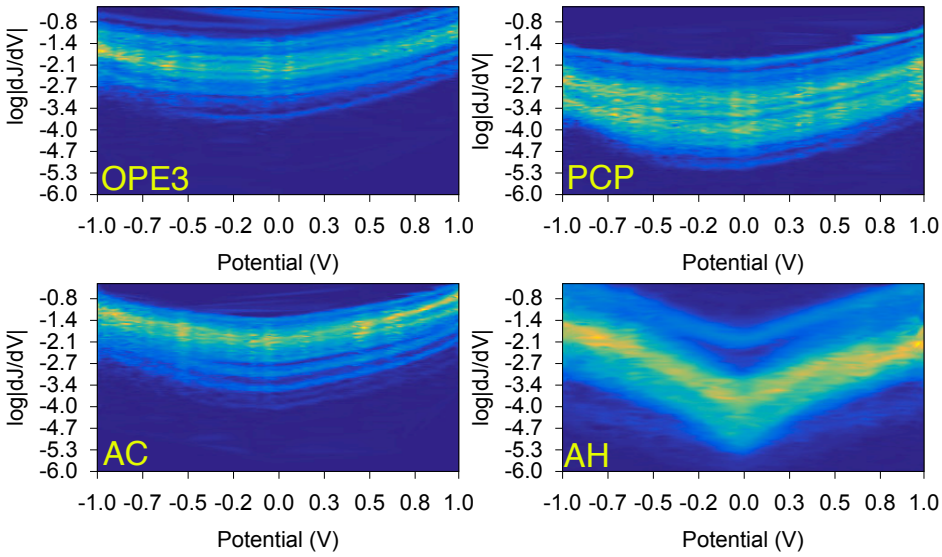

Figure 4.11 Differential conductance plots. Conductance heatmap plots of **OPE** and **PCP** (top left and right, respectively) and **AC** and **AH** (bottom left and right, respectively) showing histograms binned to $log|\frac{dJ}{dV}|$ (conductance, Y-axis) versus potential (in V, X-axis). The colors correspond to the frequencies of the histograms; lighter colors indicate higher frequencies (max ~ 150); the yellow bands are approximately $\frac{d\mu_{log}}{dV}$ (*i.e.*, from Fig. 4.1). All of the plots except for **AH** are U-shaped, which is a sign of non-resonant tunneling. The plot for **AH** has a sharp dip the center and negative curvature near ±1 V, which is a sign that a destructive interference feature exists in the bias window.

4.5. CONCLUSIONS

In molecular tunnelling junctions, charge transport is dominated by states close to E_f, but accurately determining the positions of these states in assembled junctions is a principal experimental challenge. The only experimental observable for destructive QI is lower conductance, thus claims that QI leads to the observation that a particular structure is less conductive than a reference structure in tunneling junctions rest entirely on theoretical methods such as those outlined in this paper. However, when the sharp resonance feature of destructive QI is sufficiently close to E_f (in physical junctions) it can appear as a V-shaped differential conductance plot. Next to this work, there are only two other reports of such features appearing, both involving cross-conjugated quinone derivatives of **AC**.[41, 43] In both cases QI features close to E_f appear in DFT calcula-

tions for two structures, but appear in differential conductance plots for one. Thus, we proposed the first experimental evidence of destructive QI modulated by through-space conjugation and the first observation of conformer-dependent QI. We base our claim that the interference feature of **AH** lies near E_f entirely on experimental evidence because it not possible even to estimate the electrostatics in a metal/SAM/metal junction with the available atomistic and structural information; however, deriving E_f from V_{trans} gives eminently reasonable relative level-alignments between **OPE**/**PCP** and **AC**/**AH** with respect to the HOPS. Given the similar in length and HOPS between **OPE**/**PCP** and **AC**/**AH** and the differential conductance plots, we can unambiguously ascribe the suppressed conductivity of both **PCP** and **AH** to the destructive QI in the transmission spectra of **PCP-crystal** and **AH-crystal** and conclude that J is dominated by a single conformer and that the through-space elements are better described by X-ray crystal structures than gas-phase optimized structures.

As the complexity of organic structures investigated in tunneling junctions grows, the details of molecular conformations become more important. And moving from top-down spectroscopic tools towards functional, device-like platforms[2–4, 44–48] will probably involve bottom-up molecular tunneling junctions based on SAMs,[7] in which molecules are in a (liquid) crystalline state. Such junctions represent a form of nanotechnology closest to Nature in that the nanoscopic structure and function are simultaneously and inseparably defined by the equilibrium self-assembly of molecules; differences of 0.06 Å to 0.11 Å can completely suppress QI in DFT simulations. Using QI as a probe, we can separate the effects of interrupted π conjugation from those of QI, which are normally conflated experimental observables. And in doing so we provided unambiguous evidence that through-space conjugation can cause interference effects and are not simply 'non-conjugated.' When detailed conformation and packing cannot be determined experimentally, carefully design molecular geometries on X-ray crystal structures of the pure compounds may be a better approximation of molecular conformation in densely-packed SAMs than DFT-minimized structures and transition voltages may provide a reasonable approximation for level-alignment to relate transmission calculations to SAM-based junctions. This approach to understanding transport properties

should be generalizable—even in the absence of an observable such as through-space QI—facilitating detailed theoretical and experimental studies on bottom-up, large-area molecular junctions comprising SAMs.

4.6. EXPERIMENTAL SECTION

MATERIALS AND METHODS

The synthesis of **AH, AC** and **OPE** is described elsewhere.[18] All compounds were stored in nitrogen-flushed vials and in the dark. Their structures were verified by acquiring ^{1}H-NMR and FT-IR spectra immediately prior to use and comparing to the spectra acquired immediately after purification. *pseudo*-*p*-bis((4-(acetylthio)phenyl)ethynyl)-*p*-2,2-cyclophane (**PCP**) was prepared starting from *p*-2,2-cyclophane (**1**) as shown in Figure 4.12. *p*-2,2-cyclophane (99%), (Triisopropylsilyl)acetylene (97%), tetrabutylammonium fluoride (TBAF, 1M in THF, 5% H_2O), pipsyl chloride (95%), *N,N*-dimethylacetamide (99.8%) and dichlorodimethylsilane (≥ 98.5%) were purchased from Sigma-Aldrich and used as received. $Pd(PPh_3)_3$ and CuI were purchased from ACROS Organics and stored under nitrogen in the dark at 4 °C. NEt_3 was distilled over CaH. Tetrohydrofuran (THF) was stirred for 1 h in basic alumina (Merck Millipore, 90 active) to remove the stabilizer. The rest of the solvents were used as received. ^{1}H-NMR and ^{13}C-NMR spectra were recorded on a Varian AMX400 (400 MHz) and a Varian VXR-300 (300 MHz) at room temperature. All the spectra were referenced to the solvent line of $CDCl_3$ relative to tetramethylsilane (H, 7.26 ppm; C, 77.0 ppm). FT-IR spectra were recorded on a Nicolet Nexus spectrometer using the SMART iTR for ATR measurement (diamond).

PREPARATION OF SELF-ASSEMBLED MONOLAYERS

Care must be taken when forming SAMs from conjugated "molecular wire" compounds such as these because of the tendency for the deprotected dithiol(ates) to lie flat due to their bidentate structure and favorable π-Au interactions. Self-assembled monolayers of molecular wires on Au-on-mica were previously formed from a mixture of THF and Et_3N,[9, 19] but in the current work Au^{TS} is used, which is supported by optical adhesive and is therefore incompatible with THF. Thus, the procedure was modified and SAMs were formed by incubating the thioacetate precursors with 1x1 cm template-stripped Au surfaces (100 nm-thick) overnight in 3 mL of 50 µM solution of the respective compound in freshly distilled toluene followed by addition of 0.05 mL of 17 mM diazabicycloundec-7-ene (DBU) solution in toluene 1 h prior the measurement. The substrates were then rinsed with ethanol and let to dry for 10 min.

To minimize the chance of oxidative damage to the compounds and SAMs, sample preparation, handling and measurement with the EGaIn setup were all performed in a nitrogen flow box with a controlled O_2 level between 1-3% (some O_2 is necessary to form tips of EGaIn) and humidity

below 10%. At least 20 junctions were measured on each of at least three substrates per molecule (10 scans from 0 V → 1 V → −1 V → 0 V, steps of 0.05 V) for a total of at least 600 traces per SAM. A new EGaIn tip was prepared every 5-8 junctions and flattened by gently pushing it on a Si wafer few times according to the procedure reported by Simeone et al.[29] The details of the EGaIn setup are described elsewhere in Chapter 2.

CHARACTERIZATION OF SELF-ASSEMBLED MONOLAYERS

The **AH**, **AC**, **PCP**, and **OPE** SAMs were characterized by ellipsometry, high-resolution X-ray photoelectron spectroscopy (HRXPS), and angle-resolved near-edge X-ray absorption fine structure (NEXAFS) spectroscopy. Ellipsometric measurements were acquired in air on a V-Vase Rotating Analyzer equipped with a HS-190 monochromator acquired from J. A. Woollam Co., Inc.. The samples were measured over a range from 300 nm to 800 nm with an interval of 10 nm at 65°, 70° and 75° angle of incidence. The optical parameters for the 100 nm gold layer were obtained by measuring a freshly prepared template stripped Au surface. The thickness of the SAMs was obtained by fitting the data with a two-layer model consisting in one Au layer (with the determined optical constants) and a Cauchy layer on top described by the parameters A=1.5, B=C=0. For every molecule, at least two samples were analyzed and every sample was measured in at least three different spot. The data presented in the main text are the calculated average value. The errors were always <5 % of the mean value.

The HRXPS measurements were carried our at the synchrotron storage ring MAX II at MAX-IV facility in Lund, Sweden, using the bending magnet beamline D1011 and an experimental station equipped with a SCIENTA SES200 electron energy analyzer and a partial electron yield (PEY) detector. The NEXAFS spectroscopy measurements were performed at the HE-SGM beamline (bending magnet) of a German synchrotron radiation facility, BESSY II in Berlin. A custom-designed experimental station was used.[49] All experiments were performed at room temperature and under ultra high vacuum conditions at a base pressure of $<1.5 \times 10^{-9}$ mbar. Special care was taken to avoid X-ray damage during the spectra acquisition.[50]

The HRXP spectra were recorded in the Au $4f$, S $2p$, and C $1s$ regions; the O $1s$ region was monitored as well. The spectra acquisition was performed in normal emission geometry and at photon energies of either 350 or 580 eV. The binding energy (BE) scale of every spectrum was individually calibrated using the Au $4f_{7/2}$ emission line of alkanethiolate covered Au substrate at 84.0 eV.[51] The energy resolution was better than 70-100 meV, which is noticeably smaller than the full width at half maximum (fwhm) of the emissions measured. The spectra were fitted by symmetric

Voigt functions and either Shirley-type or linear background. To fit the S $2p_{3/2,1/2}$ doublet, we used two peaks with the same fwhm, the standard[51] spin-orbit splitting of ~ 1.18 eV (verified by fit), and a branching ratio of 2 (S$2p_{3/2}$/S$2p_{1/2}$). The fits were performed self-consistently: the same fit parameters were used for identical spectral regions.

The intensity values derived within the fitting procedure were used to calculate the effective thicknesses of the SAMs studied. They were estimated on the basis of the C $1s$/Au $4f$ intensity ratio,[52] assuming a standard exponential attenuation of the photoelectron signal[53] and using the attenuation lengths typical of densely packed SAMs[54]. The spectrometer specific constants were determined using the octadecanethiol (SC18) monolayer of well-defined thicknesses as a reference. In addition, molecular packing densities in the SAMs studied were calculated, based on the S $2p$/Au $4f$ intensity ratio, using the same assumptions as in the case of the C $1s$/Au $4f$ evaluation. Only the part of the S $2p$ signal related to the thiolate was used. The SC18 monolayer served as a reference; it has a molecular density of 4.63×10^{14} cm^{-2}, which corresponds to an area per molecule of 21.6 Å^2.[55]

The NEXAFS spectra were acquired at the C K-edge in the PEY acquisition mode with a retarding voltage of 150 V, respectively. Linear-polarized synchrotron light with a polarization factor of 91 % was used. The energy resolution was approximately 0.3 eV. The incidence angle of the primary X-ray beam was varied from 90° (E vector in surface plane) to 20° (E vector nearly parallel to surface normal) in few steps to monitor the orientational order in the SAMs. This approach is based on the dependence of the cross-section of the resonant photoexcitation process on the orientation of the electric field vector of the synchrotron light with respect to the molecular orbital of interest (so-called linear dichroism in X-ray absorption).[24] Raw NEXAFS spectra were normalized to the incident photon flux by dividing a spectrum of a clean, freshly sputtered gold sample and, subsequently, were reduced to the standard form by subtracting linear pre-edge background and normalizing to the unity edge jump (determined by a nearly horizontal plateau 40 eV to 50 eV above the respective absorption edges). The photon energy scale was referenced to the most intense π^* resonance of highly oriented pyrolytic graphite at 285.38 eV.[56]

X-RAY CRYSTAL STRUCTURES

Single crystals of compounds **PCP** and **AH** were mounted on top of a cryoloop and transferred into the cold nitrogen stream (100 K) of a Bruker-AXS D8 Venture diffractometer. Data collection and reduction was done using the Bruker software suite APEX2. The final unit cell was obtained from the xyz centroids of 9991 (**PCP**) or 9896 (**AH)** reflections after integration. A multiscan absorp-

tion correction was applied, based on the intensities of symmetry-related reflections measured at different angular settings (*SADABS*). (Bruker, [2012]; APEX2 [v2012.4-3], *SAIN*T [Version 8.18C] and *SADABS* [Version 2012/1]; Bruker AXS Inc., Madison, Wisconsin, USA.) The structures were solved by direct methods using *SHELXS*, and refinement of the structure was performed using *SHLELXL*.[57] The hydrogen atoms were generated by geometrical considerations, constrained to idealized geometries and allowed to ride on their carrier atoms with an isotropic displacement parameter related to the equivalent displacement parameter of their carrier atoms. For **AH,** refinement was complicated by disorder: one of the two independent molecules in the unit cell appears to be disordered over an inversion center. Attempts to describe the disordered part by a two-site occupancy model was not satisfactory. As a result of the disorder, the metrical parameters of this molecule are not determined with high accuracy. In addition, the central anthracene core of this molecule is planar which could be an artifact enforced by the inversion symmetry. On the other hand, inspection of the atomic displacement parameters shows that the main disorder is in the plane of the molecule which seems to suggest that the molecule indeed prefers a planar conformation. The second independent molecule is well-defined and clearly shows a bent anthracene core (dihedral angle between the two flanking C6 rings of 19.05°). Crystal data and details on data collection and refinement are presented in Supplementary Table 5.8.

J/V DATA PROCESSING AND ANALYSIS

Data were parsed in a "hands-off" manner using Scientific Python to produce histograms of J for each value of V, the associated Gaussian fits (using a least-squares fitting routine) and the conductance heatmap plots. For the heatmap plots, $G = log|\frac{dJ}{dV}|$ was computed from un-smoothed numerical derivatives from which histograms of G for each value of V were constructed. The data in the heatmap plots were interpolated from Gaussian fits to the histograms of G (using a least-squares fitting routine) to provide data for values between experimental values of V. Plots were generated using GNUPLOT 5.1. Values of V_{trans} were computed from Gaussian fits to histograms of the minimum of each plot of $\ln J/V^2$ versus V^{-1}.

The semi-log plot of the J/V data in Figure 4.1 are scaled such that the magnitude of J appears to be equal for **PCP** and **AH** and for **OPE** and **AC**. Gaussian average values $\mu_{\log}$ show the trend: **AC** > **OPE** > **AH** > **PCP**. The pairs in this trend oppose both the theoretical molecular lengths and the measured thicknesses of the SAMs; *i.e.,* **PCP** is shorter than **AH**. This violation of simple length dependence underlines the complex transmission channels and QI effects in conjugated molecules.

Table 4.2 Crystallographic data for **PCP** and **AH.**

Compound	**PCP**	**AH**
Chemical formula	$C_{36}H_{28}O_2S_2$	$C_{34}H_{24}O_2S_2$
M_r	556.70	528.65
Crystallographic System	monoclinic	monoclinic
Color, Habit	colorless, block	yellow, block
size (mm)	0.48x0.14x0.14	0.24x0.22x0.07
Space Group	P2(1)/n	P2(1)/n
a (Å)	6.9148(3)	18.345(3)
b (Å)	10.7585(5)	8.1486(11)
c (Å)	18.4018(10)	28.253(4)
β (deg)	90.9049(16)	107.351(4)
V (Å^3)	6.9148(3)	18.345(3)
Z	2	8
a (Å)	6.9148(3)	18.345(3)
ρ_{calc} (g/cm^3)	1.351	1.307
μ (Mo K$^\alpha$, (cm^{-1})	0.228	0.228
F(000)	584	1656
T (K)	100(2)	100(2)
θ range (deg)	3.54 - 27.10	2.85 - 26.37
Data collected (h,k,l)	-8:7, -13:13, -23:23	-22:22, -10:10, -35:35
no. of reflections collected	23998	64871
no. of independent reflections	3017	8227
observed reflections	2753 ($F_o \geq 2\sigma(F_o)$)	5775 ($F_o \geq 2\sigma(F_o)$)
R(F) (%)	3.49	8.99
wR(F^2) (%)	9.66	25.11
GooF	1.049	1.027
Weighting a,b	7 0.0537, 0.8240	0.0986, 11.1329
Parameters refined	182	517
restraints	0	0
Residual density min, Max	-0.241, 0.536	-1.107, 1.046

Table 4.3 V_{trans} values and standard deviations and DFT frontier orbital energies for Au^{TS}/SAM//EGaIn junctions

SAM	V^{+}_{trans} [V]	V^{-}_{trans} [V]	HOPS[a] [eV]
AC	0.71 ± 0.08	-0.82 ± 0.10	−5.5713
AH	0.29 ± 0.08	-0.26 ± 0.07	−5.5452
			−5.5599[b]
OPE	0.78 ± 0.05	-0.89 ± 0.05	−5.5941
PCP	0.63 ± 0.16	-0.86 ± 0.07	−5.6711
			−5.5885[b]

[a]Highest occupied π state.

[b]Crystal structure.

CP-AFM MEASUREMENTS

CP-AFM *I-V* measurements were performed on a Bruker AFM Multimode MMAFM-2 equipped with a Peak Force TUNA Application Module (Bruker). The SAMs grown on Au-on-mica grown as previously reported, were contacted with an Au-coated silicon nitride tip with a nominal radius of 30 nm (NPG-10, Bruker, resonance frequency: 65 kHz, k: 0.35 N/M) in non-scanning mode with a force of 1.8 nN. The sample was grounded using silver paste to connect it to the grounded sample holder. The AFM tip was biased from -1 V to 1 V and from 1 V to -1 V to record the *I-V* curve (512 points per trace were taken): a max of 50 trace/re-trace cycles per junction were performed (with a min of 20). After every junction, the tip was retracted, moved to a different spot, and engaged again for a total of 40 junction per sample analyzed. Between different samples the tip was cleaned with oxygen plasma. The data were analyzed with the same software used for EGaIn using the current *I* instead of the current density. The obtained Log$I(V)$ plots are shown in Figure 4.6. For **AH** and **PCP** the detection limit of the instrument were reached for the lower biases.

CALCULATIONS

All DFT calculations were performed using ORCA 3.0.3.[58] Structures were first minimized using BP/Def2-TZV(2d) and then point energies were calculated using B3LYP/Def2-TZV(2d/sp). Single-molecule junctions were constructed by attaching the minimized or X-ray crystal structures to 12-atom Au(111) clusters via the terminal sulfur atoms at hexagonal close-pack hollow sites at a distance of 1.75 Å from the center of the hollow site. Transport calculations were performed with ARTAIOS BETA 020914 using B3LYP/G DUNNING-DZP and LANL2/LANLDZ ECPs according to pub-

lished methods.[59] Frequencies and thermochemistry were calculated using B3LYP/6-311+G* at 298K. According to frequency calculations (see Table 4.4), ΔG going from the planar to the bent geometry of **AH** is accessible at room temperature (~ −3.5 kcal/mol). This result suggests that **AH** rapidly interconverts between the bent and planar forms under the experimental conditions. In solution, this observation is confirmed by the ^{1}H-NMR spectrum of **AH** in $CDCl_3$ at 400 MHz in which the multiplicity of the signals in aromatic region, together with the singlet at 3.96 ppm for the protons in the 9 and 10 positions (the methylene bridges) are indicative of a symmetric conformation of **AH** with an inversion center. As the completely symmetric conformer of **AH** (planar) is higher in energy than the less symmetric conformer (bent), this spectrum indicates that the two conformers interconvert faster than the NMR timescale. If **AH** were trapped in the lowest-energy conformer predicted by RI-MP2/DFT, **AH-planar**, the lack of an inversion center would cause the protons on the different faces to split, leading to a doublet (or multiplet) at ~ 3.96 ppm and would likely lead to more complex splitting in the aromatics from the proximity of the periphery phenyl protons.

Table 4.4 Summary of thermochemistry calculations.

Conformer	**AH Bent**	**AH Planar**
Gibbs Free Enthalpy (eH)	−1154.30718410	−1154.31137303
Electronic Energy (eH)	−1154.65970157	−1154.66209810
Zero Point Energy (eH)	0.39592210	0.39676337
Entropy (eH)	0.06230832	0.06631054
Energy Correction (eH)	0.00283112	0.00283112
Enthalpy Correction (eH)	0.00094373	0.00094373
Total Gibbs Free Enthalpy Change		
ΔH (kcal/mol)	2.62856614	
Total Energy and Entropy Change		
Δ Electronic Energy (kcal/mol)	1.50382976	
Δ Zero Point Energy (kcal/mol)	-0.52789945	
Δ Energy Correction (kcal/mol)	0	
Δ Enthalpy Correction (kcal/mol)	0	
$-T\Delta S$ @298K (kcal/mol)	2.51140506	
ΔG (kcal/mol)	3.49	

Table 4.5 DFT gas-phase molecular properties.

Compound	Length[a] (Å)	HOMO (eV)	LUMO (eV)
AH-planar	23.3	−5.91	−1.80
AH	21.9	−5.94	−1.66
AH-crystal	23.2	−5.95	−1.56
AC	23.1	−5.45	−2.50
PCP	18.3	−5.77	−1.86
PCP-crystal	18.6	−5.75	−1.70
OPE3	18.9	−5.75	−2.13
SC18	22.7	−6.51	−0.18

[a]Without thiols

[a]Calculated using B3LYP/6-311+G*.

SYNTHESIS OF NEW COMPOUNDS

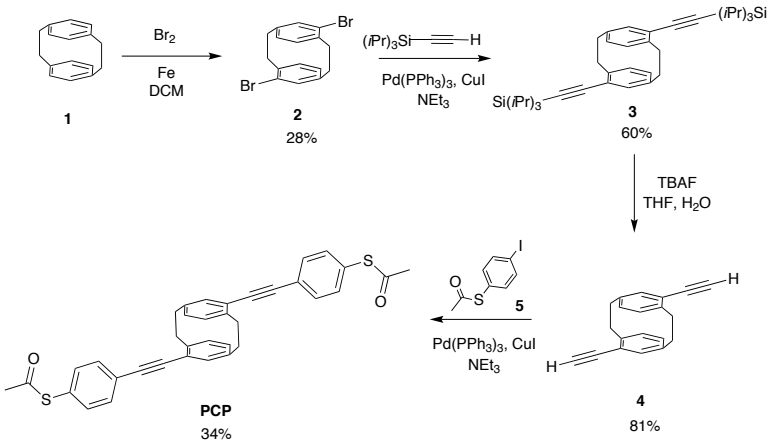

Figure 4.12 Synthesis of **PCP** molecular wire.

***pseudo-p*-dibromo-*p*-2,2-cyclophane, 2**

The synthesis of **2** was based on a literature method.[60] Under inert atmosphere (N_2), 11,552 g of **1** (55.2 mmol) were dissolved in 80 mL of CH_2Cl_2. 160 mg of Fe (2.87 mmol) were added and the reaction mixture was refluxed for 30 minutes. A solution of Br_2 in CH_2Cl_2 was prepared by mixing 7 mL of Br_2 and 40 mL of CH_2Cl_2. The first half was added over a period of 30 minutes, then the

reaction mixture was brought to reflux again and the remaining half was added over a period of 12 hours. The reaction was left at reflux for 18 hours in total. The reaction mixture was cooled down and the precipitate filtered off. The solid residue was recrystallized from $CHCl_3$ to yield 5.86 g of desired product as a white solid (28% yield). ^{1}H-NMR (400 MHz, $CDCl_3$) δ 7.14(dd, *J*=7.9, 1.7 Hz, 2H), 6.51(d, *J*=1.4 Hz, 2H), 6.44(d, *J*=7.8 Hz, 2H), 3.49(ddd, *J*=13.1, 10.4, 2.3 Hz, 2H), 3.16(ddd, *J*=12.6, 10.3, 4.9 Hz, 2H), 2.94(m, 2H), 2.85(ddd, *J*=13.2, 10.8, 4.9 Hz, 2H). IR (ATR, cm^{-1}): 2935, 2850, 1584, 1536, 1473, 1390, 1186, 1031.

***pseudo*-*p*-bis((tri-tert-butylsilyl)ethynyl)-*p*-2,2-cyclophane, 3**

In a flask under inert atmosphere (N_2), 1,00 g of **2** (2.7 mmol), 1,40 mL of (triisopropylsilyl)acetilene (6.4 mmol), 0.172 g of $Pd(PPh_3)_3$ (0.15 mmol) and 0.030 g of CuI (0.15 mmol) were added to 20 mL of NEt_3. The reaction mixture was left at reflux for 22h. The reactor was then cooled and the solvent removed under vacuum. The solid residue was stirred in 100 mL of hot n-hexane and filtered. The solvent was evaporated *in vacuo* and the product purified by recrystallization from n-hexane to obtain 715 mg of white crystals (60% yield). ^{1}H-NMR (400 MHz, $CDCl_3$) δ 7.03(dd, *J*=7.9, 1.9 Hz, 2H), 6.52(d, *J*=1.9 Hz, 2H), 6.42(d, *J*=7.8 Hz, 2H), 3.63(ddd, *J*=13.0, 10.5, 2.8 Hz, 2H), 3.17(ddd, *J*=12.8, 10.5, 4.6 Hz, 2H), 2.98(ddd, *J*=12.8, 11.7, 2.8 Hz, 2H), 2.85(ddd, *J*=12.8, 10.7, 4.6 Hz, 2H), 1.19 (s, 42H).

***pseudo*-*p*-diethynyl-*p*-2,2-cyclophane, 4**

341 mg of **3** (0.6 mmol) were dissolved in 5 mL of THF. 1.8 mL of a TBAF solution 1M in THF (1.8 mmol) were added and the solution left stirring for 20 h. The solvent was then evaporated *in vacuo* and the residue dissolved in 20 mL of CH_2Cl_2 and filtered over silica gel. The organic phase was then washed with water (3x100 mL) and brine (1x150 mL). The solvent was removed under vacuum and the product collected as a white powder, 124 mg (81% yield). ^{1}H-NMR (400 MHz, $CDCl_3$) δ 7.01(dd, *J*=8.0, 2.0 Hz, 2H), 6.56(d, *J*=1.9 Hz, 2H), 6.45(d, *J*=7.9 Hz, 2H), 3.58(ddd, *J*=13.2, 10.6, 3.0 Hz, 2H), 3.27(s, 2H), 3.19(ddd, *J*=12.7, 10.5, 4.4 Hz, 2H), 2.97(m, 2H), 2.87(ddd, *J*=13.0, 10.7, 4.5 Hz, 2H). IR (ATR, cm^{-1}): 3274, 2928, 2866, 1480, 1432, 1404, 1243, 1047, 897.

(4-iodophenyl)ethanethioate, 5

In a flask under inert atmosphere (N_2), 3.073 g of pipsyl chloride (10.2 mmol) and 2.8 mL of *N,N*-dimethylacetamide (2.63 g, 30,2 mmol) were dissolved in 80 mL of degassed 1,2-dichloroethane. In a different flask under inert atmosphere (N_2), 2.36 g of Zn (36.3 mmol) and 4.3 mL of Cl_2SiMe_2

(4.58 g, 53.3 mmol) were stirred in 80 mL of degassed 1,2-dichloroethane at 60 °C for 30 minutes, then the first solution was added. The reaction mixture was heated to 75 °C and left for 2 h. Absence of pipsyl chloride was checked via TLC (Rf ~ 0.4 in hexane). The solution was then cooled to 45 °C and 0.94 mL of acetyl chloride (1.038 g, 13.2 mmol) were added. The reactor was left at 50 °C for 30 minutes. The reaction mixture was filtered still hot and the filtrate poured in 300 mL of water. The aqueous phase was extracted with dichloromethane (3x150 mL). The organic solvent was evaporated *in vacuo* and the product purified by sublimation (70 °C, $5 \cdot 10^{-4}$ mbar) to obtain 2.420 g of white crystals (83% yield). ^{1}H-NMR (400 MHz, $CDCl_3$) δ 7.74(m, 2H), 7.13(m, 2H), 2.42(s, 3H). IR (ATR, cm^{-1}): 1691, 1464, 1381, 1353, 1119, 1087, 1004.

***pseudo-p*-bis((4-(acetylthio)phenyl)ethynyl)-*p*-2,2-cyclophane, PCP**

In a flask under inert atmosphere (N_2), 82 mg of **4** (0.32 mmol), 342 mg of **5** (1.32 mmol), 23 mg of $Pd(PPh_3)_3$ (0.02 mmol) and 3.8 mg of CuI (0.02 mmol) were stirred in 8 mL of NEt_3. The system was heated to 70 °C and left for 18 h. The reaction mixture was poured in 100 mL of water which was carefully acidified with HCl 6 M. The aqueous layer was extracted with dichloromethane (3x20 mL). The product was recrystallized twice from dichloromethane to obtain 61 mg of a slightly-yellow powder (34% yield). ^{1}H-NMR (400 MHz, $CDCl_3$) δ 7.61(m, 4H), 7.44(m, 4H), 7.01(dd, *J*=7.8, 1.9 Hz, 2H), 6.60(d, *J*=1.9 Hz, 2H), 6.51(d, *J*=7.9 Hz, 2H), 3.66(ddd, *J*=13.2, 10.4, 2.9 Hz, 2H), 3.22(ddd, *J*=13.1, 10.3, 4.7 Hz, 2H), 3.06(ddd, *J*=12.9, 11.7, 2.9 Hz, 2H), 2.94(ddd, *J*=12.4, 10.7, 4.7 Hz, 2H), 2.46(s, 6H). IR (ATR, cm^{-1}): 2935, 1698, 1487, 1409, 1396, 1118, 1089, 948.

BIBLIOGRAPHY

[1] Nerngchamnong, N.; Yuan, L.; Qi, D.-C.; Li, J.; Thompson, D.; Nijhuis, C. A. *Nature Nanotech.* **2013**, *8*, 113–8.

[2] Ferri, V.; Elbing, M.; Pace, G.; Dickey, M. D.; Zharnikov, M.; Samorì, P.; Mayor, M.; Rampi, M. A. *Angew. Chem. Int. Ed.* **2008**, *47*, 3407–3409.

[3] Kronemeijer, A. J.; Akkerman, H. B.; Kudernac, T.; van Wees, B. J.; Feringa, B. L.; Blom, P. W. M.; de Boer, B. *Adv. Mater.* **2008**, *20*, 1467–1473.

[4] Seo, S.; Min, M.; Lee, S. M.; Lee, H. *Nature Comm.* **2013**, *4*, 1920.

[5] Snider, R. M.; Strycharz-Glaven, S. M.; Tsoi, S. D.; Erickson, J. S.; Tender, L. M. *Proc. Natl. Acad. Sci. USA* **2012**, *109*, 15467–15472.

[6] Love, J.; Estroff, L.; Kriebel, J. K.; Nuzzo, R.; Whitesides, G. M. *Chem. Rev.* **2005**, *105*, 1103–1170.

[7] Zhang, Y.; Zhao, Z.; Fracasso, D.; Chiechi, R. C. *Is. J. Chem.* **2014**, *54*, 513–533.

[8] Solomon, G. In *Handbook of Single-Molecule Electronics*; Frederiksen, T., Ed.; Pan Stanford Publishing, 2015; Chapter First-principles simulations of electron transport in atomic-scale systems, pp 79–116.

[9] Fracasso, D.; Valkenier, H.; Hummelen, J. C.; Solomon, G. C.; Chiechi, R. *J. Am. Chem. Soc.* **2011**, *133*, 9556–9563.

[10] Perrin, M. L.; Frisenda, R.; Koole, M.; Seldenthuis, J. S.; Celis, G. A.; Valkenier, H.; Hummelen, J. C.; Renaud, N.; Grozema, F. C.; Thijssen, J. M.; Dulic, D.; van der ZantHerre S. J., *Nature Nanotech.* **2014**, *9*, 830–834.

[11] Solomon, G. C.; Herrmann, C.; Vura-Weis, J.; Wasielewski, M. R.; Ratner, M. A. *J. Am. Chem. Soc.* **2010**, *132*, 7887–7889.

[12] Xiang, D.; Jeong, H.; Lee, T.; Mayer, D. *Adv. Mater.* **2013**, *25*, 4845–4867.

[13] Frisenda, R.; Janssen, V. A. E. C.; Grozema, F. C.; van der Zant, H. S. J.; Renaud, N. *Nat. Chem.* **2016**, *advance online publication.*

[14] Weiss, E. A.; Chiechi, R. C.; Kaufman, G. K.; Kriebel, J. K.; Li, Z.; Duati, M.; Rampi, M. A.; Whitesides, G. M. *J. Am. Chem. Soc.* **2007**, *129*, 4336–4349.

[15] Lykkebo, J.; Gagliardi, A.; Pecchia, A.; Solomon, G. C. *J. Phys. Chem.* **2014**, *141*, –.

[16] Rissner, F.; Egger, D. A.; Natan, A.; Körzdörfer, T.; Kümmel, S.; Kronik, L.; Zojer, E. *J. Am. Chem. Soc.* **2011**, *133*, 18634–18645.

[17] Chiechi, R. C.; Weiss, E. A.; Dickey, M. D.; Whitesides, G. M. *Angew. Chem. Int. Ed.* **2008**, *120*, 148–150.

[18] Valkenier, H.; Guédon, C. M.; Markussen, T.; Thygesen, K. S.; van der Molen, S. J.; Hummelen, J. C. *Phys. Chem. Chem. Phys.* **2014**, *16*, 653–662.

[19] Valkenier, H.; Huisman, E. H.; van Hal, P. A.; de Leeuw, D. M.; Chiechi, R. C.; Hummelen, J. C. *J. Am. Chem. Soc.* **2011**, *133*, 4930–4939.

[20] Tai, Y.; Shaporenko, A.; Rong, H.-T.; Buck, M.; Eck, W.; Grunze, M.; Zharnikov, M. *J. Phys. Chem. B* **2004**, *108*, 16806–16810.

[21] Yuan, L.; Jiang, L.; Thompson, D.; Nijhuis, C. A. *J. Am. Chem. Soc.* **2014**, *136*, 6554–6557.

[22] Chen, J.; Wang, Z.; Oyola-Reynoso, S.; Gathiaka, S. M.; Thuo, M. *Langmuir* **2015**, *31*, 7047–7054.

[23] Kong, G. D.; Kim, M.; Cho, S. J.; Yoon, H. J. *Angewandte Chemie International Edition* **2016**, *55*, 10307–10311.

[24] Stohr, J. *NEXAFS Spectroscopy*; Springer-Verlag Berlin Heidelberg, 1992.

[25] Hamoudi, H.; Kao, P.; Nefedov, A.; Allara, D. L.; Zharnikov, M. *Beilstein journal of nanotechnology* **2012**, *3*, 12–24.

[26] Shaporenko, A.; Adlkofer, K.; Johansson, L.; Tanaka, M. *Langmuir* **2003**,

[27] Schneebeli, S. T.; Kamenetska, M.; Cheng, Z.; Skouta, R.; Friesner, R. A.; Venkataraman, L.; Breslow, R. *J. Am. Chem. Soc.* **2011**, *133*, 2136–2139.

[28] Van Dyck, C.; Ratner, M. A. *Nano Lett.* **2015**, *15*, 1577–1584.

[29] Simeone, F. C.; Yoon, H. J.; Thuo, M. M.; Barber, J. R.; Smith, B.; Whitesides, G. M. *J. Am. Chem. Soc.* **2013**, *135*, 18131–18144.

[30] Datta, S. *Quantum Transport: Atom to Transistor*; Cambridge University Press, 2005.

[31] Heimel, G.; Romaner, L.; Zojer, E.; Bredas, J.-L. *Acc. Chem. Res.* **2008**, *41*, 721–729, PMID: 18507404.

[32] VerwÃ¼ster, E.; Hofmann, O. T.; Egger, D. A.; Zojer, E. *The Journal of Physical Chemistry C* **2015**, *119*, 7817–7825.

[33] Heimel, G.; Romaner, L.; Brédas, J.-L.; Zojer, E. *Phys. Rev. Lett.* **2006**, *96*, 196806.

[34] Egger, D. A.; Zojer, E. *The Journal of Physical Chemistry Letters* **2013**, *4*, 3521–3526.

[35] Kovalchuk, A.; Abu-Husein, T.; Fracasso, D.; Egger, D. A.; Zojer, E.; Zharnikov, M.; Terfort, A.; Chiechi, R. C. *Chem. Sci.* **2016**, *7*, 781–787.

[36] Alloway, D. M.; Hofmann, M.; Smith, D. L.; Gruhn, N. E.; Graham, A. L.; Colorado, R.; Wysocki, V. H.; Lee, T. R.; Lee, P. A.; Armstrong, N. R. *J. Phys. Chem. B* **2003**, *107*, 11690–11699.

[37] Beebe, J. M.; Kim, B.; Frisbie, C. D.; Kushmerick, J. G. *ACS Nano* **2008**, *2*, 827–832.

[38] Dwight S Seferos,; Amy Szuchmacher Blum,; Kushmerick, J. G.; Guillermo C Bazan, *J. Am. Chem. Soc.* **2006**, *128*.

[39] Seferos, D. S.; Trammell, S. A.; Bazan, G. C.; Kushmerick, J. G. *Proc. Natl. Acad. Sci. USA* **2005**, *102*, 8821–8825.

[40] Chen, L.; Wang, Y.-H.; He, B.; Nie, H.; Hu, R.; Huang, F.; Qin, A.; Zhou, X.-S.; Zhao, Z.; Tang, B. Z. *Angew. Chem. Int. Ed.* **2015**, *54*, 4231–4235.

[41] Guédon, C. M.; Valkenier, H.; Markussen, T.; Thygesen, K. S.; Hummelen, J. C.; van der Molen, S. J. *Nature Nanotech.* **2012**, *7*, 305–309.

[42] Garrigues, A. R.; Yuan, L.; Wang, L.; Mucciolo, E. R.; Thompon, D.; del Barco, E.; Nijhuis, C. A. *Sci. Rep.* **2016**, *6*, 26517.

[43] Rabache, V.; Chaste, J.; Petit, P.; Della Rocca, M. L.; Martin, P.; Lacroix, J.-C.; McCreery, R. L.; Lafarge, P. *Journal of the American Chemical Society* **2013**, *135*, 10218–10221.

[44] van Hal, P. A.; Smits, E. C. P.; Geuns, T. C. T.; Akkerman, H. B.; De Brito, B. C.; Perissinotto, S.; Lanzani, G.; Kronemeijer, A. J.; Geskin, V.; Cornil, J.; Blom, P. W. M.; de Boer, B.; de Leeuw, D. M. *Nature Nanotech.* **2008**, *3*, 749–754.

[45] Nijhuis, C. A.; Reus, W. F.; Siegel, A. C.; Whitesides, G. M. *J. Am. Chem. Soc.* **2011**, *133*, 15397–15411.

[46] Pourhossein, P.; Chiechi, R. C. *ACS Nano* **2012**, *6*, 5566–5573.

[47] Li, T. et al. *Adv. Mater.* **2013**, *25*, 4164–4170.

[48] Wan, A.; Jiang, L.; Sangeeth, C. S. S.; Nijhuis, C. A. *Adv. Funct. Mater.* **2014**, *24*, 4442–4456.

[49] Nefedov, A.; Wöll, C. *Surface Science Techniques* **2013**,

[50] Zharnikov, M. *J. Electron Spectrosc. Relat. Phenom.* **2010**, *178–179*, 380–393.

[51] Briggs, D. *Handbook of X-Ray Photoelectron Spectroscopy C. D. Wanger, W. M. Riggs, L. E. Davis, J. F. Moulder and G. E.Muilenberg Perkin-Elmer Corp., Physical Electronics Division, Eden Prairie, Minnesota, USA, 1979. 190 Pp. 195*; Heyden & Son Ltd., 1981; Vol. 3; pp v–v.

[52] Thome, J.; Himmelhaus, M.; Zharnikov, M.; Grunze, M. *Langmuir* **1998**, *14*, 7435–7449.

[53] Ratner, B. D.; Castner, D. G. *Surface Analysis - The Principal Techniques*; John Wiley & Sons, Ltd, 1997; pp 47–112.

[54] Lamont, C. L. A.; Wilkes, J. *Langmuir* **1999**, *15*, 2037–2042.

[55] Schreiber, F. *Prog. Surf. Sci.* **2000**, *65*, 151–257.

[56] Batson, P. E. *Phys. Rev. B* **1993**, *48*, 2608–2610.

[57] Sheldrick, G. M. *Acta Crystallographica Section A* **2008**, *64*, 112–122.

[58] Neese, F. *Wiley Interdiscip. Rev.: Comput. Mol. Sci.* **2012**, *2*, 73–78.

[59] Herrmann, C.; Solomon, G. C.; Subotnik, J. E.; Mujica, V.; Ratner, M. A. *J. Chem. Phys.* **2010**, *132*, 024103.

[60] Reich, H. J.; Cram, D. J. *J. Am. Chem. Soc.* **1969**, *91*, 3527–3533.

5

PROPERTIES OF MOLECULAR JUNCTIONS COMPRISING ANTHRAQUINOID COMPOUNDS

In molecular tunneling junctions, cross-conjugation tends to give rise to destructive quantum interference effects that can be tuned by changing the electronic properties of the molecules. Here we present a systematic study of junctions comprising a series of compounds characterized by an identical cross-conjugated anthraquinoid skeleton but bearing different substituents in the 9 and 10. This affects the energy and localization of their frontier orbitals. We compared experimental results across three different experimental platforms in both single-molecule and large-area junctions, and combined the results with theoretical modelsto eliminate from platform-specific effects.

I would like to thank S. Soni and Prof. R.C. Chiechi for the help in the computation; and E. Sauter and Prof. M. Zharnikov for the help in the characterization of the monolayers; X. Qiu and Dr. Y. Ai performed the CP-AFM and the STM-BJ experiments respectively.

5.1. INTRODUCTION

The field of molecular electronics aims to investigate the charge transport through single-molecules and molecular ensembles with the goal of translating their electronic and steric properties into functional devices that can interface with modern integrated circuits. In this sense, molecules are particularly interesting thanks to their intrinsic quantomechanical nature that can give rise to unique phenomena with no straightforward analogs in semiconductor-electronics.[1, 2] An example we already discussed in the previous chapter is quantum interference (QI), a collection of phenomena related to Fermions whose wave functions can interfere with themselves.[3–5] In the case of molecular tunneling junctions, destructive QI can lower the transmission probability across the molecule, which lowers the conductance between the electrodes by orders of magnitude without altering the tunneling distance, paving the path for hyper-resistive molecular insulators and thermoelectric materials.[6, 7] Systems in which QI can be toggled on and off by external stimuli are of paramount interest to design devices that can molecule-scale inputs to macroscopic outputs, such as molecular switches, memories, and transistors.[8] For these reasons, the effects of QI on molecular charge transport has been the object of both theoretical and experimental studies across multiple platforms.

In π-conjugated molecules, QI effects are often observed in molecules with cross-conjugation,[9–12] meta-substitution,[13, 14] or, as we previously showed, peculiar spatial arrangements.[15, 16] To be able to translate these functionalities in actual devices, it is not only necessary to understand the relations between QI and charge transport on a fundamental level, but also to translate this knowledge to design principles that can be used to achieve a better structure-function control in device-relevant contexts. The realization of the latter is still largely lacking. One reason is that phenomenological observations are often reported for a specific molecule in an specific experimental context and platform to elucidate a fundamental relationship or property rather than function. To exploit QI phenomena as functional control over conductance, the energy of the interference feature has to be close to the Fermi level (E_f) inside the assembled junction. The most basic level of control is using functional groups with different electron-withdrawing/donating properties to affect the electronic levels of the mo-

lecule and move the energy of the feature, but without the guidance of empirical relationships, the position of the feature can be far from optimal.[14, 17–19]

Molecules containing an anthraquinone core are often cited as examples when discussing the relation between cross-conjugation and QI in tunneling junctions,[11, 20–24] but the effect of the conjugation pattern itself and the role of the electronegativity of the oxygen atoms in such structures have only been marginally addressed in the literature.[25] Molecular wire-like compounds incorporating anthraquinone present advantages such as the chemical inertness, a straightforward preparation and well characterized redox properties. Yet, in a scenario where the electronic properties of the wires are of paramount importance for the investigation of QI effects in a junction, the quinoid functionality offers comparatively little tunability as a cross-conjugated moiety. Nonetheless, it is a readily-accessible synthon for systematic investigations into QI in π-conjugated molecules.

In this chapter, we discuss a series of molecular wires with identical molecular skeletons and binding groups to the parent anthraquinone wire (**AQ**),[11] but with different CX_2 groups in place of the oxygen in the carbonyl, thus changing energies and localization of the molecular orbitals (MO), molecular geometry, and the distribution of electron density, without altering the cross-conjugated core. These compounds are shown in Figure 5.1. We investigated their tunneling charge-transport properties both *in silico* and in three different experimental platforms, namely single-molecule scanning tunneling microscope break-junctions (STM-BJs) and large-area junctions comprising self-assembled monolayers (SAMs) using conducting probe-AFM (CP-AFM) and liquid eutectic Ga-In (EGaIn) top contacts.[26] We also discuss the accessibility of molecular modifications synthetically, including some that have been studied theoretically, but that are unstable or otherwise experimentally inaccessible.

With this approach we were able to: (I) gain a better understanding of the nature of carbonyls as cross-conjugating units; (II) investigate, both theoretically and experimentally, the effect of side CX_2 groups on the position of the QI resonance with respect to **AQ**; (III) observe how the degree of orbital overlap vis-a-vis the torsion angle of the cross-conjugated core (caused by steric bulk) affects QI; (IV) explore the parameter space of

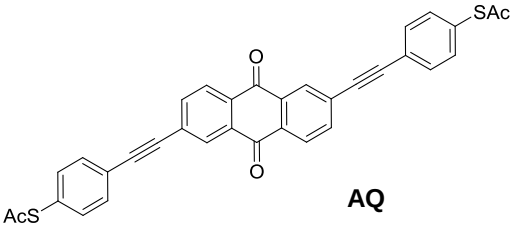

AQ

All-Carbon:

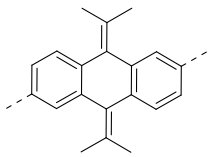

AMe

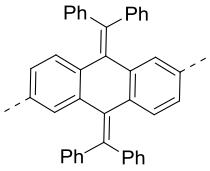

APh

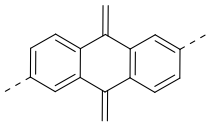

A(CH$_2$)

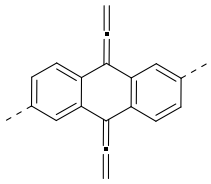

A(All)

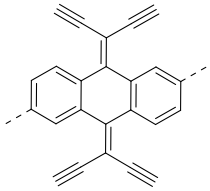

A(Alk)

With Heteroatoms:

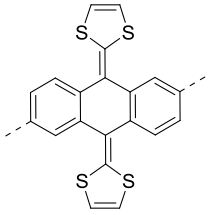

ATTF

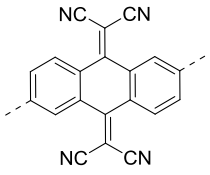

TCNAQ

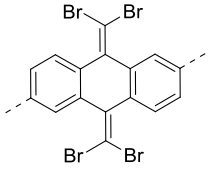

ABr

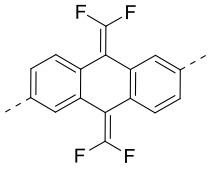

AF

Figure 5.1 The molecules investigated in this study. The cores of the all-carbon and heteroatom-containing molecules are attached to the same phenylacetylene arms as **AQ** at the positions indicated with dashed lines.

chemical modifications that are accessible starting from the anthraquinone core of the wires and their stability and (V) isolate many platform-specific variables such as electrode composition and collective effects.

5.2. DESIGN AND TRANSPORT CALCULATIONS

Figure 5.1 shows a series of molecular wires characterized by an anthraquinoid core but bearing different functionalities in the 9 and 10 positions. Via a carbon-carbon double bond in place of the carbonyl group, it is possible to investigate the effect of the quinone moiety on tunneling transport compared to compounds that have the same conjugation pattern but that are not quinones (*i.e.*, they are quinoids). Our focus is on compounds that have been proposed and studied theoretically, but that have yet to be synthesized and studied experimentally, such as **A(CH$_2$)** and **TCNAQ**.[20] Others have been reported, but were investigated for narrowly for very specific phenomena like the redox properties of **ATTF**.[27] We also include in the series molecules that are structurally/electronically similar, for example substituting Br for CN, to investigate the influence of small variations in the molecular identity on tunneling charge-transport. The presence of exocyclic sp^2 carbons can allow the manipulation of the electronic properties of the molecule synthetically over a wide range of functionalities. The insertion of side-groups with different electron-donating/withdrawing and steric properties can affect both the energy landscape of the molecule and the geometry of the core. The effect of the different substitutions on the frontier orbitals of the molecules, which dominate tunneling charge-transport, together with the bending of the anthraquinoid core are summarized in Table 5.1. The synthesis of some of compounds in Fig. 5.1 may have been attempted but, as we discuss later, were impossible or led to unstable products, which we believe is important to report.

The energies of the frontier orbitals for the all-carbon derivatives **A(CH$_2$)**, **AMe**, **APh**, and **A(All)**, are similar [−5.5(1) eV and −1.9(2) eV, respectively] showing that the effect of these substituents on the electronics of the core is comparable; however, there are clear differences between these compounds and **AQ**, whose LUMO and HOMO are more than 1 eV and 0.5 eV lower in energy, respectively. The smaller frontier orbital gap (E_g)

Table 5.1 Calculated HOMO, LUMO and frontier orbital gaps and angles for the wires proposed in Figure 5.1. Numbers in parenthesis are from X-Ray crystal structures.

	AQ	**AMe**	**APh**	**A(CH_2)**	**A(All)**	**A(Alk)**	**ABr**	**ATTF**	**TCNAQ**	**AF**
LUMO (eV)	−3.24	−1.72	−1.87	−2.05	−1.92	−2.79	−2.35	−1.91	−3.99	−2.21
HOMO (eV)	−5.98	−5.44	−5.48	−5.62	−5.44	−5.60	−5.80	−4.86	−6.19	−5.77
Band gap (eV)	2.74	3.72	3.61	3.56	3.52	2.80	3.45	2.94	2.20	3.56
ϕ (degree, °)	0	47	47 (45)	27	0	38	47 (44)	36	36	31

for **A(CH_2)** and **A(All)** compared to **AMe** and **APh** correlate with the degree of planarity of the molecule, *i.e.*, a higher degree of conjugation. Interestingly, **A(Alk)** is an outlier in the hydrocarbon series: its LUMO is localized on the core, does not span the whole molecule between the electrodes (Figure S18) and has a relatively low energy (only 0.5 eV above that of **AQ**), demonstrating the surprising electron-withdrawing properties of the ethynyl moieties.

When heteroatoms are introduced, the effects on the orbital energies are more dramatic, which is particularly obvious for compounds bearing extended tetrathiafulvalene or tetracyanoanthraquinodimethane cores (**ATTF** and **TCNAQ** respectively).[27] These cores are known for their redox properties, which make the former a good electron donor and the latter a good electron acceptor. Indeed, the desirable properties of these cores are preserved in the wires: **ATTF** is characterized by the highest-lying HOMO in the series (1.1 eV higher than **AQ**), while **TCNAQ** exhibits the lowest-lying LUMO (0.8 eV lower than **AQ**). The functionalization of the anthraquinodimethane core with four halogen substituents, as in the case of **ABr** and **AF**, lowers the energy of both frontier orbitals but not as effectively as the aforementioned compounds.

Following a simple two-dimensional tight-binding model — as done previously for **PCP** and **AH** (Chapter 4) —, all the cross-conjugated compounds are predicted to show destructive QI as a result of the bond alternation.[5, 20, 28] In such approach, the molecular skeleton is represented by a network where every atom is considered as a single node bound to its nearest neighbors and to the leads: destructive QI translates in a sharp and narrow dip in the transmission probability vs. energy of the tunnelling electrons plot, which should translate in a lower tunnelling rate for the junction.

In this simplest scenario, discussed to consider the effects arising from the molecu-

lar skeleton, the identity of every atom and the bending of the core are neglected. This means that, in such model, no distinction is made between molecules like **AQ** and **A(CH$_2$)** or **TCNAQ** and **A(Alk)**, which will be defined by the same 2D nodes. More refined 2D-methods can account for the electronic effects,[14] but this is out of the scope of the discussion.

The results for this transport model, obtained using the GOLLUM sotfware package, are shown in Figure 5.2. Although different molecular skeletons affect the shape of the dip, the latter is always present except in the cases of **AC** (which is linearly conjugated) and **A(All)**. The reason why the latter behaves like **AC** - for magnitude and shape - has to do with an artifact of the model just introduced: when only the connection between the atoms are considered, no distinction can be made between **A(All)** and a fully conjugated anthracene-core wire with two ethynyl substituents in position 9 and 10; the software is evidently more prone on picking on the second one. With some chemical insight one could decide not to account for the terminal atom of the allene moiety, trivially reducing this case to that of **A(CH$_2$)** (and **AQ**), but even with this approach we are making a drastic approximation by treating in the same way the sp^2 carbon of the methylene in **A(CH$_2$)** and the the sp carbon in the middle of the allene group, while at the same time disregarding the terminal carbon which also has available p-orbitals. These observations show that the tight-binding model, despite being very simple and elegant, is not useful to describe this specific case.

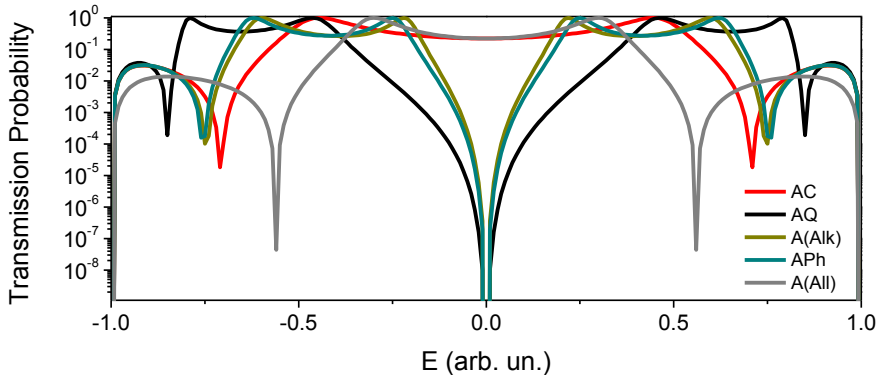

Figure 5.2 Transmission probability vs. energy of tunnelling electron of 2D-nodes grids corresponding to the molecular skeleton of the anthraquinoid series.

The presence of pendant groups bearing different substituents changes the electronics of the molecule and can affect the position and the shape of the QI feature with respect to the Fermi energy (E_f) inside the junction, thereby affecting the measured conductance differently. This phenomena has been explored theoretically and experimentally in the case of meta-substituted benzene and biphenyl in single-molecule junctions, but not in large-area junctions.[14, 18, 19, 29] Moreover, the torsional angle introduced in the core by the bulky pendant groups might also affect the QI features by means of through-space interactions, which are expected to differ in single-molecule junctions and in monolayers, in which molecules tend to planarize.[16]

To gain a better understanding of the overall effect of the substituents on the charge transport across the molecule, we computed the transmission probability as a function of energy for various molecules as shown in Figure 5.1 using their minimized DFT geometry between two electrodes. The results are proposed in Figure 5.3.

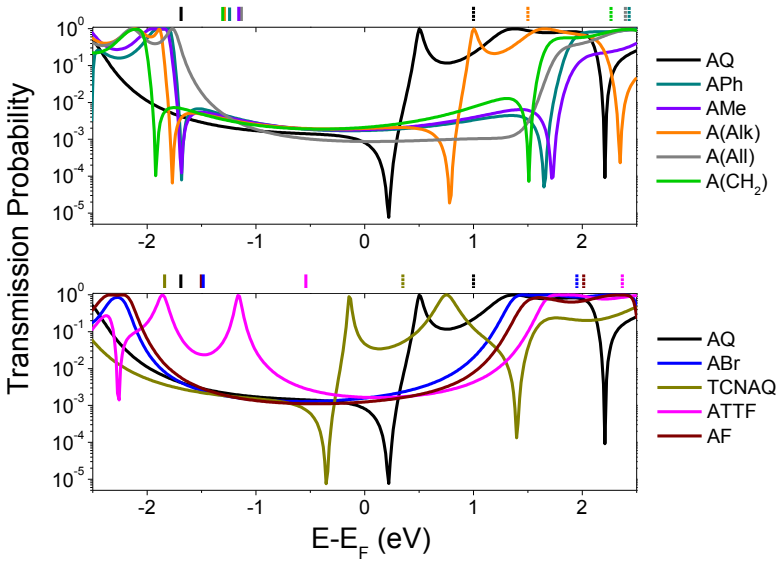

Figure 5.3 Calculated transmission probability as a function of electron energy (with respect to E_f= −4.3 eV, see the Methods section for more details) of different molecular wires. Top: all-carbon wires; bottom: wires containing herteroatoms. **AQ** is reported in both the plots as reference. The gas-phase DFT HOMO (solid lines) and LUMO (dashed lines) energies are shown across the top X-axis with respect to E_f. The non-reported LUMO values were characterized by a $E_{LUMO} - E_f > 2.5$ eV.

The calculations were performed on single-molecules, as calculations on SAMs of these molecules are complex and the details of molecular conformation and packing are unknowable. Although the properties of molecules are affected by collective effects that may arise in a SAM (*e.g.*, the alignment of dipole moments, effects on the geometry of the molecules),[8, 16, 30, 31] studies show that it is possible to achieve good qualitative agreements between single-molecular calculations and experimental results in large-area molecular junctions comprising SAMs,[25, 32] particularly for what concerns trends.

The spectra shown in Figure 5.3 feature sharp dips in transmission, which we attribute to destructive QI. When the energy of the dip is found near E_f, QI can substantially depress the tunneling probability between the two electrodes, which we observe as a decrease in conductance.

As can be seen in the top panel of the figure 5.3, the all-carbon wires (except **A(All)** and **A(Alk)**) show analogues transport properties, comparable to what was already predicted for **A(CH$_2$)** by Valkenier *et al.*.[20] **A(All)**, on the other hand, only shows a suppressed transmission, meaning that the position of the interference dip with respect to $E_f$is significantly different from the former compound. There are several potential causes for this differnce. The angle of the core is remarkably different, with **A(All)** (just like **AQ**) being the only molecule that is completely planar (see table 5.1). However, altering the torsional angles (φ) *in silico* only shifts the energy of the feature by a few meV without affecting shape or general features (Figure 5.4).[33]

That steric effects only affect the charge transport marginally when compared to the electronic contributions is also evident from the comparison of the spectra in Figure 5.3 and φ in Table 5.1 for which there is no obvious trend. More likely is that the difference we observed has to do with the different hybridization of the central carbon of the allene compared to the metylene of **A(CH$_2$)** (*i.e.*, sp instead of sp^2). The allene moiety, despite being traditionally seen as having the carbons in position 1 and 3 as non-conjugated, is not innocent and does not behave like a simple carbon-carbon double bond in the case of tunneling transport,[34] thus making the case of **A(All)** significantly different from that of **A(CH$_2$)**. This is also noticeable in the different spacial distribution and symmetry of

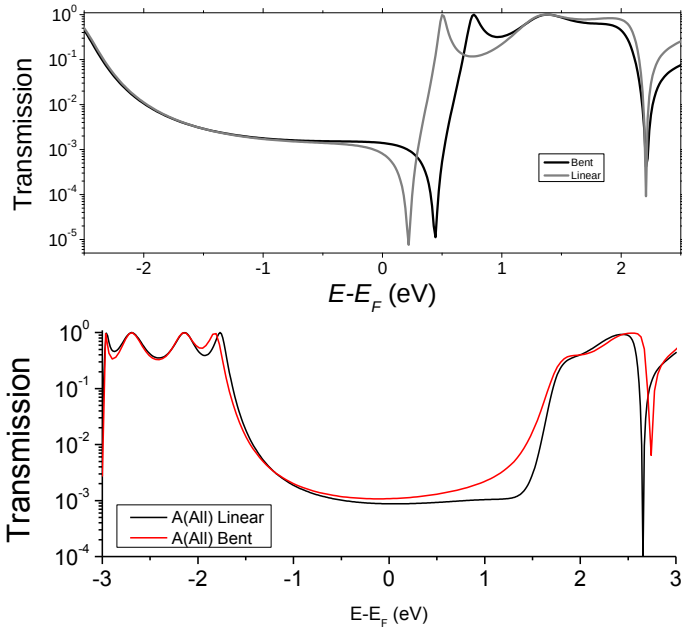

Figure 5.4 Transmission Probability of: **AQ** wire in the linear (DFT optimized structure) and bent form with an angle of 47° (top), **A(All)** in the linear (DFT optimized structure) and bent formwith an angle of 35° (bottom). The value of E_{F} used here to reference the energy axis is −4.3 eV.

the highest occupied π-state (HOPS) and the lowest unoccupied π-state (LUPS) of these two molecules (Figure 5.5).

The transmission probability plots of **ABr** and **AF** are also featureless and similar in magnitude to the former all-carbon derivatives around E_{f}. Apparently, the similarity in the electronic characteristics of these two wires is reflected in their transport properties, irrespective of the differences in the electronegativities of the halogen atoms and the fact that ϕ for **AF** is smaller. Likewise, **ATTF** does not show any QI feature in the frontier orbital gap. Yet, its line-shape in Figure 5.3 differs considerably from the compounds discussed thus far. The high-lying HOMO (the highest in the series) results in a high-transmission resonance 0.9 eV below E_{f}.

Interestingly, the three molecules characterized by the lowest LUMO energies in the entire series—**A(Alk)**, **AQ**, and **TCNAQ**—show a single, sharp feature. Starting from the former, the feature falls closer to E_{f}as the LUMO energy decreases; as the electron-with-

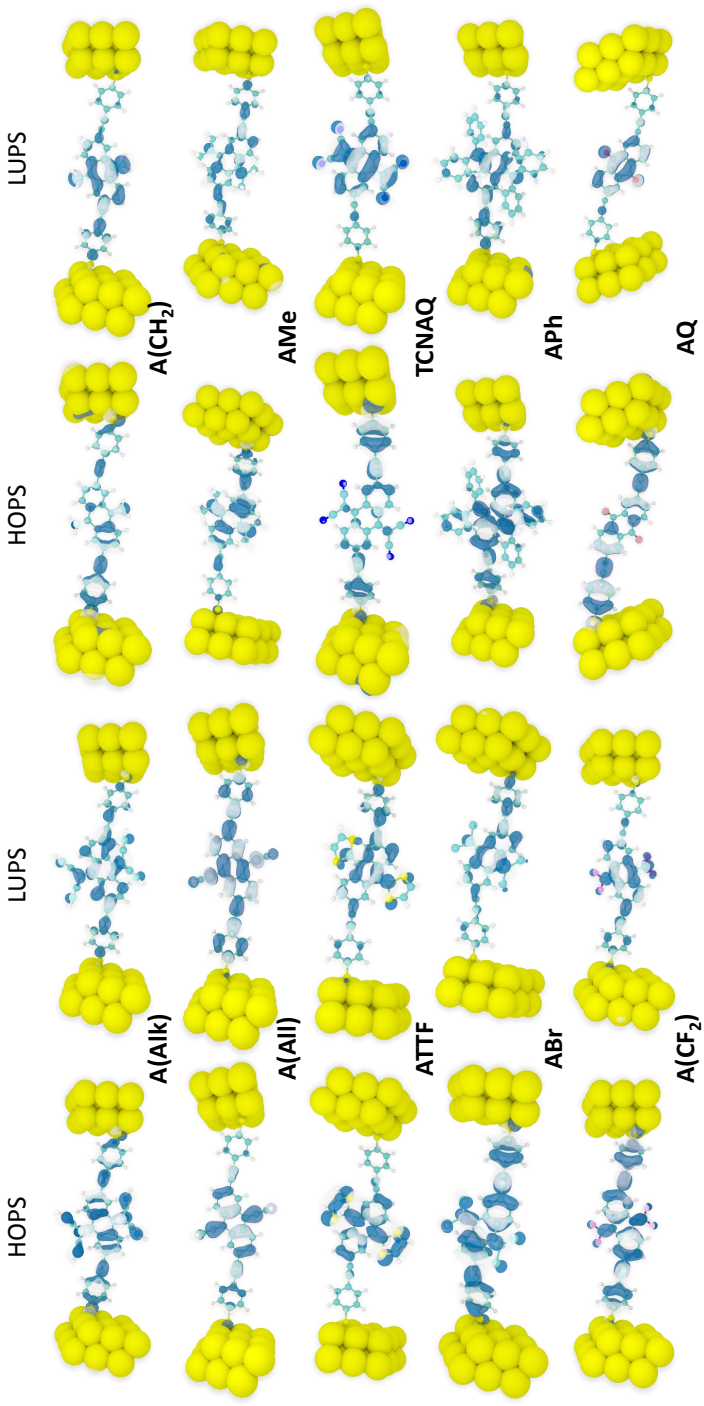

Figure 5.5 Frontier Molecular Orbitals in the ideal metal-molecule-metal junctions; Highest Occupied π-State (HOPS) and Lowest Unoccupied π-State (LUPS) for the molecular series studied in this paper.

drawing character of the pendant group increases (*i.e.*, the LUMO moves down in energy), the energy of the interference feature is shifted to lower values.[18] It was an interesting correlation that **AQ**, **TCNAQ**, and **A(Alk)** with the transmission spectra shifted towards lower electron energies have core-localized LUPS, while **ATTF** that has a transmission spectrum shifted towards the higher electron energies has a core-localized HOPS (Figure 5.5, a correlation that we previously observed benzodithiophenes.[25]

In this section, we discussed how different molecular properties can affect the transmission between the electrodes using computational methods. We argue that one of the limitations of using **AQ** to investigate the correlations between QI and cross-conjugation is its peculiar energetic situation: if a low lying and/or core-localized LUMO is necessary to observe the QI feature in anthraquinoid molecules, then there are only a few compounds we can access bearing functionalities with a comparable (or increased) electron-withdrawing behavior with respect to **AQ**. While an *in silico* approach allows us to vary the molecular energetics continuously and at will, in static molecular junctions (*e.g.*, devices) we can only observe the properties of synthetically accessible compounds in a particular conformation.

5.3. SYNTHESIS

It is not uncommon in molecular electronics to find theoretical studies predicting interesting properties in compounds without regard to synthetic accessibility.[20, 35, 36] Practical synthetic constraints often require extrapolating these findings to analogous compounds to validate them experimentally. These constraints, in turn, inform theorists which compounds and structural motifs warrant further investigation. As shown Figure 5.6, the synthesis of **AQ** from 2,6-dibromo-anthraquinone (**1**) core is straightforward according to literature procedures.[11] An ideal convergent synthesis would begin by derivatizing **1** and follow the same route as **AQ** however, the stability of **1** and the functional group tolerance of Sonagashira chemistry precluded that approach.

Of the proposed compounds in Fig. 5.1, **ATTF** was the most straightforward to synthesize from **1**: first, we obtained **3** from dimethyl 2-(1 3-dithiole)phosphonate, then we prepared **4** (the 2,6-diethynyl derivative of **3**) via Sonogashira coupling. Following a

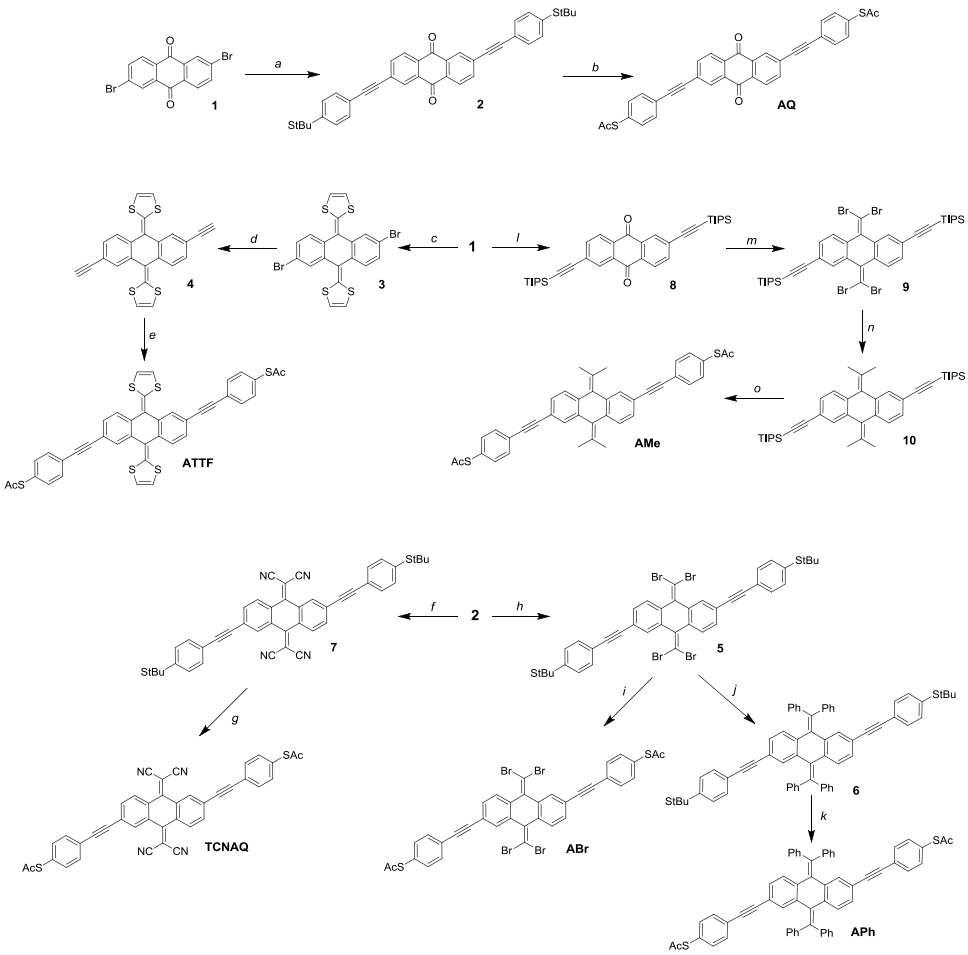

Figure 5.6 Reaction scheme for the synthesis of the wires: a) tert-butyl(4-ethynylphenyl)sulfide, $Pd(PPh_3)_4$, CuI, NEt_3, THF; b) BBr_3, AcCl, DCM/toluene 1:1; c) dimethyl-(1,3-dithiol)-2-ylphosphonate, nBuLi, THF; d) 1) TMS-acetylene, $Pd(PPh_3)_4$, CuI, NEt_3; 2) TBAF, H_2O, THF; e) S-(4-iodophenyl) ethanethioate, $Pd(PPh_3)_4$, CuI, NEt_3, THF; f) malononitrile, $TiCl_4$, pyridine, $CHCl_3$; g) AcCl, $TiCl_4$, DCM; h) PPh_3, CBr_4, DCM; i) AcCl, $TiCl_4$, DCM; j) $PhB(OH)_2$, K_2CO_3, $Pd(PPh_3)_4$, toluene; k) AcCl, $TiCl_4$, DCM; l) TIPS-acetylene, $Pd(PPh_3)_4$, CuI, NEt_3, THF; m) PPh_3, CBr_4, DCM; n) B-MeO-9-borabycyclononane, MeLi, $Pd(PPh_3)_4$, THF; o) AcCl, $TiCl_4$, DCM.

desilanization, we prepared the final wire using Pd/CuI mediated cross-coupling between **4** and (4-iodo)phenylthioacetate. The other compounds in Figure 5.1 required the installation of functional groups later in the synthetic route: in the case of **TCNAQ**, for instance, the malononitrile derivative of **1** cannot be cross-coupled using Sonogashira chemistry.[37] Thus, we installed the functional group on **2** to form **7**, from which we obtained the dithioacetate-wire with one more step.

Following the same approach, we prepared **ABr** using a Corey-Fuchs reaction to obtain **6** followed by the replacement of the *tert*-butyl groups. This dibromovinyl functionality is also a useful synthon, allowing the preparation of the all-carbon derivatives **APh** and **AMe** via Suzuki coupling. It is worth mentioning that, compared to the other compounds, the latter tend to become dark within days if not kept in the dark, which is an indication of the relative instability of many anthraquinoids towards Glich-like polymerization.[38]

While we were able to synthesize these aforementioned compounds, the others presented in Figure 5.1 remain elusive. All attempts to prepare **A(CH_2)**, **AF**, **A(All)**, and **A(Alk)** were either unsuccessful or the final compounds could not be isolated, presumably because they lack sufficient steric bulk to inhibit spontaneous polymerization.

In the case of **A(CH_2)** the simplest all-carbon derivative of **AQ**, proposed by Valkenier *et al.*,[20] all our synthetic attempts were unsuccessful. While **1**, **2**, nor anthraquinone did not react in Wittig conditions, the use of other methods (involving for example titanium-carbene complexes) yielded in black residue that showed equivocal evidence of the desired products. This is probably due to the limited stability of the 9,10-anthraquinonedimethane core which was reported to readily polymerize unless kept in extremely diluted solutions.[38] The same reactions performed on diphenylketone yielded the expected products, emphasizing the different reactivity of quinoid structures compared to ketones.

As mentioned earlier we also observed limited stability in the case of **AMe**. In particular, when we tried a procedure similar to that for the preparation of **ATTF**, we did not obtain any product from the replacement of the StBu groups with SAc in **11** using $TiCl_4$ as shown in in Figure 5.7. On top of that, when compared to the other compounds,

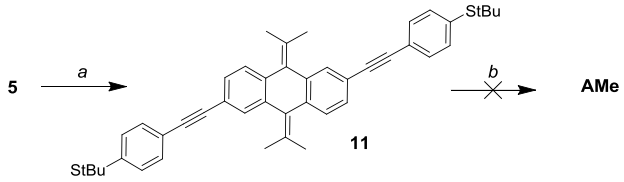

Figure 5.7 Reaction scheme for a proposed synthesis of **AMe**: a) B-MeO-9-borabycyclononane, MeLi, $Pd(PPh_3)_4$, THF; b) AcCl, $TiCl_4$, DCM.

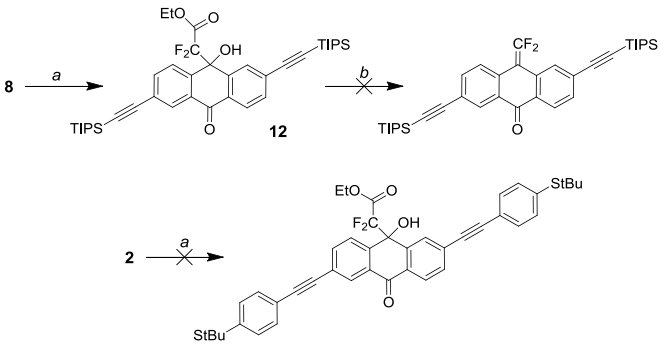

Figure 5.8 Reaction scheme for a proposed synthesis of **AF**: a) Ethyl bromodifluoroacetate, $ZnCl_2$, THF; b) AcOH, Ac_2O.

AMe tend to become dark within days if not kept in the dark. We believe that this limited stability has the same thermodynamic origin of the aforementioned **A(CH$_2$)**, with the difference that in this latter case the methyl groups slow down the kinetics.

As for **A(CH$_2$)**, we were not able to perform the synthesis of its fluorinated analogue, **AF**. While we were able to react anthraquinone core in a Reformatsky-type reaction using 2,2-bromo-difluoro-ethylacetate (**12**), elimination of the ester group in acid conditions did not produce the expected difluorovinyl functionality but a dark residue from which we could only recover starting material (Figure 5.8. Our hypothesis is that, if a difluorovinyl group is formed during the reaction conditions, it can follow the same face as the the methylene derivative of anthraquinone core previously reported.

Among the all-carbon analogues of **AQ**, **A(All)** is of particular interest as it should retain the same flatness of the core. We tried the synthesis by reduction of the correspondent propargyl alcohol (**13**) to the allene moiety but it was unsuccesful as the aromatic

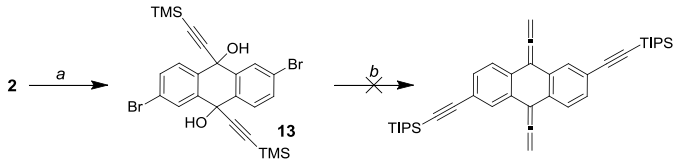

Figure 5.9 Reaction scheme for a proposed synthesis of **A(All)**: a) lithium TMS-acetylide, THF; b) *o*-nitrobenzenesulfonylhydrazide, triflate Ag(I), triflic acid, nitromethane.

core rearranges to anthracene instead. If the TMS groups are removed from **13**, the core rapidly rearranges to anthraquinone by loosing acetylene.

Finally, considering the reactivity of **5**, we decided to prepare **A(Alk)** from **6**, the all-carbon equivalent of **TCNAQ**, in Sonogashira conditions and using TMS-protected ethynyl groups. Anyway, such compound was found not to be stable and turned darker even when kept in the dark under nitrogen atmosphere.

To summarize, unfortunately, many anthraquinoid molecules are not accessible by chemical synthesis and therefore cannot be studied in any experimental platform. Often the compounds can be prepared, but either cannot be isolated or decompose too quickly to perform conductance measurements, which is a fundamental limitation that cannot be circumvented. While we could not prepare compounds such as **A(CH_2)** and **AF**, we were still able to prepare others that show similar transport properties when compared to these former *in silico*, as it is the case of **APh** and **ABr**. In such case studies, when trying to investigate relations between QI and molecular structure, one cannot overlook the chemical stability of the studied compounds: the risk is that one might jump to conclusions that are more relevant to peculiar case rather than building general design rules for molecular electronics.

5.4. PREPARATION AND CHARACTERIZATION OF SAMS

Single-molecule junctions are useful for validating theoretical and computational models because they can be described accurately *in silico*, but static, single-molecule devices have thus far presented an insurmountable challenge. Ensemble junctions, by contrast, are prohibitively complex to model accurately, but can be translated to devices.[8, 39]

Table 5.2 Characterization of SAMs using HRXPS and NEXAFS data.

	Packing density (10^{14} molecules cm^{-2})	Thickness (nm)	Tilt angle (°)
AQ[a]		20.1	
ABr	2.7 ± 0.2	18.0 ± 0.5	35.5
APh	2.9 ± 0.2	20.3 ± 0.5	33.5
ATTF	2.7 ± 0.2	17.9 ± 0.5	31.0
TCNAQ	2.3 ± 0.2	18.7 ± 0.4	~35

[a]From ref. 11

The dynamic nature of SAMs and the collective effects present in molecular ensembles make them particularly difficult to study and to elaborate *in silico*.[8, 16, 30, 31]

We grew SAMs of the compounds mentioned in the previous section on Au-on-mica (Au^{mica}) and template-stripped Au (Au^{TS}).[40] These Au substrates are both atomically flat but different in nature, being the former characterized by highly crystalline Au(111) terraces and the latter by mostly flat amorphous grains of Au. Care has to be taken when growing SAMs of bis-functionalized molecules (such as the ones presented here) as they could tend to lay flat on the surface.[41] The nature and the quality of the SAMs on Au^{mica} were investigated using standard and synchrotron photoelectron spectroscopy (see Methods section). For the compounds introduced earlier, with the exception of **AMe**, the molecules were found to stand upright with only one sulfur bound to the gold, which can be determined from the XPS spectra in the S2p region (Figure 5.10). Most of the wires produced two signals: one at ~164.0 eV compatible with the S atoms on the top of the SAM, and another at ~162.0 eV that we ascribed to Au-bound sulfur. The analyzed SAMs showed a similar packing density and tilt angle with respect to the metal surface (Table 5.2).

The reasons why **AMe** does not form good SAMs are unclear, but could be related to the reactivity of the molecule: the difficulties encountered during the synthesis, as well as the limited air-stability of **AMe** shows that the compound is more reactive than the other wires and, in the closely packed environment of the SAM, could indeed show

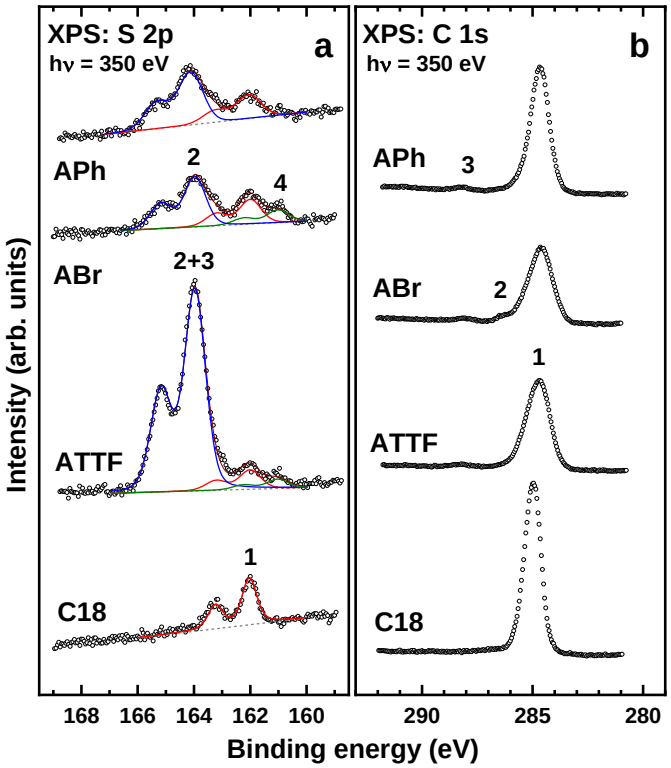

Figure 5.10 S 2p (a) and C 1s (b) XP spectra of the **APh**, **ABr**, and **ATTF** SAMs as well as reference **C18** monolayer. The spectra were acquired at a photon energy of 350 eV. The S 2p spectra are decomposed into individual doublets, drawn by different colors and marked by numbers (see text for details); individual peaks in the C 1s spectra are marked by numbers as well (see text for details).

further reactivity that inhibits the formation of a densely packed SAM.

But **AMe** is not the only compound to give unusual results. Among the proposed series, the SAM of **TCNAQ** showed a peculiar feature: the XPS signal of the N1s orbital was characterized by an extra peak that is not present in the unbound molecules, which we ascribed to reduced nitrogen species.

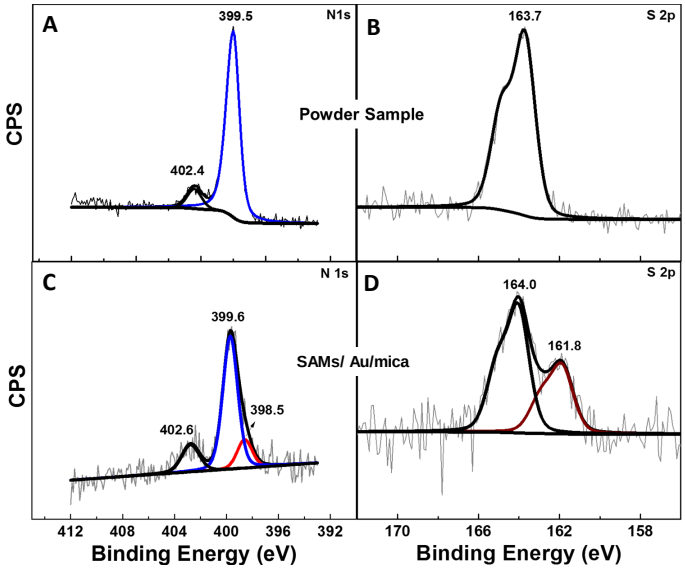

Figure 5.11 XPS spectra of N 1s and S 2p2/3 core levels for powder samples of **TCNAQ** (top) and SAMs of **TCNAQ** on Au-on-mica (bottom). The peak at 398.5 eV, which is present only in the monolayer, indicates the presence of a non-stoichiometric, reduced nitrogen-containing species.

Physisorbed monolayers of tetracyanoquinodimethane (which constitute the core of our wire) and related molecules on Au and other noble metals are known to generate spontaneous charge transfer from the metal to the molecules, whose reduced state can be observed in the XPS signal:[42] there, the molecule is directly adsorbed onto the metal substrate while, in the case of SAMs of TCNAQ, the redox-active core is bound through a phenylacetylene arm that is coupled to the surface through a covalent S-Au bond; thus, charge-transfer (redox) can still occur in a geometry that is compatible with the formation of metal-molecule-metal junctions. In the XPS spectra, about 14% of TCNAQ molecules in the SAM are in a reduced state. It is worth mentioning that the presence of

even a small fraction of reduced molecules could have drastic effects on the charge transport properties of the monolayer, by forming a linearly conjugated and more conductive species.[43, 44] We will examine in depth **TCNAQ** SAMs in next chapter.

Cases like those of **AMe** and **TCNAQ** shed light on another issue that can limit the connection between theory and the preparation of working devices, namely the translation of molecular properties across different environments. While one can address the physical and chemical characteristics of a molecule using both computational and experimental techniques—from the isolated gas-phase scenario to the infinite close-packed crystal—it is still hard to predict the behavior of an ensemble of molecules in a 2D matrix bound to a metal. A better understanding of the latter is necessary in order to move closer to the realization of real devices: specific functionalities that are chosen by design to generate certain effects, may behave in unpredictable ways in the complex environment of a device in virtue of their specific chemical nature, thus complicating the role of certain compounds as materials in molecular electronics.

5.4.1. MOLECULAR JUNCTIONS COMPRISING SAMS

Molecular tunneling junctions comprising SAMs are of primary technological relevance for the realization of molecular-electronic devices.[1] When compared to single-molecule junctions, the former are more complex to model and it is not clear what functionalities can be translated efficiently to large area-devices.[45] For this reason an empirical approach can be useful in addressing the electrical properties of SAMs, and it is particularly effective when they are investigated and compared across different platforms and substrates.

We evaluated the electrical properties of the SAMs in large-area Au^{mica} or Au^{TS}/SAM//EGaIn junctions and small-area Au^{mica}/SAM//Au junctions using CP-AFM (where '/' and '//' denoted covalent and Van der Waals interactions, respectively). All EGaIn junctions were measured in a nitrogen atmosphere containing 1 % to 3 % O_2 and relative humidity below 15 %, the details of which are described in Chapter 2. We believe that the use of different experimental techniques is of paramount importance to separate the intrinsic molecular properties from features arising from the method employed. Next to

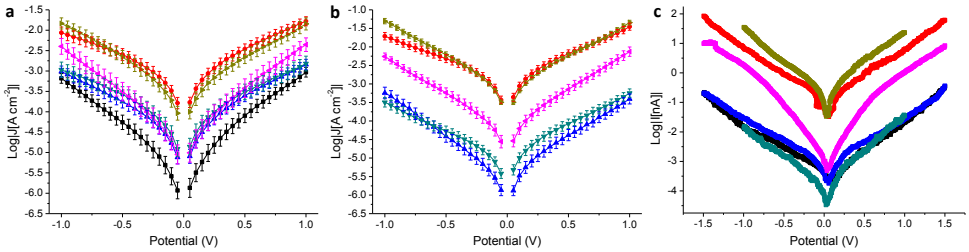

Figure 5.12 Electrical characterization of tunneling junctions obtained as Au^{mica}/SAM//EGaIn (**a**), Au^{TS}/SAM//EGaIn (**b**), and Au^{mica}/SAM/Au (**c**) comprising **AQ** (black), **AC**(red), **APh** (cyan), **ABr** (blue), **ATTF** (pink), and **TCNAQ** (yellow). Error bars in **a** and **b** are confidence intervals ($\alpha = 0.05$). Error bars in **c** are omitted for clarity.

Table 5.3 Summary of electrical characteristics of Large Area Au/SAM//EGaIn junctions.

		AQ	AC	APh	ABr	ATTF	TCNAQ
Au^{mica}	Yield (%)	96	77	56	85	76	69
	$\log\|J\|$ (0.1 V)	-5.5 ± 0.2	-3.4 ± 0.1	-4.5 ± 0.2	-4.7 ± 0.2	-4.6 ± 0.2	-3.7 ± 0.2
	$\log\|J\|$ (0.75 V)	-3.5 ± 0.1	-2.1 ± 0.2	-3.2 ± 0.2	-3.2 ± 0.1	-2.9 ± 0.2	-2.3 ± 0.2
Au^{TS}	Yield (%)	-	98	100	100	100	100
	$\log\|J\|$ (0.1 V)	-	-3.1 ± 0.1	-5.0 ± 0.1	-5.5 ± 0.2	-4.2 ± 0.2	-3.2 ± 0.1
	$\log\|J\|$ (0.75 V)	-	-1.8 ± 0.1	-3.7 ± 0.1	-4.0 ± 0.1	-2.6 ± 0.1	-1.8 ± 0.1

the cross-conjugated wires presented in Figure 5.1, we also measured as reference a wire of similar length that is linearly conjugated, bearing an anthracene core substituted in the 2 and 6 positions by the same (ethynyl)phenyl-thioacetate arms, **AC**, that we already used in Chapter 4. The results for the EGaIn measurements are shown in Figure 5.12a and b, and summarized in Table 5.3.

As can be seen in the J/V plot for Au^{mica}/SAM//Ga_2O_3/EGaIn junctions (Figure 5.12a), through most of the bias window, the current densities of the investigated SAMs follow the order **TCNAQ** ≈ **AC** > **APh** ≈ **ABr** ≈ **ATTF** > **AQ**. This result suggests no dependence of the conductance with the torsional angle of the core as predicted by our calculations; *i.e.*, the degree of conjugation between the ends of the wire does not strongly affect the tunneling probability.

Surprisingly, **TCNAQ** was as conductive as **AC**, despite the latter being linearly conjugated; however, this unusually high conductance can be ascribed to the partial reduc-

tion of SAMs of **TCNAQ**, which, in contrast to the neutral molecule, is linearly conjugated: although only a small fraction of the molecules in the SAM is found in that state (about 14%), by drawing an analogy with the current that flows through a series of resistors in parallel, 1-2% of more conductive molecules is enough to dominate the charge transport across the whole junction.[46] The special case of **TCNAQ** will be investigated further in the next Chapter.

The shapes of the J/V curves of **ATTF** and **AQ** are steeper and more symmetrical than those of the other molecules, which causes **ATTF** to be more conductive than **APh** and **ABr** at higher biases. A slight asymmetry in Metal/SAM//EGaIn junctions comprising conjugated molecules is expected because of the non-identical interfaces between the two ends of the molecules and the electrodes. In the case of **AQ**, we ascribed the J/V characteristics of the junctions to QI. We discussed this observation in detail in a previous study where we showed that the differential conductance plot (Log$|dJ/dV|$) of Au^{mica}/**AQ**//Ga_2O_3/EGaIn junctions are characterized by negative curvature.[25]

In this study, we wanted to better highlight the differences in the J/V line-shapes for the different systems and gain better insight of the transport mechanism. For these reasons we decided to plot the collected data as normalized differential conductance (NDC).[47] The results are shown in Figure 5.13.

Compared to the plots introduced above, in NDC heatmaps the systems are represented on the same scale independently of the magnitude of the current density and can be easily compared, revealing information about transmission features close to E_f.[**?**] The NDC heatmaps for **AQ** and **ATTF** are significantly steeper and sharper around 0 V compared to the other compounds. While for **AQ** we ascribed this finding to QI, we believe the explanation to be different in the case of **ATTF**: for this system, we ascribe such line shape to the low lying HOMO of such molecule, which can also result in a rapidly increasing tunneling probability around E_f(Fig. 5.3) which is also responsible for the higher $|J|$ at higher bias when compared to **APh** and **ABr**. The plot of **TCNAQ** is also interesting as it describes a bowl shaped NDC though the QI feature is predicted to be less than 0.2 eV away from E_f. This observation could support the presence of (linearly conjugated) reduced molecules in the SAM which dominates the conductance charac-

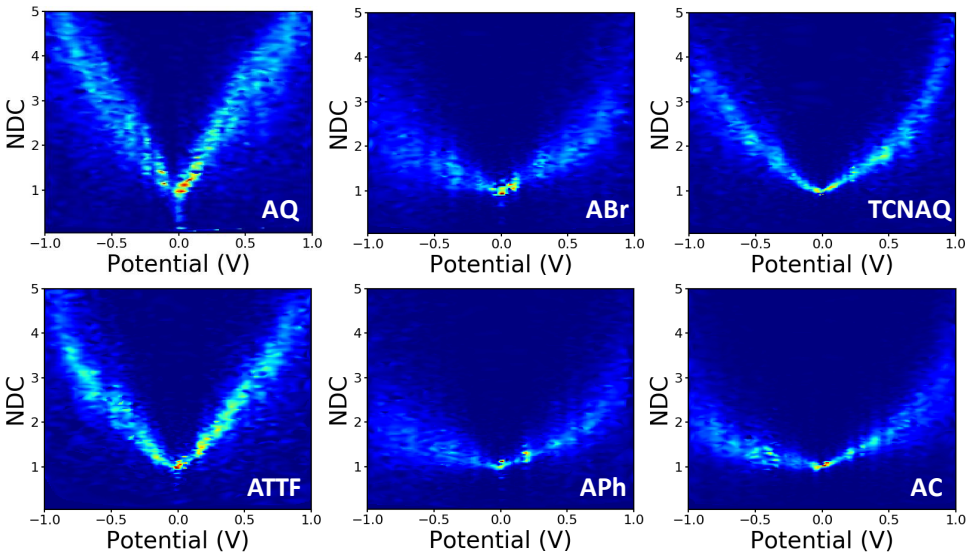

Figure 5.13 Normalized Differential Conductance heatmaps for Au^{mica}/SAM//EGaIn junctions comprising **AQ**, **ABr**, **TCNAQ**, **ATTF**, **APh**, **AC**.

teristics of the junction as discussed earlier.[44]

In the case of Au^{TS}/SAM//EGaIn junctions (Figure 5.12b and Table 5.3), we found a similar trend in J as we saw for Au^{mica} (Figure 5.12a) with some differences: I) the current density values for the different SAMs are spread over a larger codomain of $\log|J|$; II) the yield of the working junctions was significantly higher; III) the statistical variance in J was smaller; and IV) it was not possible to measure **AQ** because of the extremely low yield of the working junctions (specifically in the low O_2/humidity conditions used throughout this study). These results show that, although the nature of the SAM (and hence the data collection) is influenced by the substrate, the transport characteristics of the identical molecules on the different Au surfaces are comparable and show similar properties. Compared to the case on Au^{mica}, **ATTF** appears now to be more conductive than **APh** and **ABr** over the entirety of the accessible bias window; this observation could be due to the wider distribution of the values of J in the case of Au^{TS}, which can enhance the differences between the different compounds.

We observed the same trend in Au^{mica}/SAM//Au junctions (Figure 5.12c and Table 5.4), in which again the conductance of **ATTF** is significantly different from that of the

Table 5.4 Summary of electrical characteristics of Small Area Au^{mica}/SAM//Au junctions.

	AQ	AC	APh	ABr	ATTF	TCNAQ
$\log\|J\|(0.1\,V)$	-3.6 ± 0.2	-1.3 ± 0.1	-3.9 ± 0.4	-3.4 ± 0.2	-2.9 ± 0.2	-0.8 ± 0.4
$\log\|J\|(0.75\,V)$	-2.1 ± 0.2	0.3 ± 0.3	-2.0 ± 0.3	-2.0 ± 0.2	-0.5 ± 0.2	0.9 ± 0.4

other compounds. The trend in $\log|J|$ for the different SAMs was maintained with the exception that we were not able to distinguish between **AQ**, **APh**, and **ABr**, because of the low currents produced by the smaller contact-area of this technique (see Methods section).

5

Compared to EGaIn junctions, by using an AFM tip as top electrode we can contact an area several orders of magnitude smaller (70-100 molecules):[48] the fact the trend is preserved across the series excludes the influence of defects and/or artifacts that are present in large-area junctions as determining factors in conductance of the junctions. This is of particular relevance in the case of **TCNAQ**, indicating that the high conductance is indeed a property of the SAM on Au and not an observation only relative to the Au/SAM//EGaIn system. It is also important for the potential application of large-area tunneling junctions in devices.

In this section we investigated the electrical properties of SAMs of anthraquinoid compounds on two different experimental platforms and found that their conductances roughly follow the order **TCNAQ≈AC>ATTF>APh≈ABr>AQ**. These findings show that the large-area techniques used are sensitive enough to differentiate molecular junctions comprising molecules with identical bond-topology and different electronic structure, but only when the latter change drastically (as it is expected from the calculation) or the nature of the molecule is not changed by the interaction with the substrate. When new functionalities are incorporated into a molecule to affect the transmission probability, they influence steric and electronic properties as well, which may contribute to the overall properties of the junctions and the SAMs in general. Surprisingly, steric effects play a negligible role in tunneling charge-transport through SAMs.

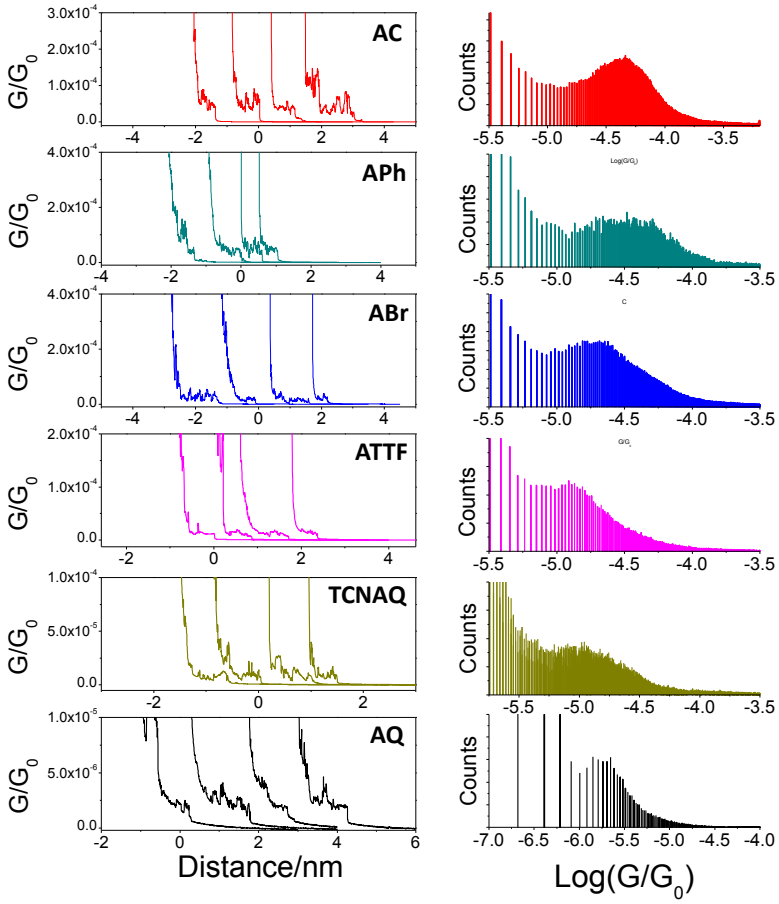

Figure 5.14 Results for STM-BJ measurements for the different anthraquinoid wires: example of traces (left), distribution of plateau conductance values as $Log(G/G_0)$ (right).

5.4.2. SINGLE-MOLECULE TUNNELLING JUNCTIONS

To gain further understanding of the transport properties of the proposed molecules opposed to effects that may arise in the SAM, we measured the compounds in single-molecule junctions using an STM-BJ setup. The obtained results together with examples of plateaus measured are shown in Figure 5.14.

We found surprisingly good (nearly-linear) agreement between these data and those obtained from large-area EGaIn junctions as one can see in Figure 5.15: the conductance of **AC** was the largest in both STM-BJ and EGaIn junctions and that of **AQ** was the

lowest, while **ABr**, **APh**, and **ATTF** fell somewhere in the middle. This trend was expected from the theoretical transport calculation (Figure S19), where **AQ** and **TCNAQ** were the only two compounds of the synthesized series to show a pronounced QI dip near E_f. In tunneling junctions comprising SAMs, the behavior of **TCNAQ**deviated sharply from theory; however, in single-molecule junctions its conductance was reduced and similar to that of **AQ**. This observation highlights the unexpected role the SAM can play in determining the electrical properties of a large-area junction. The broadening that one might expect from intermolecular interactions appears to have little effect on tunneling charge-transport, rather, it is the stabilization of charges in ensembles of that make the difference.[44]

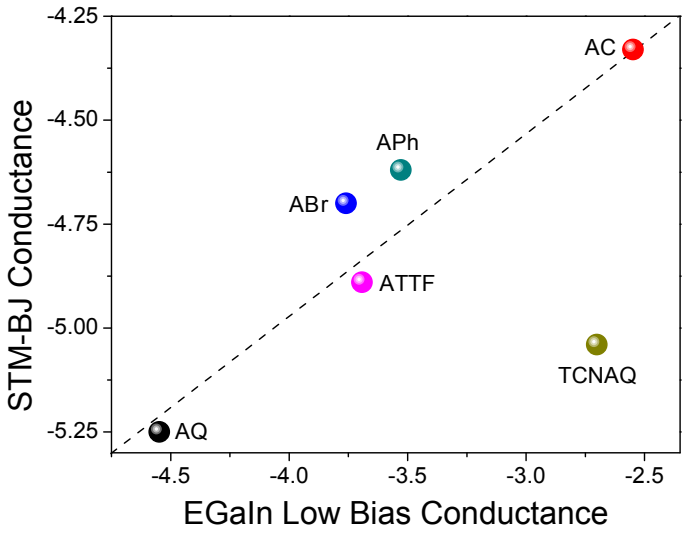

Figure 5.15 Confrontation between the values of conductance obtained for single-molecule STM-BJ at $0.1V$ (y-axis) and low-bias conductance extracted from Au^{mica}/SAM//EGaIn junctions (x-axis). Both data set are presented in a logarithmic scale. The dashed line is to be intended as a eye-guide for deviation from linearity.

Together, these observations show that, for the most part, the experimental trends in conductance in single-molecule and ensemble junctions using different electrodes, substrates and contact-areas are preserved and can relate to theoretical calculations. This is remarkable if we consider the different variables that affect the different measurements and that are intrinsic part of the different methodologies used. However, cross-platform

characterization remains the best method for establishing structure-function relationships as it ensures that a particular observation is not tied to a unique experimental platform and is likely to be preserved in whatever device platforms emerge in the future.[8]

5.5. CONCLUSIONS

The aim of this study was to investigate the charge transport properties of a series of cross-conjugated molecular wires characterized by a molecular skeleton identical to **AQ** but with different electronic structure and torsional angles. We achieved this both *in silico* and across different experimental platforms, including both single-molecule and large-area junctions. We found similar trends between the calculated transmission probability and the different experimental platforms despite the myriad factors external to the gas-phase electronic and physical structure of molecules that can lead to very different properties in different experimental contexts. Thanks to this approach we were able to find strong evidences that ultimately the level-alignment in assembled junctions will determine the observed conductance and that the torsional angle of the core seems to affect QI to a surprisingly small extent in the case of anthraquinoid compounds in contrast to what observed in other systems,[16, 49] thus making the former interesting candidates for the potential application in real devices. The analogies we found, however, are limited to the subset of the molecules studied computationally that we were able to synthesize and measure: compounds like **A(CH$_2$)** have been proposed in the literature,[20] but cannot be prepared because the tendency of anthraquinoids to polymerize is exacerbated by electron-withdrawing/donating substituents, requiring substantial steric bulk to produce stable compounds. While the distortions to the π-system imposed by this bulk has a surprisingly small effect on tunneling charge-transport, it limits the scope of accessible functional groups. One important finding of this study is that anthraquinone is a terrible platform for tuning QI features synthetically. We suggest benzodithiophenes as an alternative.[25]

5.6. EXPERIMENTAL SECTION

MATERIALS

All reagents were purchased from Sigma-Aldrich, Acros, or TCI Europe and used as received unless otherwise stated. Triethylamine and $CHCl_3$ were distilled over CaH and P_2O_5 respectively, and used within 10 days. Acetonitrile, dichloromethane (DCM), toluene, tetrahydrofuran (THF) were obtained anhydrous from a house system. NMR spectra were recorded on a Varian AMX400 (400 MHz) and referenced to the solvent peak ($CDCl_3$: H, 7.26 ppm; C, 77 ppm) relative to tetramethylsilane. S,S'-((anthracene-2,6-diylbis(ethyne-2,1-diyl))bis(4,1-phenylene)) diethanethioate (**AC**), 2,6-dibromoanthraquinone (**1**), 2,6-bis((4-(tert-butylthio)phenyl)ethynyl)anthracene-9,10-dione (**2**), S,S'-(((9,10-anthraquinone-2,6-diyl)bis(ethyne-2,1-diyl))bis(4,1-phenylene)) diethanethioate (**AQ**), and S-(4-iodophenyl) ethanethioate (**IPhSAc**, were prepared elsewere.[11]

Template stripped metal substrates were prepared by depositing a 100 nm-thick layer of metal on a Si wafer in a metal evaporator. 1x1x0.3 cm glass slides were glued to the deposited metal using an UV-curable optical adhesive (Norland series 60). The samples were cleaved from the wafer with the help of a razor and immediately used. Au on mica (1x1 cm, 200 nm thick Au) was obtained from Phasys (Switzerland) and kept in the original packing in a glovebox until use.

SAMS FORMATION

All the SAMs were prepared under nitrogen atmosphere. For Au on mica substrates, the metal surfaces (1x1 cm, 200 nm thick Au, obtained from Phasis, Switzerland) were incubated for two days in a 0.5 mM solutions of the different molecular wires in dry chloroform to which 0.3 mL of distilled triethylamine were added according to a know procedure.[11] The SAMs were finally rinsed with dry chloroform and let dry for 20 minutes before the measurement. DCM instead of chloroform was used in the case **AQ** as it gave less dispersion in the data. The current values between the two SAMs did not differ significantly as can be seen in Figure 5.16.

For template-stripped metal substrates (Au^{TS}), the SAMs were formed by incubating a 1x1 cm template-stripped metal surface (100 nm-thick) overnight in 3 mL of a 50 µmol solution of the compound in dry toluene followed by addition of 0.05 mL of 17 mM diazabicycloundec-7-ene (DBU) solution in dry toluene 1.5 hours prior the measurement, according to a known procedure.[50] The substrates were then rinsed with ethanol and let to dry for 30 minutes before performing the measurements. We described preparation and characterization of SAMs of **AC** in Chapter 4.

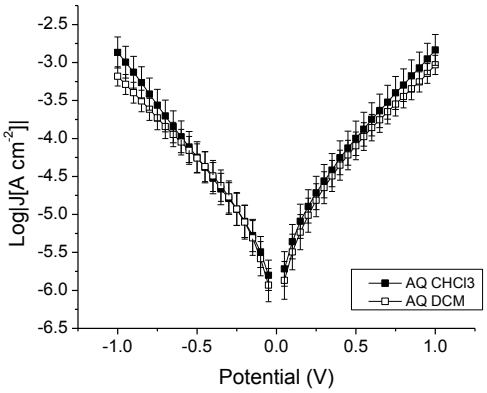

Figure 5.16 $Log|J|$ vs. V plot for Au^{mica}/**AQ**//EGaIn junctions comprising SAMs grown from $CHCl_3$ (solid squares) or DCM (open squares). Error bars represent confidence intervals ($\alpha = 0.05$).

5

SPECTROSCOPIC CHARACTERIZATION OF THE SAMS

The **TCNAQ** monolayer is characterized in detail somewhere in Chapter 6. Representative of the entire series, some of the films addressed in this study were characterized by synchrotron-based X-ray photoelectron spectroscopy (XPS) and near-edge X-ray absorption fine structure (NEXAFS) spectroscopy to verify their SAM character and to determine their basic parameters. The measurements were performed at the dipole-magnet HE-SGM beamline at the German Synchrotron Radiation Facility, BESSY II in Berlin. The description of the experimental setup, the relevant experimental parameters, and the details of the data evaluation procedure can be found elsewhere.[25] The data for SAMs of **AQ** can be found in previous publications from our group.[11, 25] The data for the **APh**, **ABr**, and **ATTF** films are presented below. The S 2p XP spectra of these films in Figure 5.10a exhibit characteristic signals of thiolate at ~162.0 eV for S 2p3/2 (**1**) and unbound SAc groups at 163.9 −164.1 eV for S 2p3/2 (**2**), with much higher intensity of the latter signals, because of the differences in the attenuation for the buried (thiolate) and terminal (SAc) groups.[51, 52] These spectra suggest that the molecules are indeed assembled upright, in the SAM fashion, with one of the terminal SAc groups bound to the substrate and another one exposed to the SAM-ambient interface, where it can be contacted by the EGa-In electrode. The doublet at 163.9 −164.1 eV is especially strong for the **ATTF** SAM because the signal of the unbound SAc groups (**2**) overlaps with the contribution of the sulfur atoms in the 1,3-dithiole moieties (**3**), appearing at the same binding energy. In addition, there is a weak signal of atomic sulfur at 161.0 eV for S 2p3/2 (**4**) in some of the spectra; such a minor contamination is frequently observed in the S 2p XP spectra of thiolate

SAMs.[52] Based on the intensity of the thiolate signal, packing density of the **APh**, **ABr**, and **ATTF** SAMs was calculated, taken the S2p/Au4f intensity ratio as a measure and the octadecanethiolate SAM (**C18**) with a known packing density of 4.63×10^{14} molecules/cm^2 [53] as the reference. The resulting values are compiled in Table 5.2. They are quite similar with respect to each other but somewhat smaller than that for the reference **C18** SAM, which is understandable in view of the bulky character of their backbone core. The C 1s XP spectra of the **APh**, **ABr**, and **ATTF** SAMs in Figure 5.10b are dominated by the strong signal of the molecular backbone at 284.5 −284.7 eV (**1**) accompanied by a shoulder at ~286.3 eV (**2**) and a weak peak at 288.1 eV (**3**). The shoulder, observed in the spectrum of the **ABr** SAM only, stems from the carbon atoms bound to Br, with the latter atoms being clearly observed in the respective Br 3d XP spectrum (Figure 5.17). The weak peak is most likely related to a minor C=O or COOH contamination,[54] which is hardly avoidable in view of the steric constrains upon the molecular assembly of such complex molecules with a bulky backbone core.

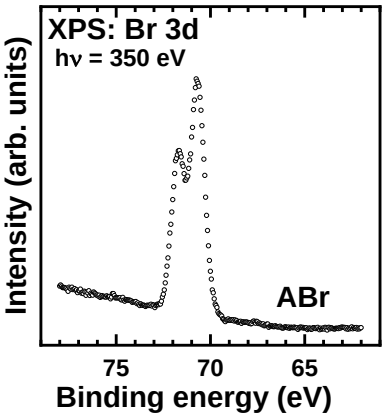

Figure 5.17 Br 3d XP spectrum of the **ABr** SAM. The spectrum was acquired at a photon energy of 350 eV.

Based on the C1s/Au4f intensity ratio, the effective thickness of the **APh**, **ABr**, and **ATTF** SAMs was evaluated, taking the **C18** SAM with a known thickness of 20.9(2) Å as the reference. The resulting values are compiled in Table 5.2. They correspond to monomolecular films (as expected) but are smaller than the lengths of the respective molecules, which suggest that the molecules in the SAMs are tilted. Additional information is provided by the NEXAFS data. The C K-edge NEXAFS spectra of the **APh**, **ABr**, and **ATTF** SAMs acquired at an X-ray incidence angle of 55° are presented in Figure 5.18. At this particular orientation the spectra are exclusively representative of the electronic structure of the monolayers.[55] The spectra exhibit the characteristic

shape and the characteristic absorption resonances of the oligo(phenyleneethynylene) (OPE)[56–58] and oligophenyl[59] compounds, above all the slightly asymmetric, joint π^*/π_1^* resonance at ~285.0 eV (**1**). This resonance is particular pronounced in the spectrum of the **APh** SAM, because of the strong contribution of the 'side' phenyl rings. The resonances at 287.3 eV (**2**) and 288.9 eV (**3**) have most likely the Rydberg and π_2^* character, respectively, while the broader resonances at higher photon energies have the σ^* character.[56–59] Significantly, the intensity of the resonance at 288.9 eV (**3**), which can contain a contribution of carboxyl,[54, 60] is comparably small, which means, in accordance with the XPS data (see above), a minor character of this contamination.

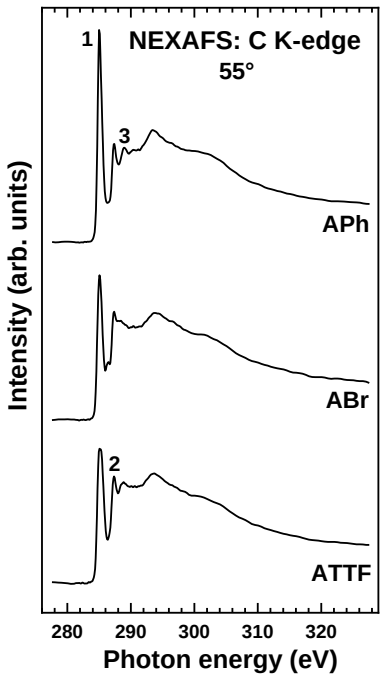

Figure 5.18 C K-edge NEXAFS spectra of the **APh**, **ABr**, and **ATTF**SAMs acquired at an X-ray incidence angle of 55°. The most prominent resonances are marked by numbers (see text for details).

The NEXAFS spectra of the **APh**, **ABr**, and **ATTF** SAMs exhibit quite small linear dichroism (dependence of the resonance intensity on the angle of X-ray incidence) which can both mean a disordered film or a molecular inclination close to a tilt angle of 35°.[55] Evaluation of the entire set of the NEXAFS data, based on the standard formalism for a vector-like orbital (π_1^* in the given case),[55] resulted in average molecular tilt angles of 33.5°,35.5°, and 31.0° for the **APh**, **ABr**, and **ATTF** SAMs respectively. Note that these values should be considered as tentative only, reflecting

an upright (even though with a tilt) molecular orientation in the SAMs studied.

ELECTRICAL CHARACTERIZATION OF LARGE AREA EGAIN JUNCTIONS

All the electrical characterizations were performed in a controlled nitrogen atmosphere containing 1-3% O_2 and RH< 15% as described in Chapter 2. For each compound, both on Au^{mica} and Au^{TS}, 3 or 4 substrates were measured. For each sample, we measured 15 Au/SAM//EGaIn junctions (5 scans from $0V \rightarrow 1V \rightarrow -1V \rightarrow 0V$, steps of 0.05 V, 0.1 s delay between steps) for a total of at least 75 traces per sample. A new EGaIn tip was prepared every 5 junctions. Junctions that shorted at any point during the scans were considered failed junction for the yield calculations. The number of traces measured for each molecule/substrate combination is reported in 5.5. Data for **AC** on Au^{TS} were collected and analyzed in Chapter 4.

5

ELECTRICAL CHARACTERIZATION OF SMALL AREA CP-AFM JUNCTIONS

CP-AFM $I-V$ measurements were performed on a Bruker AFM Multimode MMAFM-2 equipped with a PeakForce TUNA Application Module (Bruker). The SAMs were contacted with a Au-coated silicon nitride tip with a nominal radius of 130 nm (NPG-10, Bruker; tip A, resonant frequency = 65 kHz, spring constant = 0.35 N/m; tip B, resonant frequency = 23 kHz, spring constant = 0.12 N/m; tip C, resonant frequency = 56 kHz, spring constant 0.24 N/m; tip D, resonant frequency = 18 kHz, spring constant 0.06 N/m; tip A was chosen in this work) in TUNA mode. The AFM tip was grounded and all samples were prepared on Au^{TS}/Au$mica$ and biased from -1.5 V to +1.5 V and from +1.5 V to -1.5 V (TCNAQ and APh were measured from -1.0 V to +1.0 V) to record the I-V curves: a max of 10 trace/retrace cycles per junction were captured and each trace contains 512 data points. The top electrode was removed from SAMs and reapplied between junctions.

PROCESS OF J-V DATA

These data were parsed in a "hands-off" manner using Scientific Python to produce histograms of J for each value of V, the associated Gaussian fits (using a least-squares fitting routine) as described elsewhere.[16] The same raw data were used to produce the NDC plots. Low bias conductance values were obtained from a linear fit of the $J-V$ plots considering the data points between -0.1 V and +0.1 V.

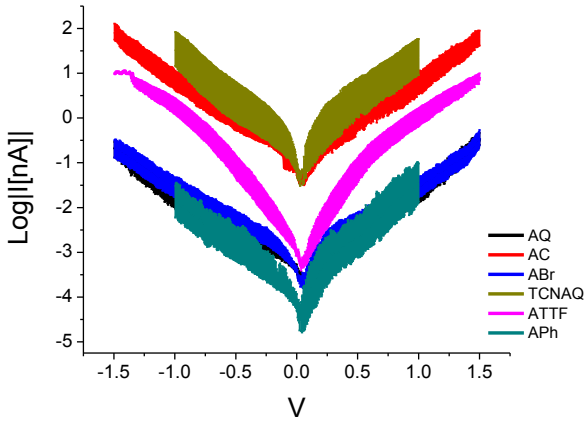

Figure 5.19 Electrical characterization of tunnelling junctions obtained as Au^{mica}/SAM/Au comprising **AQ** (black), **AC**(red), **APh** (cyan), **ABr** (blue), **ATTF** (pink), and **TCNAQ** (yellow). Error bars are confidence intervals ($\alpha = 0.05$).

Table 5.5 Number of traces analyzed per molecule per substrate/measurement condition.

	Au^{mica}	Au^{TS}	CP-AFM
AQ	220	-	469
AC	355	490	509
APh	295	225	109
ABr	225	225	1343
TCNAQ	225	225	799
ATTF	225	225	1248

SINGLE MOLECULE CONDUCTANCE MEASUREMENT

The STM break-junction experiments were performed with a Molecular imaging system using PicoScan software. We used a commercial Au on mica substrate (1x1 cm, Phasys, Switzerland) and a gold tip similar to that described in elsewhere.[61] Prior to each experiment, the substrate was briefly annealed using a hydrogen flame. The STM tip was prepared by cutting a 0.25 mm gold wire (99.999%). The STM cell was cleaned with piranha solution (98% H_2SO_4:30% H_2O_2=3:1 v/v) and then sonicated three times in MilliQ water. We carried out the conductance measurements in a 0.1 mM mesitylene solution of the different compounds. Prior to the measurement, a small amount of NEt_3 was added into solution in order to cleave the thioacetate group.[41] Prior to the STM break junction measurement, the quality of the substrate was checked by scanning its surface in STM mode. Clear images and sharp atomic steps usually indicates a clean substrate and a

Table 5.6 Number of selected traces and values of conductance for STM-BJ experiments.

	Number of selected traces	$Log(G/G_0)$
AC	710	-4.3
ABr	429	-4.7
APh	113	-4.6
ATTF	360	-4.9
TCNAQ	350	-5.1
AQ	775	-5.3

sharp tip. After ensuring the tip and Au/Mica substrate were in good conditions, the STM feedback loop was turned off. Then the tip was precisely driven by the piezo, leading to a repeatedly in and out of contact with the substrate. During such movements, the molecules may bridge both the tip and the substrate electrodes. Meanwhile, current versus tip travel time ($I(s)$) curves are recorded. Single molecular conductance is determined by the current plateau as well as the conductance histogram constructed from large number of individual events. All the traces are recorded when the STM tip was pulled away from the substrate and under the bias voltage of $0.1V$. The $I(s)$ traces are presented in the left part of Figure 5.14 with arbitrary x-axis offsets. The dramatic conductance drop associated with the tip stretching suggests a decrease in the number of molecules involved in the junctions. The last conductance plateau is usually taken as the single molecular conductance. Higher conductance steps (as found for example in the case of **AC** in Figure 5.14) suggest that double molecules may contribute to the conductance of the junctions. To determine the conductance of the single molecules, 5000 current-distance traces are acquired for statistical studies. The conductance maximum of the peaks for the different compounds is reported in Table 5.6 together with the number of selected traces.

CALCULATIONS

TIGHT-BINDING/HÜCKLE MODEL

For simplicity, all the atoms were approximated by a single Slater orbital of the same kind whose energy was set to 0 eV, and the coupling energy from the orbital overlap was set to -1 eV for the nearest neighbors (*i.e.*, two sp^2 atoms connected by a bond). The leads, consisting in infinite Au chains, were coupled to the previously mentioned two carbon atoms connected to the rings with a coupling magnitude of 0.5 eV. Transmission probabilitu vs. energy plots were obtained using the GOLLUM software package. Changing the orbital site energy or the coupling energy affect the

secondary features of the plots, but not the position of the dip at 0 eV.

DFT SIMULATIONS

We used ORCA[62, 63] software package for quantum mechanical calculations to perform the Density Functional Theory (DFT) calculations on single molecules and single molecular junctions. We used ARTAIOS-030417 software package for transport calculations, to generate transmission probability spectra[64, 65]. The procedure is described below step-by-step.

MOLECULAR GEOMETRY OPTIMIZATION

We minimised the geometries of the molecules included in this study terminating with thiol groups on both ends using the ORCA software package[62, 63]. We used the default Ahlrichs split-valence $def2-SVP$ basis sets (ORCA option *Acc-Opt*, that calls the BP functional) with tight SCF and geometry convergence criteria[66]. The energy of the optimized gas-phase geometry obtained in this calculation was calculated in the next step. The angles ϕ reported in Table 1 in the main text were calculated as angle between the centroids of the benzene ring and the mean point between the position 9 and 10 of the anthraquinoid core. As angle ϕ increases, also the angle between the hypothetical plane of the molecule (as it was flat) and the lateral double bonds increase with a similar trend.

SINGLE POINT GAS-PHASE ENERGY CALCULATIONS

We used the ORCA package also for calculating the gas-phase energies for all the molecules. We used the optimized geometries to calculate the single-point gas-phase energies using $B3LYP/G$ functional and $LANL2DZ$ Los Alamos double-valence basis set. The energy values of the frontier π-states of the molecule, *i.e.*, the HOMO (Highest Occupied Molecular Orbital) and LUMO (Lowest Unoccupied Molecular Orbital) are tabulated in the Table 5.7.

SINGLE POINT ENERGY CALCULATIONS WITH ELECTRODES

Attaching Electrodes: We attached the minimized geometries to two 18-atom Au electrode clusters after manually deleting the terminal thiol's hydrogen atom. The geometries of the electrode clusters used in these calculations had two layers of 9 atoms each, arranged in a hexagonal close-packed fcc Au-111 surface (see Fig. 5.5). The Au-Au distance was set to 2.88 Å. S-Au distance was maintained at a value of 2.48 Å and S was attached to the center of the hexagonal close-pack hollow site, taken from literature[67]. This is all similar to previously reported work[68]. We kept the geometrical parameters of these electrodes and the electrode material same throughout all these calculations, so that qualitative comparisons could be drawn, while varying the molecule in

Table 5.7 Table showing the values of E_{HOMO}, E_{LUMO}, E_{HOPS} and E_{LUPS}, the energies of the frontier molecular orbitals in gas-phase optimized geometry and the ideal metal-molecule-metal junctions, calculated in sections 5.6 and 6.8. All the values are in the units of eV.

	E_{HOMO}	E_{LUMO}	E_{HOPS}	E_{LUPS}
AQ	-5.98	-3.24	-6.35	-3.44
AMe	-5.44	-1.72	-5.75	-2.03
APh	-5.48	-1.87	-5.74	-2.17
A(CH_2)	-5.62	-2.05	-5.89	-2.33
A(All)	-5.44	-1.92	-5.80	-2.25
A(Alk)	-5.60	-2.79	-5.85	-2.32
ABr	-5.80	-2.35	-6.24	-2.70
ATTF	-4.86	-1.91	-5.12	-2.21
TCNAQ	-6.19	-3.99	-6.45	-4.19
AF	-5.77	-2.21	-6.21	-2.44

the junction. After attaching the molecules to the electrodes, we then calculated the single-point energies using the standard SCF convergence criteria using the *Orca* DFT package. $B3LYP/G$ DFT method was applied and $LANL2DZ$ basis set was used, same as in previous section. Please note, the transmission calculations, described later in section 6.8, were not performed on these geometries.

Frontier Molecular Orbitals: From this single-point energy calculation, we obtained the values of E_{HOPS} and E_{LUPS} of the metal-molecule-metal junction, which is tabulated in table 5.7. We also generated the frontier molecular π-orbitals, HOPS and LUPS, using the VMD and Blender software[69], which are shown in figure 5.5.

TRANSPORT PROPERTIES

For computing the electron transmission probability as a function of the energy of the electron, we ran single point energy calculations on molecules without Au electrode clusters and terminating with S atoms (*i.e.*, without H atoms on terminal thiols), using the same *Orca* parameters as in section 6.8. We extracted the Hamiltonian (Fock) and overlap matrices from the output of these single-point energy calculations with the commands 'Print[P_Iter_F] 1', 'Print[P_Overlap] 1', 'Print[P_Mos] 1', 'Print[P_InputFile] 1' in the '%output' section. Further, in the artaios input para-

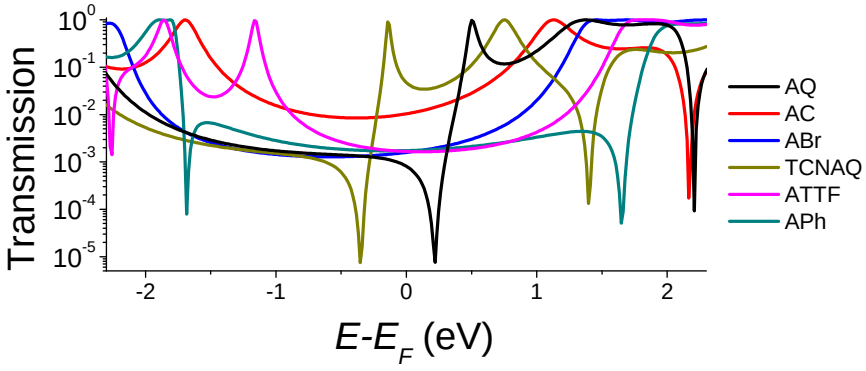

Figure 5.20 Transmission Probability of the anthraquinoid molecular wires measured on the experimental platforms versus energy of the electron referenced to a $E_f$value of −4.3 eV.

meter file[64, 65], the two terminal S atoms in all the diradical molecules served as the left and right leads, while the rest of the molecule served as the central moiety. Thus, we effectively calculated the transmission probability of the electron traveling across the molecular backbone, without the Au metal clusters.

The transmission probability of the compounds that we were able to synthesize and measure experimentally are summarized in Figure 5.20.

Estimation of E_F: The transmission spectra obtained from the *artaios* calculations give the transmission probability versus the absolute electron energy referenced to the vacuum level. To make the qualitative analysis of the position of the resonance peaks corresponding to the frontier orbitals and the QI dips in the transmission spectra, it is necessary to align the electron energy axis (x-axis) with respect to the energy of the Fermi level of the bulk electrode material (E_F). It is non-trivial to find a reasonable value of E_F because of the limitations of DFT calculations. In our previous works, we have used techniques like transition voltage spectroscopy or experimental cyclic voltammetry data to find a E_F value as reference, starting from the frontier energy levels[16, 25]. The same methodology can not be applied in this work because the inherent dissimilar and unique properties of the molecular wires measured in this work. For instance, using transition voltage values for the series doesn't work because the differential conductance curves have different line shapes, and therefore, the obtained transition voltage parameters may or may not refer to the same electronic properties of the individual molecules. (For example, the transition voltage values for **AQ** is smaller than **TCNAQ**, *i.e.*, the LUMO of **AQ** should be lower, however, according to CV the

LUMO of **AQ** is higher than **TCNAQ**.) We used the E_f of −4.3 eV to scale the energy axis in all the transmission curve graphs. It is known that the E_F of EGaIn electrode is about −4.3 eV[70]. And also, this value of E_F for Au is also supported by several already reported UPS measurements where it has been established experimentally that aliphatic and conjugated SAMs on Au substrates shift the E_F values of Au by 0.85 and 0.98 eV, respectively (*i.e.*, from E_F =−5.2 eV for a clean gold surface to E_F = −4.2 eV to −4.4 eV for Au covered with SAMs)[71–73]. Thus using E_F value of −4.3 eV makes it more realistic to make qualitative comparisons between the trends in transmission calculations with the trends in experimental measurements on Au/SAM//EGaIn platforms. This methodology is same as our previously published works.[25]

SYNTHESIS

2,2'-(2,6-dibromoanthracene-9,10-diylidene)bis(1,3-dithiole), 3

In a dry 100 mL flask under N_2, 186 mg of dimethyl-(1,3-dithiol)-2-ylphosphonate (0.87 mmol) were dissolved in 50 mL of dry THF and the solution cooled down to −80 °C in a EtOH/dry ice bath. 0.54 mL of nBuLi 1.6 M in hexanes (0.87 mmol) were added and the solution kept under stirring for 30 minutes. 80 mg of **1** were then added and the reaction left to rise at room temperature overnight. The THF was removed under vacuum. The residue was then dissolved in $CHCl_3$, extracted with water, and dried over Na_2SO_4. The product was finally recrystallized from $CHCl_3$/hexane as red needle-like crystals (80 mg, 68% yield). Multiple batches were prepared with yield 50-70%. ^{1}H-NMR (400 MHz, $CDCl_3$): δ 7.80 (d, J = 1.9 Hz, 2H), 7.54 (d, J = 8.3 Hz, 2H), 7.39 (dd, J = 8.3, 2.0 Hz, 2H), 6.34 (s, 2H). ^{13}C-NMR (101 MHz, $CDCl_3$) δ 140.66, 139.80, 136.71, 131.44, 130.33, 128.97, 122.29, 122.20, 120.00.

((9,10-di(1,3-dithiol-2-ylidene)-9,10-dihydroanthracene-2,6-diyl)bis(ethyne-2,1-diyl))bis-(trimethylsilane), 4.1

In a dry Schlenk under N_2, 100 mg of **3** (0.19 mmol) were dissolved in 15 mL of dry THF. 10 mL of freshly distilled NEt_3 were added and the solution bubbled with N_2. 0.14 mL on TMS-acetylene (0.68 mmol) were added, followed by 15 mg of $Pd(PPh_3)_4$ and 5 mg of CuI. The reaction was left at 40 °C for 2 days. The solvents were removed and the reside dissolved in DCM and extracted with HCL 1 M and water until neutrality was reached. The organic phase was then preadsorbed on silica and purified on a short column (SiO_2, hexane/ethylacetate 4:1). A yellow solid was obtained (97 mg, 85% yield). ^{1}H-NMR (400 MHz, $CDCl_3$): δ 7.76 (d, J = 1.5 Hz, 2H), 7.60 (d, J = 8.0 Hz, 2H), 7.36 (dd, J = 8.0, 1.5 Hz, 2H), 6.33 (d, J = 1.3 Hz, 4H).

2,2'-(2,6-diethynylanthracene-9,10-diylidene)bis(1,3-dithiole), 4

In a 250 mL flask, 97 mg of **4.1** (0.17 mmol) were dissolved in 125 mL of THF and the solution was placed in an ice bath. 0.5 mL of tetrabutylammoniumfluoride 1 M in THF (containing 5% vv. water) (0.42 mmol) were added dropwise and the reaction was left stirring at room temperature for 30 minutes. The solution was then filtered through a pad of silica and the solvent removed under vacuum. The product was recrystallized from $CHCl_3$/hexane as red elongated crystals (50 mg, 68% yield). ^{1}H-NMR (400 MHz, $CDCl_3$): δ 7.79 (d, J = 1.6 Hz, 2H), 7.63 (d, J = 8.0 Hz, 2H), 7.39 (dd, J = 8.0, 1.6 Hz, 2H), 6.31 (s, 4H), 3.10 (s, 2H). ^{13}C-NMR (101 MHz, $CDCl_3$) δ 145.89, 138.26, 137.91, 132.38, 131.01, 127.57, 123.04, 122.17, 120.00, 86.41, 70.61.

S,S'-(((9,10-di(1,3-dithiol-2-ylidene)-9,10-dihydroanthracene-2,6-diyl)bis(ethyne-2,1-diyl)) bis(4,1-phenylene)) diethanethioate, ATTF

In a dry Schlenk under N_2, 42 mg of **4** (0.10 mmol) and 90 mg of **IPhSAc** (0.32 mmol) were dissolved in 10 mL of dry THF. 2 mL of freshly distilled NEt_3 followed by 12 mg of $Pd(PPh_3)_4$ and 5 mg of CuI were added and the reaction was left at 40 °C overnight. The solvents were removed under vacuum and the residue dissolved in $CHCl_3$ and water. HCl 1 M was added dropwise until neutrality was reached. The organic phase was then extracted with water, dried over Na_2SO_4, and preadsorbed on silica. The product was purified via column chromatography (SiO_2, hexane:ethylacetate 2:1 increasing to 1:1) and it was recrystallized from DCM/hexane. It was obtained as a red solid (26 mg, 36% yield). ^{1}H-NMR (400 MHz, $CDCl_3$): δ 7.84 (d, J = 1.6 Hz, 2H), 7.68 (d, J = 8.0 Hz, 2H), 7.58 (d, J = 1.7 Hz, 4H), 7.44 (dd, J = 8.0, 1.7 Hz, 2H), 7.40 (d, J = 8.2 Hz, 4H), 6.34 (s, 4H), 2.43 (s, 6H). ^{13}C-NMR (101 MHz, $CDCl_3$) δ 196.10 , 173.76 , 140.64 , 138.05 (d, J = 4.4 Hz), 136.85 , 134.86 , 131.97 , 130.62 , 130.53 , 127.67 , 127.26 , 123.25 , 122.99 , 120.04 , 94.04 , 91.61, 32.93. Elemental analysis, exp. (calc., %): C 66.01 (65.90); H 3.38 (3.32); O 4.31 (4.39); S 26.30 (26.39).

(((9,10-bis(dibromomethylene)-9,10-dihydroanthracene-2,6-diyl)bis(ethyne-2,1-diyl))bis-(4,1-phenylene))bis(tert-butylsulfide), 5

In a dry 50 mL flask under N_2 were introduced 300 mg of **2** (0.51 mmol) and 1.1 g of PPh_3 (4.1 mmol) and the flask put in an ice bath. 680 mg of CBr_4 (2.1 mmol) were added immediately followed by 25 mL of ice-cold dry DCM dropwise while stirring the formed slurry. After 3 hours the ice bath was removed and the system allowed to rt overnight. The system was then heated to 40 °C for 2 hours and the hot solution filtered to remove the precipitate (mainly **2**). The solution was pread-

sorbed on silica and the product purified via column chromatography (SiO_2, hexane/ethylacetate 17:1, Rf= 0.9). A yellow solid was obtained (228 mg, 49% yield). ^{1}H-NMR (400 MHz, $CDCl_3$): δ 8.00 (d, J = 1.6 Hz, 2H), 7.83 (d, J = 8.1 Hz, 2H), 7.55 – 7.41 (m, 10H), 1.30 (s, 18H). ^{13}C-NMR (101 MHz, $CDCl_3$) δ 142.64, 140.99, 139.88, 138.47, 138.04, 136.36, 134.21, 133.22, 132.81, 130.47, 125.82, 124.81, 94.31, 92.80, 92.76, 49.21, 33.65.

S,S'-(((9,10-bis(dibromomethylene)-9,10-dihydroanthracene-2,6-diyl)bis(ethyne-2,1-diyl)) bis(4,1-phenylene)) diethanethioate, ABr

In a dry 50 mL flask under N_2, 80 mg of **5** (0.09 mmol) and 1.38 mL of acetylchloride (19.3 mmol) were dissolved in 28 mL of a 1:1 dry DCM/dry toluene solution. 2.67 mL of a BBr_3 solution 1 M in DCM (2.7 mmol) were added dropwise and the reaction left for 4.5 hours. The mixture was then poured in 150 mL water and 50 mL of DCM were added. The water phase was neutralized using a saturated solution of $NaHCO_3$. The organic phase was extracted with water, dried over Na_2SO_4, and DCM let evaporate. The product was purified using column chromatography (SiO_2, DCM/hexane 4:1, Rf= 0.7) and recrystallized from hexane to obtain yellow cubic crystals suitable for X-ray diffraction (40 mg, 52% yield). ^{1}H-NMR (400 MHz, $CDCl_3$): δ 7.99 (d, J = 1.6 Hz, 2H), 7.83 (d, J = 8.1 Hz, 2H), 7.56 (d, J = 8.3 Hz, 4H), 7.45 (dd, J = 8.1, 1.7 Hz, 2H), 7.40 (d, J = 8.3 Hz, 4H), 2.44 (s, 6H). ^{13}C-NMR (101 MHz, $CDCl_3$) δ 195.97, 140.95, 138.47, 138.15, 136.89, 134.89, 133.28, 132.88, 131.11, 130.48, 126.72, 124.66, 94.39, 92.95, 92.59, 32.96.

(((9,10-bis(diphenylmethylene)-9,10-dihydroanthracene-2,6-diyl)bis(ethyne-2,1-diyl))bis-(4,1-phenylene))bis(tert-butylsulfide), 6

In a 50 mL flask equipped with a cooler, 212 mg of **5** (0.24 mmol) and 176 mg of phenylboronic acid (1.44 mmol) were dissolved in 25 mL of toluene and the solution was bubbled with N_2. 1 mL of a degassed 1:1 EtOH/water solution was added followed by 20 mg of $Pd(PPh_3)_4$ and 265 mg of K_2CO_3. The reaction was kept at refulx for 22 hours. The solvent was rotavaped and the residue dissolved in DCM and extracted with water. The organic phase was preadsorbed on silica and purified over a short column (SiO_2, DCM/hexane 1:3 to pure DCM). The product was finally recrystallized from $CHCl_3$/hexane and obtained as off-yellow needle crystals suitable for X-Ray diffraction (155 mg, 73% yield). ^{1}H NMR (400 MHz, DMSO-d6) δ 7.68 – 7.04 (m, 34H), 1.23 (s, 18H).

S,S'-(((9,10-bis(diphenylmethylene)-9,10-dihydroanthracene-2,6-diyl)bis(ethyne-2,1-diyl)) bis(4,1-phenylene)) diethanethioate, APh

In a dry 100 mL flask under N_2, 68 mg of **5** (0.08 mmol) and 1.19 mL of acetylchloride (16.7 mmol) were dissolved in 40 mL of a 1:1 dry DCM/dry toluene solution. 2.30 mL of a BBr_3 solution 1 M in DCM (2.3 mmol) were added dropwise and the reaction left for 4.5 hours. The mixture was then poured in 150 mL water and 75 mL of $CHCl_3$ were added. The water phase was neutralized using a saturated solution of $NaHCO_3$. The organic phase was extracted with water, brine, and dried over Na_2SO_4. The product was purified using column chromatography (SiO_2, $CHCl_3$/hexane 8:1, Rf= 0.8) and finally recrystallized from hexane to obtain an off-white solid. (33 mg, 48% yiled). ^{1}H-NMR (400 MHz, $CDCl_3$): δ 7.50 – 7.21 (m, 32H), 6.97 (d, J = 8.1 Hz, 2H), 6.91 (d, J = 8.1 Hz, 2H), 2.43 (s, 6H). ^{13}C-NMR (101 MHz, $CDCl_3$) δ 196.13, 144.60, 144.43, 144.10, 140.53, 140.29, 136.96, 136.81, 134.72, 133.96, 132.16, 132.10, 131.19, 131.08, 130.75, 130.43, 129.83, 129.65, 122.39, 93.86, 32.94. HR-MS ESI for $C_{60}H_{41}O_2S_2$ calcd mass 857.25425, found 857.25646.

2,2'-(2,6-bis((4-(tert-butylthio)phenyl)ethynyl)anthracene-9,10-diylidene)- dimalononitrile, 7

In a dry 100 mL flask equipped with a cooler under N_2, 133 mg of **2** (0.23 mmol) and 65 mg of malononitrile (0.93 mmol) were dissolved in 50 mL of dry $CHCl_3$. The solution was brought to reflux and 0.10 mL of $TiCl_4$ (0.93 mmol) and 0.15 mL of pyridine (1.89 mmol) were added. The system was left at reflux for 18 hours. The reaction mixture was quenched with 50 mL of water. The water phase was extracted with chloroform thrice and the combined organic phases were extracted twice with water. They were then dried over sodium sulfate and the solvent removed in vacuum. The residue was adsorbed on silica and purified via coloumn chromatography (SiO_2, hexane:ethyl acetate 6:1, R_f= 0.35). A red solid is obtained (73 mg, 44% yield). ^{1}H NMR ($CDCl_3$, 400MHz): 8.32 (d, *J*= 1.5 Hz, 2H), 8.22 (d, *J*= 8.2 Hz, 2H), 7.82 (dd, *J*= 1.5, 8.2 Hz, 2H), 7.56-7.51 (m, 8H), 1.31 (s, 18H). ^{13}C NMR ($CDCl_3$, 400MHz): 161.38, 139.87, 137.82, 137.58, 134.51, 133.19, 132.65, 131.52, 131.00, 130.41, 124.56, 115.51, 115.39, 97.86, 90.98, 86.16, 49.46, 33.69.

S,S'-(((9,10-bis(dicyanomethylene)-9,10-dihydroanthracene-2,6-diyl)-bis (ethyne-2,1-diyl)) bis(4,1-phenylene)) diethanethioate, TCNAQ

In a dry 50 mL flask under N_2, 89 mg of **7** (0.15 mmol) were dissolved in 25 mL of dry DCM. The solution was placed in an ice bath and 3 mL of acetyl chloride (42 mmol) were added. Then 0.03 mL of $TiCl_4$ (0.32 mmol) were added slowly. The reaction was left under stirring in the ice bath for

3.5 hours, then 20 mL of water were added. The water phase was extracted once with DCM, then the combined organic phases were extracted with water four times. The solutes were adsorbed on silica and the product purified via column cromatography (SiO_2, hexane:ethyl acetate 3:1, R_f= 0.1, slowly increasing to 1:1). The product was finally recrystallized from toluene to form opaque red crystals (47 mg (48% yield). ^{1}H NMR ($CDCl_3$, 400MHz): 8.33 (d, *J*= 1.6 Hz, 2H), 8.23 (d, *J*= 8.2 Hz, 2H), 7.84 (dd, *J*= 1.6, 8.2 Hz, 2H), 7.60 (d, *J*= 7.9, 4H), 7.45 (d, *J*= 7.9, 4H), 2.45 (s, 6H). ^{13}C NMR ($CDCl_3$, 400MHz): . Elemental analysis, exp. (theo.): C 73.42% (73.60%), H 3.24% (3.09%), N 8.18% (8.58%), S 9.36% (9.82%), O 5.80% (4.91%).

2,6-bis((triisopropylsilyl)ethynyl)anthracene-9,10-dione, 8

In a dry 500 mL flask under N_2, 3.0 g of **1** (8.2 mmol), 4.6 mL of (triisopropylsilyl)acetylene (21 mmol), 250 mg of $Pd(PPh_3)_4$, and 100 mg of CuI were dissolved in 200 mL of dry THF and 10 mL of NEt_3. The solution was heated to 65 °C and left under stirring 16 hours. The solvent was removed under vacuum and dissolved in $CHCl_3$. The solution was extracted with HCl 1 M and brine, then it was dried over Na_2SO_4 and the solvent removed. The product was finally recrystallized from hexane as an off-white powder (2.1 g, 44% yield). ^{1}H-NMR (400 MHz, $CDCl_3$): δ 8.35 (d, J = 1.6 Hz, 2H), 8.25 (d, J = 8.0 Hz, 2H), 7.84 (dd, J = 8.0, 1.6 Hz, 2H), 1.16 (s, 42H).

((9,10-bis(dibromomethylene)-9,10-dihydroanthracene-2,6-diyl)bis(ethyne-2,1-diyl))bis-(tri- isopropylsilane), 9

In a dry 50 mL flask under N_2 were introduced 900 mg of **8** (1.5 mmol) and 2.9 g of PPh_3 (12.3 mmol) and the flask put in an ice bath. 1.8 g of CBr_4 (5.5 mmol) were added immediately followed by 25 mL of ice-cold dry DCM dropwise while stirring the formed slurry. The system allowed to rt overnight. The solution was filtered and the filtrate preadsorbed on silica. The product was purified over a short silica column (hexane) and obtained as a white solid after the solvent was removed in vacuum (1.3 g, 91% yield). ^{1}H-NMR (400 MHz, $CDCl_3$): δ 7.92 (d, J = 1.7 Hz, 2H), 7.75 (d, J = 8.1 Hz, 2H), 7.38 (dd, J = 8.1, 1.7 Hz, 2H), 1.12 (s, 42H). ^{13}C-NMR (101 MHz, $CDCl_3$) δ 141.04, 138.32, 137.97, 133.60, 133.22, 130.26, 125.23, 108.95, 95.16, 94.21, 21.38, 13.99.

((9,10-di(propan-2-ylidene)-9,10-dihydroanthracene-2,6-diyl)bis(ethyne-2,1-diyl))bis-(tri- isopropylsilane), 10

In a dry 100 mL flask equipped with a cooler under N_2, 2.1 mL of MeLi 1.6 M in Et_2O (3.4 mmol) and 3.4 mL of B-Methoxy-9-BBN 1M in hexanes (3.4 mmol) were added to 50 mL of dry THF. 653 mg

of **9** (0.74 mmol) and 86 mg of $Pd(PPh_3)_4$ were introduced and the system heated to reflux for 10 hours. The solvent was then removed under vacuum and the solid residue extracted with hot hexane. The solution was filtered trhough a plug of silica to obtain the pure product as an off-white solid (332 mg, 72% yield). ^{1}H-NMR (400 MHz, $CDCl_3$): δ 7.47 (s, 2H), 7.27 (s, broad, 4H), 2.12 (s, 6H), 2.07 (s, 6H), 1.13 (s, 42H).

2,6-diethynyl-9,10-di(propan-2-ylidene)-9,10-dihydroanthracene, 10.1

In a 250 mL flask, 332 mg of **10** (0.53 mmol) were dissolved in 125 mL of THF and the solution was put in an ice bath. 1.34 mL of tetrabutylammonium fluoride 1M in THF (containing 5% vv. water, 1.34 mmol) were added dropwise and the reaction was allowed to room temperature overnight. The solution was dried with Na_2SO_4 and preadsorbed on silica to be purified over a short silica column (hexane). The product was obtained as a white solid (160 mg, 99% yield). ^{1}H-NMR (400 MHz, $CDCl_3$): δ 7.51 (s, 2H), 7.32 (s, 4H), 3.05 (s, 2H), 2.11 (s, 6H), 2.08 (s, 6H). ^{13}C-NMR (101 MHz, $CDCl_3$) δ 141.80, 141.12, 133.78, 133.67, 133.23, 131.41, 130.34, 121.21, 86.76, 79.26, 34.26.

S,S'-(((9,10-di(propan-2-ylidene)-9,10-dihydroanthracene-2,6-diyl)bis(ethyne-2,1-diyl))bis (4,1-phenylene)) diethanethioate, AMe

In a dry Schlenk under N_2, 145 mg of **10.1** (0.47 mmol) and 386 mg of **IPhSAc** (1.39 mmol) were dissolved in 10 mL mL of dry THF. 60 mg of $Pd(PPh_3)_4$ and 32 mg of CuI were added followed by 1.5 mL of freshly distilled NEt_3 and the reaction was left at 50 °C overnight. The solution was poured in 100 mL DCM and 50 mL water under stirring and HCl 6 M was added dropwise until neutrality was reached. The organic phase was then extracted with water, dried over Na_2SO_4, and preadsorbed on silica. The product was purified via column chromatography (SiO_2, hexane:ethylacetate 5:1, Rf=0.4) and recrystallized from hexane. It was obtained as a white solid (95 mg, 33% yield). ^{1}H-NMR (400 MHz, $CDCl_3$): δ 7.57 – 7.52 (m, 6H), 7.41 – 7.31 (m, 8H), 2.43 (s, 6H), 2.15 (s, 6H), 2.11 (s, 6H). ^{13}C-NMR (101 MHz, $CDCl_3$) δ 193.47, 143.99, 138.98, 138.57, 134.18, 132.13, 130.99, 130.70, 130.66, 130.46, 128.32, 127.77, 124.75, 119.34, 30.26, 23.05. Elemental analysis, exp. (calc., %): C 78.41 (78.91), H 5.18 (5.30), O 5.65 (5.26), S 10.76 (10.53). HR-MS APCI for $C_{40}H_{33}O_2S_2$ calcd 609.19165, found 609.19429.

ethyl 2,2-difluoro-2-(9-hydroxy-10-oxo-2,6-bis((triisopropylsilyl)ethynyl)-9,10-dihydranthracen-9-yl)acetate, 12

In a dry 50 mL flask under N_2, 280 mg of **8** (0.49 mmol) and 0.1 mL of ethyl bromodifluoroacetate (0.79 mmol) were dissolved in 25 mL of dry THF and the solution placed in an ice bath. 0.8 mL of $ZnCl_2$ 0.9 M in hexanes (0.72 mmol) were added dropwise and the system was allowed to roo tmeperature overnight. 15 mL of HCl 1 M were added and the organic phase was extracted with NH_4Cl. It was then dried over Na_2SO_4. The product was obtained as an orange oil (255 mg, 80% yield). ^{1}H-NMR (400 MHz, $CDCl_3$): δ 8.22 (d, J = 1.7 Hz, 1H), 8.09 (d, J = 8.1 Hz, 1H), 7.97 (d, J = 1.5 Hz, 1H), 7.81 (d, J = 8.2 Hz, 1H), 7.70 (dd, J = 8.2, 1.8 Hz, 1H), 7.52 (dd, J = 8.1, 1.5 Hz, 1H), 2.48 (broad, 1H), 2.02 (q, J = 7.4 Hz, 2H), 1.15 (d, J = 3.3 Hz, 42H), 0.34 (t, J = 7.4 Hz, 3H).

2,6-dibromo-9,10-bis((trimethylsilyl)ethynyl)-9,10-dihydroanthracene-9,10-diol, 13

In a dry 100 mL flask under N_2, 1.15 mL of TMS-acetylene (8.2 mmol) were dissolved in 50 mL of dry THF and the solution moved in an ice/NaCl bath. 5.05 mL of *n*-butyllithium 1.6 M in hexanes (8.1 mmol) was added slowly and the system left for 1 hour. 500 mg of **1** (1.37 mmol) were added and the system allowed to rt ovetrnight. The solution was extracted with NH_4Cl aq. sat., dried over Na_2SO_4, and adsorbed on neutral alumina. It was purified through a small column (neutral Al_2O_3, hexane/ethylacetate 1:1). A yellow oil was obtained (336 mg, 44% yield). ^{1}H-NMR (400 MHz, $CDCl_3$): δ 8.16 (d, J = 1.9 Hz, 2H), 7.87 (d, J = 8.3, 2H), 7.54 (dd, J = 8.4, 2.0 Hz, 2H), 3.78 (s, 2H), 0.15 (s, 18H).

(((9,10-di(propan-2-ylidene)-9,10-dihydroanthracene-2,6-diyl)bis(ethyne-2,1-diyl)) bis(4,1-phenylene))bis(tert-butylsulfane), 11

In a dry 50 mL flask equipped with a cooler under N_2, 0.25 mL of MeLi 1.6 M in Et_2O (0.4 mmol) and 0.40 mL mL of B-Methoxy-9-BBN 1M in hexanes (0.4 mmol) were added to 25 mL of dry THF. After 10 minutes, 82 mg of **5** (0.1 mmol) and 10 mg of $Pd(PPh_3)_4$ were introduced and the system heated to reflux for 1 hour. The solvent was then removed under vacuum and the oily residue dissolved in DCM and filtered. The solution was absorbed on silica and purified through column chromatography (SiO_2, hexane/ethylacetate 10:1). The product was obtaine das an off-white solid (61 mg, 96% yield). ^{1}H-NMR (400 MHz, $CDCl_3$): δ 7.59 – 7.42 (m, 8H), 7.41 – 7.29 (m, 6H), 2.15 (s, 6H), 2.11 (s, 6H), 1.30 (s, 18H). ^{13}C-NMR (101 MHz, $CDCl_3$) δ 138.88, 138.57, 137.21, 131.45, 130.92, 130.61, 128.54, 128.42, 128.26, 127.76, 123.84, 119.48, 91.45, 88.38, 46.44, 30.98, 29.68.

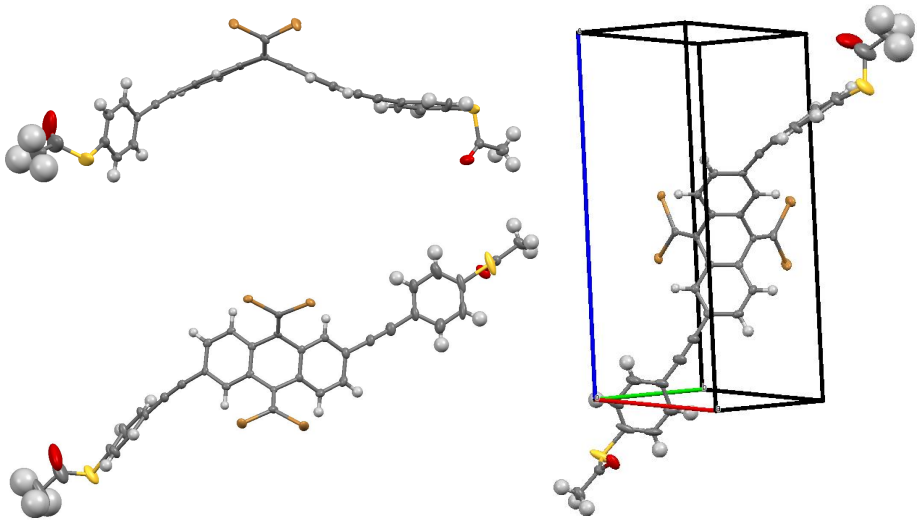

Figure 5.21 Crystal structure of **ABr**.

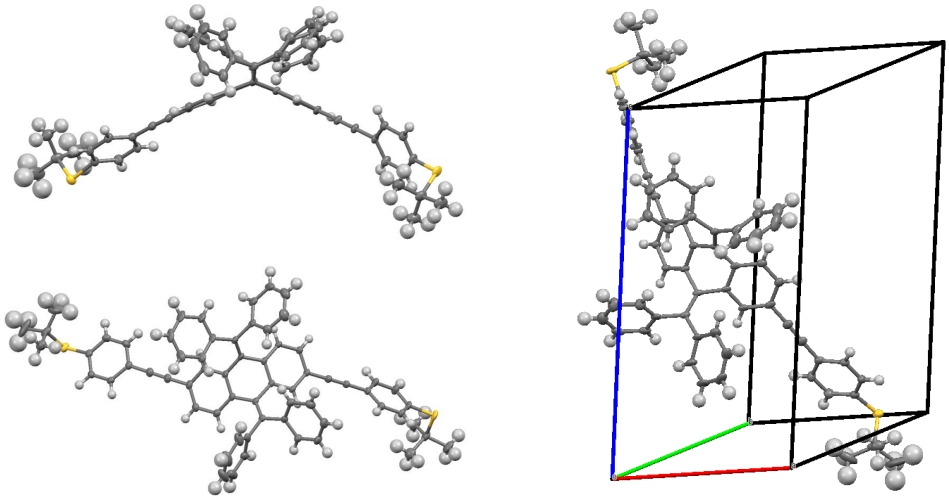

Figure 5.22 Crystal structure of **6**

Table 5.8 Crystallographic data for **ABr** and **APh**.

Compound	**ABr**	**APh**
Chemical formula	$C_{36}H_{20}Br_4O_2S_2$	$C_{64}H_{52}S_2$
M_r	868.28	885.17
Crystallographic System	triclinic	triclinic
Color, Habit	colorless, platelet	colourless, needle
Space Group	P -1	P -1
a (Å)	7.9990(5)	10.0873(7)
b (Å)	12.0346(8)	16.6335(12)
c (Å)	17.8718(11)	19.3200(19)
α (deg)	96.267(2)	69.741(3)
β (deg)	90.136(3)	87.735(3)
γ (deg)	108.018(2)	81.507(3)
V (Å^3)	1625.09(18)	2465.1(4)
Z	2	2
ρ_{calc} (g/cm^3)	1.774	1.193
μ (Mo K$^\alpha$, (cm^{-1})	0.71703	0.71073
F(000)	848	936
T (K)	100(2)	100(2)
θ range (deg)	2.74 - 27.19	3.018 - 26.428
Data collected (h,k,l)	-10:10, -15:15, -22:22	-12:12, -15:17, -24:24
no. of reflections collected	35850	31372
no. of independent reflections	9986	10012
observed reflections	7160 ($F_o \geq 2\sigma(F_o)$)	7103 ($F_o \geq 2\sigma(F_o)$)
R(F) (%)	6.44	5.73
wR(F^2) (%)	9.12	12.78
GooF	1.020	1.022
Parameters refined	399	601
restraints	20	0

BIBLIOGRAPHY

[1] Vilan, A.; Aswal, D.; Cahen, D. *Chem. Rev.* **2017**, *117*, 4248–4286.

[2] Xiang, D.; Wang, X.; Jia, C.; Lee, T.; Guo, X. *Chem. Rev.* **2016**, *116*, 4318–4440.

[3] Solomon, G. C. *Cross Conjugation: Dendralene, Radialene and Fulvalene Chemistry*; Wiley-VCH Verlag GmbH & Co. KGaA, 2016; pp 397–412.

[4] Lambert, C. J. *Chem. Soc. Rev.* **2015**, *44*, 875–888.

[5] Lambert, C. J.; Liu, S.-X. *Chem. Eur. J.* **2017**, *24*, 4193–4201.

[6] Garner, M. H.; Li, H.; Chen, Y.; Su, T. A.; Shangguan, Z.; Paley, D. W.; Liu, T.; Ng, F.; Li, H.; Xiao, S.; Nuckolls, C.; Venkataraman, L.; Solomon, G. C. *Nature* **2018**, *406*, 1.

[7] Nozaki, D.; Avdoshenko, S. M.; Sevinçli, H.; Cuniberti, G. *Journal of Applied Physics* **2014**, *116*, 074308–.

[8] Puebla-Hellmann, G.; Venkatesan, K.; Mayor, M.; Lörtscher, E. *Nature* **2018**, *559*, 232–235.

[9] Markussen, T.; Stadler, R.; Thygesen, K. S. *Nano Lett.* **2010**, *10*, 4260–4265.

[10] Tsuji, Y.; Hoffmann, R.; Movassagh, R.; Datta, S. *J. Chem. Phys.* **2014**, *141*, 224311–.

[11] Fracasso, D.; Valkenier, H.; Hummelen, J. C.; Solomon, G. C.; Chiechi, R. C. *J. Am. Chem. Soc.* **2011**, *133*, 9556–9563.

[12] Pedersen, K. G. L.; Borges, A.; Hedegård, P.; Solomon, G. C.; Strange, M. *J. Phys. Chem. C* **2015**, *119*, 26919–26924.

[13] Manrique, D. Z.; Huang, C.; Baghernejad, M.; Zhao, X.; Al-Owaedi, O. a.; Sadeghi, H.; Kaliginedi, V.; Hong, W.; Gulcur, M.; Wandlowski, T.; Bryce, M. R.; Lambert, C. J. *Nat. Commun.* **2015**, *6*, 6389.

[14] Gantenbein, M.; Wang, L.; Al-jobory, A. A.; Ismael, A. K.; Lambert, C. J.; Bryce, M. R. *Sci. Rep.* **2017**, *7*, 1794.

[15] Solomon, G. C.; Herrmann, C.; Vura-Weis, J.; Wasielewski, M. R.; Ratner, M. A. *J. Am. Chem. Soc.* **2010**, *132*, 7887–7889.

[16] Carlotti, M.; Kovalchuk, A.; Wächter, T.; Qiu, X.; Zharnikov, M.; Chiechi, R. C. *Nat. Commun.* **2016**, *7*, 13904.

[17] Lykkebo, J.; Gagliardi, A.; Pecchia, A.; Solomon, G. C. *J. Chem. Phys.* **2014**, *141*, 124119.

[18] Garner, M. H.; Solomon, G. C.; Strange, M. *J. Phys. Chem. C* **2016**, *120*, 9097–9103.

[19] Liu, X.; Sangtarash, S.; Reber, D.; Zhang, D.; Sadeghi, H.; Shi, J.; Xiao, Z.-Y.; Hong, W.; Lambert, C. J.; Liu, S.-X. *Angew. Chem., Int. Ed.* **2017**, *56*, 173–176.

[20] Valkenier, H.; Guedon, C. M.; Markussen, T.; Thygesen, K. S.; van der Molen, S. J.; Hummelen, J. C. *Phys. Chem. Chem. Phys.* **2014**, *16*, 653–662.

[21] Koole, M.; Thijssen, J. M.; Valkenier, H.; Hummelen, J. C.; Zant, H. S. J. v. d. *Nano Lett.* **2015**, *15*, 5569–5573.

[22] Baghernejad, M.; Zhao, X.; Baruël Ørnsø, K.; Füeg, M.; Moreno-García, P.; Rudnev, A. V.; Kaliginedi, V.; Vesztergom, S.; Huang, C.; Hong, W.; Broekmann, P.; Wandlowski, T.; Thygesen, K. S.; Bryce, M. R. *J. Am. Chem. Soc.* **2014**, *136*, 17922–17925.

[23] Bergfield, J. P.; Heitzer, H. M.; Van Dyck, C.; Marks, T. J.; Ratner, M. A. *ACS Nano* **2015**, *9*, 6412–6418.

[24] Guedon, C. M.; Valkenier, H.; Markussen, T.; Thygesen, K. S.; Hummelen, J. C.; Van Der Molen, S. J. *Nat. Nanotechnol.* **2012**, *7*, 305–309.

[25] Zhang, Y.; Ye, G.; Soni, S.; Qiu, X.; Krijger, T. L.; Jonkman, H. T.; Carlotti, M.; Sauter, E.; Zharnikov, M.; Chiechi, R. C. *Chem. Sci.* **2018**, *9*, 4414–4423.

[26] Chiechi, R. C.; Weiss, E. A.; Dickey, M. D.; Whitesides, G. M. *Angew. Chem., Int. Ed.* **2008**, *120*, 148–150.

[27] Garcìa, R.; Ángeles Herranz, M.; Leary, E.; Gonzàlez, M. T.; Bollinger, G. R.; Bürkle, M.; Zotti, L. A.; Asai, Y.; Pauly, F.; Cuevas, J. C.; Agraít, N.; Martín, N. *Beilstein Journal of Organic Chemistry* **2015**, *11*, 1068–1078.

[28] Solomon, G. C.; Andrews, D. Q.; Goldsmith, R. H.; Hansen, T.; Wasielewski, M. R.; Van Duyne, R. P.; Ratner, M. a. *J. Am. Chem. Soc.* **2008**, *130*, 17301–17308.

[29] Yang, Y. et al. *J. Phys. Chem. C* **2018**, *122*, 14965–14970.

[30] Lacroix, J. C. *Current Opinion in Electrochemistry* **2018**, *7*, 153–160.

[31] Kovalchuk, A.; Egger, D. A.; Abu-Husein, T.; Zojer, E.; Terfort, A.; Chiechi, R. C. *RSC Adv.* **2016**, *6*, 69479–69483.

[32] Zhang, Y.; Qiu, X.; Gordiichuk, P.; Soni, S.; Krijger, T. L.; Herrmann, A.; Chiechi, R. C. *J. Phys. Chem. C* **2017**, *121*, 14920–14928.

[33] Chen, S.; Zhou, W.; Zhang, Q.; Kwok, Y.; Chen, G.; Ratner, M. A. *J. Phys. Chem. Lett.* **2017**, *8*, 5166–5170.

[34] Garner, M. H.; Hoffmann, R.; Rettrup, S.; Solomon, G. C. *ACS Cent. Sci.* **2018**, *4*, 688–700.

[35] Tsuji, Y.; Stuyver, T.; Gunasekaran, S.; Venkataraman, L. *J. Phys. Chem. C* **2017**, *121*, 14451–14462.

[36] Garner, M. H.; Bro-Jørgensen, W.; Pedersen, P. D.; Solomon, G. C. *J. Phys. Chem. C* **2018**, –.

[37] Bureš, F.; Schweizer, W. B.; Boudon, C.; Gisselbrecht, J.-P.; Gross, M.; Diederich, F. *Eur. J. Org. Chem.* **2008**, *2008*, 994–1004.

[38] Glatzhofer, D. T.; Liang, Y.; Khan, M. A. *Organometallics* **1993**, *12*, 624–632.

[39] Green, J. E.; Wook Choi, J.; Boukai, A.; Bunimovich, Y.; Johnston-Halperin, E.; DeIonno, E.; Luo, Y.; Sheriff, B. A.; Xu, K.; Shik Shin, Y.; Tseng, H.-R.; Stoddart, J. F.; Heath, J. R. *Nature* **2007**, *445*, 414–.

[40] Weiss, E. A.; Kaufman, G. K.; Kriebel, J. K.; Li, Z.; Schalek, R.; Whitesides, G. M. *Langmuir* **2007**, *23*, 9686–9694.

[41] Valkenier, H.; Huisman, E. H.; van Hal, P. A.; de Leeuw, D. M.; Chiechi, R. C.; Hummelen, J. C. *J. Am. Chem. Soc.* **2011**, *133*, 4930–4939.

[42] Tseng, T.-C. et al. *Nat. Chem.* **2010**, *2*, 374–.

[43] Markussen, t.; Schitz, J.; Thygesen, K. S. *The Journal of Chemical Physics* **2010**,

[44] Carlotti, M.; Soni, S.; Kumar, S.; Ai, Y.; Sauter, E.; Zharnikov, M.; Chiechi, R. C. *Angew. Chem. Int. Ed.* **2018**, *0*, –.

[45] Dubi, Y. *J. Phys. Chem. C* **2014**, *118*, 21119–21127.

[46] Pourhossein, P.; Vijayaraghavan, R. K.; Meskers, S. C. J.; Chiechi, R. C. *Nat. Commun.* **2016**, *7*, 11749–.

[47] Vilan, A. *Phys. Chem. Chem. Phys.* **2017**, *19*, 27166–27172.

[48] Xie, Z.; Bâldea, I.; Demissie, A. T.; Smith, C. E.; Wu, Y.; Haugstad, G.; Frisbie, C. D. *J. Am. Chem. Soc.* **2017**, *139*, 5696–5699.

[49] Venkataraman, L.; Klare, J. E.; Nuckolls, C.; Hybertsen, M. S.; Steigerwald, M. L. *Nature* **2006**, *442*, 904–.

[50] Carlotti, M.; Degen, M.; Zhang, Y.; Chiechi, R. C. *J. Phys. Chem. C* **2016**, *120*, 20437–20445.

[51] Tai, Y.; Shaporenko, A.; Rong, H.-T.; Buck, M.; Eck, W.; Grunze, M.; Zharnikov, M. *J. Phys. Chem. B* **2004**, *108*, 16806–16810.

[52] Zharnikov, M. *J. Electron Spectrosc. Relat. Phenom.* **2010**, *178–179*, 380–393.

[53] Schreiber, F. *Prog. Surf. Sci.* **2000**, *65*, 151–257.

[54] Aitchison, H.; Lu, H.; Hogan, S. W. L.; Früchtl, H.; Cebula, I.; Zharnikov, M.; Buck, M. *Langmuir* **2016**, *32*, 9397–9409.

[55] Stohr, J. *NEXAFS Spectroscopy*; Springer-Verlag Berlin Heidelberg, 1992.

[56] Horsley, J. A.; Stöhr, J.; Hitchcock, A. P.; Newbury, D. C.; Johnson, A. L.; Sette, F. *The Journal of Chemical Physics* **1985**, *83*, 6099–6107.

[57] Yokoyama, T.; Seki, K.; Morisada, I.; Edamatsu, K.; Ohta, T. *Physica Scripta* **1990**, *41*, 189–.

[58] Hamoudi, H.; Kao, P.; Nefedov, A.; Allara, D. L.; Zharnikov, M. *Beilstein J. Nanotechnol.* **2012**, *3*, 12–24.

[59] Frey, S.; Stadler, V.; Heister, K.; Eck, W.; Zharnikov, M.; Grunze, M.; Zeysing, B.; Terfort, A. *Langmuir* **2001**, *17*, 2408–2415.

[60] Shaporenko, A.; Adlkofer, K.; Johansson, L.; Tanaka, M. *Langmuir* **2003**, *19*, 4992–4998.

[61] Zhao, A.; Tan, S.; Li, B.; Wang, B.; Yang, J.; Hou, J. G. *Phys. Chem. Chem. Phys.* **2013**, *15*, 12428–12441.

[62] Neese, F. *Wiley Interdiscip. Rev.: Comput. Mol. Sci.* **2012**, *2*, 73–78.

[63] Neese, F. *Wiley Interdisciplinary Reviews: Computational Molecular Science*

[64] Herrmann, C.; Gross, L.; Steenbock, T.; Deffner, M.; Voigt, B. A.; Solomon, G. C. ARTAIOS - A Transport Code for Postprocessing Quantum Chemical Electronic Structure Calculations, Available From https://www.chemie.uni-hamburg.de/ac/herrmann/software/index.html. 2016.

[65] Herrmann, C.; Solomon, G. C.; Subotnik, J. E.; Mujica, V.; Ratner, M. A. *J. Chem. Phys.* **2010**, *132*, 024103.

[66] Weigend, F.; Ahlrichs, R. *Phys. Chem. Chem. Phys.* **2005**, *7*, 3297–3305.

[67] Bilić, A.; Reimers, J. R.; Hush, N. S. *The Journal of Chemical Physics* **2005**, *122*, 094708.

[68] Schlicke, H.; Herrmann, C. *ChemPhysChem* **2014**, *15*, 4011–4018.

[69] Humphrey, W.; Dalke, A.; Schulten, K. *Journal of Molecular Graphics* **1996**, *14*, 33–38.

[70] Nerngchamnong, N.; Yuan, L.; Qi, D.-C.; Li, J.; Thompson, D.; Nijhuis, C. a. *Nat. Nanotechnol.* **2013**, *8*, 113–118.

[71] Cabarcos, O. M.; Schuster, S.; Hehn, I.; Zhang, P. P.; Maitani, M. M.; Sullivan, N.; Giguère, J.-B.; Morin, J.-F.; Weiss, P. S.; Zojer, E.; Zharnikov, M.; Allara, D. L. *The Journal of Physical Chemistry C* **2017**, *121*, 15815–15830.

[72] Abu-Husein, T.; Schuster, S.; Egger, D. A.; Kind, M.; Santowski, T.; Wiesner, A.; Chiechi, R. C.; Zojer, E.; Terfort, A.; Zharnikov, M. *Adv. Funct. Mater.* **2015**, *25*, 3943–3957.

[73] Kovalchuk, A.; Abu-Husein, T.; Fracasso, D.; Egger, D. A.; Zojer, E.; Zharnikov, M.; Terfort, A.; Chiechi, R. C. *Chem. Sci.* **2016**, *7*, 781–787.

6

A Two-Terminal Molecular Memory

Here we describe large-area molecular tunneling junctions comprising self-assembled monolayers of redox-active molecules that exhibit two-terminal bias switching. The as-prepared monolayers undergo partial charge-transfer to the underlying metal substrate (Au, Pt or Ag) that converts their cores from a quinoid to hydroquinoid form, thus changing the bond topology from a cross-conjugated to linearly-conjugated π system. We exploit this relationship to create non-volatile memory in proto-devices. The underlying switching mechanism reorders bond topology without changing connectivity or altering the tunneling distance or thickness of the monolayer. These results are a proof-of-concept for switching quantum interference features on and off via in operando redox chemistry.

I would like to thank S. Soni for the help with transport calculation, E. Saulter and Prof. M. Zharnikov for the syncrhotron characterization of the samples.

6.1. INTRODUCTION

In Chapter 4 and 5 we already discussed the concept of Quantum Interference (QI), a collection of phenomena related to Fermions whose wave functions can interfere with themselves; in molecular tunneling junctions, destructive QI can lower the transmission probability between the electrodes, significantly lowering conductance without altering the tunneling distance,[1] thus making the compounds that show it, good candidate fro the application in molecular switches, memory devices, or transistors.[2**?** , 3] Destructive QI effects have been studied both theoretically and in multiple experimental platforms. In π-conjugated molecules, they are generally ascribed to cross-conjugation,[4–7] meta-substitution,[8, 9] or particular spatial arrangements.[10, 11]

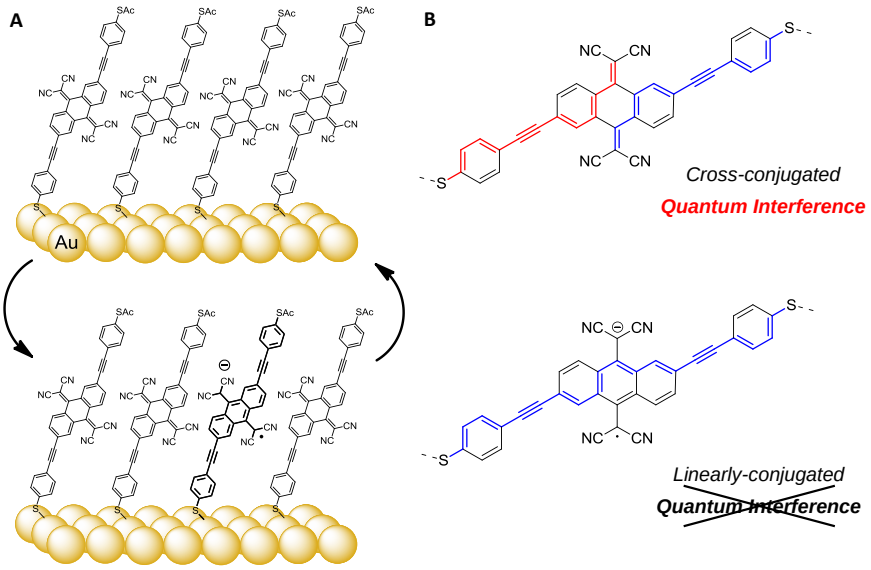

Figure 6.1 (A) A pure monolayer of **TCNAQ** in the cross-conjugated quinoid form is reversibly switched to a mixed-monolayer in which a fraction of the molecules are reduced to a linearly-conjugated, hydroquinoid form; (B) Difference in conjugation pathways between the cross-conjugated neutral form (top), which give rise to destructive QI, and the linearly-conjugated reduced form.

Of particular interest are systems capable of toggling QI effects via external inputs;[12–14] however, control over QI effects is currently limited to transient, single-molecule junctions and/or comparisons of different compounds in different environments,[15–

17] for example, the *ex operando* (electro)chemical interconversion between a cross-conjugated quinone and linearly-conjugated hydroquinone.[18, 19]

In this work we show that self-assembled monolayers (SAMs) of a cross-conjugated compound incorporating a tetracyanoquinodimethane (TCNQ) unit, **TCNAQ** (Figure 6.1, already intruduced in Chapter 5), on different metal substrates can be switched between, and addressed in, two conductance states (ON and OFF) in a two-terminal proto-device using eutectic Ga-In (EGaIn) top-contacts. We ascribe the different conductance states to the modulation of the bond topology of the molecule; **TCNAQ**—just as TCNQ—can readily accept an electron and form a stable (di)anion that converts cross-conjugated pathways to linearly-conjugated pathways, altering the transmission probability similarly to interconversion of quinones and hydroquinones (Figure 6.1).[20] A low-lying LUMO brings the reduction potential of **TCNAQ** close to the oxidation potential of Au, Ag and Pt electrodes, eliminating the need for a third electrode or redox agents.

6.2. PREPARATION AND CHARACTERIZATION OF THE SAMS

We prepared SAMs of **TCNAQ** on Au, Ag or Pt surfaces from the thioacetate precursor via *in situ* deprotection.[21] In Chapter 5 we already mentioned how, for SAMs of **TCNAQ** on Au^{mica}, X-ray photoelectron spectroscopy (XPS) spectra are consistent with upright-standing molecules attached to the surface through a single thiolate bond (Figure 6.2). Notably, the N 1s region of the XPS spectrum of the SAM features an additional peak at lower binding energy (398.5 eV) that is not present in the spectra of **TCNAQ** powder, which we ascribe to the spontaneous (partial) reduction of **TCNAQ** by the metal substrate. Similar shifts are common in monolayers of TCNQ that are spontaneously reduced by the underlying metal.[22] There, TCNQ is directly adsorbed to the metal substrate while, in SAMs of **TCNAQ**, the redox-active core is bound through a phenylacetylene arm that is coupled to the surface through a covalent S-Au bond. Thus, charge-transfer (redox) can still occur in a geometry that is compatible with the formation of metal-molecule-metal junctions. In the XPS spectra, about 14 % of **TCNAQ** molecules in the SAM are in a reduced state.

Near edge X-ray absorption fine structure (NEXAFS) measurements provided addi-

tional evidence that the nitrile groups are oriented predominantly parallel to the substrate (see Experimental Section).

The SAMs grown on Au^{TS} were of somewhat lower quality: in the N 1s spectra we found all the peaks that we reported previously and an extra peak at 400.8 eV that indicates the existence of N^+ group that we attributed to residual DBU in the SAMs;[23] the S 2p spectra shows peaks at 162.2 eV and 161.3 eV that we ascribed to gold-sulfur bonds at the regular sites and step edges respectively,[23, 24] and at 164.2 eV and 163.5 eV for disulfide in the SAM and the unbound top thioacetate. These differences between Au^{TS} and Au^{mica} did not influence the observed transport features as we will later discuss.

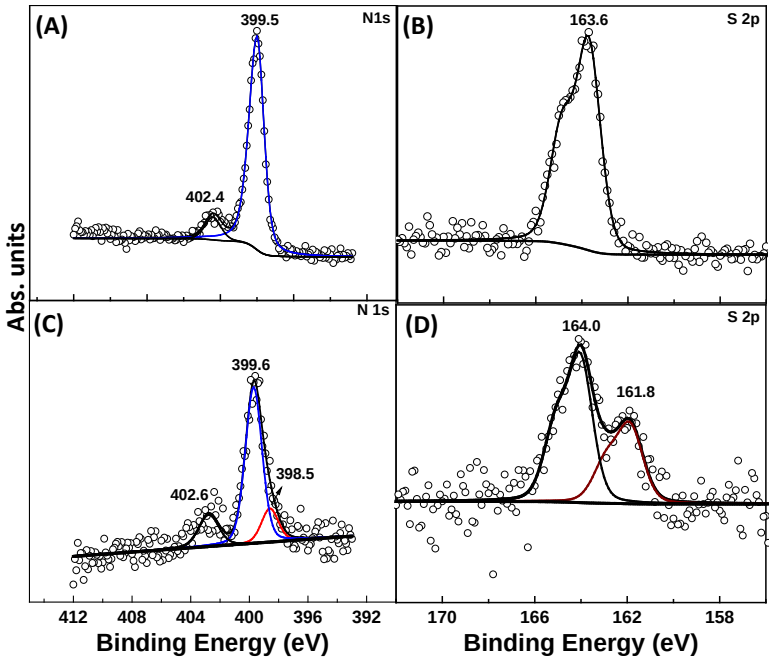

Figure 6.2 XPS spectra of N 1s (left) and S 2p2/3 (right) core levels for powder samples of **TCNAQ** (top) and SAMs of **TCNAQ** on Au^{mica} (bottom) presented in CHapter 5 but showing the raw data points as open circles instead of being connected by a line. The peak at 398.5 eV, which is present only in the monolayer, indicates the presence of a non-stoichiometric, reduced nitrogen-containing species.

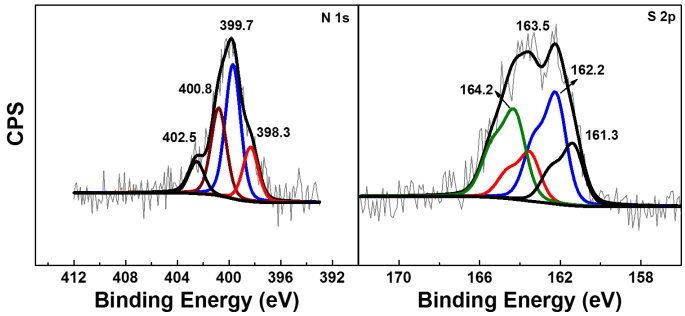

Figure 6.3 XPS spectra of N 1s and Sr 2p2/3 core levels for SAMs of **TCNAQ** on Au^{TS} deprotected by DBU. N 1s spectra: All other peaks have similar binding energy as shown in Figure 2 of the main text.

6.3. ELECTRICAL CHARACTERIZATION OF **TCNAQ** SAMS

We investigated the electrical properties of **TCNAQ** in Au^{mica}/SAM//EGaIn junctions (where '/' and '//' denoted covalent and Van der Waals interaction respectively; EGaIn stands for Gallium-Indium alloy at its eutectic composition; Au^{mica} indicates gold deposited on mica). EGaIn is a liquid metal that can be used to form stable, conformal, non-damaging contacts with SAMs with a diameter of about 20 µm.[25–27] This methodology enables the formation of junctions in multiple areas of a substrate rapidly and reproducibly, allowing the collection of statistically significant data and spectroscopic investigation of the SAM after J/V cycling.[23] As controls, we measured junctions comprising hexadecanethiol (**CSH**), a saturated molecule of similar length we already encountered in Chapter 2, and analogs of **TCNAQ** bearing an anthraquinone core (**AQ**) or a linearly-conjugated, non-redox-active anthracene core (**AC**), compounds already introduced in Chapter 5 and 4.

Figure 6.4 shows forward and reverse J/V traces for junctions comprising **TCNAQ** (A), **AC** (B), **CSH** (C) and **AQ** (D). While the J/V traces of junctions comprising the latter three compounds are perfectly overlapping, **TCNAQ** exhibits a hysteresis loop at negative bias; *i.e.*, after being biased at positive voltages, the conductance at negative bias decreases (OFF) and then recovers its initial conductance (ON) after reaching −1.00 V. A maximum ratio of J between forward and reverse scan of 2.6 occurs at −0.65 V. As shown in Figure 6.5, the hysteresis and magnitude of switching is reproducible across junctions

comprising **TCNAQ** measured on Au^{mica} and Au^{TS} and Ag^{TS}. The effect is present but diminished on Pt^{TS}. No hysteresis or switching is present on any substrate for **AC**, **AQ** or **CSH**.

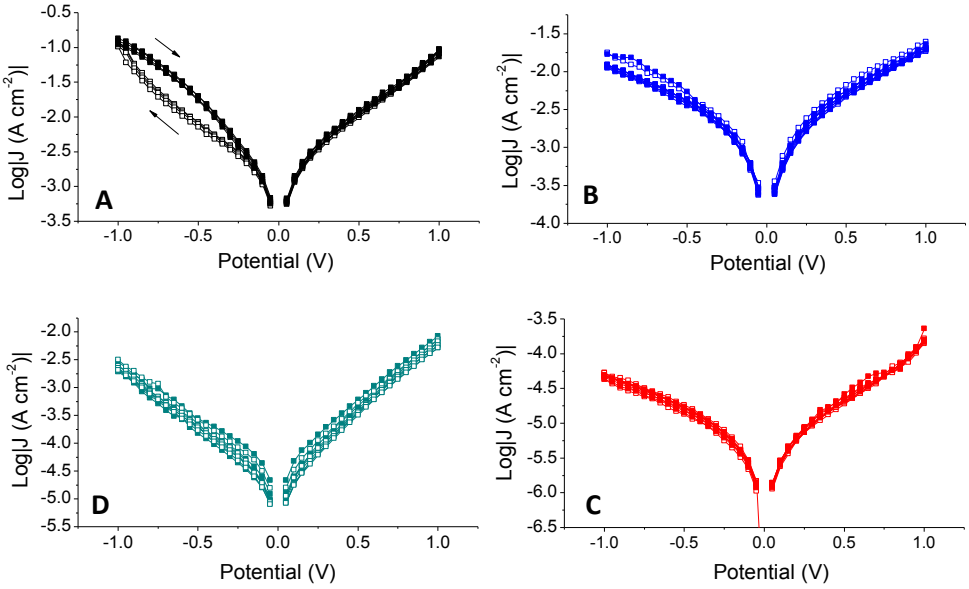

Figure 6.4 Examples of $\log|J|$ vs. V of junctions comprising SAMs of **TCNAQ** on Au^{TS} (A, black), **AC** (B, blue), **CSH** (C, red), **AQ** (on Au^{mica}, D, cyan). Solid dots represent data acquired during five forward scans ranging from −1.00 V to 1.00 V (in 0.05 V steps, acquired every 0.1 s), while open dots represent data acquired during five subsequent reverse scans from 1.00 V to −1.00 V.

Ensemble junctions comprising SAMs of **TCNAQ** exhibit a relatively high conductance, comparable to the linearly-conjugated analog **AC**, which does not exhibit any QI features. We ascribe the difference between **TCNAQ** in SAMs and in single-molecule junctions to the presence of reduced **TCNAQ** in the SAM (Figure 6.2C).[28] Tunneling charge-transport through SAMs is sensitive to the entire supramolecular structure of the monolayer, which comprises molecules in different conformations and, in the case of **TCNAQ**, redox states.[11, 29]

The addition of one or two electrons converts the cross-conjugated quinoid core into a linearly conjugated, fully aromatic hydroquinoid. (The driving force of rearomatization is the reason that TCNQ is an exceptional electron-acceptor.) Treating each mo-

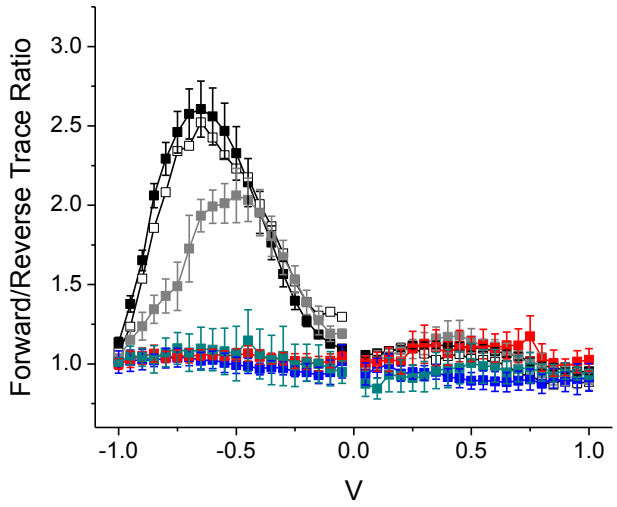

Figure 6.5 Plot of trace over retrace ratio for junctions comprising: (**A**) SAMs of **TCNAQ** on Au^{TS} (black), Au^{mica} (hollow), and Ag^{TS} (gray), **C16SH** on Ag^{TS} (red), **AC** on Au^{TS} (blue), **AQ** on Au^{mica} (cyan). Error bars represent confidence intervals with $\alpha = 0.05$ (for **TCNAQ** on Au^{mica} they were omitted for clarity).

lecule in a SAM as a resistor in parallel, it follows from Kirchoff's rules that a small fraction of reduced **TCNAQ** molecules can dominate charge-transport through the SAM due to the exponential difference in the conductance of **TCNAQ** in the cross- and linearly-conjugated (quinoid/hydroquinoid) forms.[30] Specifically, if two pathways in a SAM differ in conductance by two orders of magnitude (similar to **AQ** and **AC** at 0.50 V), the presence of only 1 % to 2 % of the more conductive pathways is sufficient to dominate the conductivity of the SAM.[31] Thus, the hysteresis and switching phenomenon are most likely caused by a shift in the equilibrium between the low- and high-conductance states of **TCNAQ**; applying a bias to the junction affects the fraction of molecules in the junction that exhibit destructive QI.

In the current work, we have no way of estimating what fraction of molecules might be in the high/low conductance states in an assembled junction, under bias. We can however estimate the percentage of reduced nitrogen species that were present in the SAM during the XPS measurement, which is about 14%.

Perhaps coincidentally, that is the almost the exact percentage at which we predict the conductance to match the high-conductance of the hysteresis loop according to a

model provided by Weiss *et al.* (Eq. 6.1) for estimating the total current flowing through a junction as a function of the fraction of molecules in the high-conductance state.[31]

$$J = \chi J_0 e^{-\beta d} + (1-\chi) J_i \tag{6.1}$$

The model uses an estimate of the value of β (the tunneling decay coefficient) for the reduced form of **TCNAQ**, which we took from the experimental value of oligo(phenylene ethylene) wires in EGaIn junctions in Chapter 2, the molecular length, injection current (J_0) and the experimental value, J_i, which is the current in the low-conductance state.

This estimate shows the height of the hysteresis loop is commensurate with the observed fraction of reduced nitrogen species that we assign to reduced **TCNAQ**. It does not, of course, explain why **TCNAQ** is as conductive as **AC**. One possibility is that **TCNAQ** adopts a more planar geometry in the SAM, which can have dramatic effects on conductance.[11] Another is that the low bandgap of reduced **TCNAQ** makes it far more conductive[32] than the model above predicts (i.e., J_0 is much larger or β is much smaller) and that a small fraction of it persists even in the low-conductance state. As Figure 6.6 shows, the influence of high-conductance molecules in a SAM is exponential and a very small amount of residual **TCNAQ** in the reduced form would be sufficient to shift the conductance to overlap with **AC**.

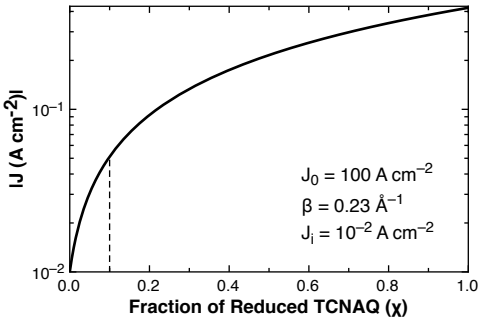

Figure 6.6 Effect on total current density J when increasing the fraction of high-conductance channels J_i according to Eq. 6.1, which was taken from Ref. 31. The dashed line corresponds to the fraction of high-conductance molecules required to give the experimentally-observed value of J ($\chi \approx 0.1$).

6.4. PERFORMANCE OF TCNAQ SAMS IN MEMORY DEVICES

Given sufficient trace/re-retrace stability, hysteresis is a form of two-terminal bias-switching,[33–48] but to translate it into a memory effect, the state of a static, two-terminal junction must be switched reversibly between at least two conductance-states *in operando*. To characterize the memory effects of Metal/SAM//EGaIn junctions, we performed Write operations (W) by applying a −1.50 V bias, which puts the junction in the high-conductance ON state and Erase operations (E) by applying 1.00 V, which puts it in the low-conductance OFF state. We read the state at −0.50 V, measuring current-densities J of 0.10 Acm^{-2} to 0.01 Acm^{-2}. Figure 6.7A compares the resulting ON/OFF ratios for junctions comprising SAMs of **TCNAQ**, **AC**, **AQ** and **CSH** on Au over four switching cycles. As expected, the ON/OFF ratio for the controls (**AC**, **AQ** and **CSH**) is 1, indicating no effect. However, **TCNAQ** exhibits ratios as high as 6 ± 2. Figure 6.7B shows that the memory effect is identical for Au^{mica} and Au^{TS}, while data for Ag^{TS} are characterized by a broader distribution which make the comparison weak. As shown in Figure 6.7, the ON/OFF ratio of **TCNAQ** slowly decreases, approaching 2 after about 10 cycles; however, even after 30 cycles, applying a −2.00 V bias restores the initial ON/OFF ratio. It is worth mentioning that, in doing so, there is a higher chance of shorting the junction.

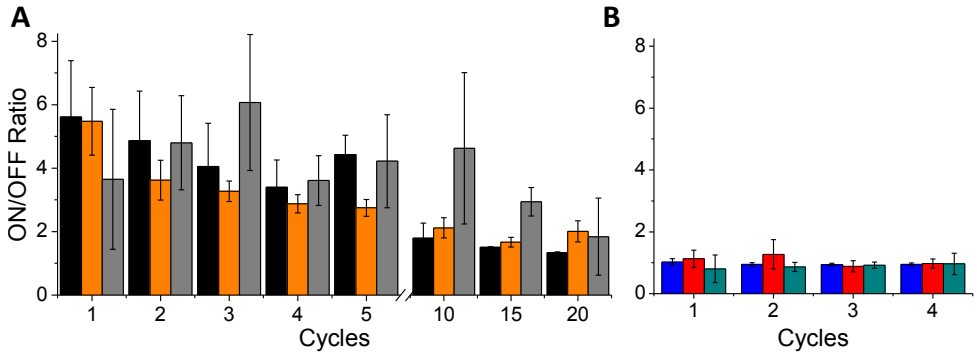

Figure 6.7 ON/OFF Ratio per n^{th} Write-Erase cycle, calculated as ratio of the current after and before the n^{th} Write operation for: (**A**) SAMs of **TCNAQ** on Au^{TS} (black), Au-on-mica (orange), and Ag^{TS} (gray), and (**B**) SAMs of C16SH on Ag^{TS} (red), AC on Au^{TS} (blue), and AQ on Au-on-mica (cyan). The error is calculated as confidence interval with $\alpha = 0.05$.

Metal/SAM//EGaIn junctions are generally stable unless a bad contact is formed.

Table 6.1 Variation in the OFF state current between one cycle and the following calculated as percentage.

Cycles	**TCNAQ** Au^{TS}	**TCNAQ** Au^{mica}	**TCNAQ** Ag^{TS}	**AQ**	**AC**	**C16SH**
1st	-21%	+1%	-44%	-21%	-12%	-10%
2nd	-17%	-30%	-5%	-16%	-18%	-17%
3rd	-15%	-20%	-17%	-9%	-18%	-11%
4th	-14%	-18%	-9%	-14%	-16%	-11%
5th	-11%	-11%	-12%	-11%	-13%	-10%
10th	-7%					
15th	-10%					
20th	-6%					

This is also the case of the $J-V$ traces recorded in this work for the various system as can be observed in Figure 6.4 where no significant variation of $Log|J(V)|$ is found across the different cycles. On the other hand, the scenario is different when it comes to the junctions used for the WRER operations: as we can observe in Figures 6.8-6.13, the values of current - both in the high and low conductance states - tend to decrease constantly with the number of WRER cycles. These data are summarized in Table 6.1.

Although the rate can differ from one system to the other, a general decrease per cycles between 10% and 20% is found among all the systems, from **TCNAQ**, to other conjugated molecules, to the saturated **C16SH**. The cause of this phenomenon is unknown, but, bearing in mind its ubiquity among the different SAMs and substrates, a viable hypothesis involves a role of the EGaIn top electrode, rather than a decaying of the monolayer cause by the repeated switching cycles. It has been shown that, when applying a bias larger than ±1 V for prolonged period of time, electrochemistry at the EGaIn oxide interface might not be negligible and play a role in the conductance of the junction:[49] when performing the WRER cycles experiments, the EGaIn electrode is suddenly exposed to relatively large opposite biases which may affect the contact (*i.e.* wetting, coupling, shape, stress, etc.) between the top electrode and the SAM, thus decreasing the current. A similar but less pronounced decrease was also found when a bias of −1 V was used in the *W* operation (about 8% per cycle).

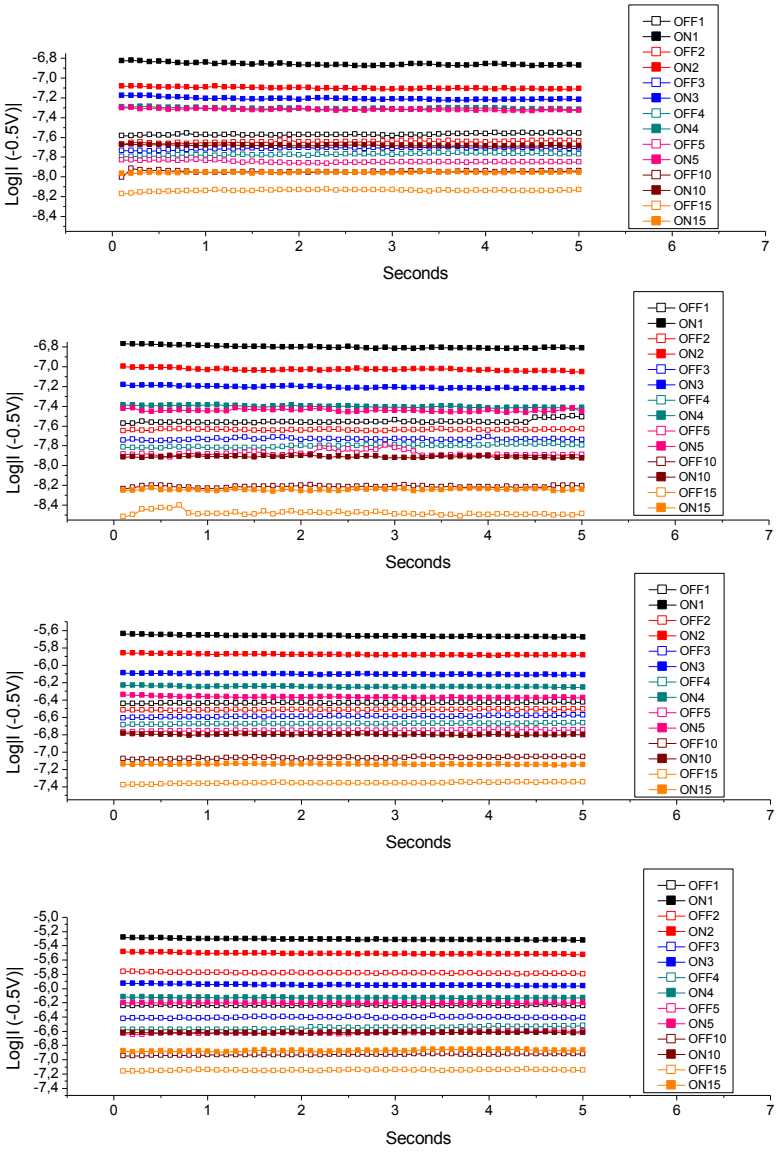

Figure 6.8 Examples of R_{ON} (solid symbols) and R_{OFF} (hollow symbols) for different Au^{mica}/**TCNAQ**//EGaIn for different cycles as reported in the legend.

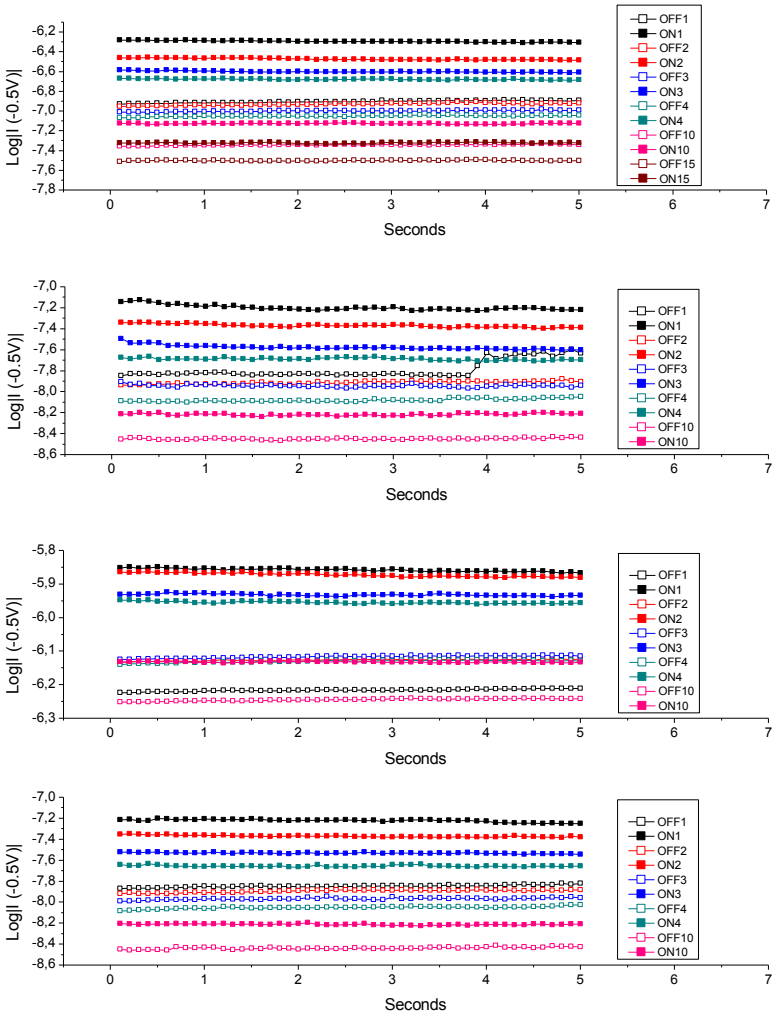

Figure 6.9 Examples of R_{ON} (solid symbols) and R_{OFF} (hollow symbols) for different Au^{TS}/**TCNAQ**//EGaIn for different cycles as reported in the legend.

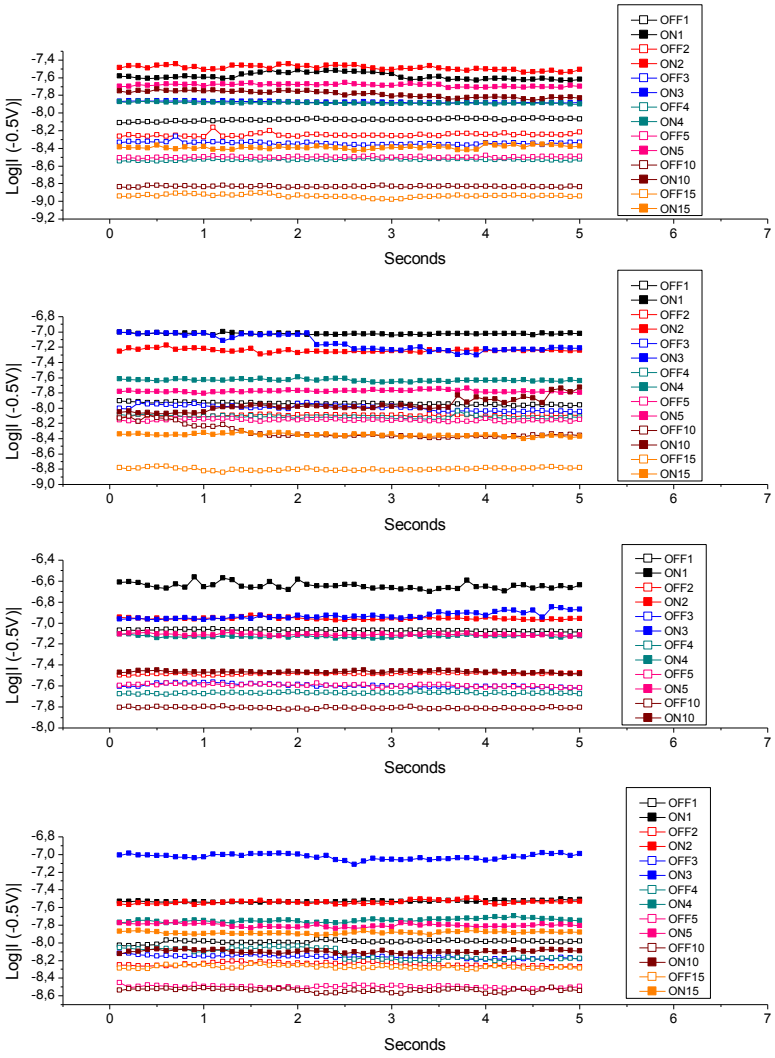

Figure 6.10 Examples of R_{ON} (solid symbols) and R_{OFF} (hollow symbols) for different Ag^{TS}/**TCNAQ**//EGaIn for different cycles as reported in the legend.

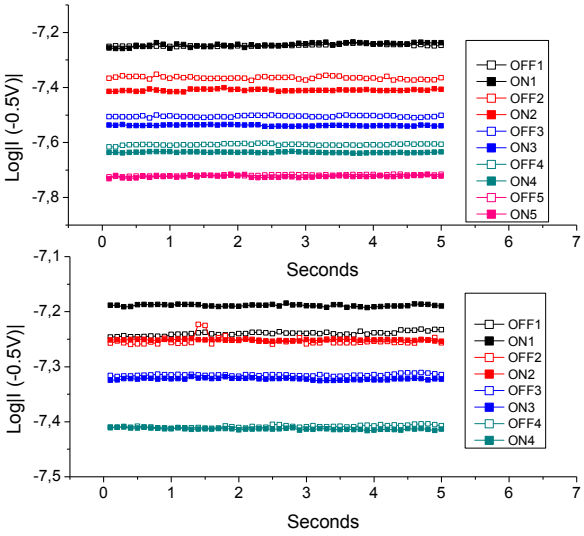

Figure 6.11 Examples of R_{ON} (solid symbols) and R_{OFF} (hollow symbols) for different Au^{TS}/**AC**//EGaIn for different cycles as reported in the legend.

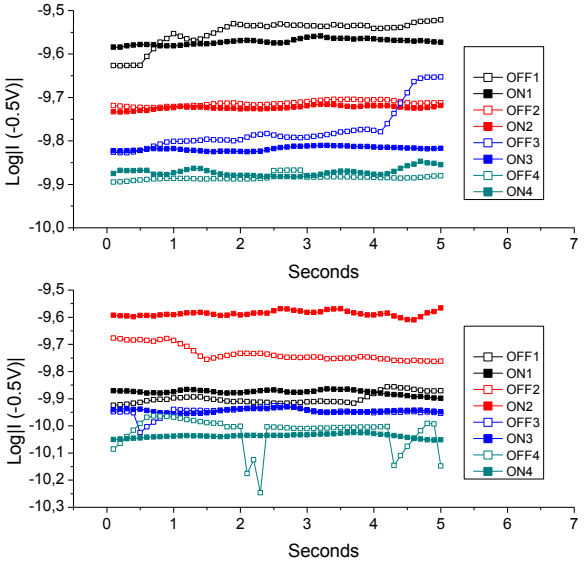

Figure 6.12 Examples of R_{ON} (solid symbols) and R_{OFF} (hollow symbols) for different Au^{TS}/**C16SH** //EGaIn for different cycles as reported in the legend.

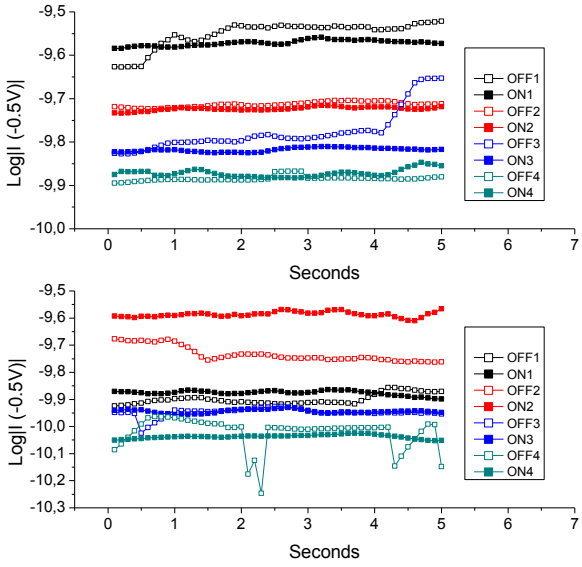

Figure 6.13 Examples of R_{ON} (solid symbols) and R_{OFF} (hollow symbols) for different Au^{mica}/**AQ**//EGaIn for different cycles as reported in the legend.

6.5. DISCUSSION OF THE MECHANISM

As we introduced in Chapter 5, in its pristine state, a destructive QI feature is clearly present in the transmission spectrum near E_f (Figure 6.14A).[50] Indeed, in Chapter 5 we observed how in single-molecule STM break-junctions comprising **TCNAQ**, this QI feature manifests as a low conductance, comparable to that of **AQ**, which is known to exhibit strong destructive QI effects in both single molecule and SAM-based junctions.[6, 32]

We already explained how the presence of a fraction of molecules in a high-conductance (reduced) state can drastically affect the conductance of a monolayer. In the case of **TCNAQ**, this make its SAM as conductive as those of **AC** rather than **AQ**. The reduced molecules on the surface form spontaneously during the SAM formation which happens under thermodynamic control: in the junction, when a bias is applied, the high electric field that forms can shift the equilibrium concentration of reduced molecules thus affecting the overall conductance; we can assume the formation of this new state to happen fast compared to the measurement time-scale, then the molecules in the monolayer

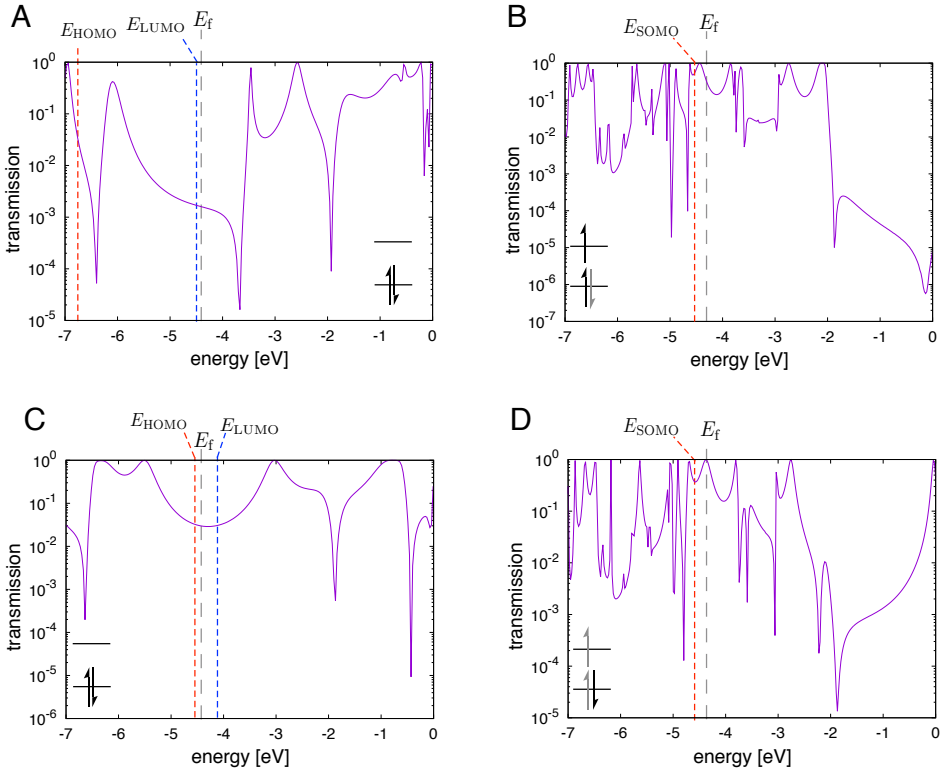

Figure 6.14 Transmission plots from DFT calculations corrected using experimental values. The energies E_{LUMO} and E_{SOMO} are shown using vertical dashed lines obtained using the experimental values from CV (Fig. 6.17). E_{HOMO} for **TCNAQ** was estimated by subtracting the onset of absorption (525 nm from E_{LUMO} from CV, Fig. 6.16) and taken from DFT for **TCNAQ**H_2, hence the large difference in E_g between the two. A) Neutral **TCNAQ**. B) The α spin channel of **TCNAQ**$^{\bullet -}$. C) Neutral **TCNAQ**H_2, the formally-reduced hydroquinoid form of **TCNAQ** in which the cross-conjugation has been deliberately broken by the addition of H_2. D) The β spin channel of **TCNAQ**$^{\bullet -}$. The gray, vertical dashed line corresponds to $E_f = -4.3$ eV. The electron configuration of the frontier orbitals relative to neutral **TCNAQ** is shown in the insets. The corrected values place the energies of E_{LUMO} and E_{SOMO} very close to E_F, in agreement with our proposed mechanism of switching. The sharp dip and depressed transmission near E_F for **TCNAQ** are absent for both spin channels of **TCNAQ**$^{\bullet -}$, but the influence of the conjugation patterns is more clearly resolved in the comparison between the two neutral species, **TCNAQ** and **TCNAQ**H_2.

Table 6.2 Incremental percentage variation of current during Read operations repeated after 5 and 20 minutes from the standard Read after a Write (ON) or Erase (OFF) operations.

	5'	+15'
ON	-31 ± 3 %	-14 ± 4 %
OFF	+4 ± 10 %	-7 ± 9 %

need to reorganize to minimize the free energy under biased condition. This generates a new stable state which accounts for the minimum energy in the system under the electric field. When we remove the bias, the system start to proceed back to its initial thermodynamic state, but this process is not instantaneous: unless energy is provided (as we do in WRER cycles), the system will go trough a series of thermodynamic minima before reaching the intial state. Kinetics become relevant for the retention of the information in the SAM. If the proposed mechanism is correct, the ON state is metastable and should slowly relax to lower conductance, since the thermodynamic minimum is the neutral, low-conductance state.

Indeed, the ON state current decreases in time with multiple read cycles, while the OFF state only shows small, stochastic fluctuations, as shown in Table 6.2. The initial ON/OFF ratio is restored after a new W cycle—*i.e.*, applying a pulse at negative bias restores the SAM to the initial state in which a greater fraction of **TCNAQ** is in the reduced state. After 5 min, without any applied bias, the ON/OFF ratio decreases to 70 % of its initial value; after 20 min it decreases to 60 %, meaning that it would take hours - if not days - for the ON state to go back to the OFF state.

6.6. STABILITY OF TCNAQ SAMS IN DIFFERENT ENVIRONMENTS

We proposed that the high conductance of molecular junctions comprising **TCNAQ** and their ability to show different conductance states, are arising from the contribution to the presence of reduced **TCNAQ** molecules in the assembly. These latter are generally stable in the SAM environment and are formed under thermodynamic conditions, yet, by considering the previous WRER measurements, it is clear how the ON/OFF Ratio and the OFF current are decreasing with the number of cycles. We argue here that this loss

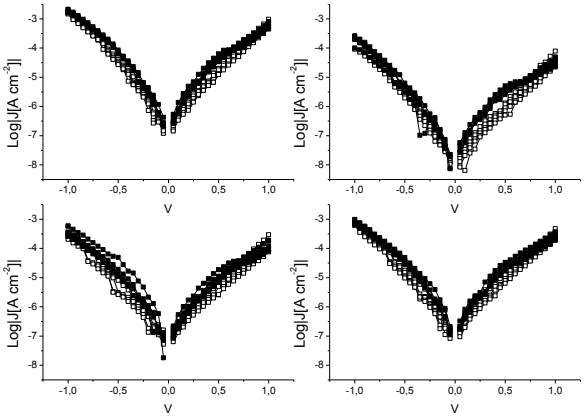

Figure 6.15 Examples of $Log|J|$ vs. V traces for Au^{TS}/**TCNAQ**//EGaIn junctions measured in ambient conditions ([O_2]= 21%; RH= 26%). Solid symbols represent forward traces from $-1V$ to $+1V$, hollow symbols reverse traces from $+1V$ to $-1V$.

in performance has to do with oxidative damage due to the presence of oxygen in the measurement environment and not with the intrinsic mechanism discussed. Unfortunately, oxygen is mandatory to form the sharp EGaIn tips used to form the junctions and cannot be completely removed during the experiments. Yet, by performing the measurements in an atmosphere with a level of O_2 between 1-3% (as described in Section 3), we can slow down the kinetics of the oxidation process thus limiting the damage to the system.[51]

When SAMs of **TCNAQ** are measured in ambient environment ([O_2]= 21%), their properties change drastically: as we can see in Figure 6.15, the current density is two order of magnitude lower than what was measured in the controlled atmosphere and the hysteresis is minimal (if at all present). When WRER operations are applied to these junctions no appreciable memory effect can be observed. These observation suggests that the level of oxygen found in air is enough to scavenge the reduced molecules and affect the properties of the SAM on the time-scale of the measurement.

If a sample is kept in the flowbox, at an oxygen concentration of 1-3%, the performances of **TCNAQ** SAMs on Au decrease more slowly. As we can see from Table 6.3, over a period of a week, both the ON/OFF ratio and the yield of working junctions tend to decrease with time, hinting to the limited stability to oxygen of the SAM more than the

Table 6.3 Summary of yield of working junctions and ON/OFF Ratios against aging time for **TCNAQ** SAMs stored in 1-3% oxygen.

	Yield	ON/OFF Ratio per n^{th} cycle				
	(%)	1^{st}	2^{nd}	3^{rd}	4^{th}	5^{th}
Day 1	100	7.3 ± 4.1	6.8 ± 2.6	6.0 ± 2.3	4.7 ± 1.0	4.5 ± 1.0
Day 2	75	4.8 ± 0.5	5.8 ± 0.26	5.1 ± 0.8	4.9 ± 0.45	4.5 ± 0.6
Day 3	50	3.6 ± 2.0	4.2 ± 0.5	5.0 ± 1.1	5.0 ± 0.7	4.3 ± 0.7
Day 6[a]	—	2.7	5.0	3.3	3.3	4.6

[a]We could only measure one junction.

measurement conditions (we assume that these latter speed up the degradation process during WRER cycles).

6.7. CONCLUSIONS

Metal/**TCNAQ**//EGaIn junctions are a form of non-volatile memory; their state is retained when the power (bias) is removed. It is difficult to contextualize **TCNAQ** further. There are examples of memory effects in molecular tunneling junctions, each demonstrating a salient feature: some exhibit high switching ratios as single-molecules, but not in (proto-)device platforms;[42, 47] some require prohibitively complex fabrication;[40] some only switch at low temperature;[33] some are resistant to fatigue when switched with light, but not with bias.[52] In simple, two-terminal proto-devices, **TCNAQ** exhibits reasonably high ON/OFF ratios that are stable for tens of minutes and that can be refreshed or re-written over at least dozens of cycles. The switching mechanism is phenomenologically unique, exploiting the coincidental alignment of a destructive QI feature and facile reduction with the Fermi level and work function of Au to enable the shift of a dynamic equilibrium of molecules in high-conductance states lacking QI features and low-conductance states with strong QI features near the Fermi level. The switching effect is molecular in nature, and further investigation and optimization can feasibly exploit this type of QI-based switching to achieve switching ratios of orders of magnitude.

6.8. EXPERIMENTAL SECTION

MATERIALS

All reagents were purchased from Sigma-Aldrich, Acros, or TCI Europe and used as received unless otheriwse stated. Triethylamine and $CHCl_3$ were distilled over CaH and P_2O_5 respectively, and used within 10 days. Toluene was obtained anhydrous from a house system. Hexadecanethiol (**C16SH**) was purified by coloumn cromatography (silica, hexane, R_f= 0.85). NMR spectra were recorded on a Varian AMX400 (400MHz) and referenced to the solvent peak ($CDCl_3$: H, 7.26 ppm; C, 77 ppm) relative to tetramethylsilane. The preparation of S,S'-(((9,10-bis(dicyanomethylene)-9,10-dihydroanthracene-2,6-diyl)bis(ethyne-2,1-diyl))bis(4,1-phenylene)) diethanethioate (**TCNAQ**) was reported in Chapter 5. S,S'-((anthracene-2,6-diylbis(ethyne-2,1-diyl))bis(4,1-phenylene)) diethanethioate (**AC**) and S,S'-(((9,10-anthraquinone-2,6-diyl)bis(ethyne-2,1-diyl))bis(4,1-phenylene)) diethanethioate (**AQ**) were prepared elsewere.[6] Template stripped metal substrates were prepared by depositing a 100 nm-thick layer of metal on a Si wafer in a metal evaporator (Au and Ag) or by e-beam (Pt). 1x1x0.3 cm glass slides were glued to the deposited metal using an UV-curable optical adhesive (Norland series 60). The samples were cleaved from the wafer with the help of a razor and immediately used. Au-on-mica (1x1 cm, 200 nm thick Au) was obtained from Phasis and kept in the original packing in a glovebox until use.

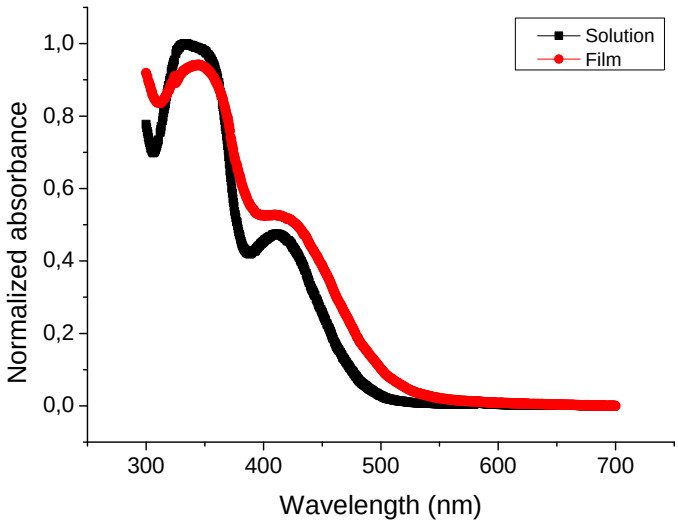

Figure 6.16 Normalized absorption spectra of **TCNAQ** : 50 μM in $CHCl_3$ (black), and drop-cast thin-film (red).

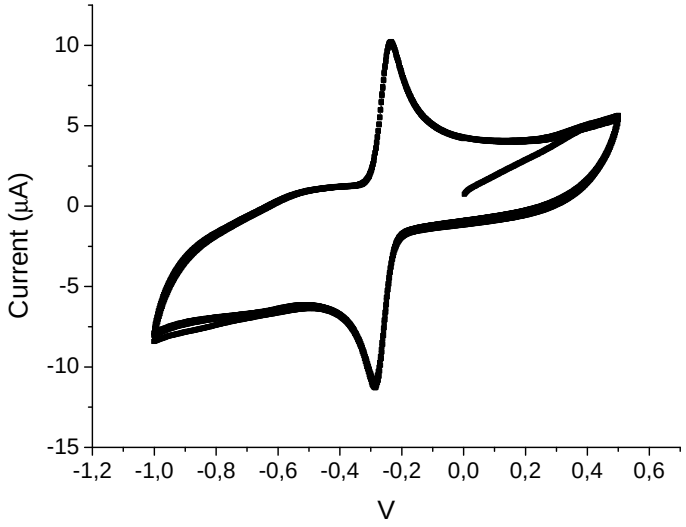

Figure 6.17 Cyclic voltammetry of **TCNAQ** 0.1 mM in acetonitrile vs. Ag/AgCl. A LUMO energy of -4.3 eV can be extracted from the plot. From the data we can extrapolate a LUMO for **TCNAQ** of −4.5 eV using the procedure reported by Huo *et al.*.[53]

PREPARATION THE SAMS

All the SAMs were prepared under nitrogen atmosphere, via *in situ* deprotection. Au^{mica} samples were prepared according to the procedure described in Chapter 5; Au^{TS}, Ag^{TS}, and Pt^{TS} samples were prepared with a procedure similar to that described in Chapter 2. SAMs of **C16SH** on Au^{TS} were prepared by immersion of the metal substrates in 3 mL of a 3 mM solution of **C16SH** in degassed ethanol overnight. The samples were then rinsed with ethanol and let to dry for 30 minutes before performing the measurements.

X-RAY PHOTOELECTRON SPECTROSCOPY

X-ray Photoelectron Spectroscopy (XPS) of **TCNAQ** SAMs on Au^{mica} and Au^{TS} was performed using a Surface Science SSX-100 ESCA instrument with a monochromatic Al K_α X-ray source ($h\nu$ = 1486.6 eV). The pressure in the measurement chamber was below 1×10^{-9} mbar during data acquisition. The electron take-off angle with respect to the surface normal was 37°. XPS spectra were analyzed using a least-squares curve fitting program (Winspec) developed in the LISE laboratory of the Facultés Universitaires Notre-Dame de la Paix (Namur, Belgium). The diameter of the analyzed area was 1 mm yielding a total experimental energy resolution of 1.1 eV. Deconvolution of

the spectra included a Shirley baseline subtraction and fitting with a minimum number of peaks consistent with the structure of the molecules on a surface, taking into account the experimental resolution.[54] The profile of the peaks was taken as a convolution of Gaussian and Lorentzian functions. Binding energies are reported ±0.1 eV and referenced to the Au 4f7/2 photoemission peak originating from the substrate, centered at a binding energy of 84 eV [55]. The uncertainty in the peak intensity determination is 2% for N and 1% S. All measurements were carried out on freshly prepared samples; on each surface 5 points were measured. The data reported for **TCNAQ** powder (Figure 6.2) were measured for a drop cast film on Au^{TS} (from 0.5 mM toluene solution): the blue and the black curves in the deconvolution of the N 1s spectra were ascribed to the cyano groups (399.5 eV) and the molecular 'shake-up' peak (402.4 eV) respectively;[22] the S 2p spectra shows a single peak at 163.6 eV from the two simmetrically identical thioacetate groups. Similar data were obtained for SAMs of **TCNAQ** on Au^{mica} (Figure 6.2): again, in the N 1s spectra we can find evidence of the cyano groups (399.6 eV) and the molecular 'shake-up' peak (402.6 eV) respectively. Anyway, compared to the powder spectra, an additional peak was observed at 398.5 eV that we attributed to an electron rich nitrogen species formed due to the charge transfer from the Au substrate to the **TCNAQ** SAM.[22] A single peak fit would necessarily leave a shoulder on the lower energy side while the use of the second peak allows a better fit of the data. The peak at 398.5 eV covers 14% of the total area of the signal. The S 2p spectra of the SAM is characterized by peaks at 164.0 eV and 161.8 eV (with an intensity ratio of 3:2) which characterize the unbound top sulfur and the S-Au bond respectively and that confirms that the molecules are indeed standing upright and bound to the metal.[11] Presence of unbound thiol and/or disulfide on the surface may contribute to the broad 164.0 eV peak.[23, 56] In Figure 6.3 we report the XPS data for SAMs of **TCNAQ** on Au^{TS}: in the N 1s spectra we found all the peaks that we reported previously in the case of the SAM on Au^{mica} with comparable binding energy and an extra peak at 400.8 eV that indicates the existence of N^+ group that we attributed to residual DBU in the SAMs.[23] The S 2p spectra shows peaks at 162.2 eV and 161.3 eV for the gold-sulfur bonds at the regular sites and step edges respectively,[23, 24] and at 164.2 eV and 163.5 eV for disulfide in the SAM and the unbound top thioacetate. **TCNAQ** SAMs on Au^{TS} are of lower quality compared to those on Au^{mica} but did not influence the memory effect.

EXPERIMENTS AT THE SYNCHROTRON

In addition to the laboratory characterization, synchrotron-based XPS and near-edge X-ray fine structure spectroscopy (NEXAFS) measurements were performed on the SAMs of **TCNAQ**; the monolayers were stored in containers for transport to the synchrotron and exposed to ambient

before and after the storage so that some degradation cannot be excluded. The experiments were carried out at the HE-SGM beamline (bending magnet) of the synchrotron storage ring BESSY II in Berlin, using a custom-made experimental station. The acquisition of the XPS spectra was conducted with a Scienta R3000 electron energy analyzer, in normal emission geometry, and at an excitation energy of 50 eV. The energy resolution was ~0.3 eV. The binding energy (BE) scale of the spectra was referenced to the Au $4f_{7/2}$ emission at 84.0 eV.[55] The acquisition of the NEXAFS spectra was carried out at the C K-edges in the partial electron yield mode with a retarding voltage of −50 V. As the primary X-ray source, linearly polarized synchrotron light with a polarization factor of ~88 % was used. The incidence angle of the X-rays, Θ was varied between the normal (Θ =90°) and grazing (Θ =20°) incidence geometry, to monitor the linear dichroism effects reflecting molecular orientation in the SAMs.[57] The photon energy (PE) scale was referenced to the pronounced $\pi*$ resonance of highly oriented pyrolytic graphite at 285.38 eV.[58] Raw NEXAFS spectra were normalized to the incident photon flux by division through a spectrum of a clean, freshly sputtered gold sample and subsequently reduced to the standard form.[57]

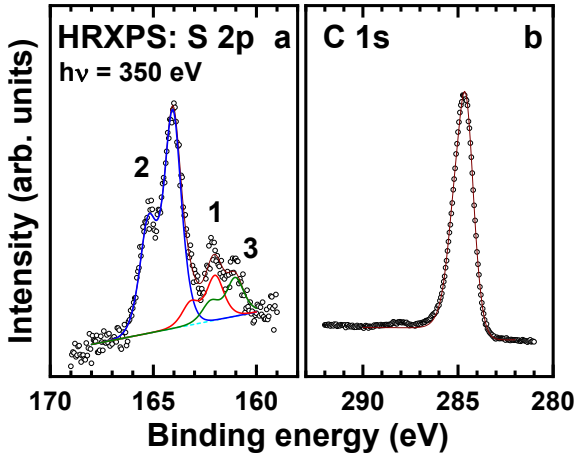

Figure 6.18 Synchrotron-based S 2p (a) and C 1s (b) XPS spectra of **TCNAQ** on Au. The S 2p spectrum is decomposed into individual doublets, drawn by different colors and marked by numbers (see text for details).

The S 2p (a) and C 1s (b) XPS spectra of **TCNAQ** on Au are presented in Figure 6.18. The S 2p spectrum in Figure 6.18a exhibits three doublets associated with thiolate bound to Au (at 162.0 eV; **1**), unbound S (at 164.0 eV; **2**), and atomically bound S (at 161.0 eV; **3**).[59] The presence of doublet **1** confirms the bonding and SAM-like assembly of **TCNAQ** on Au. The much lower intensity of this doublet as compared to **2** is related to the strong attenuation of the photoelectron signal for the

"buried" thiolate groups at the given kinetic energy of photoelectrons (~180 eV),[60] suggesting, at the same time, an upright molecular orientation. The presence of doublet **3** is presumably related to contamination or breakage of S-C bonds in some of the adsorbed molecules. The C 1s spectrum in Figure 6.18b exhibits a slightly asymmetric single peak associated with the molecular backbone of **TCNAQ**. The slight asymmetry is presumably related to the contribution of the nitrile group.[61, 62] The N 1s spectrum (not shown) exhibits a single peak at 399.5 eV, associated most likely with the contribution of the nitrile group.

Based on the C1s/Au4f and S2p(thiolate)/Au4f intensity ratios, the effective thickness and the packing densities of the **TCNAQ** monolayer on Au were calculated using standard procedures.[63, 64] For the thickness evaluation, a standard expression for the attenuation of the photoemission signal was assumed[60] and the literature values for the attenuation lengths were used.[65] The spectrometer-specific coefficients were determined by using an octadecanethiolate (C18) SAM on Au as a reference, relying on the well-known thickness of this monolayer (20.9(1) Å). In a similar fashion, this SAM (4.63×10^{14} cm^{-2})[66] served as a reference for the packing densities evaluation. According to the above evaluation, the effective thickness and the packing densities of the **TCNAQ** monolayer on Au were estimated at 18.7(4) Å and 2.3×10^{14} cm^{-2}, respectively.

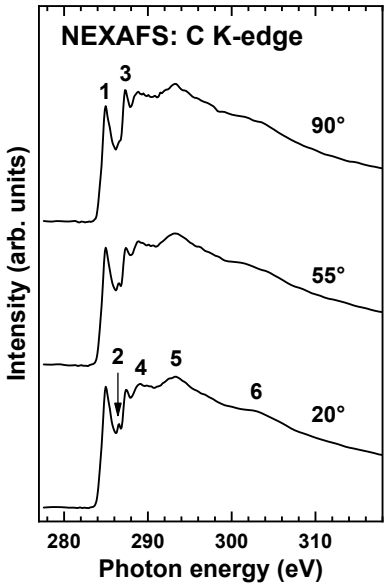

Figure 6.19 C K-edge NEXAFS spectra of the **TCNAQ** monolayer on Au acquired at X-ray incidence angles of 90°, 55°, and 20°. The spectra are shifted vertically for comparison. Characteristic absorption resonances are marked by numbers (see text for details).

The C K-edge NEXAFS spectra of the **TCNAQ** monolayer on Au acquired at X-ray incidence angles of 90°, 55°, and 20° are shown in Figure 6.19. These spectra exhibit a variety of characteristic absorption resonances. A π_1^* resonance **1** at ~285.0 eV is related to the molecular backbone of **TCNAQ** which is, presumably, also the case for π_2^* resonance **3** at 287.4 eV.[57, 61, 62] The σ^*-like resonances **4**-**6** at 289.0 eV, 293.0 eV and 303.0 eV are related to the molecular backbone, exhibiting a typical pattern for monomolecular films.[61, 62] Most interesting is however resonance **2** at 286.5 eV, which can be unequivocally ascribed to the nitrile groups of **TCNAQ**,[61, 62] supporting thus the intact character of the adsorbed molecules. Significantly, the intensity of this π^* resonance is higher at the grazing incidence as compared to the normal one, which, in view of the orientation of the respective $\pi*$ orbitals (perpendicular to the C-N bond), suggests that the nitrile groups of **TCNAQ** are predominantly oriented parallel to the substrate. Accordingly, the molecular backbones should be oriented upright. Since the other resonances in Figure 6.19, and especially the most pronounced resonance **2**, do not reveal much dichroism, the average molecular inclination in the **TCNAQ** film is presumably close to 35°, which is 90° to 55° (magic angle).

ACQUISITION AND PROCESSING OF DATA

$J-V$ CURVES

All the electrical characterizations were performed in a controlled nitrogen atmosphere containing 1-3% O_2 and RH< 15% introduced in Chapter 2. Data for SAMs of **TCNAQ** on Au^{TS} and Au^{mica}, **AQ** and **AC** on Au^{mica} were presented in Chapter 5; data for **AC** on Au^{TS} were presented in Chapter 4. For **TCNAQ** SAMs on Ag^{TS} or Pt^{TS}, 2 samples were measured with 10 junction per sample; for SAMs of **C16SH** on Au^{TS}, 2 sample were prepared and at least 5 junctions per sample were measured. 5 scans from $0V \rightarrow 1V \rightarrow -1V \rightarrow 0V$, (steps of 0.05 V, 0.1 s delay between steps) were collected for each junction. A new EGaIn tip was prepared every 3-5 junctions and flattened by gently pushing it on a Si wafer a few times according to the procedure reported by Simeone et al.[67] These data were parsed in a "hands-off" manner using Scientific Python to produce histograms of J for each value of V , the associated Gaussian fits (using a least-squares fitting routine) as described elsewhere.[11] The yield was calculated as number of junctions that did not produce a short circuit during the complete scanning cycles over the total number of probed junctions. We prepared mixed monolayers of **C16SH**/**TCNAQ** on Au^{TS} by immersing a freshly prepared sample of **C16SH** in 3 mL of a 50 µmol solution of **TCNAQ** in dry toluene followed by addition of 0.05 mL of 17 mM diazabicycloundec-7-ene (DBU) solution in dry toluene 1.5 hours prior the measurement as reported previously for SAMs of pure **TCNAQ**. When mixed monolayers **C16SH**/**TCNAQ**

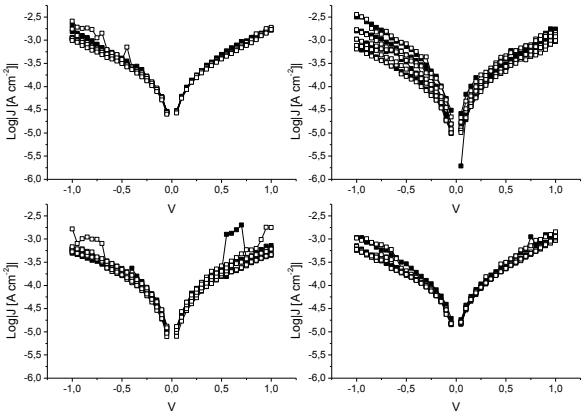

Figure 6.20 Examples of $Log|J|$ vs. V traces for Au/SAM//EGaIn junctions comprising mixed-monolayers of **C16SH** and **TCNAQ**. Solid symbols represent forward traces from $-1V$ to $+1V$, hollow symbols reverse traces from $+1V$ to $-1V$.

were prepared, the resulting junctions appeared to be more conductive compared to SAMs of pure **C16SH** but no hysteresis or memory effect were recorded (Figure 6.20)

To produce forward trace over reverse trace ratios (*F/R*, Figure 6.5), 10 junctions per system (5 traces per junction) were randomly selected and each forward trace was divided by the previous reverse trace to produce an array of values of *F/R* for each potential point that was used to compute the mean values. The error was presented as confidence interval ($\alpha = 0.05$), calculated from the standard deviation of these averages using 9 as degrees of freedom. The reason why we chose to take 10 random junctions for each system despite the fact that more were measured has to do with the comparison of the data sets between different molecules/substrates: increasing the number of junctions doesn't affect much the mean but reduces the error bars considerably, by plotting the same number of junctions for each examined system we can visually show the distribution of data in the set of a particular molecule/substrate system.

WRITE-READ-ERASE-READ (WRER) CYCLES

The WRER cycles measurements were carried on the same setup introduced in the previous subsection. A flattened EGaIn tip was brought in contact with the SAM and a bias of +1 V was applied for 30 seconds. This 'burning' operation was necessary in order to produce comparable results between different junctions: when not 'burned', the junctions gave extremely high but not reproducible ON/OFF ratios during the first 3-4 cycles (with values that spanned from 10 to more than 100); after 'burning', the junctions behaved in a much more similar manner and those were used

Table 6.4 Summary of EGaIn measurements data.

	Yield	*N* of junct.	Traces	LogJ(0.5 V)	$V_{trans}+$	$V_{trans}-$
TCNAQ Au	93%	15	75	-2.2 ± 0.2	0.53 ± 0.03	
TCNAQ Au mica	62%	45	225	-2.7 ± 0.2	0.51 ± 0.12	
TCNAQ Ag	100%	15	75	-2.4 ± 0.2	0.31 ± 0.05	
TCNAQ Pt	58%	15	75	-2.4 ± 0.2	0.56 ± 0.10	-0.50 ± 0.07
AC Au mica	61%	68	340	-2.5 ± 0.1	0.63 ± 0.14	-0.84 ± 0.12
C16SH Au	94%	17	85	-4.1 ± 0.2	0.60 ± 0.11	-0.75 ± 0.18
AQ Au mica	97%	34	170	-4.10 ± 0.2	0.21 ± 0.09	-0.28 ± 0.09

to produce the data. This points to the fact that in principle **TCNAQ** SAMs could be used to prepare devices with higher ON/OFF ratios than the ones reported in this study, but in this study we aim to characterize this effect using elements of statistical analysis. The WRER operations were performed by applying specific biases for certain periods of time and measuring the current: Read (R_{OFF}, R_{ON}; -0.5 V, 5 s); Write (W; -1.5 V, 10 s); Erase (E; +1 V, 10 s). After the initial 'burning', the junctions were found in the low conductance (OFF) state and cycles of WRER operations were carried on the same junction in the order $R_{OFF} \rightarrow W \rightarrow R_{ON} \rightarrow E$. Reads were carried on for 5 seconds, taking one point every 0.1 seconds, to ensure that the current was stable and not drifting with time; the reading bias was chosen observing the hysteresis loops obtained in the *J-V* plots. Erase and Write pulses were carried on for 10 seconds to allow the current at +1 V and -1.5 V to stabilize: surprisingly, changing the duration of the pulses down to 2.5 seconds did not affect the ON/OFF ratio, but the chances of shorting the junction in the latter scenario increased. The junctions were cycled for 20 times, after which the ON/OFF ratio usually dropped below 1.7, a value that we considered unsatisfactory. Junctions that produced a short before the 5th cycle (including during the burning) were considered non-working junctions and not included in the analyzed data. A summary of the yields and the number of junction measured per different molecule/substrate system are summarized in Table 6.5. A new EGaIn tip was formed every 3 working junctions or 3 shorts. Only 5 junctions (on 2 samples) were collected for **AC**, **AQ**, and **C16SH** as these measurements are time consuming and no effect was expected by looking at $J-V$ curves.

For every junction measured, to calculate the ON/OFF ratio for each n cycle, an array of values was created by dividing each single value of current recorded during the n^{th} R_{ON} (50 values in 5 seconds) by every single value of current during the n^{th} R_{OFF} (*i.e.* for each n cycle of a junction the array contained 50x50=2500 ON/OFF values). For each n cycle measured on different junc-

Table 6.5 Summary of EGaIn junctions used for the WRER experiments.

	WRER Yield	Number of junctions
TCNAQ Au	44%	31
TCNAQ Au mica	39%	17
TCNAQ Ag	20%	10
TCNAQ Pt	56%	5
AC	71%	5
C16SH	83%	5
AQ	60%	6

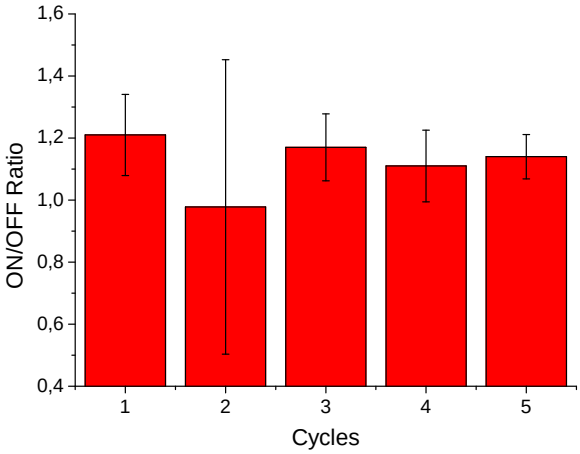

Figure 6.21 ON/OFF Ratio per n^{th} Write-Erase cycle, calculated as ratio of the current after and before the n^{th} Write operation for SAMs of **TCNAQ** on Au using $-1V$ for the Write operation. The error is calculated as confidence interval on 4 junctions with $\alpha = 0.05$.

tions of the same SAM/substrate system, we combined the aforementioned arrays and computed the mean and the standard deviation to obtain the final ON/OFF ratio. The error was presented as confidence interval ($\alpha = 0.05$), calculated from the standard deviation of these averages using the number of junctions - 1 as degrees of freedom. The ON/OFF ratio values obtained with the method mentioned above are comparable with those that can be more simply obtained by dividing for every n^{th} cycle the mean values of all the R_{ON} operations by the mean value of all the R_{OFF} operations but the aforementioned treatment is more rigorous. In Figure 6.21, we report the value of the ON/OFF ratio for 4 junctions in which a bias of $-1V$ was used to perform the W operation.

Table 6.6 ON/OFF Ratio per n^{th} Write-Erase cycle, calculated as ratio of the current after and before the n^{th} Write operation for SAMs of **TCNAQ** on Pt. The error is calculated as confidence interval with $\alpha = 0.05$

n of cycle	ON/OFF ratio
1	1.77 ± 0.35
2	1.52 ± 0.12
3	1.55 ± 0.16
4	1.42 ± 0.07

STABILITY OF TCNAQ JUNCTIONS DURING WRER OPERATIONS

We studied for how long the **TCNAQ** SAM was capable to retain the ON and the OFF states while not being constantly addressed by *R* operations. The junctions was pulsed W (or E) and the current read (R) immediately after, after 5 minutes, and after 15 additional minutes. No other bias was applied to the junction neither was the EGaIn tip moved during the time between reads. This study was performed on 6 different junctions (on 2 different samples) comprising SAMs of **TCNAQ** on Au^{TS}.

PROPERTIES OF JUNCTIONS COMPRISING SAMS OF **TCNAQ** ON Pt^{TS}

During $J-V$ sweeps characterization (measured as explained previously), we found that the current density of such system was similar to those of **TCNAQ** on the other metal substrates but no appreciable hysteresis loop was found (Figure 6.22). In order to see any effect, a larger bias window might be needed. The magnitude of hysteresis loop is bias dependent and a larger bias can indeed enhance small effects: in the case of **TCNAQ** SAMs on Pt^{TS} the hysteresis is noticeable if we extend the bias window until $-1.5V$ as we show in Figure 6.23. When performing WRER cycles (as described earlier), a small memory effect is present but its magnitude is drastically small when compared to the SAMs of the same compound on Au or Ag (Table 6.6). Seeing the limits of this system, we did not carry any further investigation.

CALCULATIONS

The calculations were performed using the *Orca 4* software package.[68, 69] The molecules were first minimized to find the gas-phase geometry and then single-point energy calculations were performed on both the gas-phase molecules and the molecules terminating with Sulphur atoms (*i.e.*, no terminal H atoms). This was also repeated for the reduced **TCNAQ** molecule. Transmission

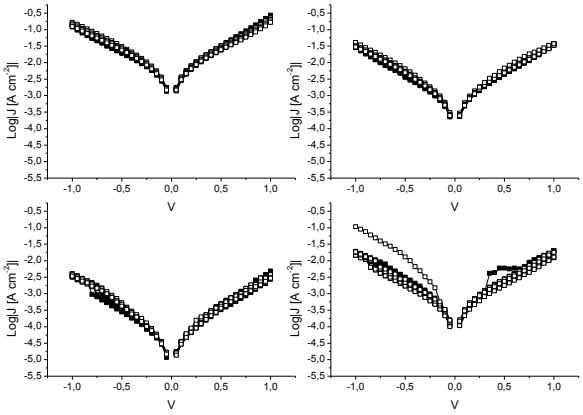

Figure 6.22 Examples of Log|J| vs. V traces for Pt/**TCNAQ**//EGaIn junctions. Hollow symbols represent forward traces from $-1V$ to $+1V$, solid symbols reverse traces from $+1V$ to $-1V$.

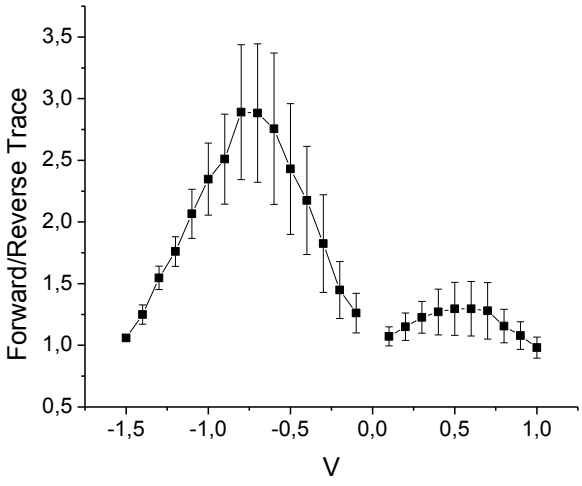

Figure 6.23 Plot of trace over retrace ratio for junctions comprising SAMs of **TCNAQ** on Pt. Compared to Figure 6.22 here the bias window spans down to $-1.5V$. Error bars represent confidence intervals with $\alpha = 0.05$.

curves were generated using the *Artaios-030417* software package on the molecules terminating with S atoms.[70]

GEOMETRY OPTIMIZATION

We optimized the neutral and the reduced forms of **TCNAQ** molecules with the hydrogens removed from the terminal thiol groups using the *Orca* software package.[68, 69] We minimized the geometries using BP/def2-SVP (BP functional, Ahlrichs split-valence basis set) with tight SCF and geometry convergence criteria, which can be accessed with the '! Acc-Opt' command.[71] Note that the removal of the hydrogen atoms broadens the terminal sulfurs compared to thiols.

SINGLE POINT ENERGY CALCULATIONS

We computed the single-point energies of the optimized geometries using B3LYP/LANL2DZ (B3LYP functional, Los Alamos double-valence basis set). We used the Gaussian-style B3LYP functional and tight SCF convergence criteria, which can be accessed with the '! DFT B3LYP/G LANL2DZ TIGHTSCF' command. We chose this functional/basis-set combination because it is recommended by the authors of the software used for transport calculations.[72]

TRANSPORT PROPERTIES

We followed the same procedures as described by Zhang *et al.*.[73] For computing the electron transmission probability plots as function of the energy of electron, we first ran single point energy calculations on molecules without hydrogen atoms on terminal sulphur groups as described in Section 6.8. The Hamiltonian (Fock) and overlap matrices were generated from the output of these energy calculations with the commands 'Print[P_Iter_F] 1', 'Print[P_Overlap] 1', 'Print[P_Mos] 1', 'Print[P_InputFile] 1' in the '%output' section. In the case of the radical anions, Hamiltonian matrices were generated for the α and β spin states. The Hamiltonian and overlap matrices were then used as inputs for *Artaios-030417* to generate the transmission curves using the non-equilibrium Green's function [70, 72] This method separates the finite cluster system into a bulk calculation / approximation for the electrodes and a central subsystem that may or may not include some of the atoms from the electrodes. We omitted the electrodes and computed the transmission between the terminal sulfur atoms. We chose E_f value of -4.3 eV[74, 75] to scale the $E - E_f$ energy axis shown in the Main Text. This value is both an approximation of the work function of Ga-In and the value of Au modified with a thiol-SAM.[76]

We omitted the electrodes because we could not capture the collective effects of the SAM, particularly in a mixed-state of neutral and reduced molecules. Thus, the energies of the orbitals

for the two anionic forms, **TCNAQ**$^{\bullet-}$ and **TCNAQ**$^{2-}$ were pushed very close to vacuum due to the absence of electrodes, counterions, solvation and the near-by molecules that would be present in a SAM. Figure 6.24 shows the physically unrealistic result of these calculations, which places unoccupied orbitals below E_f in some calculations and occupied above E_f in others. The doubly-reduced species, **TCNAQ**$^{2-}$ is particularly illustrative, placing both frontier orbitals just below 0 eV.

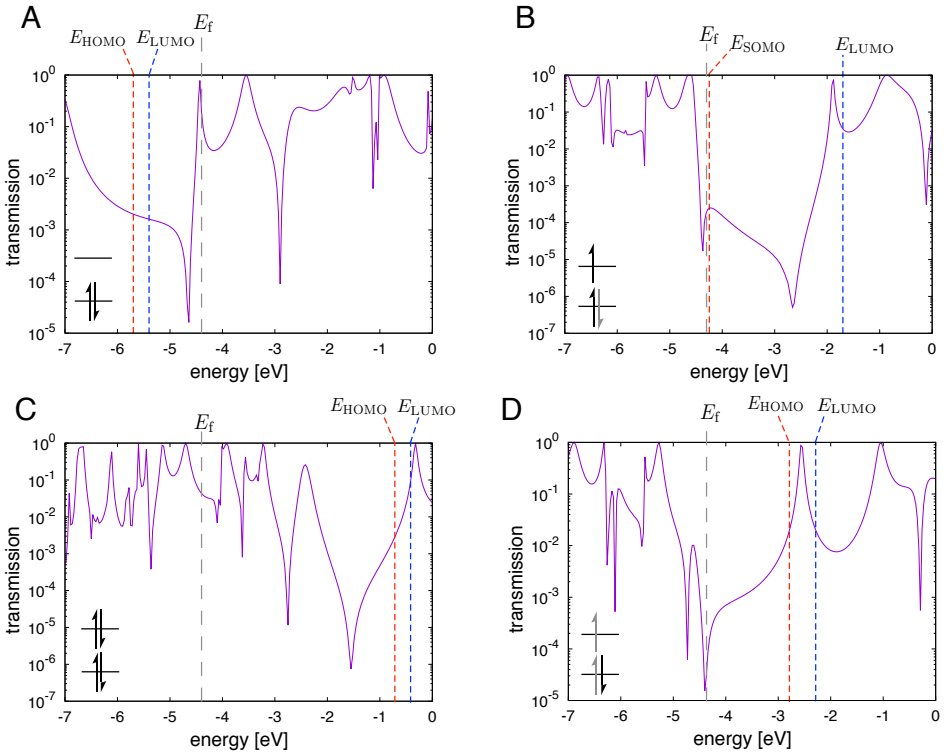

Figure 6.24 Transmission plots from uncorrected DFT calculations. A) Neutral **TCNAQ**. B) The α spin channel of **TCNAQ**$^{\bullet-}$. C) **TCNAQ**$^{2-}$. D) The β spin channel of **TCNAQ**$^{\bullet-}$. The gray, vertical dashed line corresponds to $E_f = -4.3$ eV. The electron configuration of the frontier orbitals relative to neutral **TCNAQ** is shown in the insets. The uncorrected orbital energies under-estimate the HOMO/LUMO gap of **TCNAQ** and, due to the lack of counterions and solvation, shift the orbitals of the reduced species close to vacuum.

To try to compensate for the unknowables and assumptions in the DFT calculations, we re-plotted the transmission curves using experimental values taken from CV (Fig. 6.17) and UV-Vis (Fig. 6.16) data, which provide the energies of the LUMO and SOMO of **TCNAQ** and **TCNAQ**$^{\bullet-}$ (from CV) and the frontier orbital gap of **TCNAQ** (from UV-Vis), from which the HOMO can be estimated. Note that this is a linear shift that does not correct the under-estimated E_g, which

would broaden the dip near E_f, but would not affect the interpretation of the results. Figure 6.14 shows the results of these calculations, which place the LUMO and SOMO orbtials very close in energy to $E_f = -4.3$ eV[74–76], which is both the estimated work function of EGaIn and of Au accounting for the vacuum-level shift imposed by thiol-SAMs. The loss of the suppressed transmission and sharp dip near $E_f = -4.3$ eV for **TCNAQ** is evident in both the α and β spin channels of **TCNAQ**$^{\bullet -}$. We interpret this difference as the loss of QI when the cross-conjugated core of **TCNAQ** is replaced by the linearly-conjugated core that is expected to be (by far) the dominant resonance structure of **TCNAQ**$^{\bullet -}$, however, the introduction of unpaired spins strongly affects the features of the transmission plots. Thus, we also plotted the formally reduced, but neutral hydroquinoid form, **TCNAQ**H_2, in which the cross-conjugation is deliberately removed by the addition of H_2. The comparison between **TCNAQ** and **TCNAQ**H_2 clearly highlights the role of conjugation patterns. Taken together, the data in Fig. 6.14 support our proposed mechanism, which localizes spin and charge on the central carbons of the malononitrile substituents, favoring the rearomatization of the anthracene core.

BIBLIOGRAPHY

[1] Garner, M. H.; Li, H.; Chen, Y.; Su, T. A.; Shangguan, Z.; Paley, D. W.; Liu, T.; Ng, F.; Li, H.; Xiao, S.; Nuckolls, C.; Venkataraman, L.; Solomon, G. C. *Nature* **2018**, *406*, 1.

[2] Schwarz, F.; Koch, M.; Kastlunger, G.; Berke, H.; Stadler, R.; Venkatesan, K.; Lörtscher, E. *Angew. Chem., Int. Ed.* **2016**, *55*, 11781–11786.

[3] Chen, S.; Zhou, W.; Zhang, Q.; Kwok, Y.; Chen, G.; Ratner, M. A. *J. Phys. Chem. Lett.* **2017**, *8*, 5166–5170.

[4] Tsuji, Y.; Hoffmann, R.; Movassagh, R.; Datta, S. *J. Chem. Phys.* **2014**, *141*, 224311–.

[5] Markussen, T.; Stadler, R.; Thygesen, K. S. *Nano Lett.* **2010**, *10*, 4260–4265.

[6] Fracasso, D.; Valkenier, H.; Hummelen, J. C.; Solomon, G. C.; Chiechi, R. C. *J. Am. Chem. Soc.* **2011**, *133*, 9556–9563.

[7] Pedersen, K. G. L.; Borges, A.; Hedegård, P.; Solomon, G. C.; Strange, M. *J. Phys. Chem. C* **2015**, *119*, 26919–26924.

[8] Manrique, D. Z.; Huang, C.; Baghernejad, M.; Zhao, X.; Al-Owaedi, O. a.; Sadeghi, H.; Kaliginedi, V.; Hong, W.; Gulcur, M.; Wandlowski, T.; Bryce, M. R.; Lambert, C. J. *Nat. Commun.* **2015**, *6*, 6389.

[9] Gantenbein, M.; Wang, L.; Al-jobory, A. A.; Ismael, A. K.; Lambert, C. J.; Bryce, M. R. *Sci. Rep.* **2017**, *7*, 1794.

[10] Solomon, G. C.; Herrmann, C.; Vura-Weis, J.; Wasielewski, M. R.; Ratner, M. A. *J. Am. Chem. Soc.* **2010**, *132*, 7887–7889.

[11] Carlotti, M.; Kovalchuk, A.; Wächter, T.; Qiu, X.; Zharnikov, M.; Chiechi, R. C. *Nat. Commun.* **2016**, *7*, 13904.

[12] Jeong, H.; Kim, D.; Xiang, D.; Lee, T. *ACS Nano* **2017**, *11*, 6511–6548.

[13] Selzer, Y.; Cai, L.; Cabassi, M. A.; Yao, Y.; Tour, J. M.; Mayer, T. S.; Allara, D. L. *Nano Lett.* **2005**, *5*, 61–65.

[14] Jia, C. et al. *Science* **2016**, *352*, 1443–1445.

[15] Liu, Z.; Ren, S.; Guo, X. *Top. Curr. Chem.* **2017**, *375*, 56–.

[16] Yang, G. et al. *Chem. Sci.* **2017**, *8*, 7505–7509.

[17] Liu, J.; Zhao, X.; Al-Galiby, Q.; Huang, X.; Zheng, J.; Li, R.; Huang, C.; Yang, Y.; Shi, J.; Manrique, D. Z.; Lambert, C. J.; Bryce, M. R.; Hong, W. *Angew. Chem., Int. Ed.* **2017**, *56*, 13061–13065.

[18] Koole, M.; Thijssen, J. M.; Valkenier, H.; Hummelen, J. C.; Zant, H. S. J. v. d. *Nano Lett.* **2015**, *15*, 5569–5573.

[19] Baghernejad, M.; Zhao, X.; Baruël Ørnsø, K.; Füeg, M.; Moreno-García, P.; Rudnev, A. V.; Kaliginedi, V.; Vesztergom, S.; Huang, C.; Hong, W.; Broekmann, P.; Wandlowski, T.; Thygesen, K. S.; Bryce, M. R. *J. Am. Chem. Soc.* **2014**, *136*, 17922–17925.

[20] Markussen, t.; Schitz, J.; Thygesen, K. S. *The Journal of Chemical Physics* **2010**,

[21] Valkenier, H.; Huisman, E. H.; van Hal, P. A.; de Leeuw, D. M.; Chiechi, R. C.; Hummelen, J. C. *J. Am. Chem. Soc.* **2011**, *133*, 4930–4939.

[22] Tseng, T.-C. et al. *Nat. Chem.* **2010**, *2*, 374–.

[23] Kumar, S.; van Herpt, J. T.; Gengler, R. Y. N.; Feringa, B. L.; Rudolf, P.; Chiechi, R. C. *J. Am. Chem. Soc.* **2016**, *138*, 12519–12526.

[24] Ishida, T.; Hara, M.; Kojima, I.; Tsuneda, S.; Nishida, N.; Sasabe, H.; Knoll, W. *Langmuir* **1998**, *14*, 2092–2096.

[25] Chiechi, R. C.; Weiss, E. A.; Dickey, M. D.; Whitesides, G. M. *Angew. Chem., Int. Ed.* **2008**, *120*, 148–150.

[26] Dickey, M. D.; Chiechi, R. C.; Larsen, R. J.; Weiss, E. A.; Weitz, D. A.; Whitesides, G. M. *Adv. Funct. Mater.* **2008**, *18*, 1097–1104.

[27] Cademartiri, L.; Thuo, M. M.; Nijhuis, C. A.; Reus, W. F.; Tricard, S.; Barber, J. R.; Sodhi, R. N. S.; Brodersen, P.; Kim, C.; Chiechi, R. C.; Whitesides, G. M. *J. Phys. Chem. C* **2012**, *116*, 10848–10860.

[28] Garcìa, R.; Ángeles Herranz, M.; Leary, E.; Gonzàlez, M. T.; Bollinger, G. R.; Bürkle, M.; Zotti, L. A.; Asai, Y.; Pauly, F.; Cuevas, J. C.; Agraít, N.; Martín, N. *Beilstein Journal of Organic Chemistry* **2015**, *11*, 1068–1078.

[29] Kovalchuk, A.; Egger, D. A.; Abu-Husein, T.; Zojer, E.; Terfort, A.; Chiechi, R. C. *RSC Adv.* **2016**, *6*, 69479–69483.

[30] Pourhossein, P.; Vijayaraghavan, R. K.; Meskers, S. C. J.; Chiechi, R. C. *Nat. Commun.* **2016**, *7*, 11749–.

[31] Weiss, E. A.; Chiechi, R. C.; Kaufman, G. K.; Kriebel, J. K.; Li, Z.; Duati, M.; Rampi, M. A.; Whitesides, G. M. *J. Am. Chem. Soc.* **2007**, *129*, 4336–4349.

[32] Kaliginedi, V.; Moreno-García, P.; Valkenier, H.; Hong, W.; García-Suárez, V. M.; Buiter, P.; Otten, J. L. H.; Hummelen, J. C.; Lambert, C. J.; Wandlowski, T. *J. Am. Chem. Soc.* **2012**, *134*, 5262–5275.

[33] Chen, J.; Reed, M. A.; Rawlett, A. M.; Tour, J. M. *Science* **1999**, *286*, 1550–.

[34] Chen, J.; Reed, M. *Chem. Phys.* **2002**, *281*, 127–145.

[35] Blum, A. S.; Kushmerick, J. G.; Long, D. P.; Patterson, C. H.; Yang, J. C.; Henderson, J. C.; Yao, Y.; Tour, J. M.; Shashidhar, R.; Ratna, B. R. *Nat. Mater.* **2005**, *4*, 167–.

[36] Gergel-Hackett, N.; Majumdar, N.; Martin, Z.; Swami, N.; Harriott, L. R.; Bean, J. C.; Pattanaik, G.; Zangari, G.; Zhu, Y.; Pu, I.; Yao, Y.; Tour, J. M. *J. Vac. Sci. Technol., A* **2006**, *24*, 1243–1248.

[37] Chen, Y.; Jung, G.-Y.; Ohlberg, D. A. A.; Li, X.; Stewart, D. R.; Jeppesen, J. O.; Nielsen, K. A.; Stoddart, J. F.; Williams, R. S. *Nanotechnology* **2003**, *14*, 462–.

[38] Collier, C. P.; Mattersteig, G.; Wong, E. W.; Luo, Y.; Beverly, K.; Sampaio, J.; Raymo, F. M.; Stoddart, J. F.; Heath, J. R. *Science* **2000**, *289*, 1172–.

[39] Wong, E. W.; Collier, C. P.; Běhloradský, M.; Raymo, F. M.; Stoddart, J. F.; Heath, J. R. *J. Am. Chem. Soc.* **2000**, *122*, 5831–5840.

[40] Green, J. E.; Wook Choi, J.; Boukai, A.; Bunimovich, Y.; Johnston-Halperin, E.; DeIonno, E.; Luo, Y.; Sheriff, B. A.; Xu, K.; Shik Shin, Y.; Tseng, H.-R.; Stoddart, J. F.; Heath, J. R. *Nature* **2007**, *445*, 414–.

[41] Seo, K.; Konchenko, A. V.; Lee, J.; Bang, G. S.; Lee, H. *J. Am. Chem. Soc.* **2008**, *130*, 2553–2559.

[42] Lee, J.; Chang, H.; Kim, S.; Bang, G.; Lee, H. *Angew. Chem., Int. Ed.* **2009**, *48*, 8501–8504.

[43] Pradhan, B.; Das, S. *Chem. Mater.* **2008**, *20*, 1209–1211.

[44] Seo, K.; Konchenko, A. V.; Lee, J.; Bang, G. S.; Lee, H. *J. Mater. Chem.* **2009**, *19*, 7617–7624.

[45] Li, C.; Fan, W.; Lei, B.; Zhang, D.; Han, S.; Tang, T.; Liu, X.; Liu, Z.; Asano, S.; Meyyappan, M.; Han, J.; Zhou, C. *Appl. Phys. Lett.* **2004**, *84*, 1949–1951.

[46] Li, C.; Ly, J.; Lei, B.; Fan, W.; Zhang, D.; Han, J.; Meyyappan, M.; Thompson, M.; Zhou, C. *J. Phys. Chem. B* **2004**, *108*, 9646–9649.

[47] Seo, S.; Lee, J.; Choi, S.-Y.; Lee, H. *J. Mater. Chem.* **2012**, *22*, 1868–1875.

[48] Min, M.; Seo, S.; Lee, S. M.; Lee, H. *Adv. Mater.* **2013**, *25*, 7045–7050.

[49] others,, et al. *Nanoscale* **2014**, *6*, 11246–11258.

[50] Valkenier, H.; Guedon, C. M.; Markussen, T.; Thygesen, K. S.; van der Molen, S. J.; Hummelen, J. C. *Phys. Chem. Chem. Phys.* **2014**, *16*, 653–662.

[51] Carlotti, M.; Degen, M.; Zhang, Y.; Chiechi, R. C. *J. Phys. Chem. C* **2016**, *120*, 20437–20445.

[52] Seo, S.; Min, M.; Lee, S. M.; Lee, H. *Nat. Commun.* **2013**, *4*, 1920–.

[53] Huo, L.; Zhou, Y.; Li, Y. *Macromol. Rapid Commun.* **2009**, *30*, 925–931.

[54] Shirley, D. A. *Phys. Rev. B* **1972**, *5*, 4709–4714.

[55] Moulder, J. F.; Stickle, W. F.; Sodhi, P. E., R. N. S.bol; Bomben, K. D. In *Handbook of X-Ray Photoelectron Spectroscopy: A Reference Book of Standard Spectra for Identification & Interpretation of XPS Data*; Chastain, J., Ed.; Perkin-Elmer, Physical Electronics Division, 1993.

[56] Ishida, T.; Choi, N.; Mizutani, W.; Tokumoto, H.; Kojima, I.; Azehara, H.; Hokari, H.; Akiba, U.; Fujihira, M. *Langmuir* **1999**, *15*, 6799–6806.

[57] Stohr, J. *NEXAFS Spectroscopy*; Springer-Verlag Berlin Heidelberg, 1992.

[58] Batson, P. E. *Phys. Rev. B* **1993**, *48*, 2608–2610.

[59] Zharnikov, M. *J. Electron Spectrosc. Relat. Phenom.* **2010**, *178–179*, 380–393.

[60] Ratner, B. D.; Castner, D. G. *Surface Analysis - The Principal Techniques*; John Wiley & Sons, Ltd, 1997; pp 47–112.

[61] Ballav, N.; Schüpbach, B.; Neppl, S.; Feulner, P.; Terfort, A.; Zharnikov, M. *The Journal of Physical Chemistry C* **2010**, *114*, 12719–12727.

[62] Hamoudi, H.; Kao, P.; Nefedov, A.; Allara, D. L.; Zharnikov, M. *Beilstein J. Nanotechnol.* **2012**, *3*, 12–24.

[63] Thome, J.; Himmelhaus, M.; Zharnikov, M.; Grunze, M. *Langmuir* **1998**, *14*, 7435–7449.

[64] Chesneau, F.; Schüpbach, B.; Szelagowska-Kunstman, K.; Ballav, N.; Cyganik, P.; Terfort, A.; Zharnikov, M. *Physical chemistry chemical physics : PCCP* **2010**, *12*, 12123–12137.

[65] Lamont, C.; Langmuir, J. W.; 1999, *ACS Publications*

[66] Matter, F. S. J. o. P. C.; 2004, *iopscience.iop.org*

[67] Simeone, F. C.; Yoon, H. J.; Thuo, M. M.; Barber, J. R.; Smith, B.; Whitesides, G. M. *J. Am. Chem. Soc.* **2013**, *135*, 18131–18144.

[68] Neese, F. *Wiley Interdiscip. Rev.: Comput. Mol. Sci.* **2012**, *2*, 73–78.

[69] Neese, F. *Wiley Interdisciplinary Reviews: Computational Molecular Science*

[70] Herrmann, C.; Gross, L.; Steenbock, T.; Deffner, M.; Voigt, B. A.; Solomon, G. C. ARTAIOS - A Transport Code for Postprocessing Quantum Chemical Electronic Structure Calculations, Available From https://www.chemie.uni-hamburg.de/ac/herrmann/software/index.html. 2016.

[71] Weigend, F.; Ahlrichs, R. *Phys. Chem. Chem. Phys.* **2005**, *7*, 3297–3305.

[72] Herrmann, C.; Solomon, G. C.; Subotnik, J. E.; Mujica, V.; Ratner, M. A. *J. Chem. Phys.* **2010**, *132*, 024103.

[73] Zhang, Y.; Ye, G.; Soni, S.; Qiu, X.; Krijger, T. L.; Jonkman, H. T.; Carlotti, M.; Sauter, E.; Zharnikov, M.; Chiechi, R. C. *Chem. Sci.* **2018**, *9*, 4414–4423.

[74] Abu-Husein, T.; Schuster, S.; Egger, D. A.; Kind, M.; Santowski, T.; Wiesner, A.; Chiechi, R.; Zojer, E.; Terfort, A.; Zharnikov, M. *Advanced Functional Materials 25*, 3943–3957.

[75] Kovalchuk, A.; Abu-Husein, T.; Fracasso, D.; Egger, D. A.; Zojer, E.; Zharnikov, M.; Terfort, A.; Chiechi, R. C. *Chem. Sci.* **2016**, *7*, 781–787.

[76] Cabarcos, O. M.; Schuster, S.; Hehn, I.; Zhang, P. P.; Maitani, M. M.; Sullivan, N.; Giguère, J.-B.; Morin, J.-F.; Weiss, P. S.; Zojer, E.; Zharnikov, M.; Allara, D. L. *The Journal of Physical Chemistry C* **2017**, *121*, 15815–15830.

SUMMARY

This thesis focus on the design of π-conjugated molecules of interest in the field of Molecular Electronics and the characterization of their electric properties in large-area tunnelling junctions comprising self-assembled monolayers (SAMs) obtained using an eutectic gallium-indium alloy (EGaIn) as top electrode.

In **Chapter 2** we developed a new methodology for the reliable characterization of the electronic properties of the tunnelling junctions comprising SAMs of fully conjugated oligo(phenylene-ethynylenes) molecular wires (OPEs). One can overcome the difficulties that arises when trying to characterize such systems via standard techniques by carefully controlling the atmosphere where the measurements are carried: the use of an oxygen concentration between 1 and 3% and a relative humidity below 15% was demonstrated to be optimal for the characterization of the molecular junctions. We were able to obtain a tunnelling decay coefficient for OPE wires in agreement with other values presented in the literature measured on different experimental platforms and we proved that the new conditions only affect the contact between the SAM without altering the transport mechanism. We ascribe this result to the different rehology of the EGaIn tip under these new conditions.

In **Chapter 3** we made use of the versatility of the OPE structure in being easily chemically modified without altering the molecular geometry to investigate the effect on the charge transport characteristics of molecular dipoles and the degree of interaction with the electrodes. Initially, we study SAMs of difluorinated OPEs characterized by identical molecular formula but different dipoles moments obtained by changing the substitution pattern. We found no correlation between the transport properties and the dipole, with the only exception being the derivative characterized by the fluorine atoms as close as possible to the bottom electrode surface. We then controlled the degree of interaction with the electrode by comparing the latter compounds with their analogues bearing an

extra methylene unit between the metal and the conjugated part: such modification resulted in a more symmetric current density vs. potential curve, pointing indeed to the weaker interaction of the molecular states with the substrate. Adding the methylene unit also allows for a reduced tilt angle of the molecules which could translate to a better alignment of the dipoles: while we were able to measure these changes experimentally, the effect of the dipoles in these systems appear to be rather limited. We finally, investigated the effect on the charge transport of other polar groups (pyridino, methoxy, sulfide) with particular attention to their influence at the SAM-EGaIn interface. We find that, in the case of OPEs, the presence of polar groups at the interfaces and the degree of interaction with the electrode affects the electric characteristics of the junctions more than the internal dipoles do. In particular, we found the injection current to scale with the expected free energy of the surface. We also reported a new mechanism of rectification for the pyridine-terminated molecules, which involves the creation of new interfacial states in the EGaIn oxide layer stabilized by the interaction between the pyridine nitrogen and gallium.

In **Chapter 4** we explored the effects on tunnelling transport of through-space conjugation. In particular we characterize the electrical properties of SAMs of compounds in which π-conjugated fragments are arranged face-on or edge-on and hold in close proximity by short σ-spacers. These two conformations are predicted to lead to destructive quantum interference, but, as we showed in our calculations, even small distortions of the molecular skeleton may cancel the expected effect. We found that the observation of these effects requires trapping molecules in a non-equilibrium conformation, as it is the case in SAMs. In contrast, interference effects are not present in simulations on the equilibrium, gas-phase conformation.

In **Chapter 5** we examined further the relations between bond topology and quantum interference in tunnelling junctions. In particular we investigated a series of molecular wires characterized by an identical cross-conjugated anthraquinoid skeleton but bearing different substituents that affect the energies and localization of their frontier orbitals and that can tune the quantum interference effects. We discussed in depth the design principles and the synthesis of these compounds. We compared experimental results

across three different experimental platforms, including both single-molecule and large-area junctions, and combined them with theoretical models in order to separate the intrinsic properties of the molecules from other platform-specific effects. We elucidate the role of the electronic charcteristics of the wire with respect of geometrical considerations and found a remarkable qualitative agreement between the different experimental methods.

In **Chapter 6** we discussed the peculiar case of a redox-active molecular wire introduced in the previous chapter. In particular we showed that SAMs of the latter undergo a partial charge transfer with the underlying metal which change the bond topology of the core: this results in a variation of the conductance without changing the connectivity of the tunnelling length. We then exploit this phenomena to realize novel, two-terminal, non-volatile memory proto-devices that are based on the on-off switching of destructive quantum interference.

NEDERLANDSE SAMENVATTING

Dit proefschrift richt zich op het ontwerp van belangrijke -geconjugeerde moleculen in Moleculaire Elektronica en het karakteriseren van hun elektronische eigenschappen in tunnel aansluitingen met een groot oppervlak, bestaande uit zelf-geassembleerde monolagen (SAMs) verkregen door het gebruik van een eutetisch gallium-indium legering (eGaIn) als top electrode.

In **Hoofdstuk 2** ontwikkelden wij een nieuwe procedure voor het betrouwbaar karakteriseren van elektronische eigenschappen van de tunnel aansluitingen bestaande uit SAMs van volledig geconjugeerde oligo(fenyleen-ethynyleen) moleculaire draden (OPEs). Men kan de problemen voorkomend bij standaard technieken bij het karakteriseren van deze systemen overwinnen door voorzichtig de omgeving waar de metingen worden uitgevoerd te beheren: het gebruik van een zuurstof concentratie tussen 1 en 3% en een relatieve luchtvochtigheid onder 15% betoogd optimaal te zijn voor het karakteriseren van de moleculaire aansluitingen. We waren in staat om een tunnel vervaling coëfficiënt voor OPE draden te verkrijgen in overeenkomst met andere waardes die zijn gepresenteerd in de literatuur gemeten met verschillende experimentele platformen en we bewezen dat de nieuwe omstandigheden alleen het contact tussen de SAM beïnvloed zonder het transport mechanisme te veranderen.

In **Hoofdstuk 3** gebruikten wij het makkelijk chemisch veranderen van de veelzijdigheid van de OPE-structuur zonder de moleculaire geometrie te veranderen om het effect op de lading transport eigenschappen van moleculaire dipolen en de hoeveelheid interactie met de electroden te onderzoeken. In de eerste instantie bestuderen wij SAMs van gedifluoreerde OPEs gekarakteriseerd door identieke moleculaire formules met verschillende dipool momenten verkregen door het veranderen van het substitutie patroon. Wij hebben geen correlatie tussen de transport eigenschappen en de dipool gevonden, met als enige uitzondering de afwijking gekarakteriseerd door de fluor atomen gelokaliseerd

zo dicht mogelijk bij het onderste electrode oppervlak. Daarna regelden wij de hoeveelheid interactie met de elektrode door het vergelijken van de laatst genoemde substantie met soortgelijke materie met een extra methyleengroep tussen het metaal en geconjugeerde deel: deze modificatie resulteerde in een meer symmetrische stroomdichtheid vs. potentieel kromme, inderdaad wijzend op de zwakkere interactie van de moleculaire staten met het substraat. Het toevoegen van de methyleengroep resulteert ook in een gereduceerde hellingshoek van de moleculen wat omgezet kan worden naar een betere uitlijning van de dipolen: het was mogelijk voor ons om deze veranderingen experimenteel te meten, echter bleek het effect van de dipolen in het deze systemen gelimiteerd te zijn. Uiteindelijk onderzochten wij het effect van het lading transport van andere polaire groepen (pyridino, methoxy, sulfide) met excessieve aandacht aan hun influentie bij het SAM-EGaIn grensvlak. Wij constateren dat, in het geval van OPEs, de aanwezigheid van polaire groepen bij de grensvlakken en de hoeveelheid interactie met de electrode beïnvloeden de elektronische karakteristieken van de aansluitingen meer als de interne dipolen. In het bijzonder constateerden wij dat de injectie stroom in nabijheid van de verwachte vrije energie van de oppervlakte komt. Ook rapporteerden wij een nieuw mechanisme van het gelijkrichten van de pyridine-getermineerde moleculen, waarbij het ontstaan van nieuwe grensvalk-stadia in de EGaIn oxide laag is betrokken, gestabiliseerd door de interactie tussen de pyridinestikstof en gallium.

In **Hoofdstuk 4** onderzochten wij de effecten van tunnel transport van conjugatie door ruimte. In bijzonder karakteriseren wij de elektronische eigenschappen van SAMs van materie waarin -geconjugeerde fragmenten face-on of edge-on zijn gearrangeerd en samengehouden worden in nabije afstand door korte -afstandshouder. Voorspelt is dat deze twee conformaties leiden tot destructieve kwantum interferentie, maar, zoals getoond in onze calculaties, zelfs kleine vervormingen van het moleculaire skelet kunnen het verwachte effect opheffen. Wij constateerden dat voor de observatie van deze effecten het vangen van moleculen in een niet-evenwichtige conformatie benodigd is, zoals in SAMs. Echter zijn interferentie effecten niet aanwezig in simulaties van het evenwicht in gas fase conformatie.

In **Hoofdstuk 5** bestudeerden wij de relaties tussen binding topologie en kwantum

interferentie in tunnel aansluitingen dieper. In bijzonder onderzochten wij een serie van moleculaire draden gekarakteriseerd door een identieke kruis-geconjugeerde antrachinoïde skelet met verschillende substituanten die de energieën en lokalisatie van de grenzende orbitalen beïnvloeden en die de kwantum interferentie effecten kunnen afstemmen. We discussieerden grondig de ontwerp principepen en de synthese van deze stoffen. We vergeleken experimentele resultaten over drie verschillende experimentele platformen, waaronder aansluitingen met één enkel molecuul en een groot oppervlak, en combineerden deze met theoretische modellen om zo de intrinsieke eigenschappen van de moleculen van de andere platform specifieke effecten te scheiden. Wij lichten de rol van de elektronische karakteristieken van de draad toe met betrekking tot geometrische overwegingen en constateerden een opvallende kwalitatieve overeenkomst tussen de verschillende experimentele methodes.

In **Hoofdstuk 6** discussieerden wij het eigenaardige vraagstuk van een redox-actief moleculaire draad geïntroduceerd in het vorige hoofdstuk. In bijzonder lieten we zien dat SAMs van het laatst genoemde materiaal een partiele lading verandering met de onderliggende metaal ondergaan die de binding topologie van de kern veranderen: dit resulteert in een variatie van de geleidbaarheid zonder de connectiviteit van de tunnel lengte te veranderen. We exploiteren dit fenomeen om nieuwe, duo-terminale, niet-vluchtige geheugen proto-apparaten te realiseren die zijn gebaseerd op het aan- en uitschakelen van destructieve kwantum interferentie.